



University
of Cyprus

DEPARTMENT OF PHYSICS

**SIMULATIONS OF MOLECULAR
TRANSITIONS INVOLVING SPIN,
CHARGE AND ENERGY
TRANSFORMATIONS**

DOCTOR OF PHILOSOPHY DISSERTATION

SPYROULLA A. MAVROMMATI

2022



University
of Cyprus

DEPARTMENT OF PHYSICS

**SIMULATIONS OF MOLECULAR
TRANSITIONS INVOLVING SPIN,
CHARGE AND ENERGY
TRANSFORMATIONS**

DOCTOR OF PHILOSOPHY DISSERTATION

SPYROULLA A. MAVROMMATI

A dissertation submitted to the University of Cyprus in partial fulfillment
of the requirements for the degree of Doctor of Philosophy

DECEMBER 2022

SPYROULLA A. MAVROMMATI

VALIDATION PAGE

Doctoral Candidate: Spyroulla A. Mavrommati

Doctoral Thesis Title: Simulations of molecular transitions involving spin, charge and energy transformations

*The present Doctoral Dissertation was submitted in partial fulfillment of the requirements for the degree of Doctor of Philosophy at the **Department of Physics** and was approved on the 15/12/2022 by the members of the **Examination Committee**.*

Examination Committee:

Research Supervisor: Spiros S. Skourtis, Assoc. Prof., Dept. of Physics, UCY.

Committee Member: Theodossis Trypiniotis, Asst. Prof., Dept. of Physics, UCY.

Committee Member: Grigorios Itskos, Assoc. Prof., Dept. of Physics, UCY.

Committee Member: Anastasios J. Tasiopoulos, Prof., Dept. of Chemistry, UCY.

Committee Member: Igor Schapiro, Sen. Lec., Inst. of Chemistry, HUJI.

DECLARATION OF DOCTORAL CANDIDATE

The present doctoral dissertation was submitted in partial fulfillment of the requirements for the degree of Doctor of Philosophy of the University of Cyprus. It is a product of original work of my own, unless otherwise mentioned through references, notes, or any other statements.

Spyroulla A. Mavrommati

ΠΕΡΙΛΗΨΗ

Στην παρούσα Διδακτορική Διατριβή περιγράφουμε έρευνα σχετική με μοριακές διεργασίες μεταφοράς ενέργειας (ή εξιτονίων) τριπλής κατάστασης (METK) και μεταφοράς φορτίου (ΜΦ). Μέρος της διατριβής εξηγεί πειραματικά αποτελέσματα χρονοεξαρτημένου ηλεκτρονικού παραμαγνητικού συντονισμού (ΧΗΠΣ) σε ένα οργανικό μόριο, που παρατηρούν την ‘απαγορευμένη’ μεταβαση από την βασική απλή ηλεκτρονιακή κατάσταση σε τριπλές διεγερμένες καταστάσεις. Το φάσμα ΧΗΠΣ που προέρχεται όταν το μόριο φωτοδιεγείρεται σε περιοχή πολύ ασθενούς οπτικής απορρόφησης είναι της ίδιας έντασης με αυτό που προέρχεται όταν το μόριο φωτοδιεγείρεται σε περιοχή μέγιστης οπτικής απορρόφησης. Για να εξηγήσουμε το πειραματικό αποτέλεσμα χρησιμοποιήσαμε θεωρητικά μοντέλα και χβαντικούς *ab-initio* υπολογισμούς. Η ανάλυσή μας δείχνει ότι το φαινόμενο οφείλεται στην αλληλεπίδραση ιδιοστροφορμής-τροχιακής στροφορμής (spin-orbit coupling). Η σύζευξη ιδιοστροφορμής-τροχιακής στροφορμής ανάμεσα στις απλές και τριπλές ηλεκτρονιακές καταστάσεις επιτρέπει την άμεση μετάβαση από την βασική ηλεκτρονιακή κατάσταση σε τριπλές καταστάσεις, λόγω της φωτοδιέγερσης. Οι υπολογισμοί μας δείχνουν ότι ο πληθυσμός στις τριπλές καταστάσεις είναι της ίδιας τάξης μεγέθους και για τις δύο περιοχές οπτικής απορρόφησης, και αυτός είναι ο λόγος που το σήμα ΧΗΠΣ είναι της ίδιας έντασης.

Το άλλο μέρος της διατριβής προτείνει αρχές σχεδιασμού μοριακών καλωδίων (molecular wires) τα οποία μπορούν να χρησιμοποιηθούν ως γέφυρες σε μοριακά συστήματα δότη - γέφυρας - δέκτη και τα οποία υποστηρίζουν εξαιρετικά γρήγορη METK σε πολύ μεγάλες αποστάσεις (τάξης νανομέτρων). Οι αρχές σχεδιασμού εφαρμόζονται σε πολυμερικά μόρια με π-stacked γεωμετρία ανάμεσα στις γειτονικές μονάδες μονομερών. Σύμφωνα με τις αρχές αυτές, η εσωτερική ενέργεια αναδιοργάνωσης μονομερούς πρέπει να ελαχιστοποιηθεί, και οι αλληλεπιδράσεις π-stacked μεταξύ γειτονικών μονομερών πρέπει να είναι μέγιστες, χωρίς δυναμική παραμόρφωση της γεωμετρίας. Τα χαρακτηριστικά αυτά οδηγούν σε τριπλές καταστάσεις εξιτονίων της γέφυρας οι οποίες είναι απεντοπισμένες σε όλη την γέφυρα ακόμα και σε θερμοκρασία δωματίου. Παραθέτουμε διάφορες πιθανές δομές που ικανοποιούν τα πιο πάνω κριτήρια. Για αυτές τις δομές προσομοιώνουμε την METK χρησιμοποιώντας χβαντικούς υπολογισμούς *ab-initio* ηλεκτρονιακής δομής, προσομοιώσεις μοριακής δυναμικής, και μοντέλα μήτρας πυκνότητας. Οι υπολογισμοί προβλέπουν πολύ γρήγορους ρυθμούς μετάβασης METK κατά μήκος των μοριακών γεφυρών της τάξης των 2 πικοδευτερολέπτων ακόμα και για γέφυρες μεγέθους 50 μονομερών.

Το τελευταίο μέρος της διατριβής περιγράφει δύο επιπρόσθετες μελέτες. Η πρώτη, αφορά την μοντελοποίηση METK ανάμεσα σε CdSe χβαντική τελεία (quantum dot) και σε οργανικό μόριο. Η δεύτερη, αφορά την χβαντική προσομοίωση ρυθμών ΜΦ ανάμεσα σε δύο μόρια γουανίνης. Οι μελέτες αυτές σχετίζονται με πειραματικά δεδομένα.

ABSTRACT

This Ph.D. thesis describes research work on triplet energy transfer (TET) and charge transfer (CT) processes in molecular systems. The first major part of the thesis relates to unusual experimental observations of time-resolved electron paramagnetic resonance (TR-EPR) spectra of an organic molecule. The TR-EPR spectra following optical excitation within a highly absorbing region of the molecule have similar intensities as the TR-EPR spectra following optical excitation within the non-absorbing region. Our analysis, using theoretical models and *ab-initio* quantum chemical computations, demonstrates that this phenomenon is due to an initial-state preparation effect of direct photoexcitation from the singlet ground state to excited triplet states. The direct photoexcitation leads to similar triplet-state populations for both optical excitation regions. Due to the low intersystem crossing rates from the excited singlet states, these initial triplet populations determine the intensities of the EPR spectra.

The other major part of the thesis focuses on the design of organic π -stacked molecular bridges that enable coherent TET over long distances. We propose design principles for optimizing the speed of bridge-mediated TET. These design rules imply low inner-sphere exciton reorganization energies, low static and dynamic disorder and enhanced π -stacking interactions between nearest-neighbor chromophores. These features lead to triplet exciton eigenstates that are delocalized over several units even at room temperature. We propose various molecular structures that satisfy these criteria and that can be used as bridging wires linking triplet donors to acceptors. We perform *ab-initio* electronic structure computations, molecular dynamic simulations and density matrix simulations. The computations predict fast TET along the proposed molecular bridges, with effective intra-bridge TET rates of the order of 2 psec for bridge lengths of up to 50 chromophore units.

In addition, the thesis describes smaller projects that involve modeling of TET between a CdSe quantum dot and an organic molecule, and modeling of quantum-vibrational effects of hole-transfer rates between guanine molecules. These projects are motivated by experiments.

ACKNOWLEDGMENTS

My utmost gratitude goes to my supervisor and my mentor, Associate Prof. Spiros S. Skourtis, who gave me continuous support, guidance, and valuable suggestions and advices. I appreciate all his contributions of ideas that brought my knowledge and research to a higher level. His patience with me was wonderful and I have been extremely lucky to work under his supervision all these years.

I also gratefully acknowledge Prof. Panayiotis A. Koutentis for his extensive advice and critical comments in molecular synthesis.

My sincere gratitude goes to Prof. David N. Beratan and his group members at Duke University USA, for helpful and insightful discussions and for a wonderful collaboration.

I would also like to thank the rest of my examination committee members: Assistant Prof. Theodossis Trypiniotis, Associate Prof. Grigorios Itskos, Prof. Anastasios J. Tasiopoulos and my external committee member Associate Prof. Igor Schapiro, for letting my defense be an enjoyable moment, and for their brilliant comments and feedback.

I am extremely grateful to the IT technicians of the department of Physics at the University of Cyprus, Dr. Marios Constantinou and Nicolas Kouvaros for their patience and invaluable help all these years. I could not have done my research without them.

I am also grateful for having been financially supported by the U.S. Department of Energy, Office of Basic Energy Sciences under Award DE-SC0019400, and by the Physics Department of the University of Cyprus.

I would like to thank my friends and fellow students for their love and support and for making my student life enjoyable. Special thanks should be given to my colleagues Georgia Polycarpou, Eleni Michael and Stavros Christodoulou, who were always there for me when I needed them, for believing in me and for continuous support and understanding.

Last but foremost, I specially want to thank my beloved family, my parents Andreas and Eleni, and my sister Neophyta for their endless love, support and encouragement during this long journey, especially during the hard times of writing this project.

Dedicated to my late grandmother

SPYROULLA A. MAVROMMATI

CONTENTS

List of Figures	xi
List of Tables	xxiv
1 Introduction	1
2 Quantum non-adiabatic rates in molecules and their classical limits	4
2.1 Introduction	4
2.2 Theory of non-adiabatic quantum rate in donor-acceptor complexes . .	8
2.3 Quantum rate constants for two independent sets of vibrational coordi- nates	11
2.4 Homogeneous and inhomogeneous lineshape broadening	12
2.5 Applications	14
2.5.1 Optical absorption coefficient and fluorescence efficiency	15
2.5.2 Intersystem crossing rates	16
2.5.3 Singlet and triplet energy transfer rates	16
2.5.4 Electron and hole transfer rates	20
3 The spin-orbit coupling interaction in molecules	21
3.1 Introduction	21
3.2 Derivation of the SOC Hamiltonian from the Dirac equation	23
3.3 The SOC Hamiltonian of a many-electron molecule	25
3.4 Matrix elements of the SOC operator	26
3.5 SOC in organic compounds	31
3.6 Conclusions	33
4 Quantum mechanical description of the dynamics of open quantum systems	34
4.1 The Density operator	35

4.2	Time evolution of the density operator	36
4.3	The Liouville space approach	37
4.4	The reduced density operator	39
4.5	Quantum master equation within Markov approximation	40
4.6	The Bloch equations	42
5	Principles of electron paramagnetic resonance	46
5.1	Introduction	46
5.2	Quantum mechanical description of spin in external magnetic field	48
5.3	The Bloch equations for the EPR experiment in the rotating frame	51
5.4	Sensitivity of the ground-state EPR experiment	53
5.5	The TR-EPR experiment	54
5.6	The spin-spin coupling and the zero-field splitting	55
5.6.1	Derivation of the spin-Hamiltonian	56
5.6.2	The EPR absorption pattern of a triplet state	59
5.7	Sensitivity of the TR-EPR experiment	61
6	Initial-state preparation effects in time-resolved electron paramagnetic resonance experiments	62
6.1	Introduction	62
6.2	Theoretical methods	64
6.2.1	Direct triplet formation mechanism for excitation energies below the CT band	66
6.2.2	Direct triplet formation mechanism for excitation energies within the CT band	68
6.2.3	Indirect triplet formation mechanism for excitation within the CT band	68
6.3	Computational methodology	69
6.4	Results and discussion	72
6.4.1	Direct excitation to triplet excited states from the ground state	73
6.4.2	Indirect (ISC) triplet formation mechanism for excitation within the CT band	77
6.4.3	Triplet state formation mechanism in the ground state	80
6.4.4	Sensitivity analysis	81
6.4.5	Excitation-wavelength dependence of the TR-EPR spectrum	86
6.5	Conclusions	90
	Supplementary material	91
6.6	Computation of the lowest singlet and triplet excited states of Cbz-TBT molecule	91
6.6.1	Calculation of the metric of CT molecular excitations and overcoming triplet instability problems in TD-DFT	91

6.6.2	The choice of the appropriate functional	94
6.6.3	Excited-state computations performed with CIS	97
6.7	Spin-Orbit Coupling effects	98
6.7.1	The SOC Hamiltonian in the framework of the zeroth-order approximation	98
6.7.2	SOC integrals between singlet-triplet and triplet-triplet states for the different geometric conformations of the Cbz-TBT molecule	98
6.8	Optical properties of the Cbz-TBT molecule for the different geometric conformations	100
6.8.1	Energy level diagram with the lowest singlet and triplet excitations of the Cbz-TBT molecule computed for the different geometric conformations	100
6.8.2	Derivation of the molar extinction coefficient equation	101
6.8.3	Absorption spectrum of the Cbz-TBT molecule computed for the different geometries	102
6.9	Geometric structures of the Cbz-TBT molecule	103
6.9.1	Geometric structures of ground and excited states of Cbz-TBT	103
6.9.2	Energy barrier for the conformational transitions between minimum energy PES of the T_1 manifold along the torsional angles θ_1 and θ_2	104
6.10	Populations of the Cbz-TBT molecules in the sample	106
6.10.1	Number of Cbz-TBT molecules in the ground state	106
6.10.2	Calculation of the population transfer to the T_1 manifold upon direct photoexcitation below the CT band	107
6.10.3	Calculation of the population transfer to the T_2 manifold upon direct photoexcitation inside the CT band	107
6.10.4	Number of photoexcited Cbz-TBT molecules in the S_1^{SOC} state	110
6.10.5	Calculation of the initial spin polarizations of the T_1 manifold in the presence of the external magnetic field B_0	111
6.10.6	Calculation of the ZFS polarizations of the T_1 manifold	115
6.11	Computation of singlet-to-triplet and triplet-to-triplet transition rates	116
6.12	Theoretical calculations of the EPR parameters	118
6.12.1	Zero-field splitting parameters	118
6.12.2	EPR g-tensor	126
6.12.3	Anisotropic spectra broadenings - D-strains	126
7	Computation of the non-adiabatic transition rates	127
7.1	MATLAB coding for the ISC rates using the ADF program for normal mode computations	127
7.2	Effects of temperature on hole transfer rates between two guanine molecules and the transition from the quantum to the classical rate limit	133

8	Molecular wires for efficient long-distance triplet exciton transfer	138
8.1	Introduction	138
8.2	Results and Discussion	142
8.3	Conclusions	149
	Supplementary material	150
8.4	Summary of the computational methodologies for the IF _n bridges . . .	150
8.5	SE and TE states of the IF _n bridges with n = 1,2,6,10	154
8.6	Comparison between CIS (TD-DFT) and higher-level methods for the TE energies of the IF dimer	160
8.7	Testing the accuracy of the TE energies of the donor-bridge-acceptor systems using higher-level basis sets	161
8.8	Computation of the IPR parameters	162
8.9	SE and TE computations on the perylene-based dyads	163
8.10	TET and SET couplings as a function of the inter-chromophore distance	166
8.11	Distance dependence of the intra-bridge TET rate	167
8.12	Ground state structures of the proposed IF bridges	168
9	Triplet excitation energy transfer between quantum dots and organic molecules	176
9.1	Introduction	176
9.2	A brief description of the experimental observation	177
9.3	Theoretical computations on the molecule and the QD	179
9.4	Conclusions and future work	181
10	Conclusions	182
	Bibliography	184
	Appendices	206
A	Computation of the reorganization energies using ADF	207
B	Short-time approximation of the quantum Franck-Condon factor to examine temperature effects	210
C	Intersystem crossing rates computed using the orca.asa program	214
D	MATLAB code for computing the ZFS parameters	223
E	MATLAB code for computing the MFPTs	228

LIST OF FIGURES

2.1	Schematic view of the PES of the initial I and final F states in the harmonic approximation model, shown as one-dimensional (single mode α) representation of frequency ω_α . The vibrational energy levels $E_{n_{I,\alpha}} = \hbar\omega_\alpha (n_{I,\alpha} + \frac{1}{2})$ and $E_{n_{F,\alpha}} = \hbar\omega_\alpha (n_{F,\alpha} + \frac{1}{2})$ are shown together with the squares of the vibrational wavefunctions $\langle n_{I,\alpha} n_{I,\alpha} \rangle, \langle n_{F,\alpha} n_{F,\alpha} \rangle$ superposed on them. Their energies differ from each other by $\hbar\omega_\alpha$. The overlaps between the vibrational wavefunctions belonging to the electronic state I and those belonging to the electronic state F ($\langle n_{I,\alpha} n_{F,\alpha} \rangle$) are shown in bold. The inset is a similar figure on a different scale where the mode reorganization energy λ_α is clearly shown.	7
2.2	PES of the initial I and final F electronic states indicating the definition of the activation energy E_{act}	10
2.3	PES of the donor (D) and acceptor (A) parts for the case of independent vibrational coordinates (see figure 2.1). <i>left</i> . PES of the positively charged and neutral donor. <i>Right</i> . PES of the neutral and positively charged acceptor.	13
2.4	PES in a simplified form, of the donor (D) and acceptor (A) parts for the case of independent vibrational coordinates showing the donor and acceptor mode reorganization energies.	14
2.5	Electronic structure of a 4-electron exciton system consisting two donor (D)-acceptor (A) fragments. $\psi_{D(A)}$ and $\psi_{D^*(A^*)}$ are the ground- and excited-state molecular orbitals respectively, of the $D(A)$ fragment. <i>left</i> : the ground state electronic configuration of the $D - A$ system. <i>middle</i> : an electron is promoted from the D ground state to the D excited state to generate the initial excited configuration of the system. <i>right</i> : The excited electron is transferred to the acceptor to generate the final excited configuration of the system.	17

2.6	(a) Electronic structure configuration of a ground-state ET reaction. The excess electron is initially on the donor and then it transferred to the acceptor. (b) Electronic structure configuration of a ground-state HT process. The hole is transferred from the donor to the acceptor.	20
3.1	Schematic representation of the effect of the angular momentum operators \hat{l}_x and \hat{l}_z on the p_y and p_x atomic orbitals respectively (see eq. 3.27). The positive directions of the Cartesian axes show the positive ends of the p atomic orbitals. For example, when \hat{l}_x operates p_y , p_y undergoes 90° rotation around x -axis (counterclockwise) to get p_z	29
3.2	(a) Schematic representation of the effects of the \hat{l}_x , \hat{l}_y and \hat{l}_z operators on the p_y orbital of the nitrogen atom in a monoazine. (b) Schematic diagram of the SOC matrix element between p atomic orbitals. <i>Above:</i> The SOC matrix element between the same orbitals e.g., between the two p_y orbitals is zero since the overlap between p_y and p_z is zero. <i>Below:</i> The SOC matrix element between p_y and p_z orbitals when \hat{l}_x operates, is strong because the overlap between two p_y orbitals is non-zero.	32
5.1	Energy level diagram for $S = 1/2$ system as a function of the applied magnetic field B_0 . In zero magnetic field ($B_0 = 0$) the electron spin energy levels are degenerate. Application of external magnetic field ($B_0 > 0$) lifts the degeneracy of the electron spin energy levels. The EPR signal is observed when the energy difference between the two spin states matches the frequency of the absorptive photon, $(g\beta_e B_0) / \hbar = \omega_0$	47
5.2	(a) The spin vector precesses about the magnetic field \vec{B}_0 along the z -axis of the laboratory frame (x, y, z) , with frequency of precession ω_0 . (b) The additional field \vec{B}_1 rotates in the xy plane with frequency ω_{mw}	48
5.3	(a) Precession of the magnetization about the effective magnetic field \vec{B}_{eff} with precession frequency ω_{eff} , during m.w. irradiation with amplitude ω_1 . (b) The transformation to the rotating frame (X, Y, Z) gives the effective magnetic field \vec{B}_{eff} tilted at a constant angle θ to the Z -axis.	50
5.4	Absorption (above) and dispersion (below) signals in EPR experiment plotted versus $\omega_{mw} - \omega_0$	53
5.5	Experimental setup of TR-EPR: an applied electric field (usually in the visible or infrared (IR) range) optically excites the molecular sample to a singlet excited state, and the triplet excited states are populated via ISC. An applied static magnetic field, for example in the z -direction (B_0), splits the ZFS triplet sublevels (see figure 5.7) and a second time-dependent magnetic field (B_1) linearly polarized perpendicular to the static magnetic field induces transitions between these triplet sublevels, giving rise to TR-EPR triplet signals.	55

5.6	In the absence of an external magnetic field the degeneracy of the triplet sublevels is lifted due to the SS dipolar interaction.	57
5.7	Energy level diagram of the triple state and absorption (or emission) curves when the external magnetic field is applied (a) parallel to the principal axis Z , (b) parallel to the principal axis X , and parallel to the principal axis Y . The arrows show the allowed transitions between the triplet energy levels and the energies of the allowed transitions are given by $\Delta E = W_3 - W_1$ and $\Delta E = W_3 - W_2$ (see eqs. 5.54, 5.55 and 5.56). By convention, D_Z was taken to be the value with the smaller magnitude and D_Y those with the larger magnitude.	60
6.1	Chemical structure of the Cbz-TBT molecule. It consists of a carbazole (Cbz) moiety, which is colored in blue, and a dithiophene-benzothiadiazole (TBT) unit, which is colored in red. TBT moiety is comprised of the 1,2,3-benzothiadiazole (BT) unit surrounded by two thiophene rings.	63
6.2	Experimental (black dotted line) and calculated (red line) absorption spectrum of the Cbz-TBT molecule. Computations were performed for the most probable geometry (anti_2) at the TDA/BHandHLYP/TZ2P level of theory, and solvent effects were included via COSMO model using the dielectric constant ($\epsilon = 9.8$) for dichlorobenzene. The spectrum is based on a 100 nm FWHM Gaussian broadening of the vertical transition energies and associated oscillator strengths. The CT band is centered at 473 nm (2.62 eV), and it is attributed to the transition $S_0^{\text{SOC}} \rightarrow S_1^{\text{SOC}}$ (or $S_0 \rightarrow S_1$), which is predominantly (93%) assigned to HOMO-LUMO transition. The shade areas show the experimental excitation wavelength ranges inside and outside (below) the CT band.	65
6.3	<i>Left:</i> Pure singlet ($ S_n\rangle$) states (black lines) and pure triplet state manifolds ($\{ T_{k,m_s}\rangle\}$) (light grey lines) coupled by the spin-orbit interactions. <i>Right:</i> Spin-mixed states ($ S_n^{\text{SOC}}\rangle$ and $\{ T_{k,\xi}^{\text{SOC}}\rangle\}$, dark grey lines) as linear combinations of pure singlet $ S_n\rangle$ and triplet $ T_{k,m_s}\rangle$ states (equations 6.2 and 6.3).	66

- 6.4 Direct mechanism for the formation of triplets. *Left:* Optical excitation at $t = 0$ sec induces transitions from the “mixed” ground state $|S_0^{\text{SOC}}\rangle$ to “mixed” triplet excited states $|T_{k,\xi}^{\text{SOC}}\rangle$ for excitation wavelengths below the CT band. *Right:* Optical excitation at $t=0$ sec induces transitions from the “mixed” ground state $|S_0^{\text{SOC}}\rangle$ to “mixed” singlet $|S_n^{\text{SOC}}\rangle$ and triplet $|T_{k+1,\xi}^{\text{SOC}}\rangle$ excited states for excitation wavelengths inside the CT band. Gaussian line shapes represent the excitation wavelength region below and inside the CT band. Both types of excited states ($|S_n^{\text{SOC}}\rangle$ and $|T_{k,\xi}^{\text{SOC}}\rangle$) have triplet contributions (equations 6.2 and 6.3 and figure 6.3). Thus, photoexcitation creates initial (at $t = 0$ sec) triplet populations $|\langle T_{k,m_s} | S_n^{\text{SOC}} \rangle|^2$ and $|\langle T_{k,m_s} | T_{k,\xi}^{\text{SOC}} \rangle|^2$ 67
- 6.5 Indirect mechanism for the formation of triplets. Optical photoexcitation inside the CT band at $t = 0$ sec creates an initial population of the “mixed” $|S_n^{\text{SOC}}\rangle$ state, which is approximately pure singlet state $|S_n\rangle$. At a later time after photoexcitation, the initial $|S_n\rangle$ population can transform to triplet $|T_{k,m_s}\rangle$ and $|T_{k+1,m_s}\rangle$ population via ISC (rates $k_{S_n \rightarrow T_k}$ and $k_{S_n \rightarrow T_{k+1}}$). 68
- 6.6 Schematic representation of the torsional angles determined along the conjugated backbone. θ_1, θ_2 and θ_3 are the dihedral angles of the bonds denoted by bold lines. 69
- 6.7 Minimum ground-state energy conformations and shorthand notation. anti and syn refer to the orientation of thiophene rings relative to BT (anti if the Sulfur atom of the thiophene ring points upwards relative to BT [$\theta_1 = 0^\circ$ or $\theta_2 = 0^\circ$] and syn if the Sulfur atom of the thiophene ring points downwards relative to BT [$\theta_1 = 180^\circ$ or $\theta_2 = 180^\circ$]). The numbers 1 and 2 refer to the orientation of Nitrogen atom of Cbz moiety with respect to the nearest thiophene unit: 1 if the Nitrogen atom points downwards relative to the Sulfur atom of the nearest thiophene [$\theta_3 = 180^\circ$] and 2 if the Nitrogen atom points upwards relative to the Sulfur atom of the nearest thiophene [$\theta_3 = 0^\circ$]. Percentages refer to the ground state population of relative geometries at room temperature computed according to Boltzmann statistics and energies refer to the total ground state energies computed at BHandHLYP/TZ2P level of theory. 70
- 6.8 Energy level diagram of Cbz-TBT molecule in its anti_2 geometry calculated at the TDA/BHandHLYP/TZ2P level of theory. Thick dark grey lines represent the computed spin-orbit coupled excited state energies with respect to the ground state energy. Thin black lines represent the experimental optical excitation energy regions for the TR-EPR experiment (2.14 eV - 2.88 eV for photoexcitation inside the CT band and 1.82 eV - 1.97 eV for photoexcitation below the CT band). 73

6.9	Schematic view of the PES of the singlet $ S_n\rangle$ and the triplet $ T_{k,m_s}\rangle$ excited states in the harmonic approximation model, shown for a single vibrational mode of frequency ω . The vibrational energy levels are shown in light gray and their energies differ from each other by $\hbar\omega$. The energy difference between the minimum of $ S_n\rangle$ surface and the minimum of $ T_{k,m_s}\rangle$ surface is $\Delta E_{S_n \rightarrow T_{k,m_s}}$. λ is the mode reorganization energy.	77
6.10	Population transfer to the first and second triplet excited states as a function of time. (a) Population of S_1 from 0 to 0.5 μsec . (b) Population transfer to T_2 from 0 to 0.5 μsec . (c) Population transfer to T_1 from 0 to 0.5 μsec and (d) population transfer to T_2 and T_1 for larger time scales than 0.5 μsec , namely from 0 to 0.3 msec. Initial condition for T_2 : $P_{T_2}(t=0) = 5.3 \times 10^{10}$	80
6.11	Schematic energy diagram for the conformational transitions between two different geometries (A and B) in the T_1 PES. For all the experimental excitation energies ($E_{S_0^{\text{SOC}} \rightarrow T_1^{\text{SOC}}}^{\text{exp}}$), the T_1 manifold is populated with high vibrational kinetic energy. This excess kinetic energy ($\text{KE}^{\text{excess}}$) may be large enough compared to the energy barrier (E^b) for the conformational transition between minimum energy geometries of A and B, so that each excited molecule may change its conformation through motion on the T_1 PES.	86
6.12	PES of the T_1 manifold along the torsional angles θ_1 (above) and θ_2 (below) computed at TDA/BHandHLYP/TZ2P level of theory for anti_2 geometric conformation. The two gray-dashed lines refer to the lowest and maximum experimental wavelengths used for excitation below the CT band (1.82 eV - 1.97 eV). <i>Above</i> : The barrier refers to a thiophene unit rotation that brings the Cbz-TBT molecule from anti_2 to anti-syn_2 (see figure 6.7). At $\theta_1 = 0^\circ$ the energy refers to the minimum energy conformation of the T_1 manifold of anti_2. <i>Below</i> : The barrier refers to the energy required for a BT-thiophene unit rotation that brings the Cbz-TBT molecule from anti_2 to syn-anti_2 (see figure 6.7). At $\theta_1 = 0^\circ$ the energy refers to the minimum energy conformation of the T_1 manifold of anti_2. In the picture of the molecule, the Cbz unit is excluded for simplicity.	89
6.13	Singlet-singlet and singlet-triplet vertical excitation energies of Cbz-TBT in its anti_2 conformation calculated with CAMY-B3LYP method. The percentage value on the right-hand side of each excitation is the contribution to the excitation.	94

6.14 Singlet-singlet and singlet-triplet vertical excitation energies of Cbz-TBT in its anti_2 conformation calculated using different GH and RS methods. The electronic state at zero-energy is the ground state $ S_0^{\text{SOC}}\rangle$. The $ S_1^{\text{SOC}}\rangle$ state is colored in red, the $\{ T_{1,\xi}^{\text{SOC}}\rangle\}$ manifold is colored in blue and the $\{ T_{2,\xi}^{\text{SOC}}\rangle\}$ manifold is colored in green. Left column of each method refers to the singlet states (S) and right column to the triplet states (T).	96
6.15 Singlet-singlet and singlet-triplet vertical excitation energies of Cbz-TBT in its anti_2 conformation calculated using SOC-CIS/def2-TZVP and pSOC-TDA/BHandHLYP/TZ2P methods. Left column for each method refers to the singlet states (S) and right column to the triplet states (T).	97
6.16 Energy level diagram of the Cbz-TBT molecule computed for different geometric conformations at pSOC-TDA/BHandHLYP/TZ2P level of theory. The $ S_1^{\text{SOC}}\rangle$ state is colored in red, the $\{ T_{1,\xi}^{\text{SOC}}\rangle\}$ manifold is colored in blue and the $\{ T_{2,\xi}^{\text{SOC}}\rangle\}$ manifold is colored in green. Left column of each geometric conformation refers to the singlet states (S) and right column to the triplet states (T).	100
6.17 Absorption spectrum of the different Cbz-TBT molecular conformations calculated at the optimized B3LYP/TZ2P ground-state geometries using pSOC-TDA/BHandHLYP/TZ2P level of theory (based on a 0.30 eV FWHM Gaussian broadening of the vertical transition energies and associated oscillator strength). On the inset, the frontier orbitals H (HOMO) and L (LUMO) are shown for each conformation. (a) anti_2 (b) anti_1 (c) syn-anti_2 (d) anti-syn_1 (e) anti-syn_2 (f) syn_2.	102
6.18 Schematic energy diagram for the conformational transitions between two different geometries (A and B) in the T_1 PES along the torsional angles θ_n ($n = 1, 2$). $\theta_n^{S_0(A)}$ refers to the angle θ_n of the ground state minimum energy conformation (S_0) of the initial geometry A. $\theta_n^{T_1(A)}$ refers to the angle θ_n of the minimum energy conformation of T_1 excited state of the initial geometry A. $\theta_n^{T_1(B)}$ refers to the angle θ_n of the minimum energy conformation of T_1 excited state of the final geometry B. The energy barrier was computed with respect to the ground state energy of the initial geometric conformation (A).	105
6.19 The principal axes X, Y, Z are derived from the molecular axes x, y, z . For example, the Z -axis behaves like a vector in the x, y, z plane. The magnitude of its components is given by $\langle r Z\rangle$ with $r = x, y, z$ respectively.	111

- 6.20 *First row*: Energy level diagram of the first triplet excited state sublevels as a function of the static magnetic field \vec{B}_0 aligned with the dipolar axes X, Y, Z respectively. Transitions occur at the resonance fields (down arrows correspond to emissive lines and up arrows to absorptive lines. The inset shows the ZFS triplet states ($|T_{1,X}\rangle, |T_{1,Y}\rangle, |T_{1,Z}\rangle$). *Second row*: TR-EPR spectra computed in the cases where the magnetic field \vec{B}_0 is aligned with the molecular X, Y or Z axis. *Third row*: The full powder TR-EPR spectra. Here, the transitions corresponding to the canonical field orientations (X, Y, Z) are shown as picks in the powder spectrum as indicated by the dark arrows. Lorentzian lineshape was set to 2.08 mT. The transitions can be either absorptive (A) or emissive (E). 114
- 6.21 Population transfer to the first and second triplet excited states as a function of time computed for anti-syn_1 (12%) geometric conformation. (a) Population of S_1 from 0 to 0.5 μsec . (b) Population transfer to T_2 from 0 to 0.5 μsec . (c) Population transfer to T_1 from 0 to 0.5 μsec and (d) population transfer to T_2 and T_1 for larger time scales than 0.5 μsec , namely from 0 to 0.1 msec. Initial condition for T_2 : $P_{T_2}(t = 0) = 1.1 \times 10^{10}$. 117
- 6.22 Orientation of the principal axes of the ZFS tensor computed at UNO-B3LYP/def2-TZVP level of theory for the different geometric conformations. To visualize the tensor, we used the Avogadro software package. 119
- 7.1 Flowchart showing the computational procedure we followed to compute the ISC transition rates $S_n \rightarrow T_{k,m_s}$ using the ADF program package in combination with MATLAB programming. 128
- 7.2 (a) Example of a signal in time domain ($x(t)$) and its spectrum in the frequency domain ($X(f)$). Two sinusoidal waves (1 and 2) of different frequencies are superimposed and form a signal (1+2) in the time domain. The frequency spectrum of the signal is computed from the FT of $x(t)$. It is represented by delta functions entirely localized at the two frequency components of the sinusoidal waves 1 and 2. (b) A signal is classified as continuous-time signal (above) and discrete-time signal (below). The discrete-time signal is a time sequence that has been sampled from a continuous-time signal. It takes on only a discrete set of values (samples). 130
- 7.3 Schematic diagram of a DFT pair showing that the discrete signal $x(n)$ and the discrete frequency spectrum $X(k)$ are sampled in equal intervals. In the figure, $F_s = 1/t_s$ and $t_s = \tau/N$ 131

7.4	(a) Real part of the $G(t)$ function (with cosine, see eq. 6.17). The plot shows the 135 cosine waves in the time domain, one for each normal mode of frequency ω_α . The lowest-frequency mode has the greater period of oscillation (~ 0.07 cm) (with light blue color). The time duration of the signal is chosen to be much greater than the period of oscillation of the lowest-frequency mode (i.e., $\tau = 2$ cm). (b) The ISC rate (in sec^{-1}) as a function of the frequency $\Delta E_{S_1, T_1}/\hbar$ (in cm^{-1}) for the transition $S_1 \rightarrow T_1$ in Cbz-TBT molecule. The rate at $\Delta E_{S_1, T_1}/\hbar = 9910.28 \text{ cm}^{-1}$ equals to 17.67 sec^{-1}	132
7.5	(a) Two guanine molecules take part in a hole transfer transition. The driving force is zero ($\Delta E = 0$) and the electronic coupling is $\langle G^+ G \hat{V} G G^+ \rangle = 0.03 \text{ eV}$. (b) Hole transfer rate for the transition $ G^+ G\rangle \rightarrow G G^+\rangle$, as a function of ΔE at different temperatures.	134
7.6	(a) Hole transfer rate computed using the scaled normal mode parameters at $T = 300 \text{ K}$ (black line). The fitting into Gaussian distribution (red line) reveals the rate can be described by the classical Marcus formula. The plot also shows the hole transfer rate that was computed using the unscaled frequencies and electron-phonon couplings at $T = 300 \text{ K}$. In this case, the spectrum can not be described by a Gaussian distribution. (b) Hole transfer rate computed using the scaled normal mode parameters at $T = 10 \text{ K}$. The spectrum is computed using eq. 2.29 and it is shown in red. The rate is also computed using the classical Marcus formula eq. 2.31 at $T = 10 \text{ K}$ and it is shown in black for comparison.	135
7.7	MATLAB code for the computation of the ISC rates according to equation 7.3.	137
8.1	(A) Fluorene monomer bridging unit (F1) used in ref. 1. (B) The structure of Bp-Fn-Nap systems used in ref. 1. The bridges contained one up to three F units (Fn, n=1-3). (C) Chemical structure of the proposed indenofluorene (6,12-dihydroindeno[1,2-b]fluorene) bridging monomer (IF1). (D) Molecular structure of the indenofluorene hexamer (IF6) bridge (16.9 Å length). The monomers are constrained to a rigid π -stacked geometry through two methylene linkers and the interchromophore distance is 2.8-3.0 Å. The IF6 bridge is linked to a $\text{Ru}(\text{bpy})_3^{2+}$ D and a tetracene (Tet) A in approximately 4.2 Å and 2.9 Å distance respectively.	141

- 8.2 (a) TE states of the bridge type shown in figure 8.1 computed at CIS/def2-SVP level of theory. Due to enhanced π -stacking, TE splittings are large (e.g., $\Delta E_{T_2^{(2)}-T_1^{(2)}} = 0.3$ eV for the dimer). For longer polymers the TE band structure is stabilized. (b) Single excitation molecular orbital contribution to the lowest two TE states of the IF10 (computed with isosurface value 0.01). The figure shows only the largest contributions. The notations (1),(2),(10) refer to monomer, dimer and decamer bridges respectively. 143
- 8.3 (a) Schematic diagram of the tight-binding model used to estimate the intra-bridge TET rates $k_{\text{br}} = \langle \tau \rangle_{\text{br}}^{-1}$ for a bridge with N sites (monomers). E is the monomer TE energy, $V = V_{\text{rms}}$ is the rms nearest-neighbour TET coupling and σ_E is the standard deviation of the energies E arising from dynamic disorder. The γ_i for $i = 1 - (N - 1)$ are the monomer TE population relaxation rates. Each γ_i equals $\gamma_i = k_B^{(\text{ph})}$ (monomer TE phosphorescence decay rate) and γ_N is the TET rate to an acceptor, $\gamma_N \approx k_{B \rightarrow A}^{(\text{TET})}$. The $\gamma_{i,j}$ are pure dephasing rates given by $\gamma_{i,j} = \hbar^{-1} \sqrt{\sigma_{E(i)}^2 + \sigma_{E(j)}^2}$. (b) $\langle \tau \rangle^{-1} / \gamma_N$ versus γ_N (both on a \log_{10} scale) for $N = 5$ (red) and $N = 50$ (black) with $\gamma_i = 1 \mu\text{s}^{-1}$ ($i = 1 - (N - 1)$), $\hbar\gamma_{i,j} = 0.1$ eV and $V = 0.15$ eV ($V > \sigma_E$). (c) Trapping time $\langle \tau \rangle_{\text{trap}}$ and intrinsic bridge TET time $\langle \tau \rangle_{\text{br}}$ versus γ_N , both in logarithmic scale, for $N = 5$ and $N = 50$. The circles indicate the values of γ_N for which $\langle \tau \rangle_{\text{trap}} = \langle \tau \rangle_{\text{br}}$ 145
- 8.4 *Left*: Energy level diagram of the TE eigenstates of $\text{Ru}(\text{bpy})_3^{2+}$ - IF6 - Tet system computed at wB97/def2-SVP level of theory. *Right*: Hole-particle pairs of the natural transition orbitals (NTOs) of some TE's. T_{19} is localized on D, T_1 on A, T_2 on B and T_{16} , T_{12} are D-B and D-A CT TE's. 147

8.5	(a) Structure of anthra[2,1,9-def:6,5,10-d',e',f']diisochromene-1,3,8(10H)-trione dimer with a single methyl group linkage which enforces sub-VdW π -stacking. (b) Longer polymers with single methyl group linkages between monomers twist at room temperature, breaking the π -stacking and diminishing the interchromophore TET coupling. (c) This problem can be remedied by double methyl linkages between units of anthra[2,1,9-def:6,5,10-d',e',f']diisochromene-1,3,8(3H,10H)-dione monomers. In this case π -stacking is preserved for all pairs of nearest-neighbor monomers and for each pair, $V_{\text{rms}} \geq \frac{\lambda^{\text{mon}}}{2}$. Such a wire supports long-distance coherent ET as in the case of the wires shown in figure 8.1. (d) Structure of two dicyclopenta[ghi,pqr]perylene derivatives linked with two methylene linkers to build a dimer. This type of structure also has strong TET coupling compared to the monomer reorganization energy ($V_{\text{rms}} = 0.2$ eV).	148
8.6	Schematic representation of the potential energy surfaces (PES) of the singlet ground state $S_0^{(1)}$ and the first TE state $T_1^{(1)}$ of the donor and acceptor moieties (i.e., IF monomer). The donor-to-acceptor reorganization energy λ , is the sum of the reorganization energies of the donor and acceptor, according to 8.4.	152
8.7	The IF monomers are cut off from the dimer and each monomer is capped with hydrogens at positions 5' and 11'.	153
8.8	SE states ($S^{(n)}$) of the IF _n bridges ($n = 1,2,6,10$) computed at the M06-2X/DZP level of theory using the ADF program package. The notations (1), (2), (6), (10) denote monomer, dimer, hexamer and decamer systems respectively.	154
8.9	TE states ($T^{(n)}$) of the IF _n bridges ($n = 1,2,6,10$) computed at the M06-2X/DZP level of theory using the ADF program package. The notations (1), (2), (6), (10) denote monomer, dimer, hexamer and decamer systems respectively.	155
8.10	TE states ($T^{(n)}$) of the IF _n bridges ($n = 1,2,6,10$) computed at the CIS/def2-SVP level of theory using the ORCA program package. The notations (1), (2), (6), (10) denote monomer, dimer, hexamer and decamer systems respectively.	155
8.11	Molecular structures of perylene-based dimers. (a) PDI dimer of ref. 2, (b) PDI dimer of ref. 3, (c) PMI dimer of ref. 4 and (d) TDI dimer of ref. 5 with R = Me.	163

8.12	Molecular structures of perylene-based chromophore dimers that were tested for coherent TE transport. (a) Bisbenzimidazo[2,1-a:2',1'-a']anthra[2,1,9-def:6,5,10-d'e'f']diisoquinoline-10,21-dione monomers linked with methyl groups, (b) anthra[2,1,9-def:6,5,10-d'e'f']diisoquinoline-1,3,8,10(2H,9H)-tetraone (perylene diimide) monomers linked with biphenylene bridges. ⁶	165
8.13	SET and TET couplings (in logarithmic scale) versus distance (in Å). The TET coupling drops considerably below 0.10 eV for distances greater than VdW while the SET coupling is much greater. <i>left</i> . Computations on the fluorene dimer. <i>right</i> . Computations on the PDI dimer.	166
8.14	Distance dependence of the intra-bridge TET rate (k_{br}) (in logarithmic scale) as a function of the length of the bridge. The simulations were performed for $V = 0.2$ eV, $\hbar\gamma_{\text{deph}} = 0.1$ eV and $\gamma_N = (10 \text{ nsec})^{-1}$	167
9.1	(a) Schematic representation of the TET pathways in the CdSe-BODIPY system. The BODIPY molecule is attached to the spherical surface of the CdSe NC via oxygen atoms. The QD is photo-excited at 500 nm to trigger TET to the BODIPY acceptor. According to the experimental results, TET is favored via sequential CT. (b) Schematic diagram demonstrating the possible triplet formation pathways in the QD-BODIPY complex: (i) DET pathway ($\text{QD}^*-\text{BODIPY} \rightarrow \text{QD}^{-3}\text{BODIPY}^*$) [black arrow (1)], (ii) FRET $\text{QD}^*-\text{BODIPY} \rightarrow \text{QD}^{-1}\text{BODIPY}^*$ followed by ET $\text{QD}^{-1}\text{BODIPY}^* \rightarrow \text{QD}^{-}\text{BODIPY}^+$ and back ET $\text{QD}^{-}\text{BODIPY}^+ \rightarrow \text{QD}^{-3}\text{BODIPY}^*$ [blue and yellow arrows (2)], (iii) hole transfer $\text{QD}^*-\text{BODIPY} \rightarrow \text{QD}^{-}\text{BODIPY}^+$ followed by ET $\text{QD}^{-}\text{BODIPY}^+ \rightarrow \text{QD}^{-3}\text{BODIPY}^*$ [green and yellow arrows (3)].	178
9.2	Calculated absorption spectrum of the BODIPY molecule computed at the B3LYP/TZ2P level of theory using FWHM = 25 nm. The first absorption peak is centered at 644 nm and it is attributed to the transition $S_0 \rightarrow S_1$. This transition is of HOMO→LUMO character.	180
9.3	(a) Molecular structure of the CdSe NP of 2.5 nm diameter (see ref. 263). (b) Absorption spectrum of CdSe QD computed at sTDA/TZP level of theory. (c) Frontier molecular orbitals of the CdSe QD.	181
A.1	Example of the input script of the FCF-ADF program used to compute the electron-phonon coupling parameters $\bar{\lambda}_\alpha$ for each normal mode α , for the transition $S_1 \rightarrow T_1$ in the Cbz-TBT molecule.	208
A.2	Example part of the output file of the FCF-ADF program used to compute the electron-phonon coupling parameters $\bar{\lambda}_\alpha$ for each normal mode α , for the transition $S_1 \rightarrow T_1$ in the Cbz-TBT molecule.	209

B.1	Absorption spectra computed at $T = 0$ K and $T = 300$ K temperatures using $\Gamma = 50$ cm ⁻¹ and $\Theta = 100$ cm ⁻¹ . (a) the simulations were performed for a set of low-frequency modes and (b) the simulations were performed using a set of high-frequency modes.	212
B.2	Part of the output file of the <code>orca_asa</code> program showing the intrinsic and effective broadening parameters and the relative FWHMs. The parameters Γ and Θ are defined in the input file (see figure C.2 in appendix C) but are shown also in the output file. This output file is related to the calculation shown in figure C.2 in appendix C for the $S_1 \rightarrow T_1$ transition in Cbz-TBT molecule.	213
C.1	Shifted potential surfaces model for absorption and emission in the single-mode representation. We show that the inhomogeneously broadened absorption band of width Θ_k , comes from the superposition of individual vibronic bands that are homogeneously broadened by Γ_k . . .	216
C.2	Example of the input script of the <code>orca_asa</code> program used to compute the absorption cross section $\sigma(E_L)$. The script contains the vibrational frequencies and normal modes of the S_1 excited state, and the relative displacements of the T_1 excited states of the Cbz-TBT molecule. The absorption cross section was used to deduce the ISC rate constants according to equation C.4.	218
C.3	Flowchart showing the computational procedure we followed to compute the ISC rate constants $S_n \rightarrow T_{k,m_s}$ using the <code>orca_asa</code> program implemented in the ORCA program package. The vibrational frequencies ω_j , the displacements Δ_{kj} and the SOC constants $\langle S_n \hat{H}^{\text{SOC}} T_{k,m_s} \rangle$ can be computed using any quantum chemical program. For our project we used the ADF program package.	219
C.4	Example of a single-mode system with low frequency mode. <i>Left.</i> Absorption cross section $\sigma(E_L)/E_L$ as a function of the energy E_L computed with the <code>orca_asa</code> program. <i>Middle.</i> FCF integral as a function of the energy E_L computed with our MATLAB code. <i>Right.</i> The FCFs computed with the MATLAB program are multiplied by the $\langle \text{constant} \rangle \sim 703$ to produce the absorption spectrum $\sigma(E_L)/E_L$	221
C.5	Absorption spectrum $\sigma(E_L)/E_L$ as a function of the energy E_L computed with the <code>orca_asa</code> program (red lines) and by the MATLAB code multiplied by the $\langle \text{constant} \rangle \sim 703$ (black lines). (a) single mode system with a high frequency mode $\omega = 967.9$ cm ⁻¹ , (b) two-mode system with mode frequencies $\omega_1 = 564.6$ cm ⁻¹ and $\omega_2 = 967.9$ cm ⁻¹ , (c) system with 42 modes at $T = 0$ K and (d) the same system with 42 modes at $T = 300$ K.	222

D.1 MATLAB code for the computation of the ZFS parameters according to equation D.1. 227

E.1 MATLAB code for the computation of the mean first passage times (MFPTs) by solving the Liouville equation. 230

SPYROULLA A. MAVROMMATI

LIST OF TABLES

3.1	Effects of the spin operators on the spin part of the singlet and triplet wavefunctions.	27
3.2	Effects of the orbital angular momentum operators on the p -atomic orbitals.	28
3.3	Matrix elements of \hat{H}^{SOC} between singlet and triplet states. Singlet and triplet states are defined in eq. 3.25.	30
6.1	Experimentally derived zero-field splitting (ZFS) parameters and the relative populations of the zero-field triplet sublevels ($p_1^{\text{exp}}, p_2^{\text{exp}}, p_3^{\text{exp}}$) together with the Lorentzian lineshapes obtained for the different excitation wavelengths (λ_{wav}) inside (492nm) and below (630-680 nm) the CT band. g is the factor of the electron taken to be isotropic ($g_{\text{iso}} = 2.002$). Below the CT band the ZFS parameters are different for different excitation wavelengths, thus, the TR-EPR spectra shapes are different. Inside the CT band, the ZFS parameters are the same for different excitation wavelengths, thus, the TR-EPR spectra shape are the same. For this reason, in the table only the parameters for the excitation at the maximum of the CT band are mentioned. Results were taken from ref. 7.	64
6.2	TD-DFT/TDA diagnostic indexes Λ and Δr computed using three different methods, for the Cbz-TBT molecule in its anti_2 conformation. .	91
6.3	TD-DFT/TDA vertical excitation energies in eV and the relative molecular orbital contributions computed using three different methods, for the Cbz-TBT molecule in its anti_2 conformation (H refers to HOMO and L refers to LUMO).	92

6.4	pSOC-TDA vertical excitation energies in eV computed using different methods for the Cbz-TBT molecule in its anti ₂ conformation. The molecular orbital contributions to the excitations, are shown for the singlet and triplet excited states of interest (H refers to HOMO and L refers to LUMO).	96
6.5	SOC constants between singlet and triplet excited states in eV, computed at pSOC-TDA/BHandHLYP/TZ2P level of theory for the most probable geometric conformations. The coupling between $ S_1\rangle$ and $ T_{1,m_s}\rangle$ and between $ S_1\rangle$ and $ T_{2,m_s}\rangle$ was computed at the minimum-energy conformation of S_1 and the coupling between $ T_{1,m_s}\rangle$ and $ T_{2,m_s}\rangle$ computed at the minimum-energy conformation of T_2	99
6.6	Torsional angles θ_1 , θ_2 and θ_3 for the optimized ground state, first singlet excited state and first triplet and second triplet excited state manifolds of all Cbz-TBT molecular conformations. The ground state was optimized at the B3LYP/TZ2P level of theory and the excited states were optimized at the TDA/BHandHLYP/TZ2P level.	103
6.7	Energy barrier in eV, in the first triplet excited state T_1 along the torsional angles θ_1 and θ_2 (as shown in the brackets) computed at TDA-BHandHLYP-TZ2P level of theory for the different geometric conformations.	104
6.8	Total energy of the ground state geometries computed at the BHandHLYP-TZ2P level of theory on the optimized B3LYP/TZVP minimum energy conformations, the fraction of molecules in each conformation given by Boltzmann statistical mechanics at $T = 300$ K ($\frac{P_s}{P}$), the number of molecules in each conformation in the ground state (P_s) and the relative concentration in $M = \text{molL}^{-1}$	106
6.9	Oscillator strength for the transition $S_0^{\text{SOC}} \rightarrow T_{1,\xi}^{\text{SOC}}$ ($f_{S_0^{\text{SOC}} \rightarrow T_{1,\xi}^{\text{SOC}}}$) and the relative excitation energies of the direct photo-excitation from S_0^{SOC} to $T_{1,\xi}^{\text{SOC}}$ ($E_{S_0^{\text{SOC}} \rightarrow T_{1,\xi}^{\text{SOC}}}$) for the different conformations, both computed at pSOC-TDA/BHandHLYP/TZ2P level of theory. The last column refers to the population of the first triplet excited state manifold (the range arising from FWHM = 0.1 eV - 0.5 eV).	108
6.10	Oscillator strength for the transition $S_0^{\text{SOC}} \rightarrow T_{2,\xi}^{\text{SOC}}$ ($f_{S_0^{\text{SOC}} \rightarrow T_{2,\xi}^{\text{SOC}}}$) and the energies of the second triplet excited state manifold ($E_{S_0^{\text{SOC}} \rightarrow T_{2,\xi}^{\text{SOC}}}$) and the first singlet excited state ($E_{S_0^{\text{SOC}} \rightarrow S_1^{\text{SOC}}}$) for the different conformations, both computed at pSOC-TDA/BHandHLYP/TZ2P level of theory. The last two columns refer to the population of the second triplet excited state manifold at the energies $E_{S_0^{\text{SOC}} \rightarrow S_1^{\text{SOC}}}$ and $E_{S_0^{\text{SOC}} \rightarrow T_{2,\xi}^{\text{SOC}}}$ respectively (given the range FWHM = 0.1 eV - 0.5 eV).	109

6.11	Number of molecules that populate the first singlet excited state ($P_{S_1^{\text{SOC}}}$) upon photoexcitation in each geometric conformation.	110
6.12	Oscillator strengths for the transitions $S_0^{\text{SOC}} \rightarrow T_{1,i}$, $i = l, c, u$ together with the number of molecules that populate the first triplet excited state manifold $\{ T_{1,i}\rangle\}$, $i = l, c, u$ upon photoexcitation from the singlet ground state (given the range FWHM = 0.1 eV - 0.5 eV). The relative populations $\tilde{\Pi}_i^{\text{ex}}$ are also shown.	113
6.13	Number of molecules that populate the first triplet excited state manifold $\{ T_{1,R}\rangle\}$, $R = X, Y, Z$ upon photoexcitation from the singlet ground state together with the relative oscillator strengths $f_{S_0^{\text{SOC}} \rightarrow T_{1,R}}$ (given the range FWHM = 0.1 eV - 0.5 eV). The relative populations $\tilde{\Pi}_R^{\text{ZFS}}$ are also shown.	115
6.14	Total rate constants for the transitions $S_1 \rightarrow T_2$, $S_1 \rightarrow T_1$ and $T_2 \rightarrow T_1$ and the corresponding energy differences $\Delta E_{S_1, T_1}$ (or equivalently $\Delta E_{S_1, T_1, m_s}$), $\Delta E_{S_1, T_2}$ (or equivalently $\Delta E_{S_1, T_2, m_s}$), $\Delta E_{T_2, T_1}$ (or equivalently $\Delta E_{T_2, m_s, T_1, m_s}$) computed for the most probable geometric conformations of the Cbz-TBT molecule.	118
6.15	ZFS parameters in MHz calculated at the minimum energy conformation of the T_1 manifold excited state for each geometric conformation at UNO-B3LYP/def2-TZVP level of theory and using the distributed Point-Dipole (DPD) approximation.	119
6.16	Principal values of the g-tensor computed at the minimum energy conformation of the T_1 manifold excited state for each geometric conformation using B3LYP/def2-TZVP method.	126
6.17	Experimentally derived ZFS parameters together with the Lorentzian lineshapes obtained for the different excitation wavelengths (λ_{wav}) below (630-680 nm) the CT band. ⁸ The last two columns show the D and E strains computed by fitting on the experimental spectrum.	126
7.1	Rate computed with the Fermi's Golden rule formula Vs rate computed with the Marcus formula for the hole transfer process $ G^+G\rangle \rightarrow GG^+\rangle$. The rate is given at $\Delta E = 0$	133
8.1	Hole-particle pairs of NTOs of the lowest two ($T_1^{(1)}$, $T_2^{(1)}$) TE states of the monomer, computed at the CIS/def2-SVP level of theory (based on a 0.02 isosurface value).	156
8.2	Hole-particle pairs of NTOs of the lowest two ($T_1^{(2)}$, $T_2^{(2)}$) TE states of the dimer, computed at the CIS/def2-SVP level of theory (based on a 0.02 isosurface value).	157

8.3	Hole-particle pairs of NTOs of the lowest two ($T_1^{(6)}, T_2^{(6)}$) TE states of the hexamer, computed at the CIS/def2-SVP level of theory (based on a 0.01 isosurface value).	158
8.4	Hole-particle pairs of NTOs of the lowest two ($T_1^{(10)}, T_2^{(10)}$) triplet states of the decamer, computed at the CIS/def2-SVP level of theory (based on a 0.005 isosurface value).	159
8.5	TE energies of the IF dimer computed with different <i>ab-initio</i> methods. Values are in eV.	160
8.6	Comparison of TE energies computed using the ω B97 functional with the def2-SVP and def2-TZVP basis set for the Ru(bpy ₃ ²⁺)-IF2 system. Energy values are in eV.	161
8.7	SE and TE energy splittings ($\Delta E_{SE}, \Delta E_{TE}$) of the perylene-based dimers (shown in figure 8.11) and the IF dimer. Values are in eV.	164
9.1	TD-DFT diagnostic indices Λ and Δr computed using three different methods: PBE, PBE0 and CAMY-B3LYP for the BODIPY molecule. The diagnostic tool indicates that the $S_0 \rightarrow S_1$ transition is local (for details see section 6.6).	179
C.1	Absorption cross section $\sigma(E_L)/E_L$ and FCF integrals (Int_MATLAB) computed at the energy E_L of each peak shown in figure C.4. The constant value was derived from equation C.2 for each peak.	221

CHAPTER 1

Introduction

The transport of excitation energy in molecular systems plays a crucial role in chemical science, biology and engineering.⁹⁻¹¹ In particular, molecular exciton transfer reactions between exciton-donor and exciton-acceptor moieties are key processes in the photophysics and photochemistry of organic/inorganic compounds.^{10,12-16} The major part of the thesis focuses on triplet-exciton transfer (TET) reactions.

Spectroscopic techniques such as time-resolved electron paramagnetic resonance (TR-EPR) and pump-probe transient spectroscopy are often used to explore the dynamics of excited triplet states involved in triplet exciton transfer reactions.^{17,18} In 2017, T. Biskup and his co-workers performed TR-EPR measurements in a small organic molecule (Cbz-TBT molecule, the repeat unit of the PCDTBT polymer) used in photovoltaic applications (Meyer, D. L.; Lombeck, F.; Huettner, S.; Sommer, M.; Biskup, T. *J. Phys. Chem. Lett.* **2017**, *8*, 1677-1682). They observed TR-EPR signals of similar intensities when the molecule is optically excited in its absorbing and non-absorbing regions. The authors suggested two types of pathways for the formation of triplet excited states in this molecule: (a) indirect triple-state formation, via intersystem crossing (ISC) from the photoexcited singlet state (absorbing region), (b) triplet-state formation via direct excitation from the singlet ground state (non-absorbing region). This result is quite surprising given the weak spin-orbit coupling (SOC) interactions between singlet and triplet states in organic molecules.^{19,20} Another surprising result from this experiment is that the shapes of the TR-EPR absorption and emission signals were different for different optical excitation wavelengths in the non-absorbing region, while for excitation wavelengths in the absorbing region, the TR-EPR spectral shapes remain unchanged with respect to optical wavelength.

Motivated by these unusual but interesting results, we interpret the experimental observations using theoretical models and *ab-initio* quantum chemical computations. Our theoretical work involve computations of the population transfer to the triplet excited states either via direct optical excitation from the singlet ground state,

or via ISC from the photoexcited singlet state. In addition, we compute the non-adiabatic ISC rates between the relevant singlet and triplet excited states. The rate predictions involve computations of the normal modes and reorganization energies for the singlet-to-triplet transitions, that are subsequently used to compute the rate as a Fourier transform (FT) of a quantum correlation function that contains the frequencies and reorganization energies for each normal mode. Our work demonstrates that the experimental results can be explained by an initial-state preparation effect of photoexcitation, which leads to initial populations of triplet states that are similar for both optical excitation regions. This work was published in the Journal of Chemical Physics (Mavrommati, S. A.; Skourtis, S. S. *J. Chem. Phys.*, **2020**, *152*, 044304).

Another part of the thesis is related to the design of organic molecular bridges that enable coherent long-distance TET. Fast and efficient TET over long distances is a prerequisite for triplet exciton harvesting in photovoltaics and solar energy conversion, for triplet-triplet annihilation, singlet fission processes and photocatalysis.^{21–23} However, several experimental studies of donor-to-acceptor bridge-mediated TET show strong decay of the TET transfer rate with respect to distance, indicating that long-distance TET is only favored via multi-step thermally activated hopping.^{1,24–26} The latter transport mechanism supports slow rates as compared to coherent band-like transport.^{27,28}

We propose design rules for molecular bridges with the goal to enhance the speed of bridge-mediated TET, by changing the transport mechanism from incoherent to coherent. These design rules imply low inner-sphere exciton reorganization energies, low static and dynamic disorder, and enhanced π -stacking interactions between nearest-neighbor chromophores. These features lead to triplet-exciton eigenstates that are delocalized over several units even at room temperature. We propose various molecular structures that satisfy these criteria and that can be used as bridging wires linking triplet donors to acceptors. For these structures, we perform *ab-initio* electronic-structure computations, molecular-dynamics simulations and density matrix model computations to simulate TET as a function of the molecular bridge length. Our results predict fast TET along the proposed bridges, with effective intra-bridge TET rates of the order of 2 psec for bridge lengths as long as 50 chromophore units. This work was published in the Journal of Physical Chemistry Letters (Mavrommati, S. A.; Skourtis, S. S. *J. Phys. Chem. Lett.*, **2022**, *13*, 9679-9687).

This thesis is organized as follows. In Chapter 2 we describe the theory of non-adiabatic quantum rates for ISC, energy transfer and electron/hole transfer reactions. In Chapter 3, we discuss the theory of the SOC interaction and the main mechanisms by which the SOC coupling matrix element between singlet and triplet states in aromatic molecules becomes strong. Chapter 4 summarizes the theory of the density matrix operator for open quantum systems, the Liouville space formalism and the Bloch equations. In Chapter 5 we explain the principles of EPR and TR-EPR ex-

periments using the quantum mechanical formalism of Chapter 4. Chapter 6 includes the published paper on the TR-EPR experiment (Mavrommati, S. A.; Skourtis, S. S. *J. Chem. Phys.* **2020**, *152*, 044304). In Chapter 7 we explore quantum-vibrational effects on hole-transfer rates. As an example system we consider hole transfer between guanine molecules, and study the temperature dependence of the hole-transfer rate and its deviation from classical Marcus theory. In this chapter we also describe the FT formalism for the computation of the ISC and electron/hole transfer rates, and the MATLAB code that I wrote to compute the rates using *ab-initio* derived parameters. Chapter 8 includes the published paper on long-distance bridge-mediated TET (Mavrommati, S. A.; Skourtis, S. S. *J. Phys. Chem. Lett.*, **2022**, *13*, 9679-9687). In Chapter 9 we describe work related to TET between nanocrystals and molecules. We investigate the TET mechanisms of direct Dexter energy transfer (DET) and sequential charge-transfer (CT) between a CdSe nanoparticle (NP) triplet sensitizer, and a modified structure of boron dipyrromethene (BODIPY) acceptor, linked to the NP.

My work as a PhD student at the University of Cyprus (UCY) was under the supervision of Associate Prof. Spiros S. Skourtis. A large part of the research was funded by the U.S. Department of Energy (DOE) under Award DE-SC0019400.

CHAPTER 2

Quantum non-adiabatic rates in molecules and their classical limits

In this chapter we briefly describe the theory of non-adiabatic transition rates in the golden-rule approximation. This approximation is used to determine the transition rate between initial and final quantum states that are described by a zeroth order Hamiltonian ($\hat{H}^{(0)}$) in the presence of a weak perturbation (\hat{V}). We show that this expression can be written in a more compact form by introducing a spectral density, which includes the contribution of all the vibrational modes with frequencies extending over a broad range. Once the spectral density is obtained, it can be calculated for all temperatures. We apply this theory to energy transfer (EnT), charge transfer (CT), absorption (abs) and intersystem crossing (ISC) reactions.

2.1 Introduction

The total Hamiltonian operator that describes a molecular system, is expressed as a sum of a zeroth order Hamiltonian $\hat{H}^{(0)}$ and a time-independent perturbation \hat{V}

$$\hat{H} = \hat{H}^{(0)} + \hat{V}. \quad (2.1)$$

The eigenstates $|\Psi_m^{(0)}\rangle$ and the eigenvalues E_m of the unperturbed Hamiltonian are given by solving the time-independent Schrödinger equation

$$\hat{H}^{(0)}|\Psi_m^{(0)}\rangle = E_m|\Psi_m^{(0)}\rangle. \quad (2.2)$$

In Fermi's golden rule theorem, the transition rate between a pair of initial ($|\Psi_m^{(0)}\rangle$) and final ($|\Psi_{m'}^{(0)}\rangle$) electronic-vibrational states is given, to 2nd order in \hat{V} , by^{29,30}

$$k_{\Psi_m^{(0)} \rightarrow \Psi_{m'}^{(0)}} = \frac{2\pi}{\hbar} |\langle \Psi_{m'}^{(0)} | \hat{V} | \Psi_m^{(0)} \rangle|^2 \delta(E_{m'} - E_m). \quad (2.3)$$

We apply this golden-rule formula to molecular systems that are described by the total non-relativistic Hamiltonian operator \hat{H}^{mol} , given by

$$\begin{aligned}\hat{H}^{\text{mol}} &= \hat{T}_N + \hat{H}^{\text{BO}} \\ \hat{H}^{\text{BO}} &= \hat{H}^{\text{el}} + \hat{V}_{N-N}.\end{aligned}\quad (2.4)$$

In the above equation, \hat{T}_N is the kinetic energy operator for the nuclear motion, \hat{H}^{BO} is the Born-Oppenheimer (BO) Hamiltonian operator, \hat{H}^{el} is the electronic Hamiltonian that describes the motion of the electrons in the field of the nuclei, and \hat{V}_{N-N} is the operator for Coulomb repulsion between the nuclei. The electronic Hamiltonian (\hat{H}^{el}) contains the kinetic energy of the electrons, the Coulomb attraction between electrons and nuclei, and the Coulomb repulsion between the electrons.

Let us consider the situation where the molecular system is subjected to an external field producing a perturbation \hat{V} . In this case, $\hat{H}^{(0)} = \hat{H}^{\text{mol}}$ and the eigenstates $|\Psi_m^{(0)}\rangle$ are approximated by the nuclear-vibrational BO adiabatic wavefunctions i.e., $|\Psi_m^{(0)}\rangle \Rightarrow |\zeta^{(ad)}(\vec{R}), n_\zeta^{(ad)}\rangle = |\zeta^{(ad)}(\vec{R})\rangle |n_\zeta^{(ad)}\rangle$. $|\zeta^{(ad)}(\vec{R})\rangle$ are the BO adiabatic electronic eigenstates^{10,31}

$$\hat{H}^{\text{BO}}|\zeta^{(ad)}(\vec{R})\rangle = E_{\zeta^{(ad)}}^{\text{BO}}(\vec{R})|\zeta^{(ad)}(\vec{R})\rangle, \quad (2.5)$$

and $|n_\zeta^{(ad)}\rangle$ are the vibrational eigenstates of the nuclear Hamiltonian

$$\left(E_{\zeta^{(ad)}}^{\text{BO}}(\vec{R}) + \hat{T}_N\right)|n_\zeta^{(ad)}\rangle = E_{\zeta, n_\zeta}^{(ad)}|n_\zeta^{(ad)}\rangle. \quad (2.6)$$

\vec{R} is a set of Cartesian coordinate vectors of the atoms i.e., $\vec{R} = \{\vec{R}_1, \vec{R}_2, \dots, \vec{R}_N\}$, where N is the total number of the atoms in the system. $E_{\zeta^{(ad)}}^{\text{BO}}$ is the BO adiabatic surface of the electronic state $|\zeta^{(ad)}\rangle$, and it is a function of \vec{R} . The second term in parenthesis in eq. 2.6 is the nuclei kinetic energy operator $\left(\hat{T}_N = \sum_{i=1}^N \frac{\hat{P}_i^2}{2M_i}\right)$ which is a sum of the kinetic energy operators of atom i with mass M_i , where \hat{P}_i is the respective momentum operator. \hat{T}_N acts only on the vibrational states. In the BO approximation, the unperturbed Hamiltonian of the molecular system in the basis of the adiabatic electronic eigenstates $|\zeta^{(ad)}(\vec{R})\rangle$ is given by

$$\hat{H}^{(0)} = \sum_{\zeta^{(ad)}} \hat{H}_{\zeta^{(ad)}}^{(0)} \quad (2.7a)$$

$$\hat{H}_{\zeta^{(ad)}}^{(0)} = |\zeta^{(ad)}\rangle \langle \zeta^{(ad)}| \left(E_{\zeta^{(ad)}}^{\text{BO}}(\vec{R}) + \hat{T}_N\right). \quad (2.7b)$$

(to simplify the notation for the BO wavefunction we use $|\zeta^{(ad)}(\vec{R})\rangle \rightarrow |\zeta^{(ad)}\rangle$). In contrast to cases where \hat{V} is an external perturbation, the initial and final electronic states are not eigenstates of the \hat{H}^{BO} (i.e., the eigenstates are not the $|\zeta^{(ad)}\rangle$). They are states localized in different parts of the molecule, e.g., donor or acceptor. They are

often called diabatic BO states $|\zeta^{(diab)}(\vec{R})\rangle$ ($|\zeta^{(diab)}\rangle$ for simplicity). \hat{H}^{BO} is not diagonal in the $|\zeta^{(diab)}\rangle$ basis, i.e.,

$$\begin{aligned}\hat{H}^{\text{BO}} &= \sum_{\zeta^{(diab)}} |\zeta^{(diab)}\rangle \underbrace{\langle \zeta^{(diab)} | \hat{H}^{\text{BO}} | \zeta^{(diab)} \rangle}_{E_{\zeta^{(diab)}}^{\text{BO}}(\vec{R})} \langle \zeta^{(diab)} | \\ &+ \sum_{\zeta^{(diab)}} \sum_{\zeta'^{(diab)'}} |\zeta^{(diab)}\rangle \langle \zeta'^{(diab)'} | \hat{H}^{\text{BO}} | \zeta'^{(diab)'} \rangle \langle \zeta'^{(diab)'} | \end{aligned}\quad (2.8)$$

where $E_{\zeta^{(diab)}}^{\text{BO}}(\vec{R})$ is the diabatic BO energy surface. In this case, the electronic-vibrational basis state are written as $|\zeta^{(diab)}(\vec{R}), n_{\zeta}^{(diab)}\rangle = |\zeta^{(diab)}(\vec{R})\rangle |n_{\zeta}^{(diab)}\rangle$ where $|n_{\zeta}^{(diab)}\rangle$ are the eigenstates of the nuclear Hamiltonian

$$\left(E_{\zeta^{(diab)}}^{\text{BO}}(\vec{R}) + \hat{T}_N \right) |n_{\zeta}^{(diab)}\rangle = E_{\zeta, n_{\zeta}}^{(diab)} |n_{\zeta}^{(diab)}\rangle. \quad (2.9)$$

The unperturbed molecular Hamiltonian is taken to be

$$\hat{H}^{(0)} = \sum_{\zeta^{(diab)}} \hat{H}_{\zeta^{(diab)}}^{(0)} \quad (2.10a)$$

$$\hat{H}_{\zeta^{(diab)}}^{(0)} = \sum_{\zeta^{(diab)}} |\zeta^{(diab)}\rangle \langle \zeta^{(diab)} | \left(E_{\zeta^{(diab)}}^{\text{BO}}(\vec{R}) + \hat{T}_N \right), \quad (2.10b)$$

i.e., $|\Psi_m^{(0)}\rangle = \zeta^{(diab)} |n_{\zeta}^{(diab)}\rangle$. Again, \hat{T}_N operates only on the $|n_{\zeta}^{(diab)}\rangle$. The (internal) perturbation \hat{V} is the non-diagonal part of the BO Hamiltonian, i.e.,

$$\hat{V} = \sum_{\zeta^{(diab)}} \sum_{\zeta'^{(diab)'}} |\zeta^{(diab)}\rangle \langle \zeta'^{(diab)'} | \hat{H}^{\text{BO}} | \zeta'^{(diab)'} \rangle \langle \zeta'^{(diab)'} |. \quad (2.11)$$

Within the harmonic approximation, the unperturbed Hamiltonian (eq. 2.7b and 2.10b) can be written in terms of the harmonic oscillator Hamiltonian $\hat{h}_{\zeta}^{(vib)}$ where the index ζ holds either for $\zeta^{(ad)}$ or for $\zeta^{(diab)}$ ^{9,10,32}

$$\hat{H}_{\zeta}^{(0)} = |\zeta\rangle \langle \zeta | \left(E_{\zeta}^{\text{min}} + \hat{h}_{\zeta}^{(vib)} \right). \quad (2.12)$$

E_{ζ}^{min} is the minimum of the BO PES of the electronic state $|\zeta\rangle$. The vibrational Hamiltonian $\hat{h}_{\zeta}^{(vib)}$ is a sum over the harmonic oscillator Hamiltonian of each normal mode α

$$\hat{h}_{\zeta}^{(vib)} = \sum_{\alpha} \hat{h}_{\zeta, \alpha}^{(vib)} \quad (2.13a)$$

$$\hat{h}_{\zeta, \alpha}^{(vib)} = \frac{1}{2} \left[\hat{p}_{\alpha}^2 + \omega_{\zeta, \alpha}^2 (\hat{q}_{\alpha} - q_{\zeta, \alpha}^{\text{eq}})^2 \right], \quad (2.13b)$$

where $\hat{h}_{\zeta, \alpha}^{(vib)}$ is written as a function of the mass-weighted normal-mode coordinates q_{α} .

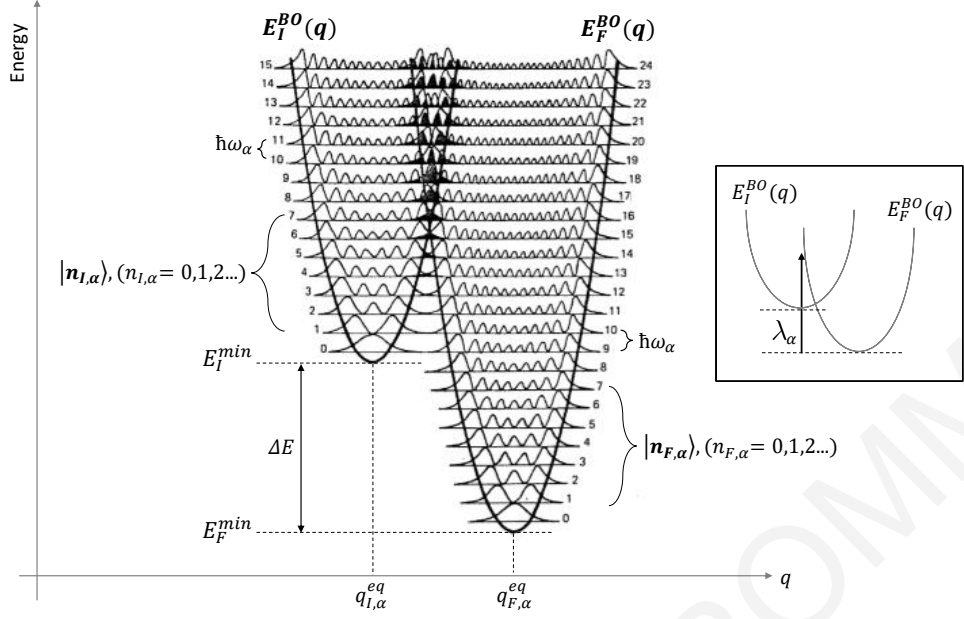


Figure 2.1: Schematic view of the PES of the initial I and final F states in the harmonic approximation model, shown as one-dimensional (single mode α) representation of frequency ω_α . The vibrational energy levels $E_{n_{I,\alpha}} = \hbar\omega_\alpha (n_{I,\alpha} + \frac{1}{2})$ and $E_{n_{F,\alpha}} = \hbar\omega_\alpha (n_{F,\alpha} + \frac{1}{2})$ are shown together with the squares of the vibrational wavefunctions $\langle n_{I,\alpha} | n_{I,\alpha} \rangle$, $\langle n_{F,\alpha} | n_{F,\alpha} \rangle$ superposed on them. Their energies differ from each other by $\hbar\omega_\alpha$. The overlaps between the vibrational wavefunctions belonging to the electronic state I and those belonging to the electronic state F ($\langle n_{I,\alpha} | n_{F,\alpha} \rangle$) are shown in bold. The inset is a similar figure on a different scale where the mode reorganization energy λ_α is clearly shown.

$\omega_{\zeta,\alpha}$ is the frequency of normal mode α that belongs to the electronic state ζ , and $q_{\zeta,\alpha}^{eq}$ is the equilibrium normal mode coordinate. \hat{p}_α is the mass-weighted momentum operator. The eigenvalues of the normal mode Hamiltonian are given by solving the eq. 2.2 for the harmonic oscillator wavefunctions $|n_{\zeta,\alpha}\rangle$

$$\hat{h}_{\zeta,\alpha}^{(vib)} |n_{\zeta,\alpha}\rangle = \hbar\omega_{\zeta,\alpha} \left(n_{\zeta,\alpha} + \frac{1}{2} \right) |n_{\zeta,\alpha}\rangle \quad (2.14)$$

where $n_{\zeta,\alpha}$ are the vibrational quantum numbers for each normal mode α corresponding to the electronic state ζ ($n_{\zeta,\alpha} = 0, 1, 2, 3, \dots, \infty$) (see figure 2.1). Therefore, the eigenenergies (E_{ζ,n_ζ}) of the Hamiltonian $\hat{H}_\zeta^{(0)}$ (eq. 2.12) are given by

$$\hat{H}_\zeta^{(0)} |\zeta\rangle |n_\zeta\rangle = \underbrace{\left[E_\zeta^{min} + \sum_\alpha \hbar\omega_{\zeta,\alpha} \left(n_{\zeta,\alpha} + \frac{1}{2} \right) \right]}_{E_{\zeta,n_\zeta}} |\zeta\rangle |n_\zeta\rangle. \quad (2.15)$$

The total vibrational wavefunction $|n_\zeta\rangle$ is a product of all the normal mode vibrational wavefunctions corresponding to the electronic state ζ , i.e., $|n_\zeta\rangle = \prod_\alpha |n_{\zeta,\alpha}\rangle$.

2.2 Theory of non-adiabatic quantum rate in donor-acceptor complexes

The thermally averaged rate for a transition from an initial electronic state I to a final electronic state F is given by (see eq. 2.3)^{9,10}

$$k_{I \rightarrow F} = \frac{2\pi}{\hbar} \sum_{n_I} P_{n_I} \sum_{n_F} |\langle \Psi_I^{(0)} | \hat{V} | \Psi_F^{(0)} \rangle|^2 \delta(E_{I,n_I} - E_{F,n_F}) \quad (2.16)$$

where n_I and n_F are sets of the normal mode vibrational quantum numbers corresponding to the initial and final electronic states i.e., $n_I = \{n_{I,1}, n_{I,2}, n_{I,3}, \dots\}$ and $n_F = \{n_{F,1}, n_{F,2}, n_{F,3}, \dots\}$. P_{n_I} is the equilibrium (canonical) probability of occupying the initial total vibrational state $|n_I\rangle$. The coupling between the states of the initial vibronic manifold $|I\rangle|n_I\rangle$ and the states of the final vibronic manifold $|F\rangle|n_F\rangle$ is described by the interaction matrix element $\langle \Psi_I^{(0)} | \hat{V} | \Psi_F^{(0)} \rangle$. Neglecting any dependence on the nuclear degrees of freedom, the coupling splits into two parts so that

$$\begin{aligned} |\langle \Psi_I^{(0)} | \hat{V} | \Psi_F^{(0)} \rangle|^2 &= |\langle I | \hat{V} | F \rangle|^2 |\langle n_I | n_F \rangle|^2 \\ &= |\langle I | \hat{V} | F \rangle|^2 \prod_{\alpha} |\langle n_{I,\alpha} | n_{F,\alpha} \rangle|^2, \end{aligned} \quad (2.17)$$

where $|\langle n_{I,\alpha} | n_{F,\alpha} \rangle|^2$ are the Franck-Condon factors (FCFs) and are the absolute squares of overlap integrals between the nuclear wavefunctions of the initial and final electronic states. Using the above result in eq. 2.16, it leads to

$$\begin{aligned} \sum_{n_I} P_{n_I} \sum_{n_F} |\langle \Psi_I^{(0)} | \hat{V} | \Psi_F^{(0)} \rangle|^2 &= \\ |\langle I | \hat{V} | F \rangle|^2 \sum_{n_{I,1}} P_{n_{I,1}} \sum_{n_{I,2}} P_{n_{I,2}} \dots \sum_{n_{I,3N-6}} P_{n_{I,3N-6}} \sum_{n_{F,1}} \sum_{n_{F,2}} \dots \sum_{n_{F,3N-6}} \prod_{\alpha=1}^{3N-6} |\langle n_{I,\alpha} | n_{F,\alpha} \rangle|^2, \end{aligned} \quad (2.18)$$

where

$$P_{n_{I,\alpha}} = \frac{e^{-E_{n_{I,\alpha}}/K_B T}}{Z} \quad (2.19)$$

is the canonical distribution for the initial vibrational states $n_{I,\alpha}$ of normal mode α (i.e., $P_{n_I} = \prod_{\alpha} P_{n_{I,\alpha}}$). $E_{n_{I,\alpha}} = \hbar\omega_{I,\alpha}(n_{I,\alpha} + \frac{1}{2})$ and Z is the partition function ($Z = \sum_{n_{I,\alpha}} e^{-E_{n_{I,\alpha}}/K_B T}$). Thus, the transition rate $k_{I \rightarrow F}$ is given by,

$$\begin{aligned} k_{I \rightarrow F} &= \frac{2\pi}{\hbar} |\langle I | \hat{V} | F \rangle|^2 \sum_{n_{I,1}} P_{n_{I,1}} \sum_{n_{I,2}} P_{n_{I,2}} \dots \sum_{n_{I,3N-6}} P_{n_{I,3N-6}} \sum_{n_{F,1}} \sum_{n_{F,2}} \dots \sum_{n_{F,3N-6}} \times \\ &\quad \prod_{\alpha=1}^{3N-6} |\langle n_{I,\alpha} | n_{F,\alpha} \rangle|^2 \delta \left(E_I^{min} + \sum_{\alpha=1}^{3N-6} \hbar\omega_{I,\alpha} \left(n_{I,\alpha} + \frac{1}{2} \right) - \right. \\ &\quad \left. \left[E_F^{min} + \sum_{\alpha=1}^{3N-6} \hbar\omega_{F,\alpha} \left(n_{F,\alpha} + \frac{1}{2} \right) \right] \right). \end{aligned} \quad (2.20)$$

The rate equation (eq. 2.20) is transformed into an integral form by introducing the lineshape function $D(\Delta E/\hbar)$ ^{9,10,31,33–35}

$$k_{I \rightarrow F} = \frac{2\pi}{\hbar} |\langle I | \hat{V} | F \rangle|^2 D(\Delta E/\hbar). \quad (2.21)$$

where $D(\Delta E/\hbar)$ reads

$$D(\Delta E/\hbar) = \sum_{n_{I,1}} P_{n_{I,1}} \sum_{n_{I,2}} P_{n_{I,2}} \cdots \sum_{n_{I,3N-6}} P_{n_{I,3N-6}} \sum_{n_{F,1}} \sum_{n_{F,2}} \cdots \sum_{n_{F,3N-6}} \times \prod_{\alpha=1}^{3N-6} |\langle n_{I,\alpha} | n_{F,\alpha} \rangle|^2 \delta \left(\Delta E + \sum_{\alpha=1}^{3N-6} \hbar \omega_{I,\alpha} \left(n_{I,\alpha} + \frac{1}{2} \right) - \sum_{\alpha=1}^{3N-6} \hbar \omega_{F,\alpha} \left(n_{F,\alpha} + \frac{1}{2} \right) \right) \quad (2.22)$$

and $\Delta E = E_I^{min} - E_F^{min}$, is the energy difference between the minimum energy values of the initial and final BO PES (see Figure 2.1). Assuming state-independent frequencies, i.e., $\omega_{I,\alpha} = \omega_{F,\alpha} \equiv \omega_\alpha$, the lineshape function can be transformed into a time integral using the Fourier representation of the delta function $\delta(x) = (2\pi\hbar)^{-1} \int_{-\infty}^{\infty} e^{ixt/\hbar} dt$,

$$D(\Delta E/\hbar) = \frac{1}{2\pi\hbar} \int_{-\infty}^{\infty} e^{i\frac{\Delta E}{\hbar}t} f(t) \quad (2.23a)$$

$$f(t) = \sum_{n_{I,1}} \sum_{n_{I,2}} \cdots \sum_{n_{I,3N-6}} P_{n_{I,1}} P_{n_{I,2}} \cdots P_{n_{I,3N-6}} \sum_{n_{F,1}} \sum_{n_{F,2}} \cdots \sum_{n_{F,3N-6}} \times \prod_{\alpha=1}^{3N-6} |\langle n_{I,\alpha} | n_{F,\alpha} \rangle|^2 e^{i \sum_{\alpha} \omega_{\alpha} (n_{I,\alpha} - n_{F,\alpha}) t} dt. \quad (2.23b)$$

Equation 2.23b yields

$$f(t) = e^{G(t) - G(0)} \quad (2.24)$$

where $G(t)$ is given by

$$G(t) = \sum_{\alpha} [q_F(\alpha) - q_I(\alpha)]^2 \{ (2\langle n_{\alpha} \rangle + 1) \cos(\omega_{\alpha} t) - i \sin(\omega_{\alpha} t) \}. \quad (2.25)$$

Therefore, the lineshape function reduces to

$$D(\Delta E/\hbar) = \frac{1}{2\pi\hbar} \int_{-\infty}^{\infty} e^{i\frac{\Delta E}{\hbar}t + G(t) - G(0)} dt. \quad (2.26)$$

The dimensionless displacement $q_F(\alpha) - q_I(\alpha)$ in eq. 2.25 between the initial (I) and final (F) PES are related to the electron-phonon couplings $\bar{\lambda}_{\alpha}$ and the mode reorganization energies λ_{α} via

$$\frac{[q_F(\alpha) - q_I(\alpha)]^2}{2} = \bar{\lambda}_{\alpha}^2 = \frac{\lambda_{\alpha}}{\hbar\omega_{\alpha}}. \quad (2.27)$$

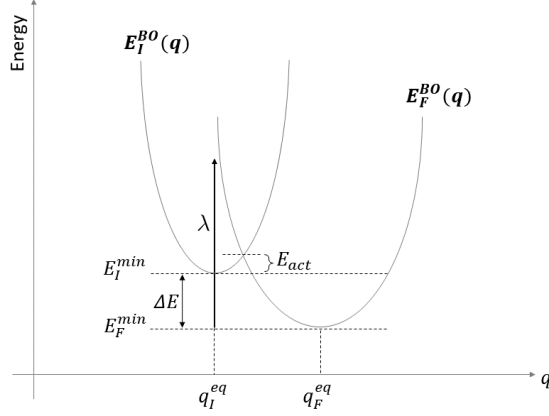


Figure 2.2: PES of the initial I and final F electronic states indicating the definition of the activation energy E_{act} .

$\langle n_\alpha \rangle$ is the thermal boson occupation number that equals to,

$$\langle n_\alpha \rangle = \left(e^{\frac{\hbar\omega_\alpha}{K_B T}} - 1 \right)^{-1} \quad (2.28)$$

where K_B is the Boltzmann constant and T is the temperature. Therefore, the transition rate is expressed as the Fourier transform (FT) of a correlation function computed at ΔE ,

$$k_{I \rightarrow F} \left(\frac{\Delta E}{\hbar} \right) = \frac{|\langle I | \hat{V} | F \rangle|^2}{\hbar^2} \underbrace{e^{-G(0)} \int_{-\infty}^{\infty} e^{G(t)} e^{i \frac{\Delta E}{\hbar} t} dt}_{\text{total FCF}} \quad (2.29)$$

$G(t)$ is simplified according to eqs. 2.25 and 2.27 as follows

$$G(t) = \sum_{\alpha} \left(\frac{\lambda_{\alpha}}{\hbar\omega_{\alpha}} \right) \{ (2\langle n_{\alpha} \rangle + 1) \cos(\omega_{\alpha} t) - i \sin(\omega_{\alpha} t) \}. \quad (2.30)$$

The FCFs are given by integrating the correlation function with respect to time (see eq. 2.29).

How does one recover the classical Marcus formula for the FCF (see below eqs. 2.31 and 2.32) from the exact quantum equation (eq. 2.29)? If all modes are classical, namely, $\langle n_{\alpha} \rangle \approx K_B T / \hbar\omega_{\alpha}$ (i.e., $K_B T \gg \hbar\omega_{\alpha}$) and $\sum_{\alpha} \bar{\lambda}_{\alpha}^2 n_{\alpha} \gg 1$, it is possible to apply the so-called short-time approximation (e.g., see refs. 9,33,35,36 and appendix B). This includes the following replacements: $\sin(\omega_{\alpha} t) \approx \omega_{\alpha} t$ and $\cos(\omega_{\alpha} t) \approx 1 - \frac{\omega_{\alpha}^2 t^2}{2}$. The non-adiabatic transition rate reduces to the classical Marcus formula^{9,10,37-42}

$$k_{I \rightarrow F} = \frac{|\langle I | \hat{V} | F \rangle|^2}{\hbar^2} \underbrace{\sqrt{\frac{\pi \hbar^2}{K_B T \lambda}} e^{-(\Delta E - \lambda)^2 / 4 K_B T \lambda}}_{\text{classical total FCF}} \quad (2.31)$$

where λ is the total reorganization energy ($\lambda = \sum_{\alpha} \lambda_{\alpha}$) and the quantity,

$$E_{act} = \frac{(\Delta E - \lambda)^2}{4\lambda} \quad (2.32)$$

is the Gibbs free energy of activation, which represents the energy required to reach the crossing point between the initial I and final F PES (see figure 2.2). Further discussion of the classical approximation and example applications of the Marcus formula are given in section 7.2.

2.3 Quantum rate constants for two independent sets of vibrational coordinates

In section 2.2 we applied the golden-rule formula to compute the transition rate from the initial state I to the final state F , assuming a common set of vibrational coordinates for both states. This is generally applied to unimolecular reactions that involve a single molecule. However, in bimolecular processes where the molecular complex consists of separate donor (D) and acceptor (A) molecules, it is more appropriate to use a separate set of vibrational coordinates, one for the donor molecule and one for the acceptor molecule. Having different sets of coordinates for the donor and acceptor moieties, it is necessary to describe the initial and final states of the donor and acceptor separately. As an example, let's consider a donor-acceptor system that undergoes hole transfer. The initial state of the entire system is $|I\rangle = |D^+A\rangle$ and the final state is $|F\rangle = |DA^+\rangle$. The PES of the initial and final states of the donor ($|D^+\rangle, |D\rangle$) and the acceptor ($|A\rangle, |A^+\rangle$) are shown in figure 2.3. The transition rate (eq. 2.16) is now given by¹⁰

$$\begin{aligned} k_{|D^+A\rangle \rightarrow |DA^+\rangle} &= \frac{2\pi}{\hbar} |\langle D^+A | \hat{V} | DA^+ \rangle|^2 \times \\ &\sum_{n_{D^+,1}} P_{n_{D^+,1}} \sum_{n_{D^+,2}} P_{n_{D^+,2}} \cdots \sum_{n_{D^+,3N-6}} P_{n_{D^+,3N-6}} \sum_{n_{A,1}} P_{n_{A,1}} \sum_{n_{A,2}} P_{n_{A,2}} \cdots \sum_{n_{A,3N-6}} P_{n_{A,3N-6}} \times \\ &\sum_{n_{D,1} n_{D,2}} \cdots \sum_{n_{D,3N-6}} \prod_{\alpha=1}^{3N-6} |\langle n_{D^+,a} | n_{D,a} \rangle|^2 \sum_{n_{A^+,1} n_{A^+,2}} \cdots \sum_{n_{A^+,3N-6}} \prod_{b=1}^{3N-6} |\langle n_{A,b} | n_{A^+,b} \rangle|^2 \times \quad (2.33) \\ &\delta \left(\left[E_{D^+}^{min} + \sum_{\alpha=1}^{3N-6} \hbar\omega_{D^+,\alpha} \left(n_{D^+,\alpha} + \frac{1}{2} \right) \right] + \left[E_A^{min} + \sum_{b=1}^{3N-6} \hbar\omega_{A,b} \left(n_{A,b} + \frac{1}{2} \right) \right] - \right. \\ &\left. \left[E_D^{min} + \sum_{\alpha=1}^{3N-6} \hbar\omega_{D,\alpha} \left(n_{D,\alpha} + \frac{1}{2} \right) \right] - \left[E_{A^+}^{min} + \sum_{b=1}^{3N-6} \hbar\omega_{A^+,b} \left(n_{A^+,b} + \frac{1}{2} \right) \right] \right). \end{aligned}$$

where $n_{X,\alpha}$ are the vibrational quantum numbers corresponding to the initial ($X = D^+$) and final ($X = D$) electronic states of the donor for each normal mode α , and $n_{Y,b}$ are the vibrational quantum numbers corresponding to the initial ($Y = A$) and final

($Y = A^+$) electronic states of the acceptor for each normal mode b . If we assume equal frequencies for the initial and final states of the donor molecule then $\omega_{D^+, \alpha} = \omega_{D, \alpha} \equiv \omega_\alpha$. In the same manner, for the acceptor molecule we have $\omega_{A, b} = \omega_{A^+, b} \equiv \omega_b$. Similarly to eqs. 2.26 and 2.29 the rate is rewritten in a more compact integrated form

$$k_{|D^+A\rangle \rightarrow |DA^+\rangle} \left(\frac{\Delta E}{\hbar} \right) = \frac{|\langle D^+A | \hat{V} | DA^+ \rangle|^2}{\hbar^2} e^{-G_{D^+D}(0)} e^{-G_{AA^+}(0)} \times \int_{-\infty}^{\infty} e^{G_{D^+D}(t)} e^{G_{AA^+}(t)} e^{i \frac{\Delta E}{\hbar} t} dt \quad (2.34)$$

where the donor and acceptor vibrational coordinates allows the transition rate to split up into a donor part and an acceptor part through the time-dependent functions $G_{D^+D}(t)$ and $G_{AA^+}(t)$

$$G_{D^+D}(t) = \sum_{\alpha} \left(\frac{\lambda_{\alpha}}{\hbar \omega_{\alpha}} \right) \{ (2\langle n_{\alpha} \rangle + 1) \cos(\omega_{\alpha} t) - i \sin(\omega_{\alpha} t) \}$$

$$G_{AA^+}(t) = \sum_b \left(\frac{\lambda_b}{\hbar \omega_b} \right) \{ (2\langle n_b \rangle + 1) \cos(\omega_b t) - i \sin(\omega_b t) \}. \quad (2.35)$$

$\lambda_{\alpha(b)}$ and $\omega_{\alpha(b)}$ are the reorganization energy and frequency of mode $\alpha(b)$ respectively, related to the donor (acceptor) coordinates. ΔE is the driving force given by the electronic energy difference of the initial $|D^+A\rangle$ and final $|DA^+\rangle$ states,

$$\Delta E = (E_{D^+}^{min} + E_A^{min}) - (E_D^{min} + E_{A^+}^{min}). \quad (2.36)$$

The total reorganization energy of the system is the sum of the energies of the donor and the acceptor (see figure 2.4),

$$\lambda = \sum_{\alpha} \lambda_{\alpha} + \sum_b \lambda_b. \quad (2.37)$$

In the high-temperature limit, the transition rate yields the Marcus formula of eq. 2.31, with the energy difference ΔE now given by eq. 2.36 and the reorganization energy λ by eq. 2.37.

2.4 Homogeneous and inhomogeneous lineshape broadening

In section 2.2 we introduced the spectral density via eq. 2.22. This lineshape expression displays the superposition of lines corresponding to transitions between the vibrational states of the reactant ($|n_I\rangle$) and product states ($|n_F\rangle$). The lines appear as δ -functions with intensities determined by the FCFs ($|\langle n_I | n_F \rangle|^2$), and each line will be broadened depending on static or dynamic effects.

To introduce homogeneous broadening, the delta function in eq. 2.22 is now

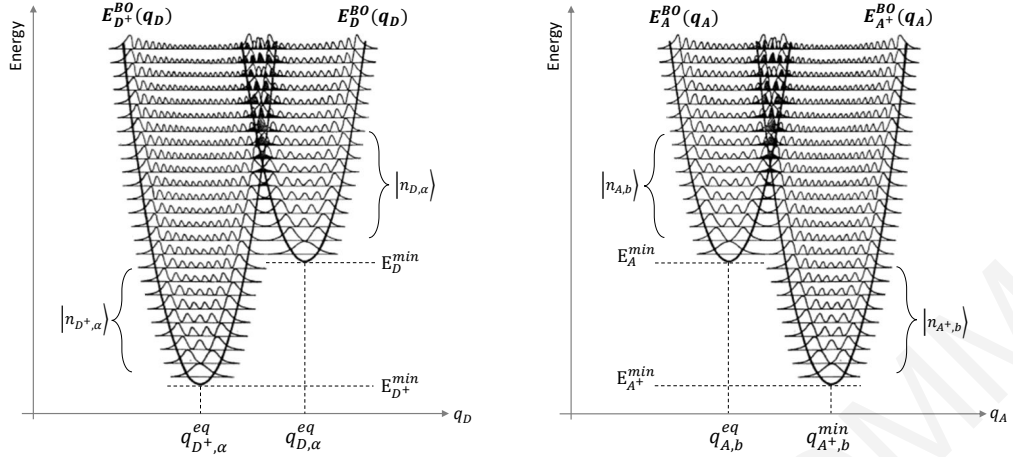


Figure 2.3: PES of the donor (D) and acceptor (A) parts for the case of independent vibrational coordinates (see figure 2.1). *left.* PES of the positively charged and neutral donor. *Right.* PES of the neutral and positively charged acceptor.

expressed as a Lorentzian distribution i.e.,

$$\mathfrak{L}(x) = \frac{1}{\pi\hbar} \frac{\Gamma}{\Gamma^2 + x^2} = \frac{1}{2\pi\hbar} \int_{-\infty}^{\infty} e^{itx - \Gamma|t|} dt. \quad (2.38)$$

In this case, $x = \Delta E + \sum_{\alpha=1}^{3N-6} \hbar\omega_{I,\alpha} (n_{I,\alpha} - n_{F,\alpha})$ (see eq. 2.22), and the lineshape function (eq. 2.23a) is now given by

$$D_{\text{hom}}(\Delta E/\hbar) = \frac{1}{2\pi\hbar} \int_{-\infty}^{\infty} e^{i\frac{\Delta E}{\hbar}t - \Gamma|t|} f(t), \quad (2.39)$$

where $f(t)$ is given by eqs. 2.23b and 2.24, i.e.,^{9,10,34}

$$D_{\text{hom}}(\Delta E/\hbar) = \frac{1}{2\pi\hbar} \int_{-\infty}^{\infty} e^{i\frac{\Delta E}{\hbar}t - \Gamma|t|} e^{G(t) - G(0)} dt. \quad (2.40)$$

The rate equation yields

$$k_{I \rightarrow F} \left(\frac{\Delta E}{\hbar} \right) = \frac{|\langle I | \hat{V} | F \rangle|^2}{\hbar^2} e^{-G(0)} \int_{-\infty}^{\infty} e^{G(t)} e^{i\frac{\Delta E}{\hbar}t - \Gamma|t|}. \quad (2.41)$$

This is the limit of homogeneous broadening and Γ is called homogeneous broadening width.

Due to disorder at the ensemble level, ΔE is considered to be a Gaussian random variable with mean $\overline{\Delta E}$ and width Θ . Under the assumption of a Gaussian distribution of the adiabatic energy differences, it is possible to modify the expression for the

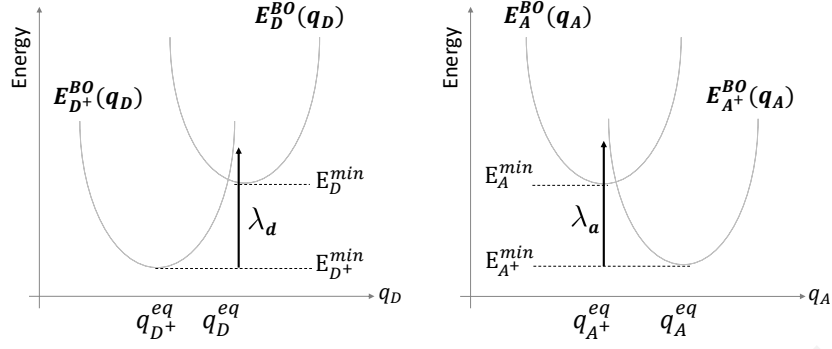


Figure 2.4: PES in a simplified form, of the donor (D) and acceptor (A) parts for the case of independent vibrational coordinates showing the donor and acceptor mode reorganization energies.

lineshape function as follows^{9,10,33,34}

$$\begin{aligned}
 D_{\text{inh,hom}}(\overline{\Delta E}/\hbar, \Theta) &= \langle D_{\text{inh,hom}}(\Delta E/\hbar) \rangle \\
 &= \int_{-\infty}^{\infty} \frac{1}{\sqrt{2\pi}\Theta} e^{-\frac{(\Delta E - \overline{\Delta E})^2}{2\Theta^2}} d\Delta E \frac{1}{2\pi\hbar} \int_{-\infty}^{\infty} e^{i\frac{\Delta E}{\hbar}t - \Gamma|t|} f(t) dt.
 \end{aligned} \tag{2.42}$$

The integration over ΔE is performed explicitly, and the lineshape function is now written as

$$D_{\text{inh,hom}}(\overline{\Delta E}/\hbar, \Theta) = \frac{1}{2\pi\hbar} \int_{-\infty}^{\infty} e^{i\frac{\overline{\Delta E}}{\hbar}t - \Gamma|t| - \frac{\Theta^2 t^2}{2}} e^{G(t) - G(0)} dt. \tag{2.43}$$

The transition rate reduces to

$$k_{I \rightarrow F} \left(\frac{\overline{\Delta E}}{\hbar} \right) = \frac{|\langle I | \hat{V} | F \rangle|^2}{\hbar^2} e^{-G(0)} \int_{-\infty}^{\infty} e^{G(t)} e^{i\frac{\overline{\Delta E}}{\hbar}t - \Gamma|t| - \frac{1}{2}\Theta^2 t^2} dt. \tag{2.44}$$

This is the limit of inhomogeneous broadening and the parameter Θ is known as the inhomogeneous broadening width.

2.5 Applications

The Franck-Condon principle for the non-adiabatic quantum rate that we introduced in the previous sections, is valid when the time-scale of the electronic transition is much slower than the vibrational motion time scales. Such types of molecular electronic transitions are induced by internal couplings e.g., electron/hole and energy transfer in donor-acceptor complexes or by external perturbations e.g., absorption or emission between ground and excited states and ISC or internal conversion (IC) between excited

states. The corresponding transition rate can be computed by combining equations 2.29 and 2.30, with the appropriate $\langle I|\hat{V}|F\rangle$. In this section, we briefly describe how these formulae are used to compute the rate constants for different types of reactions (different $\langle I|\hat{V}|F\rangle$).

2.5.1 Optical absorption coefficient and fluorescence efficiency

Optical absorption is the most common example of interaction between a molecular system and an external electromagnetic field that causes electronic transitions from the ground state of the molecule to its excited states.^{9,10,43,44} The interaction Hamiltonian for the external applied field in the electric dipole approximation reads

$$\hat{V}(t) = -\hat{\vec{\mu}} \cdot \vec{E}(t) \quad (2.45)$$

where $\vec{\mu}$ is the electronic dipole moment vector and $\vec{E}(t) = \vec{E}_0 e^{-i\omega_L t} + \vec{E}_0^* e^{i\omega_L t}$ for a monochromatic field of frequency ω_L . Within the rotating wave approximation (RWA) the electric field is simplified to $\vec{E}(t) = \vec{E}_0 e^{-i\omega_L t}$. Further, $\langle I|\hat{V}|F\rangle = \langle g|\hat{\vec{\mu}} \cdot \vec{E}_0|e\rangle$, where $|g\rangle$ is the electronic ground state in the BO approximation and $|e\rangle$ is the excited electronic state in the BO approximation. The transition rate for absorption from the ground state to a single excited state is given by (see eq. 2.20)

$$k_{g \rightarrow e} = \frac{2\pi}{\hbar} |\langle g|\hat{\vec{\mu}} \cdot \vec{E}_0|e\rangle|^2 \sum_{n_{g,1}} P_{n_{g,1}} \sum_{n_{g,2}} P_{n_{g,2}} \dots \sum_{n_{g,3N-6}} P_{n_{g,3N-6}} \sum_{n_{e,1}} \sum_{n_{e,2}} \dots \sum_{n_{e,3N-6}} \times \prod_{\alpha=1}^{3N-6} | \langle n_{g,\alpha} | n_{e,\alpha} \rangle |^2 \delta \left(\hbar\omega_L + E_g^{min} - E_e^{min} + \sum_{\alpha=1}^{3N-6} \hbar\omega_{\alpha} (n_{g,\alpha} - n_{e,\alpha}) \right), \quad (2.46)$$

where $\hbar\omega_L$ is the energy of the incident photons.

Consider that monochromatic light of frequency ω_L is incident perpendicularly onto the surface of cross section on area A of a macroscopic sample of volume v which contains N_{mol} molecules. If we take a small section of length dz and volume Adz , the decrease of the radiation field energy dE during the time interval dt is given by

$$dE = -N_{mol} \frac{Adz}{v} \hbar\omega_L k_{g \rightarrow e} dt, \quad (2.47)$$

where $N_{mol}Adz/v$ is the fraction of molecules inside the volume Adz and $\hbar\omega_L k_{g \rightarrow e} dt$ is the energy absorbed per photon in the time interval dt . The energy absorbed per unit volume is $du = dE/Adz$, and using eq. 2.47 we write

$$\frac{du}{dt} = -n_{mol} \hbar\omega_L k_{g \rightarrow e}, \quad (2.48)$$

where $n_{mol} = \frac{N_{mol}}{v}$ is the volume density of the absorbing molecules. Using the equality $\frac{du}{dt} = \frac{dI}{dz}$, where I is the field intensity and that $I = cE_0^2/2\pi$ we get

$$\frac{dI}{dz} = -\frac{2\pi n_{mol}}{cE_0^2} \hbar\omega_L k_{g \rightarrow e} I. \quad (2.49)$$

Comparing the Beer-Lambert law, $\frac{dI}{dz} = -aI$ (a is the absorption coefficient) with eq. 2.49 gives

$$a(\omega_L) = \frac{2\pi n_{mol}}{cE_0^2} \hbar\omega_L k_{g \rightarrow e}. \quad (2.50)$$

By combining eqs. 2.46, 2.50 and 2.26 we obtain an expression for the absorption coefficient

$$a(\omega_L) = \frac{4\pi^2 \omega_L n_{mol}}{3c} |\langle g | \hat{\mu} | e \rangle|^2 D\left(\omega_L + \frac{\Delta E}{\hbar}\right) \quad (2.51)$$

with $\Delta E = E_g^{min} - E_e^{min}$. In this equation $\hat{\mu}$ is the component of the electronic dipole moment vector in the direction of the field vector. The factor $\frac{1}{3}$ comes from averaging over all molecules that possesses random orientations in the sample. $D\left(\omega_L + \frac{\Delta E}{\hbar}\right)$ is the lineshape function for the absorption (see eq. 2.26). In an absorption experimental setup we usually measure the absorption cross section $\sigma(\omega_L)$ which is directly related to the absorption coefficient via $\sigma(\omega_L) = a(\omega_L)/n_{mol}$.

Similarly, the fluorescence efficiency $A(\omega_R)$ for the transition $e \rightarrow g$, is given by the following formula,

$$A(\omega_R) = \frac{4\omega_R^3 |\langle g | \hat{\mu} | e \rangle|^2}{3c^3} D\left(\frac{\Delta E}{\hbar} - \omega_R\right) \quad (2.52)$$

with $\Delta E = E_e^{min} - E_g^{min}$ and $\hbar\omega_R$ is the energy of the emitted photon. $D\left(\frac{\Delta E}{\hbar} - \omega_R\right)$ is the respective lineshape function for the emission process (see eq. 2.26). The different prefactor multiplied $|\langle g | \hat{\mu} | e \rangle|^2$ is derived from quantum electrodynamics and the Einstein coefficients for absorption and stimulated emission.⁴⁵⁻⁴⁸

2.5.2 Intersystem crossing rates

The perturbation that causes transitions between two states of different spin multiplicity is the spin-orbit coupling (SOC). For an ISC transition between the singlet $|S_n\rangle$ and triplet $|T_{k,m_s}\rangle$ ($m_s = 0, \pm 1$) excited states, the interaction term \hat{V} is replaced by the SOC interaction Hamiltonian \hat{H}^{SOC} , so that $\langle I | \hat{V} | F \rangle = \langle S_n | \hat{H}^{SOC} | T_{k,m_s} \rangle$ (see chapter 3).

2.5.3 Singlet and triplet energy transfer rates

Molecular exciton transfer (or EnT) processes often involve the transition of an electron-hole pair from an initial to a final electronic state that are separated in space. This type of transition usually occurs after photoexcitation when the molecule absorbs

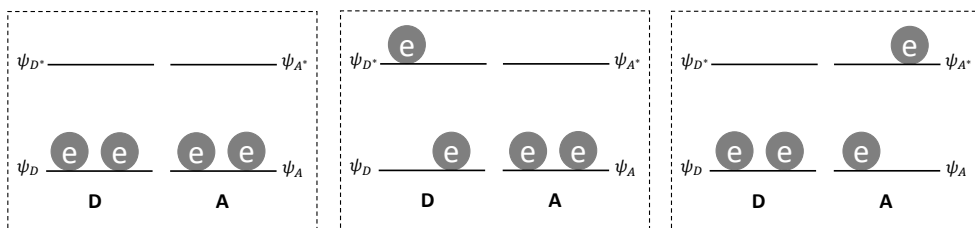


Figure 2.5: Electronic structure of a 4-electron exciton system consisting two donor (D)-acceptor (A) fragments. $\psi_{D(A)}$ and $\psi_{D^*(A^*)}$ are the ground- and excited-state molecular orbitals respectively, of the $D(A)$ fragment. *left:* the ground state electronic configuration of the $D-A$ system. *middle:* an electron is promoted from the D ground state to the D excited state to generate the initial excited configuration of the system. *right:* The excited electron is transferred to the acceptor to generate the final excited configuration of the system.

a photon and an electron moves from its occupied to its unoccupied molecular orbitals. This transition creates a bound electron-hole pair which is called donor exciton. The donor exciton may undergo inter- or intra- molecular exciton transfer transitions to form the acceptor exciton localized in another region of the molecule. To describe EnT reactions in molecules we introduce the one- and two-particle electronic Hamiltonian¹⁰

$$\hat{H}^{\text{el}} = \hat{h}^{(1e)} + \hat{h}^{(2e)}, \quad (2.53)$$

where $\hat{h}^{(1e)}$ is the one-electron Hamiltonian consisting of the kinetic energy operator for the electron motion and the operator for Coulomb attraction between the electrons and the nuclei. The two-electron Hamiltonian describes the Coulomb repulsive interactions between the electrons. In the following, we compute the interaction matrix elements between singlet exciton states and between triplet exciton states.

In the simplest case of a donor (D) - acceptor (A) system, we describe each fragment by its highest occupied molecular orbital (HOMO) [i.e., ψ_D and ψ_A] and its lowest unoccupied molecular orbital (LUMO) [i.e., ψ_{D^*} and ψ_{A^*}]. The ground state of the $D-A$ system is the single Slater-type determinant (see figure 2.5 (left))^{49,50}

$$|\Psi_0\rangle = |\psi_D a \psi_D \beta \psi_A a \psi_A \beta\rangle. \quad (2.54)$$

This is an antisymmetric wavefunction of a 4-electron system written in simplified form as a product of four spin orbitals that are formed by multiplying the spatial wavefunction ψ by the spin function (a for spin up and β for spin down). We simplify the notation and denote $\psi_i a$ by ψ_i and $\psi_i \beta$ by $\bar{\psi}_i$ ($i = D, A$) i.e.,

$$|\Psi_0\rangle = |\psi_D \bar{\psi}_D \psi_A \bar{\psi}_A\rangle. \quad (2.55)$$

The singly excited determinants for the initial state (see figure 2.5 (middle)) are written as

$$\begin{aligned} |\Psi_{I_1}\rangle &= |\psi_D \bar{\psi}_{D^*} \psi_A \bar{\psi}_A\rangle \\ |\Psi_{I_2}\rangle &= |\bar{\psi}_D \psi_{D^*} \psi_A \bar{\psi}_A\rangle. \end{aligned} \quad (2.56)$$

The first state ($|\Psi_{I_1}\rangle$) represents the case where the promoted electron in the ψ_{D^*} state has spin β while the in the second state ($|\Psi_{I_2}\rangle$) it has spin α . In a similar way the final state singly excited determinants are (see figure 2.5 (right))

$$\begin{aligned} |\Psi_{F_1}\rangle &= |\psi_D \bar{\psi}_D \psi_A \bar{\psi}_{A^*}\rangle \\ |\Psi_{F_2}\rangle &= |\psi_D \bar{\psi}_D \bar{\psi}_A \psi_{A^*}\rangle. \end{aligned} \quad (2.57)$$

The determinants $|\Psi_{I_1}\rangle, |\Psi_{I_2}\rangle, |\Psi_{F_1}\rangle$ and $|\Psi_{F_2}\rangle$ are not pure spin states i.e., they are not eigenfunctions of the \hat{S}^2 operator. By taking appropriate linear combinations of these determinants, we form spin-adapted configurations that are eigenfunctions of \hat{S}^2 . The initial and final singlet excited states are given by

$$\begin{aligned} |^1\Psi_I\rangle &= \frac{1}{\sqrt{2}} [|\Psi_{I_1}\rangle + |\Psi_{I_2}\rangle] \\ |^1\Psi_F\rangle &= \frac{1}{\sqrt{2}} [|\Psi_{F_1}\rangle + |\Psi_{F_2}\rangle], \end{aligned} \quad (2.58)$$

and the initial and final triplet excited states are given by

$$\begin{aligned} |^3\Psi_I\rangle &= \frac{1}{\sqrt{2}} [|\Psi_{I_1}\rangle - |\Psi_{I_2}\rangle] \\ |^3\Psi_F\rangle &= \frac{1}{\sqrt{2}} [|\Psi_{F_1}\rangle - |\Psi_{F_2}\rangle]. \end{aligned} \quad (2.59)$$

In the case of singlet exciton transport (SET), the interaction matrix element is $\langle I|\hat{V}|F\rangle = \langle ^1\Psi_I|\hat{H}|^1\Psi_F\rangle$ and it is given by

$$\langle ^1\Psi_I|\hat{H}|^1\Psi_F\rangle = \langle ^1\Psi_I|\hat{h}^{(1e)}|^1\Psi_F\rangle + \langle ^1\Psi_I|\hat{h}^{(2e)}|^1\Psi_F\rangle \quad (2.60a)$$

$$\langle ^1\Psi_I|\hat{h}^{(1e)}|^1\Psi_F\rangle = V_{D^*A^*}^e S_{AD} - V_{AD}^h S_{D^*A^*} \quad (2.60b)$$

$$\langle ^1\Psi_I|\hat{h}^{(2e)}|^1\Psi_F\rangle = 2(\psi_D \psi_{D^*} |\psi_A \psi_{A^*}\rangle) - (\psi_{D^*} \psi_{A^*} |\psi_D \psi_A\rangle), \quad (2.60c)$$

while in the case of triplet exciton transport (TET) the $\langle I|\hat{V}|F\rangle = \langle ^3\Psi_I|\hat{H}|^3\Psi_F\rangle$ is given by

$$\langle ^3\Psi_I|\hat{H}|^3\Psi_F\rangle = \langle ^3\Psi_I|\hat{h}^{(1e)}|^3\Psi_F\rangle + \langle ^3\Psi_I|\hat{h}^{(2e)}|^3\Psi_F\rangle \quad (2.61a)$$

$$\langle ^3\Psi_I|\hat{h}^{(1e)}|^3\Psi_F\rangle = V_{D^*A^*}^e S_{AD} - V_{AD}^h S_{D^*A^*} \quad (2.61b)$$

$$\langle ^3\Psi_I|\hat{h}^{(2e)}|^3\Psi_F\rangle = -(\psi_{D^*} \psi_{A^*} |\psi_D \psi_A\rangle). \quad (2.61c)$$

In the equations above, the ψ_i ($i = D, A$) denotes the spatial part of the wavefunctions. $V_{D^*A^*}^e$ is the $D-A$ electron transfer (ET) coupling matrix elements between the excited ψ_{D^*} and ψ_{A^*} fragment molecular orbitals, and V_{AD}^h is the $D-A$ hole transfer (HT) coupling matrix element between the ground ψ_D and ψ_A fragment molecular orbitals, i.e.,

$$\begin{aligned} V_{D^*A^*}^e &= \langle \psi_{D^*} | \hat{h}^{(1e)} | \psi_{A^*} \rangle = \int \psi_{D^*}(\vec{r}_1) \hat{h}^{(1e)} \psi_{A^*}(\vec{r}_1) d\vec{r}_1 \\ V_{AD}^h &= \langle \psi_A | \hat{h}^{(1e)} | \psi_D \rangle = \int \psi_A(\vec{r}_1) \hat{h}^{(1e)} \psi_D(\vec{r}_1) d\vec{r}_1, \end{aligned} \quad (2.62)$$

S_{DA} and $S_{D^*A^*}$ are the overlap matrix elements between the ground ψ_D and ψ_A orbitals and the excited ψ_{D^*} and ψ_{A^*} orbitals respectively, i.e.,

$$\begin{aligned} S_{D^*A^*} &= \langle \psi_{D^*} | \psi_{A^*} \rangle = \int \psi_{D^*}(\vec{r}_1) \psi_{A^*}(\vec{r}_1) d\vec{r}_1 \\ S_{AD} &= \langle \psi_A | \psi_D \rangle = \int \psi_A(\vec{r}_1) \psi_D(\vec{r}_1) d\vec{r}_1. \end{aligned} \quad (2.63)$$

$(\psi_D \psi_{D^*} | \psi_A \psi_{A^*})$ is the two-electron ‘‘Coulomb’’ integral defined by

$$\begin{aligned} (\psi_D \psi_{D^*} | \psi_A \psi_{A^*}) &= \int \psi_D(\vec{r}_1) \psi_{D^*}(\vec{r}_1) r_{12}^{-1} \psi_A(\vec{r}_2) \psi_{A^*}(\vec{r}_2) d\vec{r}_1 d\vec{r}_2 \\ &= \int |\psi_D(\vec{r}_1)|^2 r_{12}^{-1} |\psi_A(\vec{r}_2)|^2 \end{aligned} \quad (2.64)$$

and is the classical analogue of the Coulomb repulsion between the charge densities $|\psi_D(\vec{r}_1)|^2$ and $|\psi_A(\vec{r}_2)|^2$. $(\psi_{D^*} \psi_{A^*} | \psi_D \psi_A)$ is the two-electron ‘‘exchange’’ integral defined by

$$\begin{aligned} (\psi_{D^*} \psi_{A^*} | \psi_D \psi_A) &= \int \psi_{D^*}(\vec{r}_1) \psi_{A^*}(\vec{r}_1) r_{12}^{-1} \psi_D(\vec{r}_2) \psi_A(\vec{r}_2) d\vec{r}_1 d\vec{r}_2 \\ &= \int S_{D^*A^*}^e(\vec{r}_1) r_{12}^{-1} S_{DA}^h(\vec{r}_2) d\vec{r}_1 d\vec{r}_2 \end{aligned} \quad (2.65)$$

where $S_{D^*A^*}^e(\vec{r}_1) = \psi_{D^*}(\vec{r}_1) \psi_{A^*}(\vec{r}_1)$ and $S_{DA}^h(\vec{r}_2) = \psi_D(\vec{r}_2) \psi_A(\vec{r}_2)$ are the overlap densities.

In exciton transfer processes the one-electron contributions to the coupling integral is small. For large distances between the $D-A$ fragments the overlap integrals S_{AD} and $S_{D^*A^*}$ vanish and $\langle {}^1\Psi_I | \hat{h}^{(1e)} | {}^1\Psi_F \rangle$ (or $\langle {}^3\Psi_I | \hat{h}^{(1e)} | {}^3\Psi_F \rangle$) goes to zero. In addition, the exchange interaction depends on the overlap between the ground and excited orbitals of the D and A complexes (see eq. 2.65). If the two fragments are far away, the SET is determined by the Coulomb interaction (see eq. 2.60c) since the exchange interaction becomes negligible. On the other hand, the TET mechanism is strong only at short distances, given that it depends only in the exchange interaction (see eq. 2.61c).

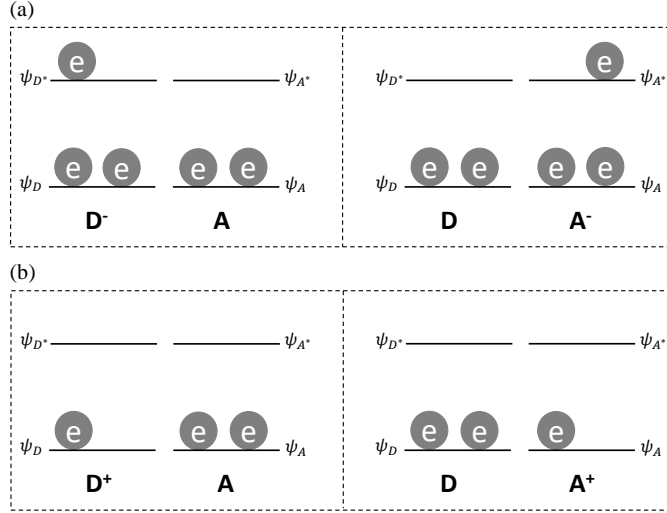


Figure 2.6: (a) Electronic structure configuration of a ground-state ET reaction. The excess electron is initially on the donor and then it transferred to the acceptor. (b) Electronic structure configuration of a ground-state HT process. The hole is transferred from the donor to the acceptor.

2.5.4 Electron and hole transfer rates

ET is the most basic type of chemical reactions in molecules. The simplest case of ET process is ground state ET and it is shown in figure 2.6(a). The determinant that describes the initial state is given by

$$|\Psi_I^{ET}\rangle = |D^- A\rangle = |\psi_D \bar{\psi}_D \psi_A \bar{\psi}_A \psi_{D^*}\rangle \quad (2.66)$$

and the final state by

$$|\Psi_F^{ET}\rangle = |DA^-\rangle = |\psi_D \bar{\psi}_D \psi_A \bar{\psi}_A \psi_{A^*}\rangle, \quad (2.67)$$

where we supposed that the excess electron has spin up. The ET matrix element yields

$$\langle I|\hat{V}|F\rangle = \langle \Psi_I^{ET}|\hat{h}^{(1e)}|\Psi_F^{ET}\rangle = V_{D^*A^*}^e. \quad (2.68)$$

Figure 2.6(b) shows the case of a HT reaction. The corresponding initial and final electronic states are written as

$$\begin{aligned} |\Psi_I^{HT}\rangle &= |D^+ A\rangle = |\psi_D \psi_A \bar{\psi}_A\rangle \\ |\Psi_F^{HT}\rangle &= |DA^+\rangle = |\psi_D \bar{\psi}_D \psi_A\rangle. \end{aligned} \quad (2.69)$$

The HT matrix element for the transition $|\Psi_I^{HT}\rangle \rightarrow |\Psi_F^{HT}\rangle$ is given by

$$\langle I|\hat{V}|F\rangle = \langle \Psi_I^{HT}|\hat{h}^{(1e)}|\Psi_F^{HT}\rangle = -V_{AD}^h. \quad (2.70)$$

CHAPTER 3

The spin-orbit coupling interaction in molecules

Consider an electron in a hydrogenic atom with a magnetic moment associated with its orbital angular momentum ($\vec{\mu}_l$), and a magnetic moment related to its spin angular momentum ($\vec{\mu}_s$). If we transform coordinates to a system where the electron is fixed and the nucleus orbiting the electron, the electron experiences a magnetic field produced by the nuclear charge. The interaction of the electron spin magnetic moment with the magnetic field is called the spin-orbit interaction or coupling (SOC). The resulting shifts and line splittings in the electronic spectrum of hydrogenic atoms caused by the SOC, is the so-called fine structure of the atomic spectrum. The SOC allows the transition between states of different spin multiplicity [e.g., singlet and triplet states via intersystem crossing (ISC)], due to the mixing of the orbital angular momentum with the spin angular momentum. In this chapter, we describe the theory and fundamental principles of the SOC interaction in molecular systems. First, we introduce the SOC operator by solving the relativistic one-particle Dirac Hamiltonian. Then, we calculate the matrix element between singlet and triplet excited states that gives rise to ISC rates. Finally, we explain the mechanism by which some organic molecules may have strong SOC.

3.1 Introduction

According to the classical interpretation of the SOC interaction, the electron (mass m_e , charge $-|e|$) performs circular motion of radius r with velocity \vec{v} in the electric field of the nucleus \vec{E}_{nuc} . Due to the counter circular motion of the nucleus relative to the electron, the electron experiences a magnetic field \vec{B}_{nuc} which is equal to^{19,32,51}

$$\vec{B}_{\text{nuc}} = \frac{\vec{E}_{\text{nuc}} \times \vec{v}}{c^2} \quad (3.1)$$

where c is the speed of light in vacuum. The electric field is related to the electric potential via $|e|\vec{E}_{\text{nuc}} = -\vec{\nabla}V$ and the momentum is given by $\vec{p} = m_e\vec{v}$. Therefore, eq.

3.1 transforms to

$$\vec{B}_{\text{nuc}} = \frac{1}{m_e |e| c^2} \vec{\nabla} V \times \vec{p}. \quad (3.2)$$

The spin magnetic moment of the electron is

$$\vec{\mu}_s = -\frac{|e| \hbar}{m_e} \vec{s} \quad (3.3)$$

where \vec{s} is the spin angular momentum. The interaction energy of the spin magnetic moment due to its motion in the magnetic field is $-\vec{\mu}_s \cdot \vec{B}_{\text{nuc}}$. Therefore, the quantum mechanical Hamiltonian is expected to be equal to $\hat{H}^{\text{SOC}} = -\vec{\mu}_s \cdot \vec{B}_{\text{nuc}}$. The exact result is

$$\hat{H}^{\text{SOC}} = \frac{1}{2m_e^2 c^2} (\vec{\nabla} V \times \hat{p}) \cdot \hat{s}, \quad (3.4)$$

where the factor $\frac{1}{2}$ is a correction obtained by use of the Dirac equation that treats the motion of the electron relativistically (see section 3.2).

In a hydrogenic atom, the potential arising from a nucleus of charge $Z|e|$ is $V = -\frac{Ze^2}{r}$ and $\vec{\nabla} V = \frac{Ze^2}{r^3} \vec{r}$. Therefore, the SOC Hamiltonian (eq. 3.4) reduces to

$$\hat{H}^{\text{SOC}} = \frac{Ze^2}{2m_e^2 c^2} \frac{1}{r^3} (\vec{r} \times \hat{p}) \cdot \hat{s} = \frac{Ze^2}{2m_e^2 c^2} \frac{1}{r^3} \vec{l} \cdot \hat{s} \quad (3.5)$$

where $\vec{l} = \vec{r} \times \vec{p}$ is the orbital angular momentum of the electron.

In a one-electron isotropic electric potential, $V = V(r)$ and $\vec{\nabla} V = \frac{1}{r} \frac{\partial V}{\partial r} \vec{r}$. In this case the SOC Hamiltonian (eq. 3.4) is given by

$$\hat{H}^{\text{SOC}} = \frac{1}{2m_e^2 c^2} \frac{1}{r} \frac{\partial V(r)}{\partial r} \vec{l} \cdot \hat{s} \equiv \xi(r) \vec{l} \cdot \hat{s} \quad (3.6)$$

where

$$\xi(r) = \frac{1}{2m_e^2 c^2} \frac{1}{r} \frac{\partial V(r)}{\partial r}. \quad (3.7)$$

The calculation of the atomic SOC matrix elements $\langle \varphi_m | \hat{H}^{\text{SOC}} | \varphi_n \rangle$ (φ_m, φ_n are the one-electron hydrogenic atomic orbitals) requires separation of the radial part of the wavefunction $\varphi_m(r, \theta, \varphi)$, namely

$$hc\zeta_{nl} = \hbar^2 \langle R(r)_{nl} | \xi(r) | R(r)_{nl} \rangle = \hbar^2 \int_0^\infty R^2(r)_{nl} \xi(r) r^2 dr, \quad (3.8)$$

where R_{nl} is the radial part of φ_m, φ_n both of which are characterized by the same principal quantum number n and same orbital angular momentum l . The quantity ζ_{nl} is the SOC constant for the orbitals φ_m and φ_n . In the case of an electron in hydrogenic atoms ($V = -\frac{Ze^2}{r}$), the SOC constant is shown to give

$$hc\zeta_{nl} = \frac{e^2 \hbar^2}{2m_e^2 c^2 a_0^3} \frac{Z^4}{n^3 l (l + \frac{1}{2}) (l + 1)} \quad (3.9)$$

where a_0 is the Bohr radius. In general, ζ_{nl} is treated as an empirical parameter whose magnitude is determinable from the experiment. Equation 3.9 shows the strong dependence of the SOC parameter on the nuclear atomic number $\sim Z^4$ (heavy atom effect).

3.2 Derivation of the SOC Hamiltonian from the Dirac equation

The fully relativistic time-independent Dirac equation that describes the motion of an electron in a potential V is written as a pair of coupled equations⁵²

$$\begin{aligned} (V - E)\Psi^L + c(\hat{\sigma}_P \cdot \hat{p})\Psi^S &= 0 \\ c(\hat{\sigma}_P \cdot \hat{p})\Psi^L + (V - E - 2m_e c^2)\Psi^S &= 0, \end{aligned} \quad (3.10)$$

where E is the energy of the particle and Ψ^L, Ψ^S are the large and small components of the wavefunction respectively. The Dirac wavefunction $\Psi(\vec{r})$ is a 4-component vector where the components ψ_1 and ψ_3 correspond to spin $\frac{1}{2}$ and the components ψ_2 and ψ_4 correspond to spin $-\frac{1}{2}$. The upper two and the lower two components are classified in a 2-component spinor i.e.,

$$\Psi(\vec{r}, t) = \begin{pmatrix} \psi_1(\vec{r}) \\ \psi_2(\vec{r}) \\ \psi_3(\vec{r}) \\ \psi_4(\vec{r}) \end{pmatrix} \implies \Psi(\vec{r}) = \begin{pmatrix} \Psi^L(\vec{r}) \\ \Psi^S(\vec{r}) \end{pmatrix}. \quad (3.11)$$

$\vec{\sigma}_P$ are the Pauli matrices defined as

$$\sigma_P^x = \begin{pmatrix} 0 & 1 \\ 1 & 0 \end{pmatrix} \quad \sigma_P^y = \begin{pmatrix} 0 & -i \\ i & 0 \end{pmatrix} \quad \sigma_P^z = \begin{pmatrix} 1 & 0 \\ 0 & -1 \end{pmatrix}. \quad (3.12)$$

We rearrange eq. 3.10 in a form so that c appears in the denominator. In that case, we can take $c \rightarrow \infty$ in order to go to the non-relativistic limit. Before allowing c to go to infinity, and provided that $(2m_e c^2 + E - V)$ is non-zero, we eliminate the small component Ψ^S (write the second eq. of 3.10 in terms of Ψ^S) so that

$$\Psi^S = (2m_e c^2 + E - V)^{-1} c(\hat{\sigma}_P \cdot \hat{p})\Psi^L. \quad (3.13)$$

Substitution of eq. 3.13 into the first eq. of 3.10 yields the effective Hamiltonian equation that operates solely on the large component Ψ^L

$$V\Psi^L + c^2(\hat{\sigma}_P \cdot \hat{p}) (2m_e c^2 + E - V)^{-1} (\hat{\sigma}_P \cdot \hat{p})\Psi^L = E\Psi^L. \quad (3.14)$$

We expand $(2m_e c^2 + E - V)^{-1}$ and we keep only terms up to first order with respect to $(m_e c^2)^{-1}$, i.e.,

$$(2m_e c^2 + E - V)^{-1} = \frac{1}{2m_e c^2} \left(1 - \frac{E - V}{2m_e c^2} + \text{higher-order terms} \right). \quad (3.15)$$

Using eq. 3.15 and the identity $[\vec{p}, V] = -i\hbar \vec{\nabla} V$ we find that

$$\hat{\sigma}_P \cdot \hat{p} \left(1 - \frac{E - V}{2m_e c^2} \right) = \left(1 - \frac{E - V}{2m_e c^2} \right) \hat{\sigma}_P \cdot \hat{p} - \frac{i\hbar}{2m_e c^2} \hat{\sigma}_P \cdot \vec{\nabla} V. \quad (3.16)$$

Approximating the term $E - V$ by the non-relativistic kinetic energy operator $\hat{p}^2/2m_e$, and substituting eqs. 3.15 and 3.16 into eq. 3.14 leads to

$$\hat{H} = \frac{1}{2m_e} \left(1 - \frac{\hat{p}^2}{4m_e^2 c^2} \right) \hat{p}^2 - \frac{i\hbar}{4m_e^2 c^2} (\hat{\sigma}_P \cdot \vec{\nabla} V) (\hat{\sigma}_P \cdot \hat{p}) + V. \quad (3.17)$$

The last term of eq. 3.17 is simplified by assuming a central potential i.e., $\vec{\nabla} V = \frac{1}{r} \frac{\partial V}{\partial r} \hat{r}$, such that

$$\begin{aligned} (\hat{\sigma}_P \cdot \vec{\nabla} V) (\hat{\sigma}_P \cdot \hat{p}) &= \frac{1}{r} \frac{\partial V}{\partial r} (\hat{r} \cdot \hat{p}) + i\hat{\sigma}_P \cdot \left(\frac{1}{r} \frac{\partial V}{\partial r} \hat{r} \times \hat{p} \right) \\ &= -i\hbar \frac{\partial V}{\partial r} \frac{\partial}{\partial r} + \frac{i}{r} \frac{\partial V}{\partial r} \hat{\sigma}_P \cdot (\hat{r} \times \hat{p}), \end{aligned} \quad (3.18)$$

where we used the Dirac relation

$$(\hat{\sigma}_P \cdot \hat{u})(\hat{\sigma}_P \cdot \hat{v}) = (\hat{u} \cdot \hat{v}) \hat{I}_2 + i\hat{\sigma}_P \cdot \hat{u} \times \hat{v}. \quad (3.19)$$

\hat{I}_2 is a 2×2 unity matrix. Using $\hat{s} = \frac{\hbar}{2} \hat{\sigma}_P$, the Hamiltonian (eq. 3.17) is rewritten as

$$\hat{H} = \hat{H}_0 - \frac{\hat{p}^4}{8m_e^3 c^2} - \frac{\hbar^2}{4m_e^2 c^2} \frac{\partial V}{\partial r} \frac{\partial}{\partial r} + \frac{1}{2m_e^2 c^2 r} \frac{\partial V}{\partial r} \hat{s} \cdot \hat{l}, \quad (3.20)$$

where

$$\hat{H}_0 = \frac{\hat{p}^2}{2m_e} + V. \quad (3.21)$$

Eq. 3.21 is the non-relativistic Schrödinger equation and the rest of the terms (in eq. 3.20) are the relativistic corrections. The first three terms constitute the so-called spin-free Hamiltonian since this part is spin-independent, while the last term of eq. 3.20 is the SOC Hamiltonian

$$\hat{H}^{\text{SOC}} = \frac{1}{2m_e^2 c^2 r} \frac{\partial V}{\partial r} \hat{s} \cdot \hat{l}. \quad (3.22)$$

This equation is similar to eq. 3.6 that we computed considering the motion of electrons and nuclei classically.

3.3 The SOC Hamiltonian of a many-electron molecule

In the case of a molecular system consisting of n electrons and N atoms, \hat{H}^{SOC} is approximated as^{19,53,54}

$$\hat{H}^{\text{SOC}} = \hat{H}_{1e}^{\text{SOC}} + \hat{H}_{2e}^{\text{SOC}} \quad (3.23a)$$

$$\hat{H}_{1e}^{\text{SOC}} = \sum_{i=1}^n \sum_{K=1}^N \xi(r_{iK}) \hat{l}_{iK} \cdot \hat{s}_i \quad (3.23b)$$

$$\begin{aligned} \hat{H}_{2e}^{\text{SOC}} = & -\frac{1}{2m_e^2 c^2} \sum_{i=1}^n \sum_{j \neq i}^n \frac{1}{r_{ij}^3} (\hat{p}_i \times \hat{r}_{ij}) \cdot \hat{s}_i \\ & + \frac{1}{m_e^2 c^2} \sum_{i=1}^n \sum_{j \neq i}^n \frac{1}{r_{ij}^3} (\hat{p}_j \times \hat{r}_{ij}) \cdot \hat{s}_i \end{aligned} \quad (3.23c)$$

where K denotes the atomic center, i and j label electrons and r_{iK} is the distance between electron i and nucleus K . The term in eq. 3.23b is the one-electron term, and describes interactions between the spin magnetic moment of electron i with the orbital magnetic moment arising from its orbiting in the field of nucleus K . The electron i either belongs to the atom K (one-center contribution), or to different atom than K (many-center contribution). The term in eq. 3.23c is a two-electron term and describes (a) interactions of the type “spin-same-orbit” related to the coupling between the spin magnetic moment and the orbital magnetic moment of electron i caused by the coulomb electrical field at i produced by all electrons j other than i (first term of the right-hand side of eq. 3.23c) and (b) interactions of the type “spin-other-orbit” related to the coupling between the spin magnetic moment of electron i and the orbital magnetic moment of electron j caused by magnetic fields due to relative orbital motion of the two electrons (second term of the right-hand side of eq. 3.23c). The one-electron term grows with the nuclear charge much faster ($\propto Z^4$) than the two-electron term does. Therefore, the second term in eq. 3.23 is usually neglected.

3.4 Matrix elements of the SOC operator

The one-electron part of the SOC Hamiltonian (eq. 3.23b) can be written in such a way that the orbital and spin factors are symmetrically or anti-symmetrically separated with respect to the interchange of the electrons, i.e.,¹⁹

$$\hat{H}_{1e}^{\text{SOC}} = \sum_{i=1}^n \sum_{K=1}^N \xi(r_{iK}) \left(\sum_{m=x,y,z} \hat{l}_{m_iK} \hat{s}_{m_i} \right) \quad (3.24a)$$

$$\begin{aligned} \hat{H}_{1e}^{\text{SOC}} &= \frac{1}{4n} \sum_{i=1}^n \sum_{j=1}^n \sum_{K=1}^N \left(\xi(r_{iK}) \hat{l}_{x_{iK}} + \xi(r_{jK}) \hat{l}_{x_{jK}} \right) (\hat{s}_{x_i} + \hat{s}_{x_j}) \\ &+ \frac{1}{4n} \sum_{i=1}^n \sum_{j=1}^n \sum_{K=1}^N \left(\xi(r_{iK}) \hat{l}_{x_{iK}} - \xi(r_{jK}) \hat{l}_{x_{jK}} \right) (\hat{s}_{x_i} - \hat{s}_{x_j}) \\ &+ \mathcal{O}(y, z) \end{aligned} \quad (3.24b)$$

where $\mathcal{O}(y, z)$ means analogous contributions from the terms with y and z components. The term $(\hat{s}_{x_i} + \hat{s}_{x_j})$ is symmetric under spin interchange, while the term $(\hat{s}_{x_i} - \hat{s}_{x_j})$ is antisymmetric. If $(\hat{s}_{x_i} + \hat{s}_{x_j})$ operates on antisymmetric spin wavefunction, it gives a function that is still antisymmetric with respect to spin interchange. On the other hand, if $(\hat{s}_{x_i} - \hat{s}_{x_j})$ operates on the same wavefunction, it gives a symmetric function with regard to spin interchange. This means that the first term on the right-hand side of eq. 3.24b preserves multiplicity and leads to multiplet splittings (triplet states with different m_s values are mixed through the SOC interaction), whereas the second term in the right-hand side of eq. 3.24b mixes states of different spin multiplicity.

Let us assume that we have a two-electron system. The corresponding wavefunctions are

$$\begin{aligned} \Psi_S &= \left(\frac{1}{\sqrt{2}} [\psi_r(1)\psi_q(2) + \psi_q(1)\psi_r(2)] \right) \left(\frac{1}{\sqrt{2}} [a(1)b(2) - b(1)a(2)] \right) = \Phi_S \Theta_{00} \\ \Psi_{T,+1} &= \left(\frac{1}{\sqrt{2}} [\psi_r(1)\psi_t(2) - \psi_t(1)\psi_r(2)] \right) a(1)a(2) = \Phi_T \Theta_{11} \\ \Psi_{T,0} &= \left(\frac{1}{\sqrt{2}} [\psi_r(1)\psi_t(2) - \psi_t(1)\psi_r(2)] \right) \left(\frac{1}{\sqrt{2}} [a(1)b(2) + b(1)a(2)] \right) = \Phi_T \Theta_{10} \\ \Psi_{T,-1} &= \left(\frac{1}{\sqrt{2}} [\psi_r(1)\psi_t(2) - \psi_t(1)\psi_r(2)] \right) b(1)b(2) = \Phi_T \Theta_{1-1} \end{aligned} \quad (3.25)$$

where a and b are the spin wavefunctions for spin up and spin down respectively. The singlet state Ψ_S is described by the singly occupied molecular orbitals ψ_r and ψ_q (where $\psi_r(1)$ is a simplified form of $\psi_r(\vec{r}_1)$). The triplet state Ψ_{T,m_s} (with $m_s = 0, \pm 1$) is described by the molecular orbitals ψ_r and ψ_t . Φ_S and Φ_T are the spatial wavefunctions

operator	Ψ_S	$\Psi_{T,+1}$	$\Psi_{T,0}$	$\Psi_{T,-1}$
$\hat{s}_{x_1} + \hat{s}_{x_2}$	0	$\Psi_{T,0}$	$\Psi_{T,+1} + \Psi_{T,-1}$	$\Psi_{T,0}$
$\hat{s}_{y_1} + \hat{s}_{y_2}$	0	$i\Psi_{T,0}$	$-i\Psi_{T,+1} + i\Psi_{T,-1}$	$-i\Psi_{T,0}$
$\hat{s}_{z_1} + \hat{s}_{z_2}$	0	$\sqrt{2}\Psi_{T,+1}$	0	$\sqrt{2}\Psi_{T,-1}$
$\hat{s}_{x_1} - \hat{s}_{x_2}$	$-\Psi_{T,+1} + \Psi_{T,-1}$	$-\Psi_S$	0	Ψ_S
$\hat{s}_{y_1} - \hat{s}_{y_2}$	$i\Psi_{T,+1} + i\Psi_{T,-1}$	$-i\Psi_S$	0	$-i\Psi_S$
$\hat{s}_{z_1} - \hat{s}_{z_2}$	$\sqrt{2}\Psi_{T,0}$	0	$\sqrt{2}\Psi_S$	0

Table 3.1: Effects of the spin operators on the spin part of the singlet and triplet wavefunctions.

of the singlet and triplet excited states respectively, and Θ_{sm_s} are the spin wavefunctions for the singlet ($s = 0, m_s = 0$) and triplet ($s = 1, m_s = 0, \pm 1$) states. We apply the operators $(\hat{s}_{x_i} + \hat{s}_{x_j})$ and $(\hat{s}_{x_i} - \hat{s}_{x_j})$ on the spin part of the states described in eq. 3.25. For example, we find that

$$\begin{aligned}
(\hat{s}_{x_1} + \hat{s}_{x_2})\Psi_{T,+1} &= \frac{1}{\sqrt{2}}[\psi_r(1)\psi_t(2) - \psi_t(1)\psi_r(2)] \times [\hat{s}_{x_1}a(1)a(1) + \hat{s}_{x_2}a(1)a(2)] \\
&= \frac{1}{\sqrt{2}}[\psi_r(1)\psi_t(2) - \psi_t(1)\psi_r(2)] \times \left[\frac{\hbar}{2}b(1)a(2) + \frac{\hbar}{2}a(1)b(2) \right] \quad (3.26a) \\
&= \frac{\hbar}{\sqrt{2}}\Psi_{T,0}.
\end{aligned}$$

$$\begin{aligned}
(\hat{s}_{x_1} - \hat{s}_{x_2})\Psi_{T,+1} &= \frac{1}{\sqrt{2}}[\psi_r(1)\psi_t(2) - \psi_t(1)\psi_r(2)] \times [\hat{s}_{x_1}a(1)a(1) - \hat{s}_{x_2}a(1)a(2)] \\
&= \frac{1}{\sqrt{2}}[\psi_r(1)\psi_t(2) - \psi_t(1)\psi_r(2)] \times \left[\frac{\hbar}{2}b(1)a(2) - \frac{\hbar}{2}a(1)b(2) \right] \quad (3.26b) \\
&= -\frac{\hbar}{\sqrt{2}}\Psi_S.
\end{aligned}$$

The effect of the various operators on the singlet and triple wavefunctions is shown in table 3.1. It is clear that the spin operators of the type $(\hat{s}_{x_i} + \hat{s}_{x_j})$ lead to mixing between different triplet-state sublevels (different m_s values) and the spin operators of the type $(\hat{s}_{x_i} - \hat{s}_{x_j})$ lead to mixing between singlet and triplet excited states. In particular, $(\hat{s}_{x_i} \pm \hat{s}_{x_j})$ and $(\hat{s}_{y_i} \pm \hat{s}_{y_j})$ mix states between which $\Delta m_s = \pm 1$ while $(\hat{s}_{z_i} - \hat{s}_{z_j})$ mixes states for which $\Delta m_s = 0$.

The angular momentum operators act solely on the angular part of the spatial wavefunction of the singlet and triplet states. The radial part is incorporated into the SOC constant ζ_{nl} (see eq. 3.8). In the following, we discuss the properties of the operators $\hat{l}_{x_{iK}}, \hat{l}_{y_{iK}}$ and $\hat{l}_{z_{iK}}$ ($\vec{l}_{iK} = l_{x_{iK}}\hat{i} + l_{y_{iK}}\hat{j} + l_{z_{iK}}\hat{k}$) and the manner by which they affect the spatial part of the wavefunction they operate on. In the one-electron one-center case (electron i belongs to atom K), the angular momentum operators are

	p_x	p_y	p_z
\hat{l}_x	0	$i\hbar p_z$	$-i\hbar p_y$
\hat{l}_y	$-i\hbar p_z$	0	$i\hbar p_x$
\hat{l}_z	$i\hbar p_y$	$-i\hbar p_x$	0

Table 3.2: Effects of the orbital angular momentum operators on the p -atomic orbitals.

defined as

$$l_x = -i\hbar \left(y \frac{\partial}{\partial z} - z \frac{\partial}{\partial y} \right) = -i\hbar \left(-\sin\varphi \frac{\partial}{\partial \theta} - \cot\theta \cos\varphi \frac{\partial}{\partial \varphi} \right) \quad (3.27a)$$

$$l_y = -i\hbar \left(z \frac{\partial}{\partial x} - x \frac{\partial}{\partial z} \right) = -i\hbar \left(-\cos\varphi \frac{\partial}{\partial \theta} - \cot\theta \sin\varphi \frac{\partial}{\partial \varphi} \right) \quad (3.27b)$$

$$l_z = -i\hbar \left(x \frac{\partial}{\partial y} - y \frac{\partial}{\partial x} \right) = -i\hbar \frac{\partial}{\partial \varphi}. \quad (3.27c)$$

(for simplicity we write $l_{m_{iK}} \equiv l_m$, $m = x, y, z$). For example, we consider the angular part of the p -atomic orbitals

$$p_x = \sqrt{\frac{3}{4\pi}} \cos\theta \quad p_y = \sqrt{\frac{3}{4\pi}} \sin\theta \cos\varphi \quad p_z = \sqrt{\frac{3}{4\pi}} \sin\theta \sin\varphi. \quad (3.28)$$

The effects of the operator \hat{l}_x on the atomic orbitals p_z and p_x (we used eqs. 3.27 and 3.28) are given by^{19,51}

$$\begin{aligned} \hat{l}_x p_z &= -i\hbar \sqrt{\frac{3}{4\pi}} \left(-\sin\varphi \frac{\partial}{\partial \theta} - \cot\theta \cos\varphi \frac{\partial}{\partial \varphi} \right) (\sin\theta \sin\varphi) \\ &= -i\hbar p_y \end{aligned} \quad (3.29a)$$

$$\begin{aligned} \hat{l}_x p_x &= -i\hbar \sqrt{\frac{3}{4\pi}} \left(-\sin\varphi \frac{\partial}{\partial \theta} - \cot\theta \cos\varphi \frac{\partial}{\partial \varphi} \right) \cos\theta \\ &= 0. \end{aligned} \quad (3.29b)$$

In the same way, the results for the action of the $\hat{l}_x, \hat{l}_y, \hat{l}_z$ operators on the p_x, p_y and p_z orbitals are collected in table 3.2. With these results we conclude that in a right-handed coordinate system, the effect of the angular momentum operator on a p orbital is to rotate the orbital counterclockwise by 90° about the axis specified by the angular momentum operator subscript (see figure 3.1), and to multiply it by $i\hbar$. Following the same procedure, we can evaluate the effect of the $\hat{l}_x, \hat{l}_y, \hat{l}_z$ operators on the d and f

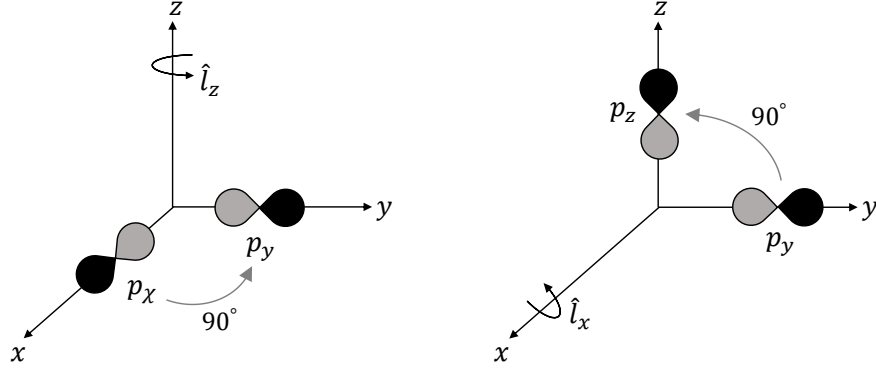


Figure 3.1: Schematic representation of the effect of the angular momentum operators \hat{l}_x and \hat{l}_z on the p_y and p_x atomic orbitals respectively (see eq. 3.27). The positive directions of the Cartesian axes show the positive ends of the p atomic orbitals. For example, when \hat{l}_x operates p_y , p_y undergoes 90° rotation around x -axis (counterclockwise) to get p_z .

orbitals.⁵¹

Now, we are ready to evaluate the SOC matrix elements between singlet and triplet states. We use eqs. 3.23b and 3.25. As an example, let us calculate the SOC matrix element between the singlet state Ψ_S and the triplet state $\Psi_{T,0}$ ^{51,55}

$$\begin{aligned}
 \langle \Psi_S | \hat{H}_{1e}^{\text{SOC}} | \Psi_{T,0} \rangle &= \langle \Psi_S | \sum_K \xi(r_{1K}) \hat{l}_{1K} \cdot \hat{s}_1 + \sum_K \xi(r_{2K}) \hat{l}_{2K} \cdot \hat{s}_2 | \Psi_{T,0} \rangle \\
 &= \langle \Phi_S | \sum_K \xi(r_{1K}) \hat{l}_{1K} | \Phi_T \rangle \langle \Theta_{00} | \hat{s}_1 | \Theta_{10} \rangle \\
 &\quad + \langle \Phi_S | \sum_K \xi(r_{2K}) \hat{l}_{2K} | \Phi_T \rangle \langle \Theta_{00} | \hat{s}_2 | \Theta_{10} \rangle.
 \end{aligned} \tag{3.30}$$

$r_{1(2)K}$ is the distance of the electron 1(2) with the nucleus K . The z -component of the spin part of eq. 3.30 gives for the term of electron 1

$$\begin{aligned}
 \langle \Theta_{00} | \hat{s}_{z1} | \Theta_{10} \rangle &= \frac{1}{2} \langle [a(1)b(2) - b(1)a(2)] | \hat{s}_{z1} | [a(1)b(2) + b(1)a(2)] \rangle \\
 &= \frac{1}{2} [\langle a(1) | \hat{s}_{z1} | a(1) \rangle \langle b(2) | b(2) \rangle - \langle b(1) | \hat{s}_{z1} | b(1) \rangle \langle a(2) | a(2) \rangle] \\
 &= \frac{\hbar}{2}
 \end{aligned} \tag{3.31}$$

In an analogous way, the z -component of the orbital part of eq. 3.30 gives

$$\langle \Phi_S | \sum_K \xi(r_{1K}) \hat{l}_{z1K} | \Phi_T \rangle = \frac{1}{2} \langle r_1 q_2 + q_1 r_2 | \sum_K \xi(r_{1K}) \hat{l}_{z1K} | r_1 t_2 - t_1 r_2 \rangle \tag{3.32}$$

where the notation r_i, t_i, q_i , ($i = 1, 2$) corresponds to the molecular orbitals $\psi_r(i), \psi_t(i), \psi_q(i)$ respectively. Applying the orthonormality of the molecular orbitals e.g., $\langle r_i | t_i \rangle = 0$ and $\langle r_i | p_i \rangle = 1$, and using the fact that the angular momentum operator \hat{l}_{z1K} acts only on

component of $\hat{H}_{1e}^{\text{SOC}}$	$\langle \Psi_S \hat{H}_{1e}^{\text{SOC}} \Psi_{T,-1} \rangle$	$\langle \Psi_S \hat{H}_{1e}^{\text{SOC}} \Psi_{T,0} \rangle$	$\langle \Psi_S \hat{H}_{1e}^{\text{SOC}} \Psi_{T,1} \rangle$
$\hat{H}_{1e,x}^{\text{SOC}}$	$\frac{1}{\sqrt{2}} \langle q \hat{H}_{l_x} t \rangle$	0	$\frac{1}{\sqrt{2}} \langle q \hat{H}_{l_x} t \rangle$
$\hat{H}_{1e,y}^{\text{SOC}}$	$\frac{1}{\sqrt{2}} i \langle q \hat{H}_{l_y} t \rangle$	0	$\frac{1}{\sqrt{2}} i \langle q \hat{H}_{l_y} t \rangle$
$\hat{H}_{1e,z}^{\text{SOC}}$	0	$-\langle q \hat{H}_{l_z} t \rangle$	0

Table 3.3: Matrix elements of \hat{H}^{SOC} between singlet and triplet states. Singlet and triplet states are defined in eq. 3.25.

electron with r_{1K} , eq. 3.32 simplifies to

$$\langle \Phi_S | \sum_K \xi(r_{1K}) \hat{l}_{z_{1K}} | \Phi_T \rangle = -\frac{1}{2} \langle r_2 | r_2 \rangle \langle q_1 | \sum_K \xi(r_{1K}) \hat{l}_{z_{1K}} | t_1 \rangle. \quad (3.33)$$

Expanding the molecular orbitals in terms of the atomic orbitals φ_μ i.e.,

$$\begin{aligned} q &= \sum_\mu c_{q\mu} \varphi_\mu \\ t &= \sum_\nu c_{t\nu} \varphi_\nu, \end{aligned} \quad (3.34)$$

the integral in eq. 3.33 yields

$$\begin{aligned} \langle \Phi_S | \sum_K \xi(r_{1K}) \hat{l}_{z_{1K}} | \Phi_T \rangle &= -\frac{1}{2} \langle \sum_\mu c_{q\mu} \varphi_\mu | \sum_K \xi(r_{1K}) \hat{l}_{z_{1K}} | \sum_\nu c_{t\nu} \varphi_\nu \rangle \\ &= -\frac{1}{2} \sum_\mu \sum_\nu c_{q\mu}^* c_{t\nu} \zeta_{nl,K} \langle \varphi'_\mu | \hat{l}_{z_{1K}} | \varphi'_\nu \rangle \end{aligned} \quad (3.35)$$

where φ' is the angular part of the atomic orbital φ . Identical results are obtained for the x - and y -components of the angular momentum operator that contains the coordinates of electron 2. The matrix element of eq. 3.35 can be evaluated, for example, for the p orbitals according to eqs. 3.29 and the results summarized in table 3.2. Therefore, we can see that the SOC integral between two states of different spin multiplicity is non-zero only if the angular orbitals $\varphi'_\nu, \varphi'_\mu$ are different. For the same orbitals the SOC integral is zero. Setting $\frac{\hbar}{2} \sum_K \xi(r_K) \hat{l}_{z_K} \equiv \hat{H}_{l_z}$, eq. 3.33 is summarized as

$$\langle \Psi_S | \hat{H}_{1e}^{\text{SOC}} | \Psi_T \rangle = -\langle q | \hat{H}_{l_z} | t \rangle. \quad (3.36)$$

The matrix elements between singlet and triplet states for the three components x, y, z , and the remaining components of the triplet states with $m_s = \pm 1$ are shown in the table 3.3.

3.5 SOC in organic compounds

As we explained in sections 3.2 and 3.3, the SOC coupling strength scales approximately with the fourth power of the nuclear charge Z , due to its leading one-electron (see eq. 3.23b) one-center (see eq. 3.9) term. As such, SOC effects are larger for the heavy element compounds. However, sometimes, small organic molecules produce SOC matrix elements that are sufficient to induce transitions between singlet and triplet states.^{55–57} For example, $n \rightarrow \pi^*$ to $\pi \rightarrow \pi^*$ transitions are proved to give stronger SOC matrix elements compared to the $\pi \rightarrow \pi^*$ and $\pi \rightarrow \pi^*$ transitions.^{19,58–61}

As an example, let us consider the SOC matrix element between singlet and triplet states of a monoazine (see figure 3.2)^{19,58,59}. The excited states are of $n \rightarrow \pi^*$ and $\pi \rightarrow \pi^*$ characters. It follows that the SOC interaction $\langle S(n, \pi^*) | \hat{H}_{1e}^{\text{SOC}} | T(\pi, \pi^*) \rangle$ has the matrix element $\langle n | \hat{H}_{1e}^{\text{SOC}} | \pi \rangle$, where $|n\rangle$ and $|\pi\rangle$ are molecular orbitals for the n and π hole orbitals. We focus on the spatial part that arises from the angular momentum operator $\langle n | \hat{H}_l | \pi \rangle$ where \hat{H}_l is the part of $\hat{H}_{1e}^{\text{SOC}}$ that includes the angular momentum operator (\vec{l}), i.e., $\hat{H}_l = \frac{\hbar}{2} \sum_K \xi(r_K) \hat{l}_K$. In terms of the atomic orbitals

$$\langle n | \hat{H}_l | \pi \rangle = \sum_{\nu} \left\langle \left[\left(\frac{2}{3} \right)^{1/2} p_{zN} + \left(\frac{1}{3} \right)^{1/2} s_N \right] \left| \hat{H}_l \right| c_{\pi\nu} \varphi_{\nu} \right\rangle. \quad (3.37)$$

We keep only one-center contributions from the Nitrogen to the integral, so that $\hat{H}_l = \hat{H}_{l,N} = \frac{\hbar}{2} \xi(r_N) \hat{l}_N$. This is because the SOC contribution at the Nitrogen center that comes from Carbons is very small (multi-center integrals are approximately zero). p_{zN} is the $2p_z$ atomic orbital and s_N is the $2s$ atomic orbital of the Nitrogen. φ_{ν} is a $2p_y$ atomic orbital on the ν th Carbon of the ring. With these assumptions, the SOC integral is written as

$$\langle n | \hat{H}_l | \pi \rangle = \left\langle \left[\left(\frac{2}{3} \right)^{1/2} p_{zN} + \left(\frac{1}{3} \right)^{1/2} s_N \right] \left| \hat{H}_{l,N} \right| c_{\pi N} p_{yN} \right\rangle, \quad (3.38)$$

and the atomic orbitals s_N , p_{yN} and p_{zN} belong to the Nitrogen atom. The contribution of the $2s$ orbital of the Nitrogen to the SOC is zero since $\hat{l}_{xN} |s_N\rangle = \hat{l}_{yN} |s_N\rangle = \hat{l}_{zN} |s_N\rangle = 0$. Therefore, $\langle s_N | \hat{H}_{l,N} | p_{yN} \rangle = 0$. In addition, using the results from table 3.2 for the effect of the \hat{l} operator on the p atomic orbitals, we deduce that

$$\langle p_{zN} | \hat{H}_{l_z,N} | p_{yN} \rangle = \langle p_{zN} | \hat{H}_{l_y,N} | p_{yN} \rangle = 0 \quad (3.39a)$$

$$\langle p_{zN} | \hat{H}_{l_z,N} | p_{zN} \rangle = \langle p_{yN} | \hat{H}_{l_z,N} | p_{yN} \rangle = \langle p_{xN} | \hat{H}_{l_z,N} | p_{xN} \rangle = 0 \quad (3.39b)$$

The results from eq. 3.39 show that the SOC is non-zero only between two different p orbitals that belong to the same center, and only via the component of \hat{H}_l whose

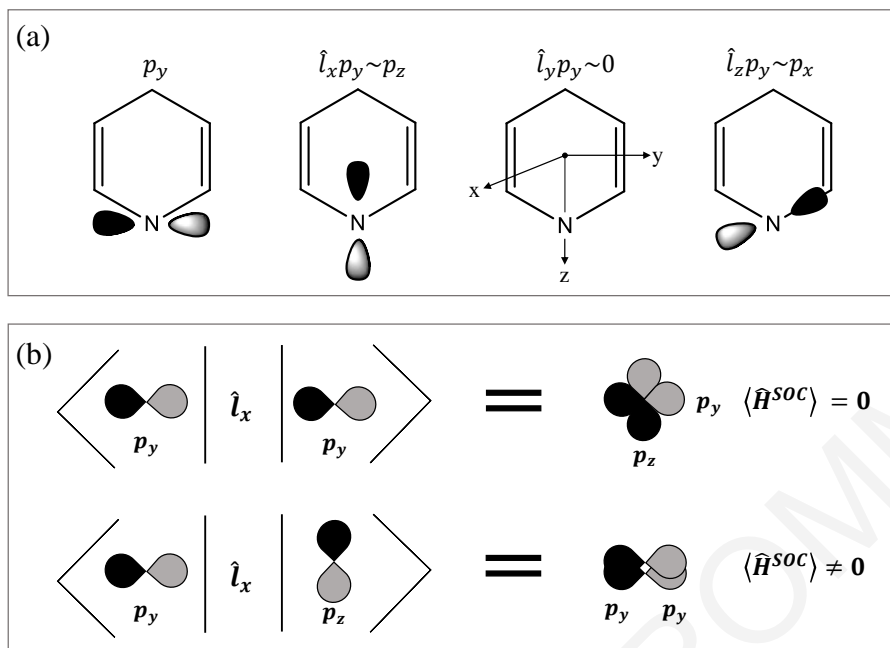


Figure 3.2: (a) Schematic representation of the effects of the \hat{l}_x , \hat{l}_y and \hat{l}_z operators on the p_y orbital of the nitrogen atom in a monoazine. (b) Schematic diagram of the SOC matrix element between p atomic orbitals. *Above:* The SOC matrix element between the same orbitals e.g., between the two p_y orbitals is zero since the overlap between p_y and p_z is zero. *Below:* The SOC matrix element between p_y and p_z orbitals when \hat{l}_x operates, is strong because the overlap between two p_y orbitals is non-zero.

axis is different from the axis that the two p orbitals lie in. Consequently, the matrix element of eq. 3.38 is simplified as

$$\langle n | \hat{H}_l | \pi \rangle = \left(\frac{2}{3} \right)^{1/2} c_{\pi N} \langle p_{zN} | \hat{H}_{l_x, N} | p_{yN} \rangle \quad (3.40)$$

this is the only non-zero contribution to the total SOC matrix element of monoazine. When \hat{l}_{xN} operates on p_{yN} it yields p_{zN} and the overlap integral $\langle p_{zN} | p_{zN} \rangle \neq 0$. This result is illustrated in figure 3.2.

The $n \rightarrow \pi^*$ to $\pi \rightarrow \pi^*$ is the most common transition that produces strong SOC interactions between singlet and triplet states in organic molecules.⁶⁰ The $\pi \rightarrow \pi^*$ to $\pi \rightarrow \pi^*$ transitions singlet-to-triplet transitions do not produce large SOC^{19,60}. As a simple example we consider the $\pi \rightarrow \pi^*$ to $\pi \rightarrow \pi^*$ transitions in the benzene molecule.^{19,62} The SOC matrix element between the singlet state $S(\pi, \pi^*)$ and the triplet state $T(\pi, \pi^*)$ reduces to

$$\langle S(\pi \rightarrow \pi^*) | \hat{H}_{1e}^{SOC} | T(\pi \rightarrow \pi^*) \rangle = - \sum_{\mu} \sum_{\nu} = c_{\pi, \mu} c_{\pi, \nu} \langle p_{z\mu} | \hat{H}_{l_z} | p_{z\nu} \rangle \quad (3.41)$$

where $\hat{H}_{l_z} = \frac{\hbar}{2} \sum_K \xi(r_K) \hat{l}_{zK}$. $p_{z\mu}$ and $p_{z\nu}$ are $2p_z$ atomic orbitals on Carbons μ and ν respectively. Obviously, the one-center terms ($\mu \in K$ and $\nu \in K$) vanish as we

explained in eq. 3.39b. The two-center terms of the type $\langle p_{z\mu} | \hat{H}_{l_z, M} | p_{z\nu} \rangle$ ($\hat{H}_{l_z, M} = \frac{\hbar}{2} \xi(r_M) \hat{l}_{z_M}$) or $\langle p_{z\mu} | \hat{H}_{l_z, N} | p_{z\nu} \rangle$ ($\hat{H}_{l_z, N} = \frac{\hbar}{2} \xi(r_N) \hat{l}_{z_N}$) are zero since $\hat{H}_{l_z, N} | p_{z\nu} \rangle = 0$ and $\langle p_{z\mu} | \hat{H}_{l_z, M}^* = 0$ (see table 3.2). Consequently, only the three-center terms survive leading to

$$\langle S(\pi \rightarrow \pi^*) | \hat{H}^{\text{SOC}} | T(\pi \rightarrow \pi^*) \rangle = - \sum_{\mu} \sum_{\nu} = c_{\pi, \mu} c_{\pi, \nu} \langle p_{z\mu} | \sum_P \hat{H}_{l_z, P} | p_{z\nu} \rangle \quad (3.42)$$

where P is an atomic center for which $\nu \neq P \neq \mu$. However, this integral is very small due to the r^{-3} dependence of \hat{H}_l . In addition, the two-electron terms of “spin-other-orbit” type that we introduced in eq. 3.23 and so far were neglected, do not contribute to the integral of eq. 3.42.⁶²

With the example of benzene we show that singlet-to-triplet transitions of $\pi \rightarrow \pi^*$ character do not exhibit strong SOC because one- and two-center contributions vanish and the three-center contribution is relatively small. Sometimes, two-center contributions are responsible for the strong SOC in organic molecules. For example, in aromatic amines the singlet and triplet states are of intramolecular charge transfer (CT) character and involve charge redistribution from one part of a molecule to the other. The two-center contribution to the SOC integral is large while the one-center terms vanish.¹⁹

3.6 Conclusions

In this chapter we use quantum mechanics and relativistic corrections to estimate the SOC matrix element between states of different spin multiplicity. We show that the SOC is strong in compounds with heavy-atom substituents because the SOC constant ζ_{nl} is analogous to Z^4 (see eq. 3.9). In small aromatic compounds, the SOC matrix element between singlet and triplet excited states is weak. This is because the singlet and triplet states in most organic molecules are of $\pi \rightarrow \pi^*$ character, and SOC interactions between singlet state $S(\pi, \pi^*)$ and triplet state $T(\pi, \pi^*)$ are of three-center type so they are negligible. Therefore, singlet and triplet states of the same configuration induce weak SOC. If organic molecules exhibit strong SOC, this usually comes from large interactions between the non-bonding molecular orbital of the singlet state $S(n, \pi^*)$ and the π orbital of the triplet state $T(\pi, \pi^*)$. These $n \rightarrow \pi^*$ to $\pi \rightarrow \pi^*$ transitions are one-center, thus, they are dominant. Finally, two-center contributions are sometimes responsible for strong mixing between the singlet and triplet states when the one-center term vanish, and this is pronounced in organic molecules with singlet and triplet states of CT character.

CHAPTER 4

Quantum mechanical description of the dynamics of open quantum systems

Time-dependent phenomena in molecular systems that are isolated from the surrounding environment, are completely described by the time-dependent Schrödinger equation. However, the model of isolated systems is unrealistic since environmental effects influence the dynamics of the quantum system. Different types of interactions that depend on the type of the environment and its coupling strength to the system, result in energy exchange between system and its environment that are termed as relaxation and dissipation. For example, if initially the energy is deposited in the system, as time passes it will be transferred to the reservoir, and in some situations it may be possible to flow back into the system. This is the type of energy exchange which is called relaxation. If energy does not move back to the system, the irreversible energy flow into the reservoir is termed dissipation.

The interaction of a system with its thermal surrounding can be experimentally studied under the influence of external electromagnetic fields. For instance, spectroscopic techniques such as absorption, pump-probe and electron paramagnetic resonance experiments are used to investigate molecular systems in solution phase (reservoir). The derived spectra resulting from electronic and vibrational transitions in the molecules, give detailed information about how the solvent molecules influence the dynamics of the molecular system under study. The corresponding theoretical description is given by the density operator (statistical operator) formalism. In this concept, the dynamics of the quantum system embedded in a macroscopic thermal reservoir, is described by density matrices and specifically with its reduction scheme. In this chapter, we briefly describe the formalism of density operator and its time evolution. In particular, we discuss the density-matrix formalism in Liouville space.

4.1 The Density operator

For a system characterized by the Hamiltonian \hat{H} and a time-dependent wavefunction $|\Psi(t)\rangle$, we use an orthonormal basis set $\{\phi_n\}$ (also denoted $|n\rangle$) to expand its wavefunction

$$|\Psi(t)\rangle = \sum_n C_n(t) |\phi_n\rangle. \quad (4.1)$$

where $\sum_n |C_n|^2 = 1$. The expectation value of an operator \hat{A} at a time t is given by

$$\langle A(t) \rangle = \langle \Psi(t) | \hat{A} | \Psi(t) \rangle = \sum_{n,n'} C_{n'}(t) C_n^*(t) \langle n | \hat{A} | n' \rangle = \sum_{n,n'} C_{n'}(t) C_n^*(t) A_{n,n'}, \quad (4.2)$$

where $C_{n'}(t) = \langle n' | \Psi(t) \rangle$ and $C_n^*(t) = \langle \Psi(t) | n \rangle$. This expression provides the idea of the density operator which is defined as^{9,10,43,63,64}

$$\hat{\rho}(t) \equiv |\Psi(t)\rangle \langle \Psi(t)|, \quad (4.3)$$

so that

$$\hat{\rho} = \sum_{n,n'} C_n(t) C_{n'}^*(t) |n\rangle \langle n'|, \quad (4.4)$$

where

$$\rho_{n,n'}(t) = \langle \phi_n | \hat{\rho} | \phi_{n'} \rangle = C_n(t) C_{n'}^*(t) \quad (4.5)$$

are the matrix elements of the density operator.

A system ensemble that is characterized by such a wavefunction $|\Psi(t)\rangle$ is said to be in a pure state. Generally, quantum system ensembles are not in a pure state, instead, they are described as a statistical mixture of pure states $|\Psi_k\rangle$. In this case, the probability of the system to be in state $|\Psi_k\rangle$ is denoted by P_k , and the corresponding density operator is defined by

$$\hat{\rho}(t) \equiv \sum_k P_k |\Psi_k(t)\rangle \langle \Psi_k(t)| \quad (4.6)$$

($P_k \geq 0$ and $\sum_k P_k = 1$). The corresponding matrix elements of the density operator are given by

$$\rho_{nn'} = \sum_k P_k \langle n | \Psi_k \rangle \langle \Psi_k | n' \rangle \quad (4.7)$$

Equation 4.6 describes a system in a mixed state (statistical mixture). The expectation value of an observable \hat{A} for a mixed state, given by

$$\langle A(t) \rangle = \sum_k P_k \langle \Psi_k(t) | \hat{A} | \Psi_k(t) \rangle = \text{Tr}\{\hat{\rho}(t)\hat{A}\} \quad (4.8)$$

where Tr denotes trace.

The density matrix of a pure or a mixed state is always Hermitian i.e., $\hat{\rho}^\dagger(t) = \hat{\rho}(t)$. Its diagonal elements ρ_{nn} are real and positive i.e., $\rho_{nn} = \sum_k P_k \langle n | \Psi_k \rangle \langle \Psi_k | n \rangle = \sum_k P_k |\langle n | \Psi_k \rangle|^2 \geq 0$. ρ_{nn} represents the probability that the system is in the corresponding single state $|n\rangle$ and is referred to as a population. The non-diagonal matrix elements $\rho_{nn'} = \sum_k P_k \langle n | \Psi_k \rangle \langle \Psi_k | n' \rangle$ ($n \neq n'$) are called coherences. If $|n\rangle = \sum_k C_{nk} \Psi_k$ and $|n'\rangle = \sum_k C_{n'k} \Psi_k$ we get $\rho_{nn'} = \sum_k P_k C_{nk}^* C_{n'k} = \langle C_{nk}^* C_{n'k} \rangle$. $\rho_{nn'}$ is an average of the cross terms $\langle n' | \Psi_k(t) \rangle \langle \Psi_k(t) | n \rangle$. As such, it describes coherent (wavefunction) evolution. The density matrix operator satisfies the property $\text{Tr}[\hat{\rho}^2(t)] \leq 1$ ($\text{Tr}[\hat{\rho}^2(t)] = 1$ only for a pure state).

4.2 Time evolution of the density operator

The time evolution of the density operator and its equation of motion can be found by taking the derivative of eq. 4.6 i.e.,

$$\frac{d\hat{\rho}(t)}{dt} = \sum_k P_k \frac{d}{dt} (|\Psi_k(t)\rangle \langle \Psi_k(t)|) \quad (4.9a)$$

$$\frac{d}{dt} (|\Psi_k(t)\rangle \langle \Psi_k(t)|) = \left(\frac{d}{dt} |\Psi_k(t)\rangle \right) \langle \Psi_k(t)| + |\Psi_k(t)\rangle \left(\frac{d}{dt} \langle \Psi_k(t)| \right). \quad (4.9b)$$

By substituting the Schrödinger equation and its Hermitian conjugate

$$\frac{d}{dt} |\Psi_k(t)\rangle = -\frac{i}{\hbar} \hat{H} |\Psi_k(t)\rangle, \quad \frac{d}{dt} \langle \Psi_k(t)| = \frac{i}{\hbar} \langle \Psi_k(t)| \hat{H} \quad (4.10)$$

we get,

$$\frac{d\hat{\rho}(t)}{dt} = -\frac{i}{\hbar} \hat{H} |\Psi_k(t)\rangle \langle \Psi_k(t)| + |\Psi_k(t)\rangle \langle \Psi_k(t)| \hat{H} \quad (4.11)$$

which finally yields,

$$\frac{d\hat{\rho}(t)}{dt} = -\frac{i}{\hbar} [\hat{H}, \hat{\rho}(t)] = -\frac{i}{\hbar} \hat{L} \hat{\rho}(t). \quad (4.12)$$

This equation of motion (eq. 4.12) is called the Liouville-von Neumann or quantum Liouville equation, and \hat{L} is the Liouville superoperator defined via the commutation

$$\hat{L} \hat{\rho}(t) \equiv [\hat{H}, \hat{\rho}(t)]. \quad (4.13)$$

The solution of the Liouville-von Neumann equation (eq. 4.12) is

$$\hat{\rho}(t) = e^{-i\hat{L}(t-t_0)/\hbar} \hat{\rho}(t=0). \quad (4.14)$$

4.3 The Liouville space approach

We introduce Liouville space, via an example of a two-level system characterized by the Hamiltonian (see eq. 2.1)

$$\hat{H} = \hat{H}^{(0)} + \hat{V}(t), \quad (4.15)$$

where $\hat{H}^{(0)}$ is the unperturbed Hamiltonian and $\hat{V}(t)$ is the time-dependent external perturbation. We denote the eigenstates of the unperturbed Hamiltonian $|a\rangle$ and $|b\rangle$ and the corresponding eigenvalues ε_a and ε_b . We assume that the diagonal matrix elements of the perturbation Hamiltonian matrix \tilde{V} are zero, so that the total Hamiltonian matrix of the system in the representation of the eigenstates of the unperturbed Hamiltonian, is simplified as

$$\tilde{H} = \begin{bmatrix} \varepsilon_a & V_{ab} \\ V_{ba} & \varepsilon_b \end{bmatrix}. \quad (4.16)$$

The density matrix of this 2×2 system has four elements

$$\tilde{\rho}(t) = \begin{bmatrix} \rho_{aa}(t) & \rho_{ab}(t) \\ \rho_{ba}(t) & \rho_{bb}(t) \end{bmatrix} \quad (4.17)$$

The time evolution of the density operator given by $\frac{d\hat{\rho}(t)}{dt} = -\frac{i}{\hbar} [\hat{H}, \hat{\rho}(t)]$ (see eq. 4.12) yields the following matrix elements

$$\dot{\rho}_{aa} = -\frac{i}{\hbar} (V_{ab}\rho_{ba} - V_{ba}\rho_{ab}) \quad (4.18a)$$

$$\dot{\rho}_{ab} = -\frac{i}{\hbar} (\varepsilon_a - \varepsilon_b)\rho_{ab} - \frac{i}{\hbar} V_{ab}(\rho_{bb} - \rho_{aa}) \quad (4.18b)$$

$$\dot{\rho}_{ba} = -\frac{i}{\hbar} (\varepsilon_b - \varepsilon_a)\rho_{ba} - \frac{i}{\hbar} V_{ba}(\rho_{aa} - \rho_{bb}) \quad (4.18c)$$

$$\dot{\rho}_{bb} = -\frac{i}{\hbar} (V_{ba}\rho_{ab} - V_{ab}\rho_{ba}). \quad (4.18d)$$

These equations can also be written as

$$\frac{d}{dt} \begin{pmatrix} \rho_{aa} \\ \rho_{ab} \\ \rho_{ba} \\ \rho_{bb} \end{pmatrix} = -\frac{i}{\hbar} \begin{bmatrix} 0 & -V_{ba} & V_{ab} & 0 \\ V_{ab} & \varepsilon_a - \varepsilon_b & 0 & V_{ab} \\ V_{ba} & 0 & \varepsilon_b - \varepsilon_a & -V_{ba} \\ 0 & V_{ba} & -V_{ab} & 0 \end{bmatrix} \begin{pmatrix} \rho_{aa} \\ \rho_{ab} \\ \rho_{ba} \\ \rho_{bb} \end{pmatrix}. \quad (4.19)$$

In eq. 4.19 the density operator is written as a 4×4 vector

$$\vec{\rho}(t) = \begin{pmatrix} \rho_{aa} \\ \rho_{ab} \\ \rho_{ba} \\ \rho_{bb} \end{pmatrix}, \quad (4.20)$$

and \tilde{L} is the 4×4 Liouvillian matrix

$$\tilde{L} = \begin{bmatrix} 0 & -V_{ba} & V_{ab} & 0 \\ V_{ab} & \varepsilon_a - \varepsilon_b & 0 & V_{ab} \\ V_{ba} & 0 & \varepsilon_b - \varepsilon_a & -V_{ba} \\ 0 & V_{ba} & -V_{ab} & 0 \end{bmatrix}. \quad (4.21)$$

In general, for a N -state system characterized by the Hamiltonian \hat{H} ($= \hat{H}^{(0)} + \hat{V}$), the eigenvectors of the zero-th order Hamiltonian $\hat{H}^{(0)}$ i.e., $|j\rangle, |k\rangle, |m\rangle, |n\rangle \dots$ constitute a complete basis set of functions in Hilbert space. The jk matrix element of the quantum Liouville equation will be given by

$$\dot{\rho}_{jk} = -\frac{i}{\hbar} \left[(\hat{H}\hat{\rho})_{jk} - (\hat{\rho}\hat{H})_{jk} \right] \quad (j, k = 1, 2, 3 \dots N). \quad (4.22)$$

The density operator has N^2 matrix elements ρ_{jk} and the Liouvillian (4.21) is a matrix with $N^2 \times N^2$ matrix elements $L_{jk,mn}$. We rewrite eq. 4.22 as

$$\begin{aligned} \frac{d\rho_{jk}}{dt} &= -\frac{i}{\hbar} \sum_m [H_{jm}\rho_{mk} - \rho_{jm}H_{mk}] \\ &= -\frac{i}{\hbar} \sum_{m,n} L_{jk,mn}\rho_{mn} \end{aligned} \quad (4.23)$$

where

$$L_{jk,mn} = H_{jm}\delta_{kn} - H_{kn}^*\delta_{jm}. \quad (4.24)$$

In matrix form, eqs. 4.23 and 4.24 are given by

$$\frac{d\vec{\rho}}{dt} = -\frac{i}{\hbar} \tilde{L}\vec{\rho} \quad (4.25)$$

where $\vec{\rho}$ is an N^2 column vector consisting of all ρ_{mn} matrix elements. \tilde{L} is an $N^2 \times N^2$ matrix consisting of all $L_{jk,mn}$ matrix elements. The space where the density operator is a vector rather than matrix, is called Liouville space.

4.4 The reduced density operator

Suppose that the total Hamiltonian of a system (S) and its surrounding bath (B) that describes the environment, is given by

$$\hat{H} = \hat{H}^{(S)}(q_S) + \hat{H}^{(B)}(q_B) + \hat{H}^{(S-B)}(q_S, q_B). \quad (4.26)$$

$\hat{H}^{(S)}$ and $\hat{H}^{(B)}$ are the Hamiltonians of the system and the bath respectively, and $\hat{H}^{(S-B)}(q_S, q_B)$ is the system-bath interaction Hamiltonian. q_S and q_B represent the system and bath degrees of freedom, respectively. The isolated system and bath eigenstates satisfy the Schrödinger equations

$$\begin{aligned} \hat{H}^{(S)}|s\rangle &= \varepsilon_a|s\rangle \\ \hat{H}^{(B)}|b\rangle &= \varepsilon_b|b\rangle. \end{aligned} \quad (4.27)$$

The product states $|sb\rangle = |s\rangle|b\rangle$ form a complete set of basis for the combined system and bath, i.e., $\sum_{s,b}|sb\rangle\langle sb| = 1$. The $|sb\rangle$ states are not eigenstates of the total Hamiltonian \hat{H} due to the interaction term $\hat{H}^{(S-B)}(q_S, q_B)$. The expectation value of any system operator $\hat{A}(q_S)$ will be given by

$$\langle \hat{A}(t) \rangle = \text{Tr} \left[\hat{\rho}(t) \hat{A}(q_S) \right] \quad (4.28)$$

where,

$$\text{Tr} \left[\hat{\rho}(t) \hat{A}(q_S) \right] = \sum_{s,b} \langle sb | \hat{\rho}(t) \hat{A}(q_S) | sb \rangle = \sum_{s,b} \sum_{s',b'} \langle sb | \hat{\rho}(t) | s'b' \rangle \langle s'b' | \hat{A}(q_S) | sb \rangle. \quad (4.29)$$

The operator \hat{A} is independent of the bath degrees of freedom so that

$$\langle s'b' | \hat{A}(q_S) | sb \rangle = \langle s' | \hat{A} | s \rangle \langle b' | b \rangle \quad (4.30)$$

and since the eigenstates of the bath system are orthonormal, i.e., $\langle b' | b \rangle = \delta_{b,b'}$, the expectation value yields

$$\langle \hat{A}(t) \rangle = \sum_{s,s'} \sum_b \langle sb | \hat{\rho}(t) | s'b \rangle \langle s' | \hat{A}(q_S) | s \rangle = \text{Tr}_S \left[(\text{Tr}_B \hat{\rho}) \hat{A} \right]. \quad (4.31)$$

The quantity

$$\hat{\sigma}(t) = \text{Tr}_B \hat{\rho}(t) \quad (4.32)$$

is the reduced system density operator whose matrix elements are given by

$$\sigma_{ss'}(t) = \sum_b \langle sb | \hat{\rho}(t) | s'b \rangle. \quad (4.33)$$

Tr_B and Tr_S denote partial trace over the bath and system degrees of freedom respectively ($\text{Tr} = \text{Tr}_B \text{Tr}_S$). The time evolution of the reduced density operator can be found from the time evolution of the density operator of the total system

$$\frac{d\hat{\rho}}{dt} = -\frac{i}{\hbar} [\hat{H}, \hat{\rho}] = -\frac{i}{\hbar} [\hat{H}^{(S)}, \hat{\rho}] - \frac{i}{\hbar} [\hat{H}^{(B)}, \hat{\rho}] - \frac{i}{\hbar} [\hat{H}^{(S-B)}, \hat{\rho}]. \quad (4.34)$$

Taking the trace Tr_B of both sides of equation 4.34 leads to

$$\frac{d\hat{\sigma}}{dt} = -\frac{i}{\hbar} [\hat{H}^{(S)}, \hat{\sigma}] - \frac{i}{\hbar} \text{Tr}_B \left([\hat{H}^{(S-B)}, \hat{\rho}] \right), \quad (4.35)$$

where $\text{Tr}_B[\hat{H}^{(S)}, \hat{\rho}] = [\hat{H}^{(S)}, \text{Tr}_B \hat{\rho}] = [\hat{H}^{(S)}, \hat{\sigma}]$. The effects of the bath on the time evolution of the system density matrix are given by the second term in eq. 4.35.

4.5 Quantum master equation within Markov approximation

Using the Markov approximation for the $\text{Tr}_B \left([\hat{H}^{(S-B)}, \hat{\rho}] \right)$ term in eq. 4.35, the equation can be reduced to the form (see refs. 9,10,43,63,64)

$$i\hbar \frac{d\hat{\sigma}(t)}{dt} = \hat{L}^{\text{coh}} \hat{\sigma}(t) + \hat{L}^{\text{diss}} \hat{\sigma}(t), \quad (4.36)$$

where

$$\hat{L}^{\text{coh}} \hat{\sigma}(t) = [\hat{H}^{(S)}, \hat{\sigma}] \quad (4.37)$$

and

$$\hat{L}^{\text{diss}} \hat{\sigma}(t) \approx \text{Tr}_B \left([\hat{H}^{(S-B)}, \hat{\rho}] \right). \quad (4.38)$$

\hat{L}^{diss} is called the dissipative part of the time evolution of $\hat{\sigma}(t)$. It contains environmental induced population-relaxation rates (between S eigenstates) and pure dephasing rates that cause the decay of coherences between system eigenstates.

We express eq. 4.36 in Liouville space such that

$$\frac{d\vec{\sigma}(t)}{dt} = -\frac{i}{\hbar} \tilde{L}^{\text{tot}} \vec{\sigma}(t) \quad (4.39)$$

where

$$\tilde{L}^{\text{tot}} = \tilde{L}^{\text{coh}} + \tilde{L}^{\text{diss}} \quad (4.40)$$

is the total Liouvillian matrix. As an example, consider a two-state system (S) with eigenstates $|a\rangle$ and $|b\rangle$ (as before). Then,

$$\tilde{L}^{\text{coh}} = \begin{bmatrix} 0 & -V_{ba} & V_{ab} & 0 \\ V_{ab} & \varepsilon_a - \varepsilon_b & 0 & V_{ab} \\ V_{ba} & 0 & \varepsilon_b - \varepsilon_a & -V_{ba} \\ 0 & V_{ba} & -V_{ab} & 0 \end{bmatrix}. \quad (4.41)$$

\tilde{L}^{diss} is a sum of a population-relaxation term and a pure dephasing term

$$\hat{L}^{\text{diss}} = \hat{L}_{\text{pr}}^{\text{diss}} + \hat{L}_{\text{pd}}^{\text{diss}}. \quad (4.42)$$

The population-relaxation Liouvillian matrix is given by

$$\tilde{L}_{\text{pr}}^{\text{diss}} = i\hbar \begin{bmatrix} -\Gamma_{a \rightarrow b} & 0 & 0 & \Gamma_{b \rightarrow a} \\ 0 & -\frac{1}{2}\Gamma_{a \rightarrow b} - \frac{1}{2}\Gamma_{b \rightarrow a} & 0 & 0 \\ 0 & 0 & -\frac{1}{2}\Gamma_{a \rightarrow b} - \frac{1}{2}\Gamma_{b \rightarrow a} & 0 \\ \Gamma_{a \rightarrow b} & 0 & 0 & \Gamma_{b \rightarrow a} \end{bmatrix} \quad (4.43)$$

where $\Gamma_{a \rightarrow b}$ is the rate for the transition from state $|a\rangle$ to state $|b\rangle$, and $\Gamma_{b \rightarrow a}$ is the respective backward rate. These types of transitions are accompanied by energy dissipation into the environment. The pure dephasing Liouvillian matrix is given by

$$\tilde{L}_{\text{pd}}^{\text{diss}} = i\hbar \begin{bmatrix} 0 & 0 & 0 & 0 \\ 0 & -\gamma_{ab} & 0 & 0 \\ 0 & 0 & -\gamma_{ab} & 0 \\ 0 & 0 & 0 & 0 \end{bmatrix} \quad (4.44)$$

where γ_{ab} are pure dephasing rates that represent elastic-type collisions without energy exchange between the system and its environment. The total Liouvillian matrix composed by the coherent and incoherent parts is written as

$$\tilde{L}^{\text{tot}} = \begin{bmatrix} -i\hbar\Gamma_{a \rightarrow b} & -V_{ba} & V_{ab} & i\hbar\Gamma_{b \rightarrow a} \\ V_{ab} & (\varepsilon_a - \varepsilon_b) - \frac{i\hbar}{T_2} & 0 & V_{ab} \\ V_{ba} & 0 & (\varepsilon_b - \varepsilon_a) - \frac{i\hbar}{T_2} & -V_{ba} \\ i\hbar\Gamma_{a \rightarrow b} & V_{ba} & -V_{ab} & i\hbar\Gamma_{b \rightarrow a} \end{bmatrix} \quad (4.45)$$

where we define the decay time T_2 as

$$\frac{1}{T_2} = \frac{1}{2}(\Gamma_{a \rightarrow b} + \Gamma_{b \rightarrow a}) + \gamma_{ab}. \quad (4.46)$$

For an $N \times N$ system, the total Liouvillian matrix elements of eq. 4.39 are summarized as follows

(i) Coherent part:

$$L_{jk,mn} = H_{jk}\delta_{kn} - H_{kn}^*\delta_{jm}, \quad H_{jk} = \langle j | \hat{H}^{(S)} | k \rangle \quad (4.47a)$$

(ii) Dissipative part:

$$L_{jk,jk} = -i\hbar \left[\frac{\sum_{e \neq j} \Gamma_{j \rightarrow e} + \sum_{e \neq k} \Gamma_{k \rightarrow e}}{2} \right] - i\hbar\gamma_{jk} \quad (4.47b)$$

$$L_{jj,jj} = -i\hbar \sum_{e \neq j} \Gamma_{j \rightarrow e} \quad (4.47c)$$

$$L_{jj,kk} = i\hbar\Gamma_{j \rightarrow k} \quad (4.47d)$$

$$\text{zero otherwise.} \quad (4.47e)$$

4.6 The Bloch equations

We use the Liouville formalism as introduced in the previous sections, in order to extract the Bloch equations of motion.^{43,65} These equations are traditionally used to interpret electron paramagnetic resonance (EPR), nuclear magnetic resonance (NMR) and nonlinear optical spectroscopies. We start from eqs. 4.39 and 4.45, i.e.,

$$\dot{\sigma}_{aa} = -\Gamma_{a \rightarrow b}\sigma_{aa} + \Gamma_{b \rightarrow a}\sigma_{bb} + \frac{i}{\hbar}(V_{ba}\sigma_{ab} - \sigma_{ba}V_{ab}) \quad (4.48a)$$

$$\dot{\sigma}_{bb} = \Gamma_{a \rightarrow b}\sigma_{aa} - \Gamma_{b \rightarrow a}\sigma_{bb} - \frac{i}{\hbar}(V_{ba}\sigma_{ab} - \sigma_{ba}V_{ab}) \quad (4.48b)$$

$$\dot{\sigma}_{ba} = -\left(i\omega_{ba} + \frac{1}{T_2}\right)\sigma_{ba} + \frac{i}{\hbar}V_{ba}(\sigma_{bb} - \sigma_{aa}), \quad (4.48c)$$

where $\omega_{ba} = \varepsilon_b - \varepsilon_a$. Note that σ_{ab} is the complex conjugate of σ_{ba} , thus, no separate equation is required. In the absence of external perturbation, $V_{ab} = V_{ba} = 0$, and using the relation $\sigma_{aa} + \sigma_{bb} = 1$, the equation of motion for the populations σ_{aa} and σ_{bb} yields

$$\dot{\sigma}_{aa} = \Gamma_{b \rightarrow a} - \sigma_{aa}(\Gamma_{a \rightarrow b} + \Gamma_{b \rightarrow a}) \quad (4.49a)$$

$$\dot{\sigma}_{bb} = \Gamma_{a \rightarrow b} - \sigma_{bb}(\Gamma_{a \rightarrow b} + \Gamma_{b \rightarrow a}) \quad (4.49b)$$

Subtracting the two equations above, we get the equation of motion for the population difference $\sigma_{bb} - \sigma_{aa}$, i.e.,

$$\dot{\sigma}_{bb} - \dot{\sigma}_{aa} = (\Gamma_{a \rightarrow b} - \Gamma_{b \rightarrow a}) - (\Gamma_{a \rightarrow b} + \Gamma_{b \rightarrow a})(\sigma_{bb} - \sigma_{aa}). \quad (4.50)$$

In thermal equilibrium, $\dot{\sigma}_{bb} = \dot{\sigma}_{aa} = 0$, so that eq. 4.50 yields

$$(\sigma_{bb} - \sigma_{aa})^{(eq)} = \frac{\Gamma_{a \rightarrow b} - \Gamma_{b \rightarrow a}}{\Gamma_{a \rightarrow b} + \Gamma_{b \rightarrow a}}, \quad (4.51)$$

which is the population difference in thermal equilibrium. We define the decay rate T_1 as

$$T_1 = \frac{1}{\Gamma_{a \rightarrow b} + \Gamma_{b \rightarrow a}} \quad (4.52)$$

and eq. 4.50 is rewritten as

$$\dot{\sigma}_{bb} - \dot{\sigma}_{aa} = -\frac{(\sigma_{bb} - \sigma_{aa}) - (\sigma_{bb} - \sigma_{aa})^{(eq)}}{T_1}. \quad (4.53)$$

Now, taking into account the external perturbation \hat{V} , eq. 4.53 for the population difference $\sigma_{bb} - \sigma_{aa}$, is expressed as

$$\dot{\sigma}_{bb} - \dot{\sigma}_{aa} = -\frac{(\sigma_{bb} - \sigma_{aa}) - (\sigma_{bb} - \sigma_{aa})^{(eq)}}{T_1} - \frac{2i}{\hbar}(V_{ba}\sigma_{ab} - \sigma_{ba}V_{ab}) \quad (4.54)$$

(see eqs. 4.48a and 4.48b). We examine the solutions to the coupled equations

$$\dot{\sigma}_{ba} = -\left(i\omega_{ba} + \frac{1}{T_2}\right)\sigma_{ba} + \frac{i}{\hbar}V_{ba}(\sigma_{bb} - \sigma_{aa}) \quad (4.55a)$$

$$\dot{\sigma}_{bb} - \dot{\sigma}_{aa} = -\frac{(\sigma_{bb} - \sigma_{aa}) - (\sigma_{bb} - \sigma_{aa})^{(eq)}}{T_1} - \frac{2i}{\hbar}(V_{ba}\sigma_{ab} - \sigma_{ba}V_{ab}) \quad (4.55b)$$

in the presence of a monochromatic, steady-state field of frequency ω . For example, the interaction Hamiltonian for a linearly polarized applied field in the x -direction, is given by

$$\hat{V} = -\hat{V}_x \cos(\omega t) = -\hat{V}_x \left(\frac{e^{-i\omega t} + e^{i\omega t}}{2} \right), \quad (4.56)$$

and the respective matrix elements are written as

$$V_{ba} = -\langle b | \frac{\hat{V}_x}{2} | a \rangle (e^{-i\omega t} + e^{i\omega t}). \quad (4.57)$$

We apply the rotating-wave approximation (RWA) i.e., we approximate V_{ba} as follows

$$V_{ba} \approx -\langle b | \frac{\hat{V}_x}{2} | a \rangle e^{-i\omega t} = -\mathcal{V}_{ba} e^{-i\omega t}. \quad (4.58)$$

Further, we introduce the following quantities

$$\sigma_{ba} = \tilde{\sigma}_{ba} e^{-i\omega t} \quad (4.59a)$$

$$\sigma_{aa} = \tilde{\sigma}_{aa} \quad (4.59b)$$

$$\sigma_{bb} = \tilde{\sigma}_{bb} \quad (4.59c)$$

where $\tilde{\sigma}_{ba}$ slowly varies in the case $\omega = \omega_{ba}$. Therefore, eqs. 4.55a and 4.55b become

$$\frac{d}{dt} \tilde{\sigma}_{ba} = \left[i(\omega - \omega_{ba}) - \frac{1}{T_2} \right] \tilde{\sigma}_{ba} - \frac{i}{\hbar} \mathcal{V}_{ba} (\sigma_{bb} - \sigma_{aa}) \quad (4.60a)$$

$$\dot{\sigma}_{bb} - \dot{\sigma}_{aa} = -\frac{(\sigma_{bb} - \sigma_{aa}) - (\sigma_{bb} - \sigma_{aa})^{(eq)}}{T_1} + \frac{2i}{\hbar} (\mathcal{V}_{ba} \tilde{\sigma}_{ab} - \tilde{\sigma}_{ba} \mathcal{V}_{ab}). \quad (4.60b)$$

These two coupled equations of motion are simplified by introducing the following quantities

$$\begin{aligned} w &= \sigma_{bb} - \sigma_{aa} \\ w^{(eq)} &= (\sigma_{bb} - \sigma_{aa})^{(eq)} \end{aligned} \quad (4.61)$$

$$\Delta\omega = \omega - \omega_{ba}$$

and we drop the subscripts on $\tilde{\sigma}_{ba}$ and \mathcal{V}_{ba} i.e., $\tilde{\sigma}_{ba} = \tilde{\sigma}$ and $\mathcal{V}_{ba} = \mathcal{V}$ for simplicity. Then, eqs. 4.60a and 4.60b are written as

$$\frac{d\tilde{\sigma}}{dt} = \left(i\Delta\omega - \frac{1}{T_2} \right) \tilde{\sigma} - \frac{i}{\hbar} \mathcal{V} w \quad (4.62a)$$

$$\frac{dw}{dt} = -\frac{w - w^{(eq)}}{T_1} + \frac{2i}{\hbar} (\mathcal{V} \tilde{\sigma}^* - \tilde{\sigma} \mathcal{V}^*). \quad (4.62b)$$

We express the density matrix element $\tilde{\sigma}$ in terms of two real quantities as follows

$$\tilde{\sigma} = \frac{1}{2}(u - iv), \quad (4.63)$$

and eq. 4.62a yields

$$\frac{d}{dt}(u - iv) = \left(i\Delta\omega - \frac{1}{T_2} \right) (u - iv) - \frac{2i}{\hbar} \mathcal{V} w \quad (4.64)$$

This equation can be separated into its real and imaginary part as follows

$$\frac{du}{dt} = \Delta\omega v - \frac{1}{T_2} u \quad (4.65a)$$

$$\frac{dv}{dt} = -\Delta\omega u - \frac{v}{T_2} + \frac{2}{\hbar} \mathcal{V} w. \quad (4.65b)$$

In the same way, if we substitute $\tilde{\sigma} = \frac{1}{2}(u - iv)$ also in eq. 4.62, we get

$$\frac{dw}{dt} = -\frac{w - w^{(eq)}}{T_1} - \frac{2}{\hbar}\mathcal{V}v. \quad (4.66)$$

The set of eqs. 4.65a, 4.65b and 4.66 are the so-called Bloch equations. The steady-state solutions are given by setting $\frac{du}{dt} = 0$, $\frac{dv}{dt} = 0$ and $\frac{dw}{dt} = 0$, i.e.,

$$u^{ss} \equiv (\tilde{\sigma}^{ss})^* + \tilde{\sigma}^{ss} = \frac{2w^{(eq)}\mathcal{V}\Delta\omega T_2^2}{\hbar[1 + \Delta\omega^2 T_2^2 + (4/\hbar^2)|\mathcal{V}|^2 T_1 T_2]} \quad (4.67a)$$

$$v^{ss} \equiv i[\tilde{\sigma}^{ss} - (\tilde{\sigma}^{ss})^*] = \frac{2w^{(eq)}\mathcal{V}T_2}{\hbar[1 + \Delta\omega^2 T_2^2 + (4/\hbar^2)|\mathcal{V}|^2 T_1 T_2]} \quad (4.67b)$$

$$w^{ss} \equiv \sigma_{bb}^{ss} - \sigma_{aa}^{ss} = \frac{w^{(eq)}[1 + (\omega - \omega_{ba})^2 T_2^2]}{1 + \Delta\omega^2 T_2^2 + (4/\hbar^2)|\mathcal{V}|^2 T_1 T_2}. \quad (4.67c)$$

where $\tilde{\sigma} = \tilde{\sigma}_{ba}$ and $\tilde{\sigma}^* = \tilde{\sigma}_{ab}$ (see eq. 4.63). Eqs 4.67a, 4.67b and 4.67c are the steady-state solutions to the Bloch equations for the time-dependent harmonic perturbation in the RWA, \mathcal{V}_{ba} . For example, in the case of absorption $\mathcal{V}_{ba} = \mu_{ba}E$ where E is the magnitude of the applied electric field. In the case of an EPR experiment, $\mathcal{V}_{ba} = \frac{g\beta_e\hbar B_1}{2}$ where B_1 is the magnitude of the detection magnetic field along in the x -direction (see chapter 5).

CHAPTER 5

Principles of electron paramagnetic resonance

5.1 Introduction

Electron Paramagnetic Resonance (EPR) spectroscopy is a well-established spectroscopic technique for studying molecular systems with unpaired electrons. Molecular species with at least one unpaired electron (paramagnets) are of particular interest since they are often chemically reactive. For example, proteins contain paramagnetic molecules in the form of stable cofactors such as transition metal ions (e.g., iron, copper, nickel) and complex organic molecules. Homogeneous catalysts, electrochemical systems and materials exposed to UV irradiation produce organic and inorganic radicals during the reactions. EPR is the most popular method of choice used to characterize and identify these paramagnetic systems, providing information about their electronic structure and dynamics.

EPR is an experimental method to study magnetic-dipole transitions induced by microwave irradiation of paramagnetic systems placed in a static magnetic field. From the transitions between the energy levels one obtains detailed information about the structural and electronic properties of the paramagnetic system. The EPR experiment of a free radical with an unpaired electron is the simplest form of EPR spectroscopy. The isolated electron possesses a spin angular momentum \vec{S} which gives rise to a spin magnetic moment $\vec{\mu}$. The two are related by the formula

$$\vec{\mu} = -g\beta_e\vec{S} \quad (5.1)$$

where β_e is the Bohr magneton defined as

$$\beta_e = \frac{e\hbar}{m_e} \quad (5.2)$$

(m_e is the mass of electron). The quantity g is the g -factor of the electron and equals to 2.0023 for a free electron. In the absence of an external magnetic field, the magnetic

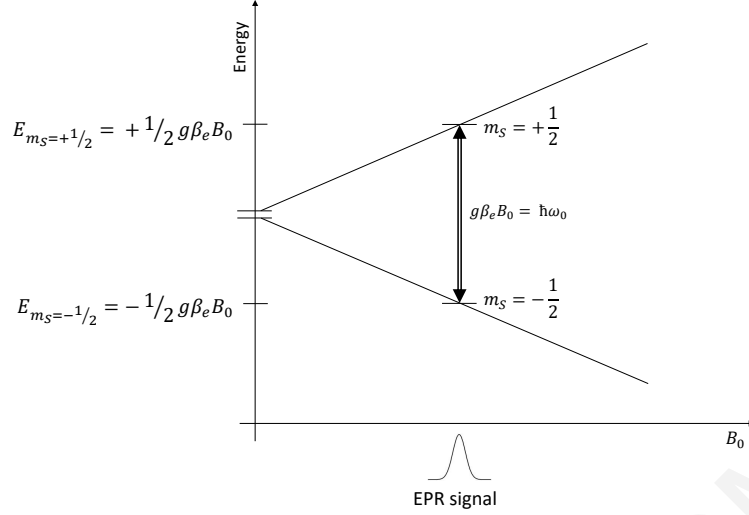


Figure 5.1: Energy level diagram for $S = 1/2$ system as a function of the applied magnetic field B_0 . In zero magnetic field ($B_0 = 0$) the electron spin energy levels are degenerate. Application of external magnetic field ($B_0 > 0$) lifts the degeneracy of the electron spin energy levels. The EPR signal is observed when the energy difference between the two spin states matches the frequency of the absorptive photon, $(g\beta_e B_0) / \hbar = \omega_0$.

dipole $\vec{\mu}$ is randomly oriented. However, if the electron is subjected to a static magnetic field \vec{B} , the magnetic dipole moment $\vec{\mu}$ experiences a torque tending to align the magnetic moment with the field. In a static magnetic field parallel to the z -direction [$\vec{B} = (0, 0, B_0)$], the degeneracy of the electron spin energy levels is lifted due to the spin magnetic quantum number m_S (e.g., $m_S = \pm 1/2$). The system in the presence of the static magnetic field B_0 is described by the Zeeman Hamiltonian^{66–71}

$$\hat{H} = g\beta_e B_0 \hat{S}_z. \quad (5.3)$$

The eigenenergies of the Zeeman Hamiltonian are

$$E_{m_S=\pm 1/2} = \pm \frac{1}{2} g\beta_e B_0 \quad (5.4)$$

(see Figure 5.1). To detect an EPR signal, an additional magnetic field \vec{B}_1 is applied perpendicular to the static magnetic field $B_0 \hat{z}$. In the usual EPR experimental setup, \vec{B}_1 is linearly polarized along the x -direction i.e., $\vec{B}_1(t) = (2B_1 \cos(\omega_{mw}t), 0, 0)$. This field can be considered as a superposition of a clockwise and a counter-clockwise rotating circularly polarized fields (\vec{B}_1^r), while the effect of the counter-rotating component is often neglected (i.e., $\vec{B}_1^r = (B_1 \cos(\omega_{mw}t), B_1 \sin(\omega_{mw}t), 0)$). The frequency ω_{mw} is usually in the microwave (mw) range. If $\omega_{mw} = \omega_0$, where

$$\omega_0 = (E_{m_S=+1/2} - E_{m_S=-1/2}) / \hbar = (g\beta_e B_0) / \hbar, \quad (5.5)$$

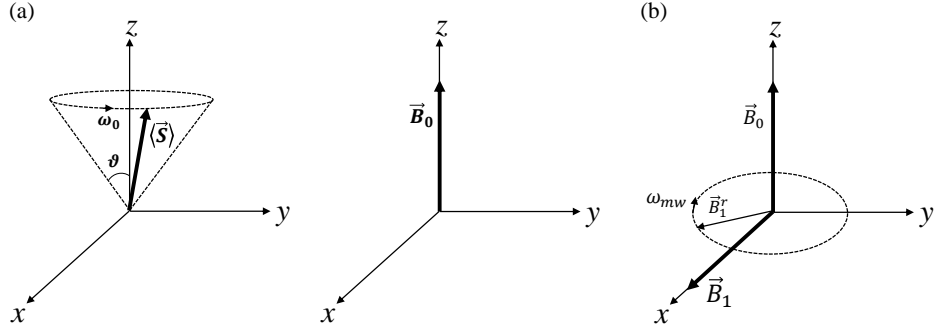


Figure 5.2: (a) The spin vector precesses about the magnetic field \vec{B}_0 along the z -axis of the laboratory frame (x, y, z) , with frequency of precession ω_0 . (b) The additional field \vec{B}_1 rotates in the xy plane with frequency ω_{mw} .

maximum absorption from the lowest- to the highest-energy spin state is obtained. This situation is described as the resonance condition and describes the fundamental principle of the EPR spectroscopy.

5.2 Quantum mechanical description of spin in external magnetic field

A particle of spin $1/2$ in a static magnetic field $B_0\hat{z}$ is described by the Hamiltonian of eq. 5.3. The eigenstates of the spin Hamiltonian are those of \hat{S}_z i.e., $|a\rangle = |\frac{1}{2}, \frac{1}{2}\rangle$ for spin up and $|b\rangle = |\frac{1}{2}, -\frac{1}{2}\rangle$ for spin down. The time-dependent wavefunction $|\Psi(t)\rangle$ of the system is a linear combination of $|a\rangle$ and $|b\rangle$, i.e.,⁷²

$$|\Psi(t)\rangle = c_a(t)|a\rangle + c_b(t)|b\rangle. \quad (5.6)$$

where the coefficients $c_a(t)$ and $c_b(t)$ equal to $c_a(t) = c_a e^{-ig\beta_e B_0 t/2}$ and $c_b(t) = c_b e^{ig\beta_e B_0 t/2}$. Without loss of generality, we can write $c_a = \cos(\vartheta/2)$ and $c_b = \sin(\vartheta/2)$, such that $|c_a|^2 + |c_b|^2 = 1$. We calculate the expectation value of \hat{S} as a function of time, i.e., $\langle \hat{S} \rangle = \langle \Psi(t) | \hat{S} | \Psi(t) \rangle$. The result is

$$\langle \hat{S}_x \rangle = \frac{\hbar}{2} \sin\vartheta \cos(\omega_0 t) \quad (5.7a)$$

$$\langle \hat{S}_y \rangle = -\frac{\hbar}{2} \sin\vartheta \sin(\omega_0 t) \quad (5.7b)$$

$$\langle \hat{S}_z \rangle = \frac{\hbar}{2} \cos\vartheta. \quad (5.7c)$$

These equations indicate that $\langle \hat{S} \rangle$ precesses at a constant angle ϑ on a cone about the magnetic field $B_0\hat{z}$, with frequency of precession equal to ω_0 (see figure 5.2(a)).

In the presence of the external time-dependent magnetic field $\vec{B}_1(t)$, the Hamil-

tonian of the system is written as (see figure 5.2(b))

$$\begin{aligned}\hat{H}(t) &= g\beta_e \left\{ B_0 \hat{S}_z + B_1 [\cos(\omega_{mw}t) \hat{S}_x + \sin(\omega_{mw}t) \hat{S}_y] \right\} \\ &= \omega_0 \hat{S}_z + \omega_1 [\cos(\omega_{mw}t) \hat{S}_x + \sin(\omega_{mw}t) \hat{S}_y],\end{aligned}\quad (5.8)$$

where $\omega_1 = g\beta_e B_1$. In a matrix form, the Hamiltonian in the basis of $|a\rangle$ and $|b\rangle$ states, is written as

$$\tilde{H} = \frac{\hbar}{2} \begin{pmatrix} \omega_0 & \omega_1 e^{-i\omega_{mw}t} \\ \omega_1 e^{i\omega_{mw}t} & -\omega_0 \end{pmatrix}. \quad (5.9)$$

Substituting eq. 5.6 in the time-dependent Schrödinger equation $i\hbar|\dot{\Psi}(t)\rangle = \hat{H}|\Psi(t)\rangle$, yields

$$i\frac{d}{dt}c_a(t) = \frac{\omega_0}{2}c_a(t) + \frac{\omega_1}{2}c_b(t)e^{-i\omega_{mw}t} \quad (5.10a)$$

$$i\frac{d}{dt}c_b(t) = -\frac{\omega_0}{2}c_b(t) + \frac{\omega_1}{2}c_a(t)e^{i\omega_{mw}t}. \quad (5.10b)$$

The magnetic field \vec{B}_1 (and the Hamiltonian) becomes time-independent in a rotating coordinate system (X, Y, Z) which rotates with the microwave frequency ω_{mw} about the z -axis (z coincides with Z). We transform to the rotating frame by making the following substitutions

$$\begin{aligned}c'_a(t) &= e^{i\omega_{mw}t/2}c_a(t) \\ c'_b(t) &= e^{-i\omega_{mw}t/2}c_b(t).\end{aligned}\quad (5.11)$$

Eqs. 5.10a and 5.10b are now given by

$$i\frac{d}{dt}c'_a(t) = -\frac{\Delta\omega}{2}c'_a(t) + \frac{\omega_1}{2}c'_b(t) \quad (5.12a)$$

$$i\frac{d}{dt}c'_b(t) = \frac{\Delta\omega}{2}c'_b(t) + \frac{\omega_1}{2}c'_a(t), \quad (5.12b)$$

where $\Delta\omega = \omega_{mw} - \omega_0$. The time-dependent Schrödinger equation for this system is written as

$$i\hbar|\dot{\tilde{\Psi}}(t)\rangle = \hat{H}^{\text{eff}}|\tilde{\Psi}(t)\rangle \quad (5.13)$$

where the wavefunction $|\tilde{\Psi}(t)\rangle$ is given by

$$|\tilde{\Psi}(t)\rangle = c'_a(t)|a\rangle + c'_b(t)|b\rangle, \quad (5.14)$$

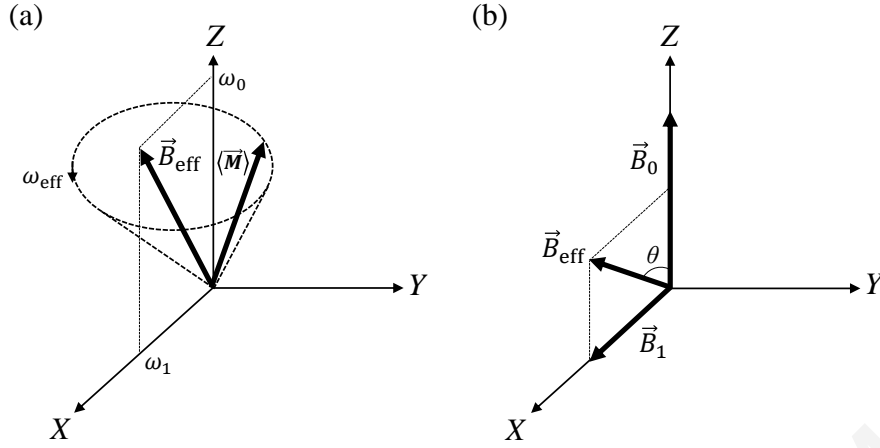


Figure 5.3: (a) Precession of the magnetization about the effective magnetic field \vec{B}_{eff} with precession frequency ω_{eff} , during m.w. irradiation with amplitude ω_1 . (b) The transformation to the rotating frame (X, Y, Z) gives the effective magnetic field \vec{B}_{eff} tilted at a constant angle θ to the Z -axis.

and the effective Hamiltonian matrix is given by

$$\tilde{H}^{\text{eff}} = \frac{\hbar}{2} \begin{pmatrix} -\Delta\omega & \omega_1 \\ \omega_1 & \Delta\omega \end{pmatrix}. \quad (5.15)$$

In terms of spin operators, the above time-independent Hamiltonian \hat{H}^{eff} in the rotating frame (X, Y, Z) is given by

$$\hat{H}^{\text{eff}} = -\Delta\omega \hat{S}_Z + \omega_1 \hat{S}_X. \quad (5.16)$$

This Hamiltonian describes the interaction of the spin with the effective magnetic field \vec{B}^{eff} which is static in the rotating frame (see figure 5.3(b))

$$\vec{B}^{\text{eff}} = \left(B_0 - \frac{\omega_{mw}}{g\beta_e} \right) \hat{Z} + B_1 \hat{X}. \quad (5.17)$$

This field makes an angle θ with the Z -axis given by

$$\tan(\theta) = \frac{\vec{B}_1}{\vec{B}_0} = \frac{\omega_1}{\omega_0}. \quad (5.18)$$

(see figure 5.3(b)). In conclusion, the effect of the time-dependent magnetic field \vec{B}_1 (in the rotating wave approximation and in the rotating frame), can be considered as an effective static magnetic field at an angle θ with respect to the original static field \vec{B}_0 .

5.3 The Bloch equations for the EPR experiment in the rotating frame

To include spin relaxation effects in EPR we need to adopt a density-matrix formalism that contains relaxation terms (see chapter 4). Below, we describe the simplest density-matrix approach involving the Bloch equations for the magnetization.

The EPR experiment probes the magnetization \vec{M} , defined by

$$M_i = ng\beta_e \langle \hat{S}_i \rangle \quad (i = X, Y, Z). \quad (5.19)$$

n is the total number of atoms per unit volume. $\langle \hat{S}_i \rangle$ is the expectation value of the operator \hat{S}_i i.e., $\langle \hat{S}_i \rangle = \text{Tr}(\hat{\sigma} \hat{S}_i)$ where $\hat{\sigma}$ is the reduced density matrix, as discussed in chapter 4. The Bloch equations for the magnetization in the absence of relaxation can be obtained starting from the equation of motion for the reduced density matrix

$$\frac{d\vec{\sigma}(t)}{dt} = -\frac{i}{\hbar} \tilde{L}^{\text{coh}} \vec{\sigma}(t) \quad (5.20)$$

where \tilde{L}^{coh} is the coherent part of the Liouvillian matrix as given by eq. 4.41. Following exactly the same procedure that we described in eqs. 4.48 - 4.66 we get the Bloch equations for the spin system (for $\mathcal{V} = \langle b | \hat{V}_x | a \rangle = \frac{g\beta_e \hbar B_1}{2}$, $\hat{V}_x = 2g\beta_e B_1 \hat{S}_x$ and $\Delta\omega = \omega_{mw} - \omega_0$). To obtain the Bloch equations for the magnetization we use eq. 5.19 leading to⁷³⁻⁷⁵

$$\frac{dM_X}{dt} = (\omega_{mw} - \omega_0) M_Y \quad (5.21a)$$

$$\frac{dM_Y}{dt} = -(\omega_{mw} - \omega_0) M_X + \omega_1 M_Z \quad (5.21b)$$

$$\frac{dM_Z}{dt} = -\omega_1 M_Y. \quad (5.21c)$$

These are the Bloch equations for the magnetization in the presence of the external alternating magnetic field \vec{B}_1 , and they are expressed in the rotating frame (X, Y, Z) . These three equations describe the time-dependence of the magnetization vector \vec{M} . They describe the precession of the magnetization in a cone of a fixed angle about the direction of the effective magnetic field \vec{B}_{eff} with frequency of precession equal to

$$\omega_{\text{eff}} = \sqrt{\Delta\omega^2 + \omega_1^2}, \quad (5.22)$$

as shown in the figure 5.3(a). For the particular case where $\omega_{mw} = \omega_0$ (and thus $\Delta\omega = 0$), so that $\vec{B}_{\text{eff}} = \vec{B}_1$, the motion of the magnetization vector is a precession about the X -axis with frequency $\omega_{\text{eff}} = \omega_1$. This is the on-resonant case and absorption between the magnetic spin states occurs.

To include relaxation effects we use the same procedure as above for the reduced density matrix, starting from equations

$$\begin{aligned}\frac{d\vec{\sigma}(t)}{dt} &= -\frac{i}{\hbar}(\tilde{L}^{\text{coh}} + \tilde{L}^{\text{diss}})\vec{\sigma}(t) \\ &= -\frac{i}{\hbar}\tilde{L}^{\text{tot}}\vec{\sigma}(t)\end{aligned}\quad (5.23)$$

where \tilde{L}^{diss} is the dissipative part of the Liouville matrix (see section 4.5). The total Liouvillian matrix is given by eq. 4.45. We obtain

$$\frac{dM_X}{dt} = (\omega_{mw} - \omega_0)M_Y - \frac{M_X}{T_2} \quad (5.24a)$$

$$\frac{dM_Y}{dt} = -(\omega_{mw} - \omega_0)M_X - \frac{M_Y}{T_2} + \omega_1 M_Z \quad (5.24b)$$

$$\frac{dM_Z}{dt} = -\frac{M_Z - M_Z^{(eq)}}{T_1} - \omega_1 M_Y. \quad (5.24c)$$

These are the Bloch equations for the magnetization with relaxation effects (T_1, T_2 see section 4.6). The steady-state solutions are obtained by setting

$$\frac{dM_X^{ss}}{dt} = 0 \quad \frac{dM_Y^{ss}}{dt} = 0 \quad \frac{dM_Z^{ss}}{dt} = 0. \quad (5.25)$$

Using eq. 5.19 and that $\langle \hat{S}_i \rangle = \text{Tr}(\hat{\sigma} \hat{S}_i)$ given by the steady-state values of $\hat{\sigma}$ discussed in chapter 4 (section 4.6), we get^{43,65,70,73-76}

$$M_X^{ss} = \frac{ng\beta_e\hbar}{2}[(\tilde{\sigma}^{ss})^* + \tilde{\sigma}^{ss}] = \frac{ng\beta_e\hbar}{2}u^{ss} \quad (5.26a)$$

$$M_Y^{ss} = \frac{ng\beta_e\hbar}{2}i[(\tilde{\sigma}^{ss})^* - \tilde{\sigma}^{ss}] = -\frac{ng\beta_e\hbar}{2}v^{ss} \quad (5.26b)$$

$$M_Z^{ss} = \frac{ng\beta_e\hbar}{2}(\sigma_{bb}^{ss} - \sigma_{aa}^{ss}) = \frac{ng\beta_e\hbar}{2}w^{ss}. \quad (5.26c)$$

By combining eqs. 4.67a-c and 5.26a-c, the steady-state solutions are written as

$$M_X^{ss} = \frac{\bar{M}_Z \omega_1 (\omega_{mw} - \omega_0) T_2^2}{1 + (\omega_{mw} - \omega_0)^2 T_2^2 + \omega_1^2 T_1 T_2} \quad (5.27a)$$

$$M_Y^{ss} = -\frac{\bar{M}_Z \omega_1 T_2}{1 + (\omega_{mw} - \omega_0)^2 T_2^2 + \omega_1^2 T_1 T_2} \quad (5.27b)$$

$$M_Z^{ss} = \frac{\bar{M}_Z [1 + (\omega_{mw} - \omega_0)^2 T_2^2]}{1 + (\omega_{mw} - \omega_0)^2 T_2^2 + \omega_1^2 T_1 T_2}. \quad (5.27c)$$

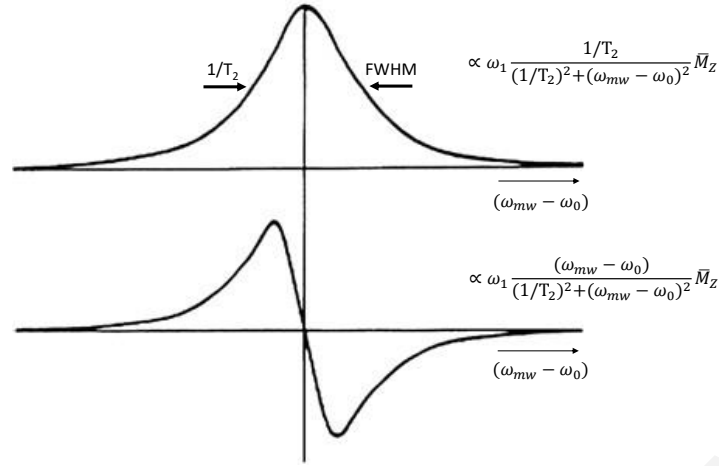


Figure 5.4: Absorption (above) and dispersion (below) signals in EPR experiment plotted versus $\omega_{mw} - \omega_0$.

where \bar{M}_Z is the value of M_Z at thermal equilibrium (dM_Z^{ss}/dt) when the applied field \vec{B}_1 is zero (see eq. 4.51). When $\omega_1^2 T_1 T_2 \ll \Delta\omega$, eqs. 5.27a-c reduce to

$$M_X^{ss} = \omega_1 \frac{(\omega_{mw} - \omega_0)}{(1/T_2)^2 + (\omega_{mw} - \omega_0)^2} \bar{M}_Z \quad (5.28a)$$

$$M_Y^{ss} = -\omega_1 \frac{1/T_2}{(1/T_2)^2 + (\omega_{mw} - \omega_0)^2} \bar{M}_Z \quad (5.28b)$$

$$M_Z^{ss} = \bar{M}_Z. \quad (5.28c)$$

The absorption signal in the EPR experiment is proportional to M_Y^{ss} , while the dispersion signal is proportional to M_X^{ss} . A plot of these signals is shown in the figure 5.4. Most EPR experiments, use the absorption signal instead of the dispersion. Eq. 5.28b for the absorption signal, corresponds to the classical Lorentzian line shape function with FWHM equals to $1/T_2$ (see figure 5.4).

5.4 Sensitivity of the ground-state EPR experiment

Ground-state EPR probes the spin dynamics of the ground electronic states of a molecule. The sensitivity of a ground-state EPR experiment is defined as the ratio of the power absorbed by magnetic resonance in the sample, to the power dissipated in the EPR resonance cavity^{70,77}

$$\text{sens} = \frac{dW/dt}{P_C}. \quad (5.29)$$

dW/dt is the energy absorbed per unit time by the sample, and P_C is the power dissipated in the resonant cavity. The cavity is a metal box in which the sample is placed. It increases the sensitivity of the spectrometer and concentrates the microwave power to the sample.^{78,79} The rate of absorption of energy is given by

$$\frac{dW}{dt} = N_{\text{tot}}(\hbar\omega) \sum_{\substack{i \neq j \\ E_i < E_j}} (P_i^{ss} k_{i \rightarrow j}^{\text{abs}} - P_j^{ss} k_{j \rightarrow i}^{\text{em}}) \quad (5.30)$$

where i and j denote the lower and upper sample energy levels E_i and E_j respectively, and $\omega = \omega_{mw}$. $P_{i(j)}^{ss}$ is the steady-state probability for the state $i(j)$ and N_{tot} is the total number of sample EPR-active spins. $k_{i \rightarrow j}^{\text{abs}}$ and $k_{j \rightarrow i}^{\text{em}}$ are the transition rates between levels i and j for absorption (abs) and emission (em) respectively. The rate of emission equals the rate of absorption, i.e., $k_{i \rightarrow j}^{\text{abs}} = k_{j \rightarrow i}^{\text{em}} = k_{i \rightarrow j}$. It is given by

$$k_{i \rightarrow j} = \frac{2\pi}{\hbar} |\langle i | \hat{\mu} \cdot \vec{B}_1 | j \rangle|^2 \mathfrak{L}(\omega) \quad (5.31)$$

where $\mathfrak{L}(\omega)$ is the Lorentzian lineshape function

$$\mathfrak{L}(x) = \frac{1}{\pi \hbar} \frac{\Gamma}{\Gamma^2 + (\omega - \omega_0)^2} \quad (5.32)$$

with $\Gamma = 1/T_2$ and $\omega_0 = \frac{E_i - E_j}{\hbar}$. The power absorbed is now simplified as

$$\frac{dW}{dt} = N_{\text{tot}}(\hbar\omega) (P_i^{ss} - P_j^{ss}) k_{i \rightarrow j} \quad (5.33)$$

and at thermal equilibrium,

$$\frac{P_j^{ss}}{P_i^{ss}} = e^{-\hbar\omega/K_B T}. \quad (5.34)$$

For example, for ground-state EPR and doublet states i.e., $|i\rangle = |\frac{1}{2}, -\frac{1}{2}\rangle$, $|j\rangle = |\frac{1}{2}, \frac{1}{2}\rangle$, if $\vec{B}_1 = \vec{B}_x$ then $\hat{\mu} \rightarrow \hat{\mu}_x$ ($\hat{\mu}_x$ is the component of the dipole moment vector in the direction of the magnetic field vector). The rate reduces to

$$k_{i \rightarrow j} = \frac{\pi B_1^2}{2\hbar} \left| \left\langle \frac{1}{2}, -\frac{1}{2} \left| \hat{\mu}_x \right| \frac{1}{2}, \frac{1}{2} \right\rangle \right|^2 \mathfrak{L}(\omega). \quad (5.35)$$

The sensitivity formula for the ground-state EPR experiment is discussed further in section 6.4.4.

5.5 The TR-EPR experiment

In the TR-EPR experiment, the sample is first optically excited by an external electric field to an excited singlet electronic state (see figure 5.5).¹⁸ The transition to an excited triplet state due to intersystem crossing (ISC) is monitored as a function

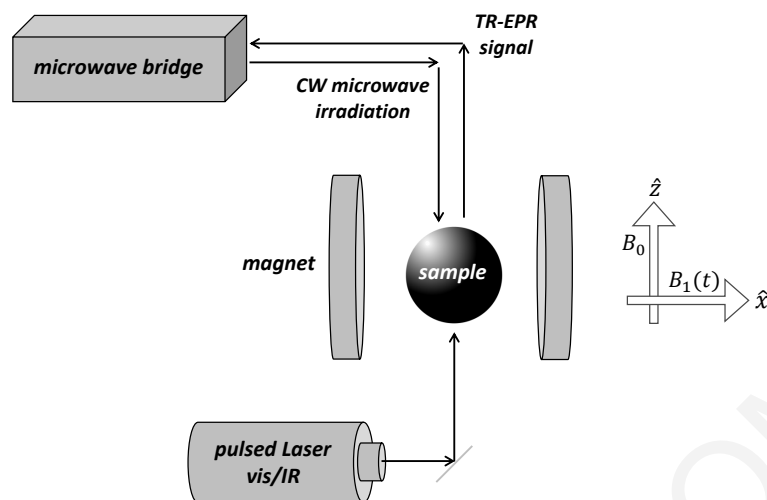


Figure 5.5: Experimental setup of TR-EPR: an applied electric field (usually in the visible or infrared (IR) range) optically excites the molecular sample to a singlet excited state, and the triplet excited states are populated via ISC. An applied static magnetic field, for example in the z -direction (B_0), splits the ZFS triplet sublevels (see figure 5.7) and a second time-dependent magnetic field (B_1) linearly polarized perpendicular to the static magnetic field induces transitions between these triplet sublevels, giving rise to TR-EPR triplet signals.

of time by an EPR experiment. In this case, absorption of the magnetic field leads to transitions between the triplet levels $m_s = 0, \pm 1$ or the ZFS eigenstates as described in the section below.

5.6 The spin-spin coupling and the zero-field splitting

In the previous sections we discussed the effect of an external magnetic field on the electronic spin states. This perturbation removes the degeneracy of the spin components and it is known as the Zeeman effect. However, the spin degeneracy is often lifted even in the absence of the external magnetic field. Interactions such as spin-orbit coupling (SOC) and spin-spin (SS) dipolar coupling between unpaired electrons, constitute the main perturbations that cause this lifting of degeneracy. In transition-metal complexes, SOC plays central role, but in organic molecules dipole-dipole interactions are dominant. This latter effect is known as the zero-field splitting (ZFS). In this section we discuss the ZFS due to SS dipolar interaction that causes a three-fold degeneracy of the triplet state.

5.6.1 Derivation of the spin-Hamiltonian

Given an arbitrary set of molecular x, y, z coordinates, the interaction Hamiltonian between two magnetic dipoles $\vec{\mu}_1$ and $\vec{\mu}_2$ is written as

$$\hat{H}_{dd} = \alpha^2 \left[\frac{\hat{\mu}_1^T \cdot \hat{\mu}_2}{r_{12}^3} - \frac{3 \left(\hat{\mu}_1^T \cdot \vec{r}_{12} \right) \left(\hat{\mu}_2^T \cdot \vec{r}_{12} \right)}{r_{12}^5} \right] \quad (5.36)$$

where \vec{r}_{12} is the vector joining the centers of the two dipoles and α is the fine structure constant ($\sim 1/137$). The magnetic moment is related to the spin angular momentum \vec{s} via $\vec{\mu} = -g\beta_e\vec{s}$. The dipole-dipole interaction Hamiltonian as a function of the spin operators is given by

$$\hat{H}_{dd} = \frac{g^2\alpha^2}{4} \left[\frac{\hat{s}_1^T \cdot \hat{s}_2}{r_{12}^3} - \frac{3 \left(\hat{s}_1^T \cdot \vec{r}_{12} \right) \left(\hat{s}_2^T \cdot \vec{r}_{12} \right)}{r_{12}^5} \right], \quad (5.37)$$

where the Bohr magneton ($\beta_e = e\hbar/m_e$) is replaced by $1/2$ (its value in atomic units), and $g = 2.0023$ (taken to be isotropic). Since $x_{12}^2 + y_{12}^2 + z_{12}^2 = r_{12}^2$, eq. 5.37 is expanded as

$$\begin{aligned} \hat{H}_{dd} = \frac{g^2\alpha^2}{4} & \left[(r_{12}^2 - 3x_{12}^2)\hat{s}_{1x}\hat{s}_{2x} + (r_{12}^2 - 3y_{12}^2)\hat{s}_{1y}\hat{s}_{2y} + (r_{12}^2 - 3z_{12}^2)\hat{s}_{1z}\hat{s}_{2z} \right. \\ & - 3x_{12}y_{12}(\hat{s}_{1x}\hat{s}_{2y} + \hat{s}_{1y}\hat{s}_{2x}) - 3x_{12}z_{12}(\hat{s}_{1x}\hat{s}_{2z} + \hat{s}_{1z}\hat{s}_{2x}) \\ & \left. - 3y_{12}z_{12}(\hat{s}_{1y}\hat{s}_{2z} + \hat{s}_{1z}\hat{s}_{2y}) \right] r_{12}^{-5}. \end{aligned} \quad (5.38)$$

Using that the total spin operator equals to $\hat{S} = \hat{s}_1 + \hat{s}_2$, and that $\hat{S}^2 = \hat{S}_x^2 + \hat{S}_y^2 + \hat{S}_z^2$, where $\hat{S}_x, \hat{S}_y, \hat{S}_z$ are the components of \hat{S} , we write the following relations

$$\hat{s}_{1x}\hat{s}_{2x} = \frac{1}{2}\hat{S}_x^2 - \frac{1}{4} \quad (5.39a)$$

$$\hat{s}_{1x}\hat{s}_{2y} + \hat{s}_{2x}\hat{s}_{1y} = \frac{1}{2}(\hat{S}_x\hat{S}_y + \hat{S}_y\hat{S}_x). \quad (5.39b)$$

Similar expressions are also applied for the \hat{S}_y, \hat{S}_z (eq. 5.39a) and $\hat{S}_x\hat{S}_z, \hat{S}_y\hat{S}_z$ (eq. 5.39b) components respectively. Now the Hamiltonian (eq. 5.38) reduces to

$$\begin{aligned} \hat{H}_{dd} = \frac{g^2\alpha^2}{8} & \left[(r_{12}^2 - 3x_{12}^2)\hat{S}_x^2 + (r_{12}^2 - 3y_{12}^2)\hat{S}_y^2 + (r_{12}^2 - 3z_{12}^2)\hat{S}_z^2 \right. \\ & - 3x_{12}y_{12}(\hat{S}_x\hat{S}_y + \hat{S}_y\hat{S}_x) - 3x_{12}z_{12}(\hat{S}_x\hat{S}_z + \hat{S}_z\hat{S}_x) \\ & \left. - 3y_{12}z_{12}(\hat{S}_y\hat{S}_z + \hat{S}_z\hat{S}_y) \right] r_{12}^{-5} \\ & = \sum_p \sum_q \Omega_{pq} \hat{S}_p \hat{S}_q \quad (p, q = x, y, z) \end{aligned} \quad (5.40)$$

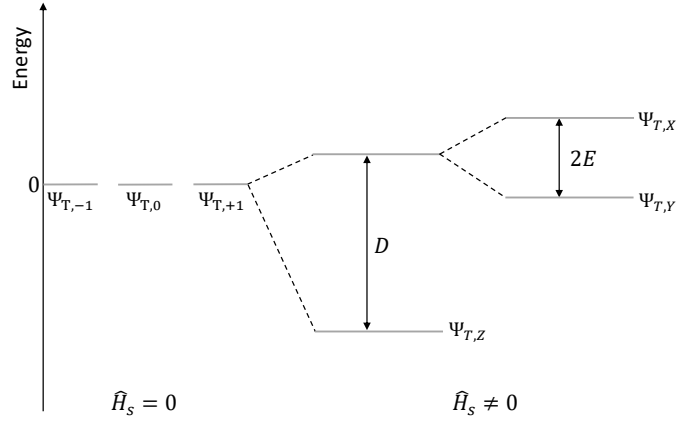


Figure 5.6: In the absence of an external magnetic field the degeneracy of the triplet sublevels is lifted due to the SS dipolar interaction.

where

$$\Omega_{pp} = \frac{g^2 \alpha^2}{8} (r_{12}^2 - 3p_{12}^2) r_{12}^{-5} \quad (5.41)$$

$$\Omega_{pq} = -\frac{3g^2 \alpha^2}{8} (p_{12} q_{12}) r_{12}^{-5} \quad (p \neq q).$$

Consider the triplet state $\Psi_{T,m_s} = \Phi_T(1,2)\Theta_{1,m_s}(1,2)$, where $\Phi_T(1,2)$ is the spatial antisymmetric wavefunction of the triplet state Ψ_{T,m_s} for electrons 1 and 2, and Θ_{s,m_s} are the respective spin wavefunctions for the triplet states ($s = 1$ and $m_s = 0, \pm 1$). The matrix elements of the Hamiltonian in the basis of the Ψ_{T,m_s} are given by

$$\begin{aligned} H_{m_s, m'_s} &= \langle \Psi_{T,m_s} | \hat{H}_{dd} | \Psi_{T,m'_s} \rangle \\ &= \langle \Phi_T(1,2) \Theta_{1,m_s}(1,2) | \sum_p \sum_q \Omega_{pq} \hat{S}_p \hat{S}_q | \Phi_T(1,2) \Theta_{1,m'_s}(1,2) \rangle \\ &= \sum_p \sum_q \langle \Phi_T(1,2) | \Omega_{pq} | \Phi_T(1,2) \rangle \langle \Theta_{1,m_s}(1,2) | \hat{S}_p \hat{S}_q | \Theta_{1,m'_s}(1,2) \rangle \\ &= \sum_p \sum_q D_{pq} \langle \Theta_{1,m_s}(1,2) | \hat{S}_p \hat{S}_q | \Theta_{1,m'_s}(1,2) \rangle. \end{aligned} \quad (5.42)$$

The integral $D_{pq} = \langle \Phi_T(1,2) | \Omega_{pq} | \Phi_T(1,2) \rangle$ does not depend on the spin, thus, eq. 5.42 is rewritten as

$$\begin{aligned} \hat{H}_{m_s, m'_s} &= \langle \Theta_{1,m_s}(1,2) | \sum_p \sum_q D_{pq} \hat{S}_p \hat{S}_q | \Theta_{1,m'_s}(1,2) \rangle \\ &= \langle \Theta_{1,m_s}(1,2) | \hat{H}_s | \Theta_{1,m'_s}(1,2) \rangle. \end{aligned} \quad (5.43)$$

where \hat{H}_s is the spin Hamiltonian. In matrix form it is written as^{19,51,66–69,71,80?}

$$\hat{H}_s = \hat{S}^T \cdot \tilde{D} \cdot \hat{S}. \quad (5.44)$$

The \tilde{D} tensor is symmetric and is called the ZFS tensor. Its (x, y, z) components are given by

$$D_{pq} = \frac{g^2 \alpha^2}{8} \left\langle \Phi(1, 2) \left| \frac{r_{12}^2 \delta_{pq} - 3pq}{r_{12}^5} \right| \Phi(1, 2) \right\rangle \quad (5.45)$$

and the trace of the ZFS matrix is zero, i.e., $tr(\tilde{D}) = D_{xx} + D_{yy} + D_{zz} = 0$.

In the principal-axes frame denoted as (X, Y, Z) , \tilde{D} is diagonal ($\tilde{D} \rightarrow \tilde{D}^d$), and the spin Hamiltonian (eq. 5.44) becomes

$$\hat{H}_s = D_X \hat{S}_X^2 + D_Y \hat{S}_Y^2 + D_Z \hat{S}_Z^2, \quad (5.46)$$

where D_X, D_Y, D_Z are the diagonal matrix elements of the 3×3 \tilde{D}^d matrix. Using the relations, $\hat{S}^2 = \hat{S}_X^2 + \hat{S}_Y^2 + \hat{S}_Z^2$ and $D_X + D_Y + D_Z = 0$, the Hamiltonian can be written as

$$\hat{H}_s = D \left[\hat{S}_Z^2 - \frac{1}{3} \hat{S}^2 \right] + E \left(\hat{S}_X^2 + \hat{S}_Y^2 \right) \quad (5.47)$$

where the quantities D and E are the ZFS parameters and are defined by

$$D = \frac{3}{2} D_Z \quad E = \frac{1}{2} (D_X - D_Y) \quad (5.48)$$

These parameters describe the separation of the three ZFS triplet sublevels in the absence of an external magnetic field (see figure 5.6). We use as a basis set the eigenfunctions of \hat{S}_Z in the principal axis, Θ_{S, M_S} (with $M_S = 0, \pm 1$) (these are not eigenstates of \hat{S}_z) to write the Hamiltonian of eq. 5.47 in a matrix form, i.e.,

$$\tilde{H}_s = \begin{pmatrix} \frac{1}{3}D & 0 & E \\ 0 & -\frac{2}{3}D & 0 \\ E & 0 & \frac{1}{3}D \end{pmatrix}. \quad (5.49)$$

The eigenvalues of \tilde{H}_s above, are given by solving $\det(\tilde{H} - W\tilde{I}) = 0$, where \tilde{I} is the unit matrix, i.e.,

$$W_1 = \frac{1}{3}D - E = -D_X \quad (5.50a)$$

$$W_2 = \frac{1}{3}D + E = -D_Y \quad (5.50b)$$

$$W_3 = -\frac{2}{3}D = -D_Z \quad (5.50c)$$

and the corresponding eigenstates are linear combinations of the eigenfunctions Θ_{S, M_S} ,

i.e.,

$$T_X = \frac{1}{\sqrt{2}}(\Theta_{1,-1} - \Theta_{1,+1}) \quad (5.51a)$$

$$T_Y = \frac{i}{\sqrt{2}}(\Theta_{1,-1} + \Theta_{1,+1}) \quad (5.51b)$$

$$T_Z = \Theta_{1,0}. \quad (5.51c)$$

5.6.2 The EPR absorption pattern of a triplet state

In an EPR experiment, a spin system is subjected to an external static magnetic field \vec{B}_0 , and the zeroth-order Hamiltonian of the triplet state in the principal axes system is given by^{19,51,66-69,71,80?}

$$\begin{aligned} \hat{H} &= \hat{H}^{\text{Zeeman}} + \hat{H}^{\text{ZFS}} \\ &= \beta_e \vec{B}_0 \cdot \tilde{g} \cdot \hat{S} + D \left[\hat{S}_Z^2 - \frac{1}{3} \hat{S}^2 \right] + E \left(\hat{S}_X^2 + \hat{S}_Y^2 \right) \end{aligned} \quad (5.52)$$

where \hat{H}^{Zeeman} is the Zeeman Hamiltonian that describes the interaction of the spin system with the external magnetic field, and \hat{H}^{ZFS} is the spin Hamiltonian that describes the magnetic dipole-dipole interactions, i.e., $\hat{H}^{\text{ZFS}} = \hat{H}_s$. Depending on the orientation of the external magnetic field with respect to the X -, Y - and Z -axes, the spin Hamiltonian is modified accordingly. When the external magnetic field is $\vec{B}_0 = B_X \hat{X} + B_Y \hat{Y} + B_Z \hat{Z}$, the Hamiltonian matrix is given by

$$\tilde{H} = \begin{pmatrix} g\beta_e B_Z + \frac{1}{3}D & \frac{1}{\sqrt{2}}g\beta_e(B_X - iB_Y) & E \\ \frac{1}{\sqrt{2}}g\beta_e(B_X + iB_Y) & -\frac{2}{3}D & \frac{1}{\sqrt{2}}g\beta_e(B_X - iB_Y) \\ E & \frac{1}{\sqrt{2}}g\beta_e(B_X + iB_Y) & -g\beta_e B_Z + \frac{1}{3}D \end{pmatrix}. \quad (5.53)$$

The corresponding eigenstates are linear combinations of the spin wavefunctions Θ_{S,M_S} , such as in eqs. 5.51a-c but with different coefficients. If the applied magnetic field is on the Z -direction ($\vec{B}_0 = B_Z \hat{Z}$) (i.e., $B_X = B_Y = 0$), the solutions of the secular determinant $\det(\tilde{H} - W\tilde{I}) = 0$, gives the following eigenvalues

$$W_1 = \frac{1}{3}D - [g^2\beta_e^2 B_Z^2 + E^2]^{1/2} \quad (5.54a)$$

$$W_2 = \frac{1}{3}D + [g^2\beta_e^2 B_Z^2 + E^2]^{1/2} \quad (5.54b)$$

$$W_3 = -\frac{2}{3}D. \quad (5.54c)$$

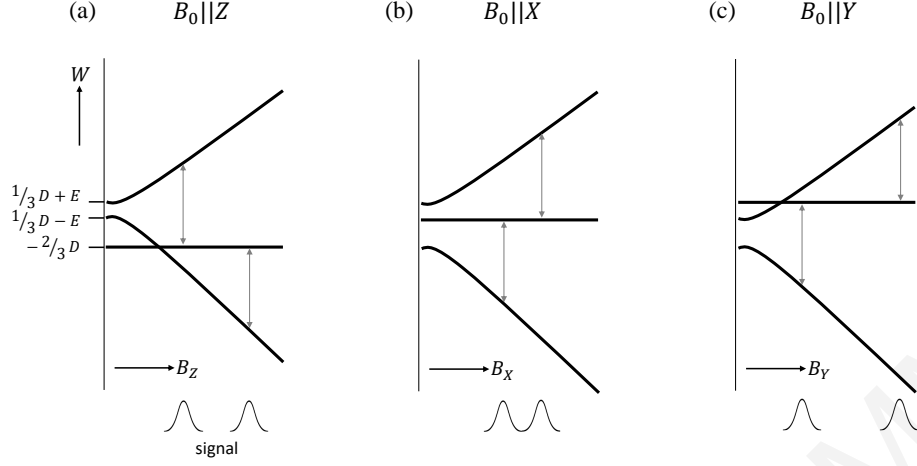


Figure 5.7: Energy level diagram of the triplet state and absorption (or emission) curves when the external magnetic field is applied (a) parallel to the principal axis Z , (b) parallel to the principal axis X , and parallel to the principal axis Y . The arrows show the allowed transitions between the triplet energy levels and the energies of the allowed transitions are given by $\Delta E = W_3 - W_1$ and $\Delta E = W_3 - W_2$ (see eqs. 5.54, 5.55 and 5.56). By convention, D_Z was taken to be the value with the smaller magnitude and D_Y those with the larger magnitude.

If the magnetic field is on the X -direction we obtain

$$W_1 = -\frac{D - 3E}{6} - \left[\frac{(D + E)^2}{4} + (g\beta_e B_X)^2 \right]^{1/2} \quad (5.55a)$$

$$W_2 = -\frac{D - 3E}{6} + \left[\frac{(D + E)^2}{4} + (g\beta_e B_X)^2 \right]^{1/2} \quad (5.55b)$$

$$W_3 = \frac{1}{3}D - E \quad (5.55c)$$

and with the field in the Y -direction we have

$$W_1 = -\frac{D + 3E}{6} - \left[\frac{(D - E)^2}{4} + (g\beta_e B_Y)^2 \right]^{1/2} \quad (5.56a)$$

$$W_2 = -\frac{D + 3E}{6} + \left[\frac{(D - E)^2}{4} + (g\beta_e B_Y)^2 \right]^{1/2} \quad (5.56b)$$

$$W_3 = \frac{1}{3}D + E. \quad (5.56c)$$

Figure 5.7 shows the energy level diagram for the triplet states when the external magnetic field is applied parallel to the principal axes. At zero magnetic field ($B_0 = 0$) the three triplet sublevels are separated due to the dipole-dipole interactions (ZFS). When the external magnetic field is switched on, the separation of the triplet energy levels increases according to the set of eqs. 5.54, 5.55 and 5.56. The energies of the allowed transitions are given by the difference $\Delta E = W_3 - W_1$ and $\Delta E = W_3 - W_2$

for each orientation of the magnetic field, e.g., in the case of B_Z the transition energy equals $\Delta E = [g^2 \beta_e^2 B_Z^2 + E^2]^{1/2} \pm D$. The allowed transitions are determined by the matrix element between the eigenstates of the Hamiltonian of eq. 5.53, when the time-dependent field \vec{B}_1 is applied i.e., $\langle i | \hat{\vec{\mu}} \cdot \vec{B}_1 | j \rangle$.

5.7 Sensitivity of the TR-EPR experiment

For the TR-EPR experiment, the sensitivity is different as compared to the ground-state EPR sensitivity. Starting from eq. 5.30, the spin levels i and j are now the triplet eigenstates of the Hamiltonian $\hat{H}^{\text{Zeeman}} + \hat{H}^{\text{ZFS}}$ (see the previous section). Also, P_i^{ss} and P_j^{ss} are the non equilibrium population probabilities that arise from ISC from the excited singlet state to the excited triplet. The sensitivity formula for the TR-EPR experiment is discussed in detail in section 6.4.4.

CHAPTER 6

Initial-state preparation effects in time-resolved electron paramagnetic resonance experiments

In this chapter we explain in detail a recent experimental observation that the time-resolved electron paramagnetic resonance spectra of an organic molecule for optical excitation within a highly absorbing region of the molecule have similar intensities as the spectra for optical excitation in a non-absorbing region [D. L. Meyer *et al.* J. Phys. Chem. Lett. **8**, 1677 (2017)]. We demonstrate that this phenomenon is due to an initial-state preparation effect of photoexcitation that leads to similar initial populations of triplet states for both optical excitation regions. Due to the low intersystem crossing (ISC) rates, the initial triplet populations are not perturbed on the time scale of the experiment, so they determine the relative intensities of the paramagnetic resonance spectra. The effect is surprising given the weak spin-orbit interactions of organic molecules. Such initial-state preparation effects are likely to occur in systems where the ISC time scales are long compared to the time scale of the experiment.

6.1 Introduction

Time-resolved electron paramagnetic resonance (TR-EPR) spectroscopy is an important experimental probe of spin dynamics in molecular photo-induced processes.^{18,81–84} In the fields of molecular and biomolecular photoexcited charge and exciton transport,¹⁶ TR-EPR spectroscopy is a sensitive probe of the dynamics of excited triplet states that are often involved in photophysical and photochemical pathways such as catalysis, singlet fission coupled to Dexter (triplet) exciton transport and sensing.^{85–88} Using TR-EPR spectroscopy to study excited state dynamics of molecular systems containing metals with large spin-orbit coupling (SOC) interactions, is particularly interesting. The excited electronic states of these systems are mixtures of singlets and triplets,⁸⁹ and the formation of triplet states can take place both initially at the optical photoexcitation step and at later time through ISC events. In such a situation,

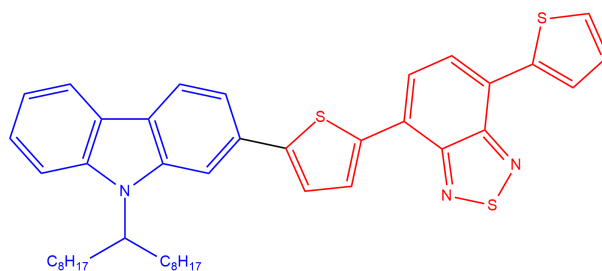


Figure 6.1: Chemical structure of the Cbz-TBT molecule. It consists of a carbazole (Cbz) moiety, which is colored in blue, and a dithiophene-benzothiadiazole (TBT) unit, which is colored in red. TBT moiety is comprised of the 1,2,3-benzothiadiazole (BT) unit surrounded by two thiophene rings.

the interpretation of TR-EPR spectra in terms of models for excited-state dynamics, requires the inclusion of initial-state preparation (non-ISC) effects on the spin dynamics. In this chapter, we demonstrate the potential importance of such effects, even in systems with low SOC such as an organic molecule.

Recently, Meyer *et al.*⁷ performed TR-EPR measurements on the Cbz-TBT molecule (figure 6.1), the repeat unit of the PCDTBT polymer (poly[N-9'-heptadecanyl-2,7-carbazole-alt-5,5,(4',7'-di-2-thienyl-2',1',3',-benzothiadiazole)]).^{90,91} The prominent optical absorption band of Cbz-TBT, the charge transfer (CT) band, is centered at 492 nm with a width (FWHM) of about 100 nm. Beyond 600 nm there is no observable absorption (see figure 6.2). The TR-EPR experiment in ref. 7 probes two types of pathways to the formation of excited triplet states, each type characterized by different optical excitation energies: inside and below the CT band (see figure 2 in ref. 7). For the two excitation regions, the experiment observes TR-EPR spectra having intensities of similar magnitudes. The similarity in the intensities of the TR-EPR spectra for the two types of optical excitations is surprising, given the negligible absorbance of Cbz-TBT beyond 600 nm (below the CT band) as compared to its significant absorbance around 492 nm (inside the CT band), and the weak SOC interactions that are typical of organic molecules.²⁰ Why is there a triplet population (required for a TR-EPR signal) for optical excitation energies in the non-absorbing region, far below the CT band? How can the TR-EPR signal in this region be of similar magnitude to the signal observed when exciting in the highly absorbing region? The main goal is to answer these questions using theoretical models and quantum chemical computations. The experiment in ref. 7, also shows that excitation inside the CT band leads to absorption and emission TR-EPR spectra whose shapes (height and width) do not change for different excitation wavelengths within the band. In contrast, excitation below the CT band, leads to TR-EPR spectra whose shapes differ for each excitation wavelength. A summary of the experimentally derived TR-EPR parameters as a function of optical excitation wavelength is shown in table 6.1. We also propose possible explanations for these observations.

λ_{wav} (nm)	D^{exp} (MHz)	E^{exp} (MHz)	p_1^{exp}	p_2^{exp}	p_3^{exp}	Γ^{exp} (mT)	g_{iso}
492	1361.6 ± 3.0	75.9 ± 1.4	0	0.138	0.862	3.42	2.002
630	1344.7 ± 1.5	77.7 ± 0.7	0	0.098	0.902	2.08	2.002
650	1317.2 ± 1.4	75.0 ± 0.7	0	0.068	0.932	1.83	2.002
680	1288.5 ± 1.3	73.7 ± 0.6	0	0.043	0.957	1.54	2.002

Table 6.1: Experimentally derived zero-field splitting (ZFS) parameters and the relative populations of the zero-field triplet sublevels ($p_1^{\text{exp}}, p_2^{\text{exp}}, p_3^{\text{exp}}$) together with the Lorentzian lineshapes obtained for the different excitation wavelengths (λ_{wav}) inside (492nm) and below (630-680 nm) the CT band. g is the factor of the electron taken to be isotropic ($g_{\text{iso}} = 2.002$). Below the CT band the ZFS parameters are different for different excitation wavelengths, thus, the TR-EPR spectra shapes are different. Inside the CT band, the ZFS parameters are the same for different excitation wavelengths, thus, the TR-EPR spectra shape are the same. For this reason, in the table only the parameters for the excitation at the maximum of the CT band are mentioned. Results were taken from ref. 7.

6.2 Theoretical methods

The total molecular Hamiltonian relevant to a TR-EPR experiment can be written in the molecular frame as

$$\hat{H} = \hat{K} + \hat{H}^{\text{BO}} + \hat{H}^{\text{SOC}} + \hat{H}^{\text{ZFS}} + \hat{H}^{\text{Zeeman}} - \hat{\vec{\mu}} \cdot \vec{E}(t) + \beta_e \hat{B}_1^T(t) \tilde{g} \hat{S} \quad (6.1)$$

where \hat{K} is the nuclear kinetic energy operator of the molecule describing the molecular vibrations, \hat{H}^{BO} is the Born-Oppenheimer Hamiltonian,⁴⁹ \hat{H}^{SOC} is the SOC Hamiltonian⁵³ (see appendix 6.7.1), $\hat{\vec{\mu}}$ is the electric dipole moment operator, $\vec{E}(t)$ is the electric field that optically excites the molecule,⁴³ and $\hat{H}^{\text{Zeeman}} = \beta_e \hat{B}_0^T \tilde{g} \hat{S}$ describes the interaction of the molecule with the static magnetic field \vec{B}_0 , where β_e is the Bohr magneton, \tilde{g} is the anisotropic g-factor (3×3) matrix of the electron and \hat{S} is the total spin operator.⁶⁸ T indicates the transposition of the respective column vector. $\hat{S}^T \tilde{D} \hat{S}$ is the Zero Field Splitting (ZFS) Hamiltonian (describing the magnetic dipole-dipole interactions) and \tilde{D} is the ZFS tensor matrix.^{51,68,69} The term $\beta_e \hat{B}_1^T(t) \tilde{g} \hat{S}$ describes the interaction of the molecule with the time dependent magnetic field $\vec{B}_1(t)$.⁴³ To describe the optical photoexcitation from the ground state to the singlet and triplet excited states taking into account spin-orbit mixing, we consider the part of the Hamiltonian $\hat{K} + \hat{H}^{\text{BO}} + \hat{H}^{\text{SOC}} - \hat{\vec{\mu}} \cdot \vec{E}(t)$. For ISC following photoexcitation, the relevant interactions are $\hat{K} + \hat{H}^{\text{BO}} + \hat{H}^{\text{SOC}}$. For the magnetic resonance spectra, we need to consider $\hat{H}^{\text{SOC}} + \hat{H}^{\text{Zeeman}} + \hat{H}^{\text{ZFS}} + \beta_e \hat{B}_1^T(t) \tilde{g} \hat{S}$.

For the eigenstates of \hat{H}^{BO} , the n -th singlet electronic state of the molecule is denoted as $|S_n\rangle$, and the k -th manifold of the triplet sublevels (in the representation of eigenstates of \hat{S}_z) is denoted as $\{|T_{k,m_s}\rangle\}$ ($m_s = 0, \pm 1$). In the presence of the SOC interactions (\hat{H}^{SOC}), the concept of a pure singlet (triplet) state is not exact

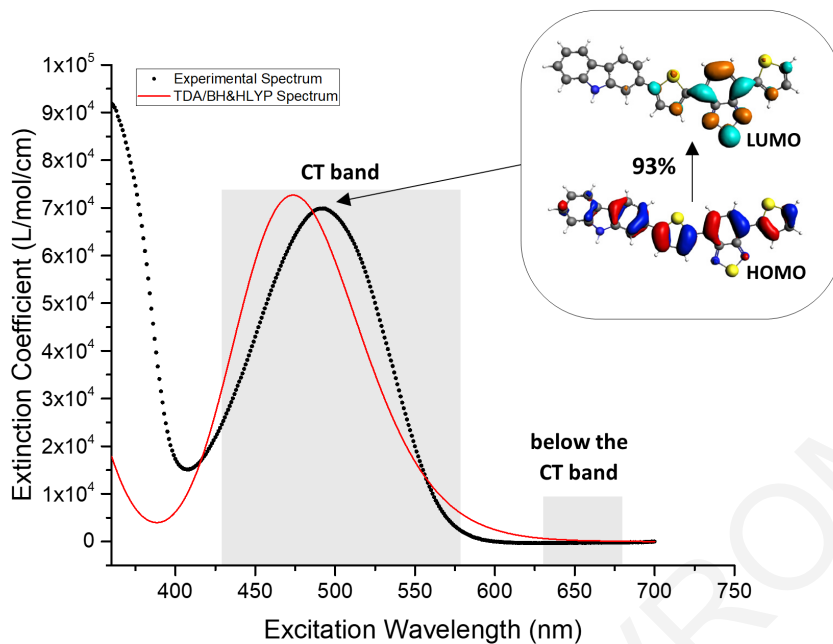


Figure 6.2: Experimental (black dotted line) and calculated (red line) absorption spectrum of the Cbz-TBT molecule. Computations were performed for the most probable geometry (anti_2) at the TDA/BHandHLYP/TZ2P level of theory, and solvent effects were included via COSMO model using the dielectric constant ($\epsilon = 9.8$) for dichlorobenzene. The spectrum is based on a 100 nm FWHM Gaussian broadening of the vertical transition energies and associated oscillator strengths. The CT band is centered at 473 nm (2.62 eV), and it is attributed to the transition $S_0^{\text{SOC}} \rightarrow S_1^{\text{SOC}}$ (or $S_0 \rightarrow S_1$), which is predominantly (93%) assigned to HOMO-LUMO transition. The shade areas show the experimental excitation wavelength ranges inside and outside (below) the CT band.

and states are “mixed”, i.e., the mixed states are eigenstates of $\hat{H}^{\text{BO}} + \hat{H}^{\text{SOC}}$ that are linear combinations of triplets and singlets.⁸⁹ However, for organic molecules, the SOC-induced singlet-triplet mixing is very small compared to pure singlet-triplet energy gaps. Thus, the mixed states are either predominantly singlet or triplet. To describe these weakly-mixed states we may apply perturbation theory with respect to \hat{H}^{SOC} (taking the zeroth-order unperturbed Hamiltonian to be \hat{H}^{BO} and the zeroth-order states to be $|S_n\rangle, |T_{k,m_s}\rangle$).^{55,61,92} We compute the mixed states from exact diagonalization of $\hat{H}^{\text{BO}} + \hat{H}^{\text{SOC}}$, but we use perturbation theory arguments to provide intuitive interpretations of our computational results.

We denote the eigenstates of $\hat{H}^{\text{BO}} + \hat{H}^{\text{SOC}}$ obtained from exact diagonalization, $|S_n^{\text{SOC}}\rangle$ and $|T_{k,\xi}^{\text{SOC}}\rangle$ where k denotes a k -th manifold of three closely spaced sublevels $\xi = A, B, \Gamma$. The notation implies that these eigenstates are either predominantly singlet or predominantly triplet. In particular, we find that each of the of the k -th manifold, is a linear combination of the $|T_{k,m_s}\rangle, m_s = 0, \pm 1$, (of the zeroth-order k -th manifold), where all $C_{m_s}^{(k,\xi)} = \langle T_{k,m_s} | T_{k,\xi}^{\text{SOC}} \rangle$ amplitudes have similar magnitudes, of

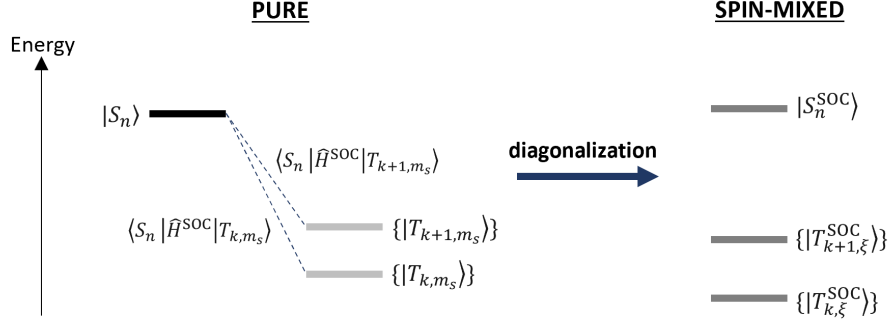


Figure 6.3: *Left:* Pure singlet ($|S_n\rangle$) states (black lines) and pure triplet state manifolds ($\{|T_{k,m_s}\rangle\}$) (light grey lines) coupled by the spin-orbit interactions. *Right:* Spin-mixed states ($|S_n^{\text{SOC}}\rangle$ and $\{|T_{k,\xi}^{\text{SOC}}\rangle\}$, dark grey lines) as linear combinations of pure singlet $|S_n\rangle$ and triplet $|T_{k,m_s}\rangle$ states (equations 6.2 and 6.3).

order of unity^{55,61,92}

$$\begin{aligned}
 |T_{k,\xi}^{\text{SOC}}\rangle \approx & \sum_{m_s=0,\pm 1} C_{m_s}^{(k,\xi)} |T_{k,m_s}\rangle + \sum_n \sum_{m_s=0,\pm 1} C_{m_s}^{(k,\xi)} \left(\frac{\langle S_n | \hat{H}^{\text{SOC}} | T_{k,m_s}\rangle}{E_{T_{k,m_s}} - E_{S_n}} \right) |S_n\rangle \\
 & + \sum_{k'} \sum_{m'_s=0,\pm 1} C_{m'_s}^{(k,\xi)} \left(\frac{\langle T_{k',m'_s} | \hat{H}^{\text{SOC}} | T_{k,m_s}\rangle}{E_{T_{k,m_s}} - E_{T_{k',m'_s}}} \right) |T_{k',m'_s}\rangle.
 \end{aligned} \tag{6.2}$$

There is also weak mixing with zeroth-order singlets $|S_n\rangle$ and other zeroth-order triplet manifolds k', m'_s (second line in eq. 6.2). Similarly, $|S_n^{\text{SOC}}\rangle$ is of predominantly singlet character and can be approximated as

$$|S_n^{\text{SOC}}\rangle \approx |S_n\rangle + \sum_k \sum_{m_s=0,\pm 1} \frac{\langle T_{k,m_s} | \hat{H}^{\text{SOC}} | S_n\rangle}{E_{S_n} - E_{T_{k,m_s}}} |T_{k,m_s}\rangle. \tag{6.3}$$

Equations 6.2 and 6.3 are good approximate descriptions of the mixed states that are obtained by exact diagonalization of the molecular Hamiltonian including \hat{H}^{SOC} (figure 6.3).

Equations 6.2 and 6.3 imply that in a mixed predominantly singlet state $|S_n^{\text{SOC}}\rangle$, there is a small pure triplet-state population i.e., $\sum_k \sum_{m_s} |\langle T_{k,m_s} | S_n^{\text{SOC}}\rangle|^2 \approx \sum_k \sum_{m_s} \left| \frac{\langle T_{k,m_s} | \hat{H}^{\text{SOC}} | S_n\rangle}{E_{S_n} - E_{T_{k,m_s}}} \right|^2$ that is much smaller than unity. Similarly, in a mixed predominantly triplet state $|T_{k,\xi}^{\text{SOC}}\rangle$, there is a small pure singlet-state population i.e., $\sum_n |\langle S_n | T_{k,\xi}^{\text{SOC}}\rangle|^2 \approx \sum_n \sum_{m_s} \left| \frac{C_{m_s}^{(k,\xi)} \langle S_n | \hat{H}^{\text{SOC}} | T_{k,m_s}\rangle}{E_{T_{k,m_s}} - E_{S_n}} \right|^2$.

6.2.1 Direct triplet formation mechanism for excitation energies below the CT band

The experiments measure TR-EPR spectra for excitation energies below the CT band, where there is no significant optical absorption. For these lowest energies, we

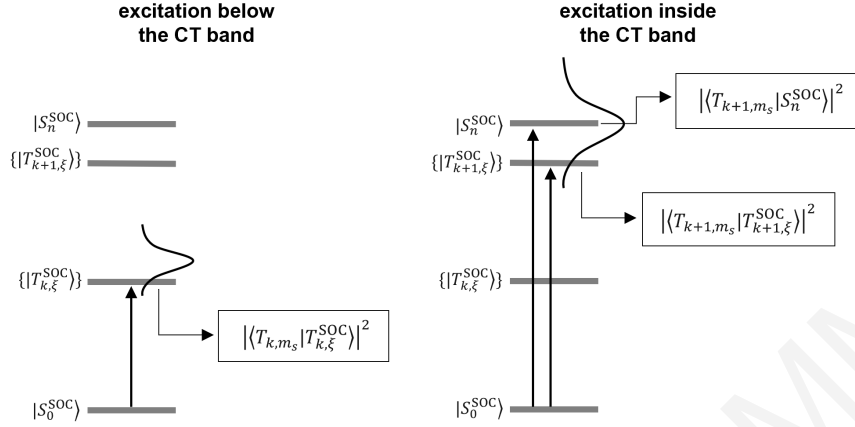


Figure 6.4: Direct mechanism for the formation of triplets. *Left:* Optical excitation at $t = 0$ sec induces transitions from the “mixed” ground state $|S_0^{\text{SOC}}\rangle$ to “mixed” triplet excited states $|T_{k,\xi}^{\text{SOC}}\rangle$ for excitation wavelengths below the CT band. *Right:* Optical excitation at $t=0$ sec induces transitions from the “mixed” ground state $|S_0^{\text{SOC}}\rangle$ to “mixed” singlet $|S_n^{\text{SOC}}\rangle$ and triplet $|T_{k+1,\xi}^{\text{SOC}}\rangle$ excited states for excitation wavelengths inside the CT band. Gaussian line shapes represent the excitation wavelength region below and inside the CT band. Both types of excited states ($|S_n^{\text{SOC}}\rangle$ and $|T_{k,\xi}^{\text{SOC}}\rangle$) have triplet contributions (equations 6.2 and 6.3 and figure 6.3). Thus, photoexcitation creates initial (at $t = 0$ sec) triplet populations $|\langle T_{k,m_s} | S_n^{\text{SOC}} \rangle|^2$ and $|\langle T_{k,m_s} | T_{k,\xi}^{\text{SOC}} \rangle|^2$.

expect that mixed predominantly triplet states of the molecule are accessible. The dipole moment operator $\hat{\mu}$ can directly couple the ground state $|S_0^{\text{SOC}}\rangle$ to $|T_{k,\xi}^{\text{SOC}}\rangle$ via the matrix element (i.e., first order in the \hat{H}^{SOC})^{55,61,93}

$$\begin{aligned} \langle T_{k,\xi}^{\text{SOC}} | \hat{\mu} | S_0^{\text{SOC}} \rangle &\approx \sum_n \sum_m \{C_{m_s}^{(k,\xi)}\}^* \langle S_n | \hat{\mu} | S_0 \rangle \left(\frac{\langle S_n | \hat{H}^{\text{SOC}} | T_{k,m_s} \rangle}{E_{T_{k,m_s}} - E_{S_n}} \right) \\ &+ \sum_{k'} \sum_{m_s} \{C_{m_s}^{(k,\xi)}\}^* \langle T_{k,m_s} | \hat{\mu} | T_{k',m_s} \rangle \left(\frac{\langle T_{k',m_s} | \hat{H}^{\text{SOC}} | S_0 \rangle}{E_{S_0} - E_{T_{k',m_s}}} \right) \end{aligned} \quad (6.4)$$

Equation 6.4 implies that the magnitude of $|\langle T_{k,\xi}^{\text{SOC}} | \hat{\mu} | S_0^{\text{SOC}} \rangle|^2$ is nonzero, although small due to the very weak SOC matrix elements (figure 6.4). Therefore, at low excitation energies, a small number of molecules can be excited to each of the k th manifold sublevels $|T_{k,\xi}^{\text{SOC}}\rangle$. This number of molecules may not be observable as absorption, but it could give a measurable TR-EPR signal since it is a triplet population, i.e., $\sum_{m_s} |\langle T_{k,m_s} | T_{k,\xi}^{\text{SOC}} \rangle|^2 \approx 1$. We will test the hypothesis that optical excitation from the ground state gives directly an initial triplet population that could be observable as a TR-EPR signal. Our computations will show that the hypothesis is consistent with the experiment in ref. 7.

INDIRECT (ISC) MECHANISM

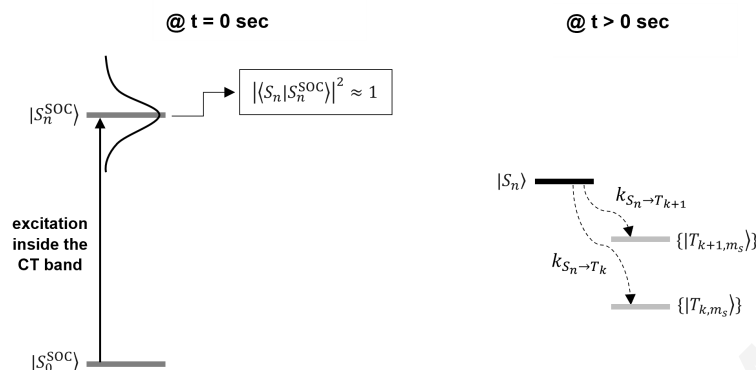


Figure 6.5: Indirect mechanism for the formation of triplets. Optical photoexcitation inside the CT band at $t = 0$ sec creates an initial population of the “mixed” $|S_n^{\text{SOC}}\rangle$ state, which is approximately pure singlet state $|S_n\rangle$. At a later time after photoexcitation, the initial $|S_n\rangle$ population can transform to triplet $|T_{k,m_s}\rangle$ and $|T_{k+1,m_s}\rangle$ population via ISC (rates $k_{S_n \rightarrow T_k}$ and $k_{S_n \rightarrow T_{k+1}}$).

6.2.2 Direct triplet formation mechanism for excitation energies within the CT band

The experiments also measure TR-EPR spectra for excitation energies within the CT band. The CT absorbance is dominated by $|S_n^{\text{SOC}}\rangle$ excited states coupled to the ground state via the transition dipole moment $\langle S_n^{\text{SOC}} | \hat{\mu} | S_0^{\text{SOC}} \rangle \approx \langle S_n | \hat{\mu} | S_0 \rangle$. For each populated $|S_n^{\text{SOC}}\rangle$, there is a probability of measuring a TR-EPR signal since $|\langle T_{k,m_s} | S_n^{\text{SOC}} \rangle|^2 \approx \left| \frac{\langle T_{k,m_s} | \hat{H}^{\text{SOC}} | S_n \rangle}{E_{S_n} - E_{T_{k,m_s}}} \right|^2$ is nonzero (eq. 6.3), albeit small. Therefore, photoexcitation in the CT band may lead to an initial small population of triplet states which are not formed by ISC from an excited singlet. It is also possible that, due to disorder, there exist high energy $|T_{k,\xi}^{\text{SOC}}\rangle$ states within the energy range of the CT band. These states could be directly populated by photoexcitation in the CT band by the mechanism discussed in section 6.2.1 (equation 6.4, figure 6.4). We will approximate the magnitude of both populations using quantum chemical computations. The three types of mechanisms for the creation of initial ($t = 0$) triplet populations upon photoexcitation are summarized in figure 6.4.

6.2.3 Indirect triplet formation mechanism for excitation within the CT band

Photoexcitation within the CT band gives rise to a large initial population of $|S_n^{\text{SOC}}\rangle$ states, which are the main absorbing states in the band and are predominantly of singlet $|S_n\rangle$ character, i.e., $|\langle S_n | S_n^{\text{SOC}} \rangle|^2 \approx 1$ (eq. 6.3). These singlets will produce at a later time after excitation, an additional population of triplets via ISC (figure 6.5). The central question is whether an EPR-observable total triplet population is formed via ISC within the timescale of the TR-EPR experiment. To address this question, we

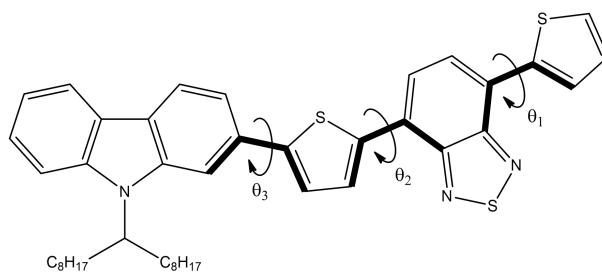


Figure 6.6: Schematic representation of the torsional angles determined along the conjugated backbone. θ_1 , θ_2 and θ_3 are the dihedral angles of the bonds denoted by bold lines.

will compute the ISC rate and the total population of triplets it gives rise to.

6.3 Computational methodology

For the quantum-chemical computations we replaced the long alkyl chains attached to the Nitrogen atom of the Cbz moiety by a Hydrogen atom in order to reduce computational cost. We performed test calculations on the full molecule to show that this replacement does not affect the electronic structure of the relevant singlet and triplet excited states of the Cbz moiety. We used the Amsterdam density functional (ADF) program package⁹⁴ for the computations of ground state⁹⁵ and excited state⁹⁶ geometries and energies, of absorption spectra^{97–99} and SOC integrals¹⁰⁰ and of reorganization energies¹⁰¹ for ISC transition rates. All electronic structure computations did not employ frozen cores nor symmetry constraints.

We computed the optimized geometries of the singlet ground state (S_0) in the gas phase using density functional theory (DFT) at the B3LYP¹⁰² level of theory with the TZ2P basis set.¹⁰³ Subsequently, these optimized geometries were used in single-point energy calculations using BHandHLYP¹⁰⁴ method in conjugation with TZ2P basis set. Our computations showed that Cbz-TBT in its ground state has several minimum energy conformations that are nearly isoenergetic. These conformations are characterized by different values of the twist angles θ_1 , θ_2 and θ_3 as shown in figure 6.6. Figure 6.7 shows the ground state energies of each conformation in eV, together with their optimized structures. The different conformations in figure 6.7 can be viewed as static disorder of the ground state ensemble.

For these ground-state geometries we obtained vertical singlet-singlet and singlet-triplet transition energies, oscillator strengths and molar absorption coefficients for the optical absorption spectra. The latter computations employed DFT in its time-dependent approach (TD-DFT) with the BHandHLYP functional and the TZ2P basis set and applied the Tamm-Dancoff approximation (TDA)¹⁰⁵ with no symmetry constraints and without frozen cores. SOC was included in the TD-DFT/TDA calculation of the excitation energies. In the first step, the spin-pure singlet and triplet ($|S_n\rangle$ and $\{|T_{k,m_s}\rangle\}$) excited states were determined by means of the zeroth-order regular approximated (ZORA) Hamiltonian in its scalar approximation.^{106–108} In the second step, the

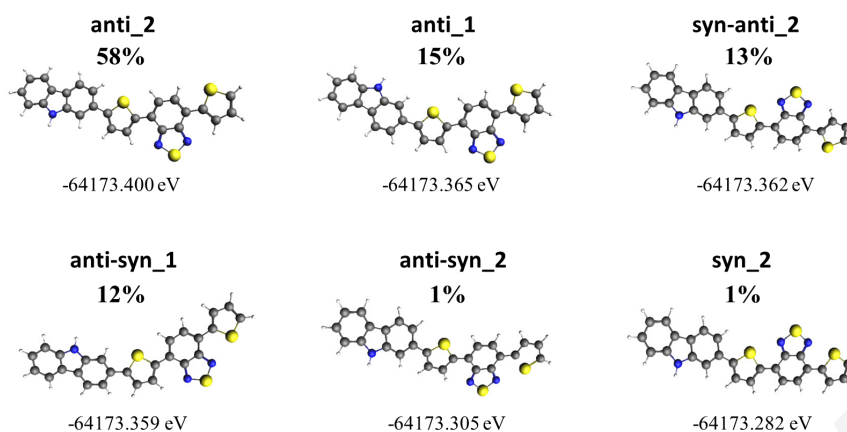


Figure 6.7: Minimum ground-state energy conformations and shorthand notation. anti and syn refer to the orientation of thiophene rings relative to BT (anti if the Sulfur atom of the thiophene ring points upwards relative to BT [$\theta_1 = 0^\circ$ or $\theta_2 = 0^\circ$] and syn if the Sulfur atom of the thiophene ring points downwards relative to BT [$\theta_1 = 180^\circ$ or $\theta_2 = 180^\circ$]). The numbers 1 and 2 refer to the orientation of Nitrogen atom of Cbz moiety with respect to the nearest thiophene unit: 1 if the Nitrogen atom points downwards relative to the Sulfur atom of the nearest thiophene [$\theta_3 = 180^\circ$] and 2 if the Nitrogen atom points upwards relative to the Sulfur atom of the nearest thiophene [$\theta_3 = 0^\circ$]. Percentages refer to the ground state population of relative geometries at room temperature computed according to Boltzmann statistics and energies refer to the total ground state energies computed at BHandHLYP/TZ2P level of theory.

SOC Hamiltonian was applied as a perturbation (pSOC) and the SOC matrix elements between the excited states $|S_n\rangle$ and $\{|T_{k,m_s}\rangle\}$ were computed. On the diagonal, the singlet and triplet energies are added. The mixed spin-orbit coupled excited states $|S_n^{\text{SOC}}\rangle$ and $|T_{k,\xi}^{\text{SOC}}\rangle$ are calculated as linear combinations of the pure states by exact diagonalization of the SOC matrix.¹⁰⁹

The quality of the above-mentioned computations of the excited states can always be tested against the experimental absorption spectrum for the case of singlet excitations (e.g., see figure 6.2). However, the experimental spectrum cannot be used to gauge the quality of the computed triplet excitation energies since these excitations have negligible absorption compared to the singlets. Therefore, we need further tests of our computational results and to this end we also performed additional relativistic pSOC-TD-DFT/TDA computations using another hybrid functional (M062X^{110,111}) and five long-range corrected (LRC) hybrid functionals¹¹² (LCY-BLYP,^{113,114} wB97,¹¹⁵ wB97X,¹¹⁵ wB97X-D,^{116–118} CAMY-B3LYP^{112,119}) with TZ2P basis set. The choice of these functionals required examining the CT character of the lowest-lying excited states of Cbz-TBT molecule, by computing a metric of the electronic excited states. This includes the calculation of the following: (i) the Λ -index developed by Tozer¹²⁰, which is based on the degree of spatial overlap between the occupied and virtual orbitals involved in an excitation, (ii) the Δr -index developed by Adamo¹²¹ which is based on the measure of the average hole-electron distance upon excitation. The combination

of these two diagnostic quantities determines the type of the transition (e.g., local or CT) and their values are associated with the choice of an appropriate functional (see section 6.6.2, figure 6.14 and table 6.4 for all the details). In addition to the use of pSOC-TD-DFT/TDA we also performed configuration interaction singles (CIS) computations using the ORCA-4.0.1 program package¹²² (with def2-TZVP¹²³ basis set). The absolute excitation energies of the triplets, and the energy gaps between them are very similar to those computed with pSOC-TD-DFT/TDA methods. Although CIS methods tend to overestimate the absolute singlet excitation energies, they are known to perform well for triplet excitations.¹²⁴

We used the most probable ground-state geometries in figure 6.7 as starting points for geometry optimizations in the lowest singlet and the triplet excited state manifolds (S_1, T_1, T_2) using TD-DFT/TDA with the BHandHLYP functional and the TZ2P basis set (see section 6.9.1). We also computed parts of the potential energy surfaces (PES) of T_1 for different values of inter-ring torsional coordinates (via geometry optimizations at constrained values of θ_1 and θ_2 in the range $0^\circ \leq \theta_n \leq 180^\circ$ with $n = 1, 2$).

For the computations of the reorganization energies for ISC transitions, we first diagonalized the mass-weighted Hessian matrix \tilde{H} by $L^T \tilde{H} L = \omega^2$ on the optimized excited electronic structures to obtain the frequencies (where L denotes the eigenvectors and ω the eigenvalues).^{125,126} Then, we used the FCF (Frank-Condon factors) auxiliary program as implemented in ADF to compute normal modes and reorganization energies for each normal mode.^{127,128} All computations employed the BHandHLYP functional and TZ2P basis set with the TDA.

The EPR computations for the g-tensor in $\hat{H}^{\text{Zeeman}} = \beta_e \hat{B}_0^T \hat{g} \hat{S}$ in eq. 6.1 were performed at the optimized geometry of the first triplet excited state (T_1) using the “eprnmr” module of ORCA-4.0.1 in combination with the B3LYP functional¹²⁹ and the def2-TZVP basis set. Finally, the D-tensor in $\hat{H}^{\text{ZFS}} = \hat{S}^T \tilde{D} \hat{S}$ of eq. 6.1 and the corresponding ZFS parameters (D and E values) of the T_1 manifold were computed using the spin-unrestricted natural orbital (UNO) approach⁹³ of the ORCA 4.0.1 program package (with the B3LYP functional and def2-TZVP basis set). We calculated TR-EPR ZFS parameters where only the spin-spin contribution to the ZFS parameter D was considered.¹³⁰ The parameters were also computed using improved densities according to the Distributed Point-Dipole (DPD) model as described in ref. 131. The molecular orbital contributions to the triplet excited states (T_1) were written in the basis of the atomic orbitals and the coefficients of the linear combinations were used to predict the spin-density matrix and the “gross” spin populations. The orbitals were extracted by *ab-initio* using ADF with the BHandHLYP/TZ2P method at the optimized geometries of the triplet excited states.

6.4 Results and discussion

Our computations showed that Cbz-TBT in its ground state has several minimum energy conformations that are nearly isoenergetic (figure 6.7). These conformations are characterized by different values of the twist angles θ_1, θ_2 and θ_3 . We estimated the fraction of molecules in the ground state ensemble for each conformation i , given by $\frac{P_i}{P} = e^{\varepsilon_i/K_B T} / \sum_{j=1}^M e^{-\varepsilon_j/K_B T}$, where P is the total number of molecules, M is the total number of minimum energy conformations, K_B is the Boltzmann constant, T is the temperature and ε_i is the energy gap between the lowest energy ground state conformation and conformation i . Figure 6.7 shows the ground state energies of each conformation together with their optimized structures and their Boltzmann population fractions. According to our computations, the anti_2 conformation is the energetically most favorable structure which is found in 58% of molecules in the sample. This result is in accordance with the literature.^{132,133} The vertical excitation energy computations described below are for the most stable ground-state geometry (anti_2). Computations for the other geometries in figure 6.7 are described in the appendix 6.5.

The experimental optical spectrum of the molecule in the *o*-dichlorobenzene solvent consists of two main peaks centered at 492 nm (CT band) and 350 nm respectively (i.e., see Meyer *et al.* ref. 7 and figure S5 in their supporting info). We simulated the UV/VIS absorption spectrum of the molecule in the *o*-dichlorobenzene solvent using the COSMO (Conductor Screening Model)¹³⁴ at the TDA/BHandHLYP/TZ2P level of theory with a dielectric constant $\varepsilon = 9.8$ (for dichlorobenzene). Our simulations agree very well with the experimental observations of the lowest energy excitations which are relevant to this experiment. We also find two main peaks for the absorption spectrum, the lowest energy peak centered at 473 nm (CT band attributed to the transition $S_0 \rightarrow S_1$).¹³⁵ The maximum absorption coefficient of the CT band given by the TD-DFT computations is similar to the experimental value which is of the order of $10^5 \text{ L} \cdot \text{mol}^{-1} \cdot \text{cm}^{-1}$ but slightly blue-shifted (~ 19 nm difference, 0.1 eV)⁷ [see figure 6.2].

The lowest absorption (CT) band peak is attributed to the transition $S_0^{\text{SOC}} \rightarrow S_1^{\text{SOC}}$ (approximately $S_0 \rightarrow S_1$). This transition is predominantly (93%) HOMO \rightarrow LUMO. The electron density of the LUMO orbital is largely localized on the central BT unit and the electron density of the HOMO orbital is mostly localized on the backbone (excluding thiadiazole ring). Thus, the $S_0 \rightarrow S_1$ transition involves a CT excitation with a redistribution of electron density from the conjugated backbone of the molecule toward the central BT unit (CT band).

The energy level diagram with the singlet and triplet states of the molecule is shown in figure 6.8 together with the experimental excitation wavelengths for optical excitations outside and inside the CT band. The results indicate that the first ($\{|T_{1,\xi}^{\text{SOC}}\}$) and second ($\{|T_{2,\xi}^{\text{SOC}}\}$) manifolds (excitation energies of 1.65 eV and 2.65

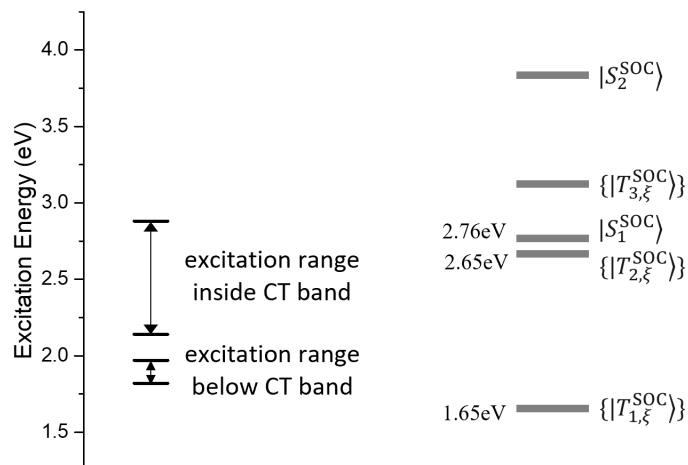


Figure 6.8: Energy level diagram of Cbz-TBT molecule in its anti₂ geometry calculated at the TDA/BHandHLYP/TZ2P level of theory. Thick dark grey lines represent the computed spin-orbit coupled excited state energies with respect to the ground state energy. Thin black lines represent the experimental optical excitation energy regions for the TR-EPR experiment (2.14 eV - 2.88 eV for photoexcitation inside the CT band and 1.82 eV - 1.97 eV for photoexcitation below the CT band).

eV respectively) lie below the first $|S_1^{\text{SOC}}\rangle$ excited state (2.76 eV). $\{|T_{1,\xi}^{\text{SOC}}\rangle\}$ has very low energy compared to the other excited states and it is the only manifold whose vibrational energy spectrum lies in the energy region of the experimental excitation wavelengths outside the CT band (e.g. 1.82 eV - 1.97 eV). In addition, for the lowest excitation energies within the CT band, only $\{|T_{1,\xi}^{\text{SOC}}\rangle\}$ is accessible, while $|S_1^{\text{SOC}}\rangle$ and $\{|T_{2,\xi}^{\text{SOC}}\rangle\}$ lie in the energy region of higher-energy experimental excitation wavelengths within the CT band.

6.4.1 Direct excitation to triplet excited states from the ground state

Direct excitation below the CT band

The absorption coefficient (absorbance) $a(E)$ at a given photon excitation energy E is given by¹³⁶

$$a(E) = \varepsilon(E)cl, \quad (6.5)$$

where c the concentration of molecules, l is the optical path length and ε is the molar extinction coefficient¹³⁷

$$\varepsilon(E) = \sum_J \varepsilon_J(E) = \sum_J C \frac{1}{\text{FWHM}} f_J e^{-2.77 \left(\frac{E - \Delta E_J}{\text{FWHM}} \right)^2}. \quad (6.6)$$

In equation 6.6, the sum is over transitions to final states $J : S_0^{\text{SOC}} \rightarrow J$. Inside the sum, the band shape for each transition is approximated by a Gaussian function whose full width at half maximum (FWHM) accounts for vibrational and/or solvent induced broadening. $C = \frac{\pi}{2 \ln(10)} \frac{N_A e^2 \hbar}{m_e c \varepsilon_0} 2 \sqrt{\frac{\ln(2)}{\pi}}$ where N_A is Avogadro's constant, e the electron charge, m_e the electron mass, and ε_0 the vacuum permittivity (see section 6.8.2). ΔE_J is the excitation energy (in eV) for the transition to the J th excited state from the ground state S_0^{SOC} . f_J is the corresponding oscillator strength^{61,137}

$$f_J = \frac{8\pi^2(m_e c^2)}{3(hc)^2 e^2} \Delta E_J |\langle \Psi_J | \hat{\mu} | \Psi_i \rangle|^2, \quad (6.7)$$

where, Ψ_i and Ψ_J are the initial (S_0^{SOC}) and final states J of the J th transition, respectively.

To compute the approximate number of molecules that populate the first triplet excited state $|T_{1,\xi}^{\text{SOC}}\rangle$ upon photoexcitation at energy $E_{S_0^{\text{SOC}} \rightarrow T_{1,\xi}^{\text{SOC}}} = \Delta E_{S_0^{\text{SOC}} \rightarrow T_{1,\xi}^{\text{SOC}}}$ we will use the following formula⁴⁷

$$P_{T_{1,\xi}^{\text{SOC}}}(E_{S_0^{\text{SOC}} \rightarrow T_{1,\xi}^{\text{SOC}}}) = I_0 \times \left\{ 1 - 10^{-a_{S_0^{\text{SOC}} \rightarrow T_{1,\xi}^{\text{SOC}}}(E_{S_0^{\text{SOC}} \rightarrow T_{1,\xi}^{\text{SOC}}})} \right\} \times \frac{1}{hc/\lambda_{\text{wav}}}, \quad (6.8)$$

where I_0 is the incident energy and λ_{wav} the excitation wavelength. The quantity $a_{S_0^{\text{SOC}} \rightarrow T_{1,\xi}^{\text{SOC}}}(E_{S_0^{\text{SOC}} \rightarrow T_{1,\xi}^{\text{SOC}}})$ is the absorption coefficient for direct excitation to the triplet excited state $|T_{1,\xi}^{\text{SOC}}\rangle$, i.e.,

$$a_{S_0^{\text{SOC}} \rightarrow T_{1,\xi}^{\text{SOC}}}(E_{S_0^{\text{SOC}} \rightarrow T_{1,\xi}^{\text{SOC}}}) = \varepsilon_{S_0^{\text{SOC}} \rightarrow T_{1,\xi}^{\text{SOC}}}(E_{S_0^{\text{SOC}} \rightarrow T_{1,\xi}^{\text{SOC}}}) cl, \quad (6.9)$$

$\varepsilon_{S_0^{\text{SOC}} \rightarrow T_{1,\xi}^{\text{SOC}}}(E_{S_0^{\text{SOC}} \rightarrow T_{1,\xi}^{\text{SOC}}}) = C \frac{1}{\text{FWHM}} f_{S_0^{\text{SOC}} \rightarrow T_{1,\xi}^{\text{SOC}}}$ is the contribution of the $S_0^{\text{SOC}} \rightarrow T_{1,\xi}^{\text{SOC}}$ transition to the total molar extinction coefficient $\varepsilon(E_{S_0^{\text{SOC}} \rightarrow T_{1,\xi}^{\text{SOC}}})$ at the excitation energy $E_{S_0^{\text{SOC}} \rightarrow T_{1,\xi}^{\text{SOC}}} = \Delta E_{S_0^{\text{SOC}} \rightarrow T_{1,\xi}^{\text{SOC}}}$ of the first triplet excited state $|T_{1,\xi}^{\text{SOC}}\rangle$. The total number of molecules that populate the first triplet excited state manifold is

$$P_{T_1^{\text{SOC}}}(E_{S_0^{\text{SOC}} \rightarrow T_1^{\text{SOC}}}) = \sum_{\xi} P_{T_{1,\xi}^{\text{SOC}}}(E_{S_0^{\text{SOC}} \rightarrow T_{1,\xi}^{\text{SOC}}}). \quad (6.10)$$

Using the program ADF, the extinction coefficient at the maximum of the CT band, $\varepsilon(E_{S_0^{\text{SOC}} \rightarrow S_1^{\text{SOC}}})$, was computed to be in the range $5.90 \times 10^4 - 2.94 \times 10^5 \frac{\text{L}}{\text{mol}\cdot\text{cm}}$ [using broadening parameters FWHM = 0.1 eV - 0.5 eV for the most probable geometry (anti_2)]. This result is in accordance with the experimental one, where the extinction coefficient was measured to be of the order of $10^5 \frac{\text{L}}{\text{mol}\cdot\text{cm}}$ with a fitted band broadening of 0.4 eV - 0.5 eV.⁷ The approximate agreement between experiment and theory indicates that we can use the ADF to approximate $\varepsilon_{S_0^{\text{SOC}} \rightarrow T_{1,\xi}^{\text{SOC}}}(E_{S_0^{\text{SOC}} \rightarrow T_{1,\xi}^{\text{SOC}}})$ in eq. 6.9. We computed $\varepsilon_{S_0^{\text{SOC}} \rightarrow T_{1,\xi}^{\text{SOC}}}(E_{S_0^{\text{SOC}} \rightarrow T_{1,\xi}^{\text{SOC}}})$ for each populated geometry (figure

6.7) and used the computed value in eqs 6.9, 6.8, 6.10 to calculate $P_{T_1^{\text{SOC}}}$. For each conformation, we used the experimental values for c, l and I_0 ⁷ (see section 6.10.2). Adding the $P_{T_1^{\text{SOC}}}(E_{S_0^{\text{SOC}} \rightarrow T_{1,\xi}^{\text{SOC}}})$ of all populated geometries (each multiplied by the geometry probability), we found that the ensemble-average total number of molecules placed in the first triplet excited state via direct excitation at $E_{S_0^{\text{SOC}} \rightarrow T_{1,\xi}^{\text{SOC}}}$ equals to $\bar{P}_{T_1^{\text{SOC}}}(E_{S_0^{\text{SOC}} \rightarrow T_{1,\xi}^{\text{SOC}}}) = (1.3 - 6.5) \times 10^{10}$.

In contrast to conventional cw-EPR spectroscopy with Boltzmann-populated triplet sublevels, in TR-EPR spectroscopy the signal depends on nonequilibrium (polarized) sublevel populations that enhance the signal-to-noise characteristics as compared to conventional EPR. The predicted total initial triplet population, which only involves the 1st triplet manifold, is in the range $10^{10} - 10^{11}$ that is detectable by cw-EPR and is likely detectable by TR-EPR^{18,138} (see section 6.4.4).

Direct excitation inside the CT band

Our computations show that the second triplet excited state lies inside the CT band and it is energetically close to the first singlet excited state (see figure 6.8). Hence, upon photoexcitation at the maximum of the CT band, there will be an initial population in the second triplet excited state $|T_{2,\xi}^{\text{SOC}}\rangle$. A lower bound for this population can be estimated using eq. 6.8 and the relative absorbance to the second triplet excited state, given by

$$a_{S_0^{\text{SOC}} \rightarrow T_{2,\xi}^{\text{SOC}}}(E_{S_0^{\text{SOC}} \rightarrow S_1^{\text{SOC}}}) = \varepsilon_{S_0^{\text{SOC}} \rightarrow T_{2,\xi}^{\text{SOC}}}(E_{S_0^{\text{SOC}} \rightarrow S_1^{\text{SOC}}}) cl, \quad (6.11)$$

$\varepsilon_{S_0^{\text{SOC}} \rightarrow T_{2,\xi}^{\text{SOC}}}(E_{S_0^{\text{SOC}} \rightarrow S_1^{\text{SOC}}}) = C \frac{1}{\text{FWHM}} f_{S_0^{\text{SOC}} \rightarrow T_{2,\xi}^{\text{SOC}}} \exp \left[-2.77 \left(\frac{E_{S_0^{\text{SOC}} \rightarrow S_1^{\text{SOC}}} - \Delta E_{S_0^{\text{SOC}} \rightarrow T_{2,\xi}^{\text{SOC}}}}{\text{FWHM}} \right)^2 \right]$ is the contribution of the $S_0^{\text{SOC}} \rightarrow T_{2,\xi}^{\text{SOC}}$ transition to the total molar extinction coefficient $\varepsilon(E_{S_0^{\text{SOC}} \rightarrow S_1^{\text{SOC}}})$ at the excitation energy of the maximum of the CT band, $E_{S_0^{\text{SOC}} \rightarrow S_1^{\text{SOC}}}$.

To compute the total number of molecules that populate the second triplet excited state manifold at the excitation wavelength of the first singlet excited state, we used eq. 6.8 (but now for $|T_{2,\xi}^{\text{SOC}}\rangle$ state) where we also added the contributions from the most probable conformations (e.g., see eq. 6.10) [see section 6.10.3]. Using broadening parameters $\text{FWHM} = 0.1 \text{ eV} - 0.5 \text{ eV}$, the estimated ensemble-average number equals $\bar{P}_{T_2^{\text{SOC}}}(E_{S_0^{\text{SOC}} \rightarrow S_1^{\text{SOC}}}) = (2.1 - 3.2) \times 10^{11}$. Hence, excitation at the center of the CT band will create an initial population of molecules in the 2nd triplet states that can give a measurable TR-EPR signal^{18,138} (see section 6.4.4).

In the experiment, the TR-EPR signals are detected at different optical excitation wavelengths throughout the CT band, (i.e., 430 nm - 580 nm), that include wavelengths below the CT maximum. The computed energy of $S_0^{\text{SOC}} \rightarrow T_{2,\xi}^{\text{SOC}}$ lies

within this optical excitation range, so we also estimated the initial triplet population for this energy. The absorption coefficient is

$$a_{S_0^{\text{SOC}} \rightarrow T_{2,\xi}^{\text{SOC}}} \left(E_{S_0^{\text{SOC}} \rightarrow T_{2,\xi}^{\text{SOC}}} \right) = \varepsilon_{S_0^{\text{SOC}} \rightarrow T_{2,\xi}^{\text{SOC}}} \left(E_{S_0^{\text{SOC}} \rightarrow T_{2,\xi}^{\text{SOC}}} \right) cl, \quad (6.12)$$

where $\varepsilon_{S_0^{\text{SOC}} \rightarrow T_{2,\xi}^{\text{SOC}}} \left(E_{S_0^{\text{SOC}} \rightarrow T_{2,\xi}^{\text{SOC}}} \right) = C \frac{1}{\text{FWHM}} f_{S_0^{\text{SOC}} \rightarrow T_{2,\xi}^{\text{SOC}}}$ is the contribution of the $S_0^{\text{SOC}} \rightarrow T_{2,\xi}^{\text{SOC}}$ transition to the total molar extinction coefficient $\varepsilon \left(E_{S_0^{\text{SOC}} \rightarrow T_{2,\xi}^{\text{SOC}}} \right)$ at the excitation energy of the second triplet excited state, $E_{S_0^{\text{SOC}} \rightarrow T_{2,\xi}^{\text{SOC}}}$. By using exactly the same procedure as before (eqs. 6.12, 6.8, 6.10 for $|T_{2,\xi}^{\text{SOC}}\rangle$), we estimated that the ensemble-average total number of molecules that directly populate the second triplet excited state at the excitation wavelength of $E_{S_0^{\text{SOC}} \rightarrow T_{2,\xi}^{\text{SOC}}}$ to be $\bar{P}_{T_2^{\text{SOC}}} \left(E_{S_0^{\text{SOC}} \rightarrow T_{2,\xi}^{\text{SOC}}} \right) = 2.4 \times 10^{11} - 1.2 \times 10^{12}$ (see section 6.10.3). In summary, photoexcitation within the CT band creates an initial ($t = 0$ sec) population of molecules in the 2nd triplet excited state. This population is $10^{11} - 10^{12}$ and it is sufficient for a detectable TR-EPR signal (see section 6.4.4).

Within the CT band, the most absorbing state is $|S_1^{\text{SOC}}\rangle$ which is predominantly singlet with a small triplet component (eq. 6.3). The small triplet component could give a TR-EPR signal and for completeness we will also estimate the corresponding triplet population. The maximum number of molecules that populate $|S_1^{\text{SOC}}\rangle$ is⁴⁷

$$P_{S_1^{\text{SOC}}} \left(E_{S_0^{\text{SOC}} \rightarrow S_1^{\text{SOC}}} \right) = I_0 \times \left\{ 1 - 10^{-a_{S_0^{\text{SOC}} \rightarrow S_1^{\text{SOC}}} \left(E_{S_0^{\text{SOC}} \rightarrow S_1^{\text{SOC}}} \right)} \right\} \times \frac{1}{hc/\lambda_{\text{wav}}}. \quad (6.13)$$

For each molecule in state $|S_1^{\text{SOC}}\rangle$, the probability of a measurement that collapses the system to a triplet state is $|\langle T_{k,m_s} | S_1^{\text{SOC}} \rangle|^2 = \frac{\langle T_{k,m_s} | \hat{H}^{\text{SOC}} | S_1 \rangle}{E_{S_1} - E_{T_{k,m_s}}}$. Thus, the number of molecules in $|S_1^{\text{SOC}}\rangle$ that would give a TR-EPR signal right after photoexcitation is,

$$\bar{P}_{S_1^{\text{SOC}}}^{\text{EPR}} = P_{S_1^{\text{SOC}}} \left(E_{S_0^{\text{SOC}} \rightarrow S_1^{\text{SOC}}} \right) \times \sum_k \sum_{m_s} |\langle T_{k,m_s} | S_1^{\text{SOC}} \rangle|^2. \quad (6.14)$$

This number was estimated to be 2.4×10^8 using exact diagonalization of $\hat{H}^{\text{BO}} + \hat{H}^{\text{SOC}}$ to obtain the $|\langle T_{k,m_s} | S_1^{\text{SOC}} \rangle|^2$ values. The number is lower than the population arising by the other direct mechanism described above.

We conclude that upon photoexcitation inside the CT band, the second triplet manifold is directly populated, and its initial population is in the range $10^{11} - 10^{12}$. In contrast, for photoexcitation below the CT band the first triplet manifold is directly populated, because the T_2 manifold is energetically inaccessible. Its initial population is in the range $10^{10} - 10^{11}$. We will show that populations are measurable by TR-EPR in section 6.4.4.^{18,138}

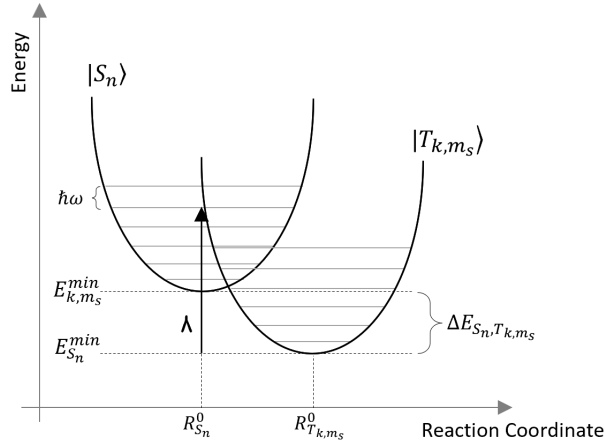


Figure 6.9: Schematic view of the PES of the singlet $|S_n\rangle$ and the triplet $|T_{k,m_s}\rangle$ excited states in the harmonic approximation model, shown for a single vibrational mode of frequency ω . The vibrational energy levels are shown in light gray and their energies differ from each other by $\hbar\omega$. The energy difference between the minimum of $|S_n\rangle$ surface and the minimum of $|T_{k,m_s}\rangle$ surface is $\Delta E_{S_n \rightarrow T_{k,m_s}}$. λ is the mode reorganization energy.

6.4.2 Indirect (ISC) triplet formation mechanism for excitation within the CT band

Excitation within the CT band leads to a high initial population of $|S_1^{\text{SOC}}\rangle$ which is predominantly singlet ($|S_1\rangle$). As time proceeds after photoexcitation, the initial singlet state population may transform to a triplet population via ISC. To gauge this mechanism, we need to compute the ISC rates. For this computation, the relevant component of the Hamiltonian in eq. 6.1 is $\hat{K} + \hat{H}^{\text{BO}} + \hat{H}^{\text{SOC}}$. We may use Fermi's golden rule because the singlet-triplet SOCs are very weak. The ISC rate from $|S_n\rangle$ to $|T_{k,m_s}\rangle$ for a model with one vibrational mode of frequency ω (see chapter 2.2 and figure 6.9) is¹⁰

$$k_{S_n \rightarrow T_{k,m_s}} = \frac{2\pi}{\hbar} |V_{S_n, T_{k,m_s}}|^2 \sum_{n_S} \sum_{n_T} \frac{e^{-E_{n_S}/K_B T}}{Z} |\langle n_S | n_T \rangle|^2 \times \delta \left(E_{S_n}^{\text{min}} + E_{n_S} - (E_{T_{k,m_s}}^{\text{min}} + E_{n_T}) \right) \quad (6.15)$$

In eq. 6.15, $V_{S_n, T_{k,m_s}} = \langle S_n | \hat{H}^{\text{SOC}} | T_{k,m_s} \rangle$ is the SOC matrix element between the $|S_n\rangle$ and $|T_{k,m_s}\rangle$ states and Z is the partition function. $E_{S_n}^{\text{min}}$ and $E_{T_{k,m_s}}^{\text{min}}$ are the energies of the $|S_n\rangle$ and $|T_{k,m_s}\rangle$ states at their minimum-energy molecular geometries (minima of the $|S_n\rangle$ and $|T_{k,m_s}\rangle$ diabatic Born-Oppenheimer surfaces). E_{n_S} and E_{n_T} are the energies of the vibrational levels of the $|S_n\rangle$ and $|T_{k,m_s}\rangle$ diabatic Born-Oppenheimer surfaces, i.e., $E_{n_S(n_T)} = \hbar\omega \left(n_{S(T)} + \frac{1}{2} \right)$.

Eq. 6.15 for the ISC rate can be generalized to a multi-mode form, which may

be written as a Fourier transform of a correlation function computed at the frequency of the energy gap $\Delta E_{S_n, T_{k, m_s}} = E_{S_n}^{min} - E_{T_{k, m_s}}^{min}$ (see chapter 2.2)^{9,34,139}

$$k \left(\frac{\Delta E_{S_n, T_{k, m_s}}}{\hbar} \right) = \frac{|V_{S_n, T_{k, m_s}}|^2}{\hbar^2} e^{-G(0)} \int_{-\infty}^{\infty} dt e^{i \frac{\Delta E_{S_n, T_{k, m_s}}}{\hbar} t - \Gamma |t|} e^{G(t)}. \quad (6.16)$$

In eq. 6.16 Γ is a homogeneous broadening width and

$$G(t) = \sum_{\alpha} \left(\frac{\lambda_{\alpha}}{\hbar \omega_{\alpha}} \right) \{ (2 \langle n_{\alpha} \rangle + 1) \cos(\omega_{\alpha} t) - i \sin(\omega_{\alpha} t) \}, \quad (6.17)$$

where the summation is over the normal modes α of the system of frequencies ω_{α} , λ_{α} is the reorganization energy of mode α and $\langle n_{\alpha} \rangle = (e^{\hbar \omega_{\alpha} / K_B T} - 1)^{-1}$, the thermal average of the phonon occupation number n_{α} at temperature T .

To implement eqs. 6.15 and 6.17 we computed the normal mode parameters at the TD-DFT level using geometry optimization for $|S_1\rangle$ and $|T_{k, m_s}\rangle$ for the most probable conformation anti_2 (as described in section 6.11). Subsequently, using the FCF module of ADF we extracted the electron-phonon coupling parameters $\bar{\lambda}_{\alpha} = (\frac{\omega_{\alpha}}{2\hbar})^{1/2} \vec{k}_{\alpha}$, where \vec{k}_{α} is the vector of equilibrium-position displacements of all atoms for the transition $S_1 \rightarrow T_{k, m_s}$ and for the normal mode α .^{127,128} $\bar{\lambda}_{\alpha}$ is directly related to the mode reorganization energy via $\lambda_{\alpha} = \hbar \omega_{\alpha} \bar{\lambda}_{\alpha}^2$.¹⁰¹ We wrote a MATLAB program that uses these computed parameters to calculate the ISC rates via eqs. 6.15 and 6.17. In our calculations $\Gamma = 10^{12} \text{ sec}^{-1}$, which corresponds to a typical vibrational relaxation rate of a picosecond.

To understand how the ISC mechanism affects the TR-EPR signal we need to compute the population transfer via ISC (as a function of time) from the first singlet state to the two lowest-energy triplet excited states. To this end we solve the following approximate kinetic equations for total populations⁴²

$$\begin{aligned} \frac{dP_{S_1}}{dt} &= -(k_{S_1 \rightarrow T_2} + k_{S_1 \rightarrow S_0} + k_{S_1 \rightarrow T_1}) P_{S_1} + k_{T_2 \rightarrow S_1} P_{T_2} + k_{T_1 \rightarrow S_1} P_{T_1} \\ \frac{dP_{T_2}}{dt} &= k_{S_1 \rightarrow T_2} P_{S_1} - (k_{T_2 \rightarrow S_1} + k_{T_2 \rightarrow T_1} + k_{T_2 \rightarrow S_0}) P_{T_2} + k_{T_1 \rightarrow T_2} P_{T_1} \\ \frac{dP_{T_1}}{dt} &= k_{S_1 \rightarrow T_1} P_{S_1} + k_{T_2 \rightarrow T_1} P_{T_2} - (k_{T_1 \rightarrow T_2} + k_{T_1 \rightarrow S_1} + k_{T_1 \rightarrow S_0}) P_{T_1}. \end{aligned} \quad (6.18)$$

Apart from the ISC rates, these equations include fluorescence and phosphorescence rates as well as transition rates between the triplet manifolds, e.g. $k_{T_2 \rightarrow T_1}$ and $k_{T_1 \rightarrow T_2}$. These triplet-to-triplet rates are induced by the SOC interaction and are computed using the methodology of equations 6.16 and 6.17 and pSOC-TD-DFT/TDA computations. In the rate eqs. 6.16 and 6.17, $P_{T_2} = \sum_{m_s} P_{T_2, m_s}$ and $P_{T_1} = \sum_{m_s} P_{T_1, m_s}$. The total rates are defined as follows, $k_{S_1 \rightarrow T_k} = \sum_{m_s} k_{S_1 \rightarrow T_{k, m_s}}$ for $k = 1, 2$ and $k_{T_2 \rightarrow T_1} = \sum_{m_s} \sum_{m_s'} k_{T_{2, m_s} \rightarrow T_{1, m_s'}}$. The total $S_1 \rightarrow T_1$ and $S_1 \rightarrow T_2$ ISC rates are $k_{S_1 \rightarrow T_1} = 1.77 \times 10^1 \text{ sec}^{-1}$ with $\Delta E_{S_1, T_{1, m_s}} = 1.23 \text{ eV}$ and $k_{S_1 \rightarrow T_2} = 4.00 \times 10^3 \text{ sec}^{-1}$

with $\Delta E_{S_1, T_2, m_s} = 0.16$ eV (for the SOC value at the minimum-energy geometry of S_1). The total $T_2 \rightarrow T_1$ rate is $k_{T_2 \rightarrow T_1} = 7.63 \times 10^3 \text{ sec}^{-1}$ with $\Delta E_{T_2, m_s, T_1, m_s} = 1.07$ eV (SOC value at the minimum-energy geometry of T_2). The backward rates are given by, $k_{f \rightarrow i} = k_{i \rightarrow f} e^{-\Delta E_{if}/K_B T}$.

The fluorescence rate $k_{S_1 \rightarrow S_0}$ as well as the total phosphorescence rates $k_{T_2 \rightarrow S_0}$ and $k_{T_1 \rightarrow S_0}$, were estimated from the fluorescence and phosphorescence lifetimes (τ_J) as computed by ADF, using the respective oscillator strengths f_J of the vertical transitions $S_0^{\text{SOC}} \rightarrow J$ at the minimum energy conformation of J , where J is S_1^{SOC} , $T_{1,\xi}^{\text{SOC}}$ and $T_{2,\xi}^{\text{SOC}}$. For each excitation, the radiative lifetimes are related to the respective oscillator strengths via the following equation¹⁴⁰

$$\frac{1}{\tau_J} = \frac{2\Delta E_J^2 f_J}{c^3}, \quad (6.19)$$

where c is the speed of light and ΔE_J is the excitation energy for the transition to the J th excited state from the ground state S_0^{SOC} . All the quantities in eq. 6.19 are in atomic units (a.u.). The estimated fluorescence rate is $k_{S_1 \rightarrow S_0} = 2.78 \times 10^8 \text{ sec}^{-1}$, in accordance with previous experimental measurements (e.g., see refs. 141–143), and the estimated phosphorescence rates are $k_{T_2 \rightarrow S_0} = \sum_{m_s} k_{T_2, m_s \rightarrow S_0} = 2.47 \text{ sec}^{-1}$ and $k_{T_1 \rightarrow S_0} = \sum_{m_s} k_{T_1, m_s \rightarrow S_0} = 6.41 \times 10^{-2} \text{ sec}^{-1}$, which are typical for organic molecules (e.g., see ref. 19).

In solving eq. 6.18, we set $P_{T_1}(t=0) = 0$, $P_{T_2}(t=0) = (6.3 \times 10^9 - 5.3 \times 10^{10})$, the total population that comes from the direct photoexcitation inside the CT band (computed as described in sections 6.4.1 and 6.10.3) and $P_{S_1}(t=0) = 1.3 \times 10^{15}$, the population transfer to the first singlet excited state upon photoexcitation to the CT band (see section 6.10.4), both of them only for the most probable geometry, anti-2.

Figure 6.10 shows a representative plot of the populations as a function of time for the total T_1, T_2 populations using the initial conditions for $t = 0$ sec mentioned above. The experimental time that passes between photoexcitation and triplet signal observation is approximately $0.5 \mu\text{sec}$.⁷ We checked the population transfer within the experimental time scale as well as for larger time scales. The initial total T_2 populations ($\sim 10^{10}$ molecules which is measurable by EPR) slightly increases within a μsec and retains measurable values for approximately 0.2 - 0.3 msec. The total T_1 population increases to measurable values ($\sim 10^{10}$ molecules) after approximately 10 - 30 μsec . The ranges in time scales are due to the range of initial T_2 populations (see section 6.4.1).

The above results show that, although ISC from the lowest singlet excited state generates triplet state population after photoexcitation within the CT band, this population is not much greater than the initial triplet state population that is formed directly by absorption from the ground state (as described in the previous sections). This trend is also observed from our computations using other starting geometries other

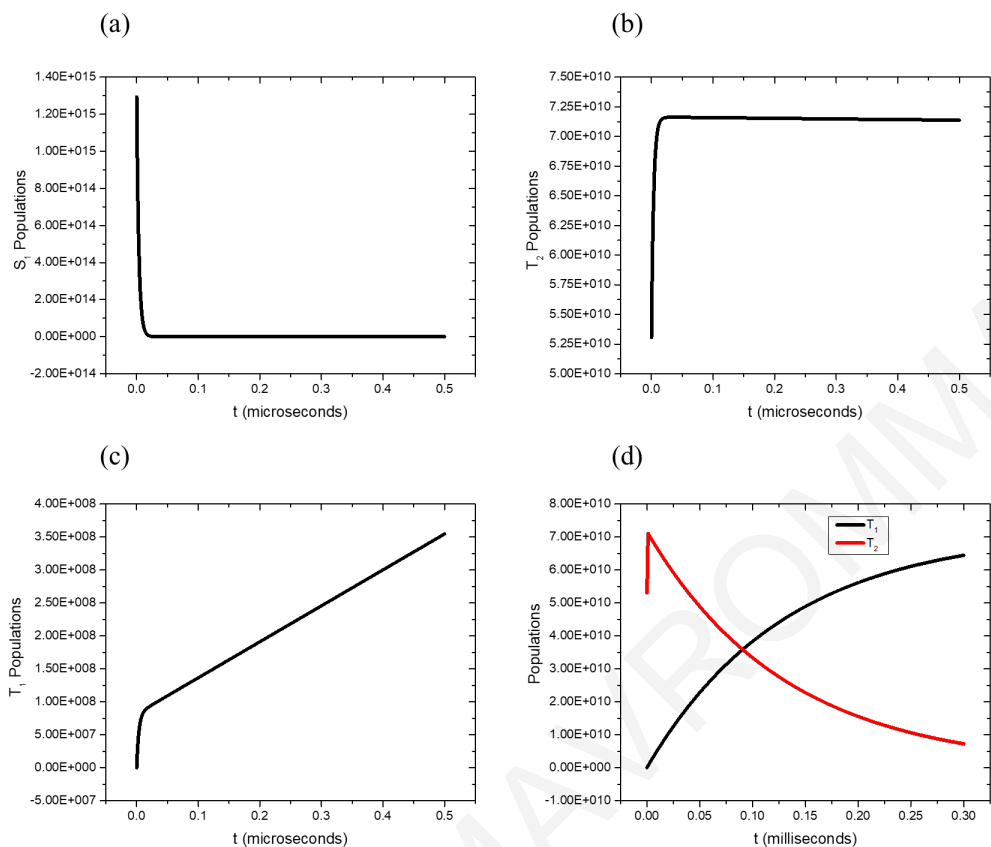


Figure 6.10: Population transfer to the first and second triplet excited states as a function of time. (a) Population of S_1 from 0 to 0.5 μsec . (b) Population transfer to T_2 from 0 to 0.5 μsec . (c) Population transfer to T_1 from 0 to 0.5 μsec and (d) population transfer to T_2 and T_1 for larger time scales than 0.5 μsec , namely from 0 to 0.3 msec. Initial condition for T_2 : $P_{T_2}(t=0) = 5.3 \times 10^{10}$.

than anti_2 (see section 6.9.2).

The results of sections 6.4.1 and 6.4.2 suggest a plausible explanation of the observation in ref. 7 that photoexcitation in the highly-absorbing CT band region gives a TR-EPR signal of approximately the same intensity as the TR-EPR signal for photoexcitation in the non-absorbing region, below the CT band. Both types of photoexcitations lead to similar initial populations of triplet states. Due to the very low ISC rates, on the time scale of the TR-EPR experiment, there is no substantial increase in the total triplet state population arising from the lowest singlet state following the excitation in the CT band.¹⁴⁴ Therefore, the initial triplet populations largely determine the TR-EPR signal strength for both excitation regions. In section 6.4.4 below, we demonstrated that these initial populations are sufficient for the observation of a TR-EPR signal.

6.4.3 Triplet state formation mechanism in the ground state

The above SOC induced mechanism suggests that triplet EPR signal could also be observed in the ground state, which is predominantly singlet with a small

triplet contribution (e.g., eq. 6.3). For each molecule in the ground state $|S_0^{\text{SOC}}\rangle$, the probability of a measurement that collapses the system to a triplet state $|T_{k,m_s}\rangle$ is $|\langle T_{k,m_s}|S_0^{\text{SOC}}\rangle|^2 = \left| \frac{\langle T_{k,m_s}|\hat{H}^{\text{SOC}}|S_0\rangle}{E_{S_0} - E_{T_{k,m_s}}} \right|^2$. Thus, the number of molecules in $|S_0^{\text{SOC}}\rangle$ that would give a conventional cw-EPR signal is given by

$$\bar{P}_{S_0^{\text{SOC}}}^{\text{EPR}} = P_{S_0^{\text{SOC}}} \times \sum_k \sum_{m_s} |\langle T_{k,m_s}|S_0^{\text{SOC}}\rangle|^2, \quad (6.20)$$

where $P_{S_0^{\text{SOC}}}$ is the total number of molecules in the ground state for each minimum-energy conformation (see section 6.10.1). We used full diagonalization of $\hat{H}^{\text{BO}} + \hat{H}^{\text{SOC}}$ to estimate the coefficients $\langle T_{k,m_s}|S_0^{\text{SOC}}\rangle$. The ensemble-average total triplet population from the mixed $|S_0^{\text{SOC}}\rangle$ ground state is computed to be 8.7×10^9 . This number is in the limits of the sensitivity of EPR spectroscopy without field modulation¹³⁸ (see section 6.4.4).

6.4.4 Sensitivity analysis

The basic formula for sensitivity analysis of ground-state CW-EPR without field modulation, (since the TR-EPR experiment does not involve field modulation), is based on the ratio of the power absorbed by magnetic resonance in the sample (denoted dW^{gs}/dt , where “gs” denotes ground state), to the power dissipated in the resonant cavity (denoted as P_C),^{70,77}

$$\text{ratio}(N_{\text{tot}}^{gs}) = \frac{dW^{gs}/dt}{P_C} = \frac{k_{i \rightarrow j}(\hbar\omega)N_{\text{tot}}^{gs}(\tilde{\Pi}_i^{gs} - \tilde{\Pi}_j^{gs})}{\frac{1}{Q_0}\omega\frac{B_1^2}{2\mu_0}V_C}. \quad (6.21)$$

In the numerator above, $\frac{dW^{gs}}{dt} = k_{i \rightarrow j}(\hbar\omega)N_{\text{tot}}^{gs}(\tilde{\Pi}_i^{gs} - \tilde{\Pi}_j^{gs})$, where $k_{i \rightarrow j} = \frac{\pi B_1^2}{2\hbar^2} |\mu_{ij}|^2 f(\omega)$ is the rate of transition between levels $|i\rangle$ and $|j\rangle$ induced by the oscillatory magnetic field of amplitude B_1 and frequency ω . N_{tot}^{gs} is the total number of paramagnetic centers in the sample and $\tilde{\Pi}_{i(j)}^{gs} = N_{i(j)}^{gs}/N_{\text{tot}}^{gs}$ are the ground-state fractional populations of the levels (giving rise to spin polarization). $f(\omega) = \Delta\omega/\pi((\omega - \omega_0)^2 + \Delta\omega^2)$ is a Lorentzian lineshape function (with resonance frequency ω_0 and width $\Delta\omega$), and $\mu_{ij} = \langle j|\hat{\mu}|i\rangle = g\beta_e\sqrt{S(S+1)}$ (S for spin) is the magnetic dipole matrix element. In the denominator of the ratio, $P_C = \frac{1}{Q_0}\omega\frac{B_1^2}{2\mu_0}V_C$ is the power dissipated by the cavity, where Q_0 is the quality factor of the unloaded cavity and V_C is its volume. μ_0 is the magnetic permeability constant. In the analysis that leads to the equation for sensitivity, an equivalent circuit represents the generic spectrometer response.⁷⁰ The change in power level of the cavity due to absorption is related to the corresponding voltage response V_{det} in the detector circuit of resistance R_{det} and to the incident power on the resonator P_{inc} , via the equation $\frac{4\delta V_{\text{det}}}{\sqrt{P_{\text{inc}}R_{\text{det}}}} = \text{ratio}(N_{\text{tot}}^{gs})$. Using the equation of the transition rate $k_{i \rightarrow j}$ in eq. 6.21 for the ratio relates δV_{det} to the ab-

sorption rate and thus to the total number of spins N_{tot}^{gs} and the spin polarization. The minimum detectable signal $\delta V_{\text{det}}^{\text{min}}$ is defined as being equal to the detector rms noise voltage, i.e., $\delta V_{\text{det}}^{\text{min}} = V_{\text{rms}}^{\text{noise}} = \sqrt{FR_{\text{det}}K_B T df}$, where df is the bandwidth of the detecting amplifying system and F its noise factor. The minimum detectable signal, thus, determines the minimum detectable number of paramagnetic centers $N_{\text{tot}(gs)}^{\text{min}}$ via the equation $\frac{4V_{\text{rms}}^{\text{noise}}}{\sqrt{P_{\text{inc}}R_{\text{det}}}} = \text{ratio} \left(N_{\text{tot}(gs)}^{\text{min}} \right)$. Assuming resonance, i.e., $f(\omega = \omega_0) = (\pi \Delta\omega)^{-1}$ in eq. 6.21, one gets for the minimum detectable number of paramagnetic centers

$$N_{\text{tot}(gs)}^{\text{min}} \approx \frac{\Gamma V_C}{Q_0 \mu_0 g \beta_e S(S+1) \left(\tilde{\Pi}_i^{gs} - \tilde{\Pi}_j^{gs} \right)} \sqrt{\frac{FK_B T df}{P_{\text{inc}}}}, \quad (6.22)$$

where $g\beta_e\Gamma = \hbar(\Delta\omega)$. For the case of thermal equilibrium (ground state CW-EPR) $\tilde{\Pi}_i^{gs} - \tilde{\Pi}_j^{gs} \approx \hbar\omega_0/(2K_B T)$, and writing $\hbar\omega_0 = g\beta_e B_0$, gives^{68,79,145,146}

$$N_{\text{tot}(gs)}^{\text{min}} \approx \frac{K_B T \Gamma V_C}{\mu_0 g^2 \beta_e^2 S(S+1) B_0 Q_0} \sqrt{\frac{FK_B T df}{P_{\text{inc}}}}. \quad (6.23)$$

This is the approximate equation often quoted as a starting point for CW-EPR sensitivity without field modulation. In the experiment of Meyer *et. al.*⁷ at each value of the scanning magnetic field, the signal is recorded 1000 times and averaged, and all background signal is subtracted. Therefore, the noise level is effectively reduced, with respect to eq. 6.23 by a factor of $1/\sqrt{1000}$, and $N_{\text{tot}(gs)}^{\text{min}}$ above should be replaced by $\bar{N}_{\text{tot}(gs)}^{\text{min}} = \frac{1}{\sqrt{1000}} N_{\text{tot}(gs)}^{\text{min}}$ (this issue is further qualified below). The approximate EPR parameters of the experiment of ref. 7 are $V_C = 2 \times 10^{-7} \text{ m}^3$ (cylindrical cavity of 5 mm diameter and 10 mm height), $T = 80 \text{ K}$, $P_{\text{inc}} = 2 \text{ mW}$, $Q_0 \approx 4000$, $df = \frac{\nu_{\text{res}}}{Q_0} = 2.4 \text{ MHz}$ ($\nu_{\text{res}} = 9.7 \text{ GHz}$ is the resonance frequency), $F = 10 - 100$, $\Gamma \approx 2 \text{ mT}$, and $B_0 = 370 \text{ mT}$ (the latter two are taken from the experimental spectra at the excitation wavelength of $\lambda_{\text{wav}} = 630 \text{ nm}$ ⁷). If the experiment in ref. 7 were ground state CW-EPR without field modulation, $\bar{N}_{\text{tot}(gs)}^{\text{min}} \approx 10^{10} - 10^{11}$ (given the range $F = 10 - 100$).

To adopt this approximate formula to TR-EPR we need to go back to eq. 6.22, replace $N_{\text{tot}(gs)}^{\text{min}}$ by $N_{\text{tot}(ex)}^{\text{min}}$, the number of molecules that are directly excited to the triplet states upon photoexcitation (if there were ISC we would need to include that population too) and replace $\tilde{\Pi}_i^{gs} - \tilde{\Pi}_j^{gs}$ by typical nonequilibrium initial values $\tilde{\Pi}_i^{\text{ex}}(t=0) - \tilde{\Pi}_j^{\text{ex}}(t=0)$ (created by photoexcitation), which we can compute from our *ab-initio* results. Following the same line of argument as above, we arrive at the TR-EPR adapted formula

$$N_{\text{tot}(ex)}^{\text{min}} \approx \frac{\Gamma V_C}{Q_0 \mu_0 g \beta_e S(S+1) \left(\tilde{\Pi}_i^{\text{ex}}(t=0) - \tilde{\Pi}_j^{\text{ex}}(t=0) \right)} \sqrt{\frac{FK_B T df}{P_{\text{inc}}}}, \quad (6.24)$$

where now $N_{\text{tot}(ex)}^{\text{min}}$ refers to the total population of excited triplets, obtained by photoexcitation and observed on the time scale of the TR-EPR experiment, and $\tilde{\Pi}_i^{\text{ex}}(t=$

$0) - \prod_j^{\tilde{ex}} (t=0)$ are typical non-equilibrium (initial) fractional populations of the triplet sublevels prior to equilibration in the triplet manifold. For the experiment of ref. 7, $N_{\text{tot}(ex)}^{\text{min}}$ should be replaced by $\bar{N}_{\text{tot}(ex)}^{\text{min}} = \frac{1}{\sqrt{1000}} N_{\text{tot}(ex)}^{\text{min}}$, as mentioned before. Below, we compute the fractional populations using the oscillator strengths for the singlet-to-triplet transitions computed in section 6.4.1.

The component of the total molecular Hamiltonian (eq. 6.1) that describes the spin components of the electronic states and the interactions with the magnetic fields is given by $\hat{H}^{\text{SOC}} + \hat{H}^{\text{ZFS}} + \hat{H}^{\text{Zeeman}} + \beta_e \vec{B}_1(t)^T \tilde{g} \hat{S}$, where $\hat{H}^{\text{Zeeman}} = \beta_e \vec{B}_0^T \tilde{g} \hat{S}$ and $\hat{H}^{\text{ZFS}} = \hat{S}^T \tilde{D} \hat{S}$. Our computations of the \tilde{g} tensor show it to be highly isotropic with a value of $g = 2.003$, in agreement with the experiment (e.g., see table I and ref. 7). Therefore we can write $\hat{H}^{\text{Zeeman}} = \beta_e \vec{B}_0^T \tilde{g} \hat{S} = g \beta_e \vec{B}_0^T \hat{S}$ and $\beta_e \vec{B}_1^T \tilde{g} \hat{S} = g \beta_e \vec{B}_1^T \hat{S}$, where $g \approx 2$. Furthermore, the computed energy differences between the predominantly three sublevels within each $\{|T_{k,\xi}^{\text{SOC}}\rangle\}$ manifold (the $|T_{k,\xi}^{\text{SOC}}\rangle$ are the eigenstates of $\hat{H}^{\text{BO}} + \hat{H}^{\text{SOC}}$), are three orders of magnitude smaller than the energy difference predicted by diagonalizing $\hat{H}^{\text{SOC}} = \hat{S}^T \tilde{D} \hat{S}$ using the experimentally derived D and E values shown in table 6.1 (10^{-9} eV for SOC versus 10^{-6} eV for ZFS). Thus, within each triplet manifold the spin states at zero magnetic field are determined by the Hamiltonian $\hat{H}^{\text{ZFS}} = \hat{S}^T \tilde{D} \hat{S}$ which is dominant compared to \hat{H}^{SOC} . We denote the eigenstates of $\hat{H}^{\text{ZFS}} + \hat{H}^{\text{Zeeman}}$ for the k th triplet manifold $\{|T_{k,i}\rangle\}$, $i = l, c, u$ (lower, center, upper) [see section 5.6]. These are the absorptive and emissive states of the EPR component of the TR-EPR experiment for the particular manifold. To estimate the population transfer upon photoexcitation to these triplet sublevels ($\{|T_{k,i}\rangle\}$, $i = l, c, u$), we should first calculate the oscillator strengths for the transitions $S_0^{\text{SOC}} \rightarrow T_{k,i}$ following the procedure described in section 6.4.1. To this end, we write the eigenstates $|T_{k,i}\rangle$ in the basis of the $\{|T_{k,\xi}^{\text{SOC}}\rangle\}$ states,

$$|T_{k,i}\rangle = \sum_{\xi} |T_{k,\xi}^{\text{SOC}}\rangle \langle T_{k,\xi}^{\text{SOC}} | T_{k,i}\rangle. \quad (6.25)$$

Since the oscillator strength for the transition $S_0^{\text{SOC}} \rightarrow T_{k,i}$ is related to the squared transition dipole moment $|\langle S_0^{\text{SOC}} | \hat{\mu} | T_{k,i}\rangle|^2 \approx \sum_{\xi} |\langle T_{k,\xi}^{\text{SOC}} | T_{k,i}\rangle|^2 |\langle S_0^{\text{SOC}} | \hat{\mu} | T_{k,\xi}^{\text{SOC}}\rangle|^2$ via eq. 6.7, its value can be given using the calculated oscillator strengths of the transitions $S_0^{\text{SOC}} \rightarrow T_{k,\xi}^{\text{SOC}}$ ($f_{S_0^{\text{SOC}} \rightarrow T_{k,\xi}^{\text{SOC}}}$) as follows:

$$f_{S_0^{\text{SOC}} \rightarrow T_{k,i}} \approx \sum_{\xi} |\langle T_{k,\xi}^{\text{SOC}} | T_{k,i}\rangle|^2 f_{S_0^{\text{SOC}} \rightarrow T_{k,\xi}^{\text{SOC}}} \quad (6.26)$$

The initial population transfer to the $\{|T_{k,i}\rangle\}$ manifold following photoexcitation is calculated according to eq. 6.8.

We used the EasySpin software package¹⁴⁷ available for MATLAB to compute the TR-EPR resonance field positions for absorption and emission with the field vector aligned with the D -tensor axes (the principal axis system X, Y, Z). We used the

routine “eigfields”. Parameters included were the isotropic g value and the experimental ZFS parameters for the excitation wavelength $\lambda_{\text{wav}} = 630$ nm (below the CT band) ($D = 1345$ MHz, $E = 78$ MHz). For each value of the computed resonance fields ($\vec{B}_0||X$, $\vec{B}_0||Y$, $\vec{B}_0||Z$), we calculated the matrix elements of the Hamiltonian $\hat{H}^{\text{Zeeman}} + \hat{H}^{\text{ZFS}}$ using the routine “sham”. The diagonalization of this Hamiltonian matrix gives the eigenstates $|T_{k,l}\rangle$, $|T_{k,c}\rangle$ and $|T_{k,u}\rangle$. From these computations, we obtain the relative fractional populations that should be inserted in eq. 6.24, i.e., $\tilde{\Pi}_i^{\text{ex}}(t=0) = \frac{P_{S_0^{\text{SOC}} \rightarrow T_{k,i}}}{\sum_{i=l,c,u} P_{S_0^{\text{SOC}} \rightarrow T_{k,i}}}$. The computed values of $\tilde{\Pi}_i^{\text{ex}}(t=0) - \tilde{\Pi}_j^{\text{ex}}(t=0)$ are typically 0.3-0.7 (see section 6.10.5 for the reproduction of the experimental TR-EPR spectra). Using these polarizations together with the above-mentioned experimental parameters of ref. 7 in eq. 6.24, we obtain $\bar{N}_{\text{tot}(\text{ex})}^{\text{min}} \approx 10^9 - 10^{10}$ (the range arising from $F = 10 - 100$). This minimum number of spins is below our estimated number of excited triplet states ($10^{10} - 10^{12}$).

The second approach to computing the sensitivity, better approximates the experimental procedure. In the experiment, for a given static magnetic field and in the presence of a weak perpendicular time-dependent magnetic field (magnitude denoted as B_1), the ensemble is photoexcited ($t = 0$) and the time evolution of the EPR absorption or emission is recorded. This procedure is repeated 1000 times and an average time-dependent signal is derived (and background signal is subtracted). The resulting time-dependent signal rises and decays within 1-2 μs after the laser flash reaching maximum in approximately half a microsecond. It is then time averaged over 200 ns centered around 500 ns (which corresponds to the maximum-signal time). The procedure is then repeated for another value of the time-independent magnetic field value.⁷

Since the reported intensities at a given static magnetic field are time averages of the time-dependent absorption (emission) intensity, it follows that $\tilde{\Pi}_i^{\text{ex}}(t=0) - \tilde{\Pi}_j^{\text{ex}}(t=0)$ in eq. 6.24 should be replaced by a time average $\langle \tilde{\Pi}_i^{\text{ex}}(t) - \tilde{\Pi}_j^{\text{ex}}(t) \rangle$. To approximate this time average for the case of a resonant field (e.g., maximum absorption or emission) we use the Bloch equation in the rotating wave approximation (RWA).⁴³ As we have shown from the rate computations, after initial excitation, there is no exchange in populations between the different excited triplet manifolds and no ISC or phosphorescence on the time scale of the experiment. Therefore, the Bloch equation should describe only spin relaxation within a triplet manifold that leads to intramanifold thermal equilibration following the non-equilibrium initial polarization (a discussion of this regime is given in ref. 144). Thus, we solve for the time evolution of a three-sublevel density matrix $\sigma_{i,j}(t)$ in the basis of the $\hat{H}^{\text{ZFS}} + \hat{H}^{\text{Zeeman}}$ eigenstates computed using EasySpin (i.e., $\{|T_{k,i}\rangle\}$, $i = l, c, u$). We solve the Liouville equation $\frac{d}{dt}\vec{\sigma}(t) = \tilde{L}^{\text{RWA}}\vec{\sigma}(t)$, where $\vec{\sigma}(t)$ is the density matrix vector (9×1) and \tilde{L}^{RWA} is the Bloch equation Liouvillian (9×9)⁹

$$\begin{aligned}
\frac{d}{dt}\sigma_{i,i}(t) &= -i \sum_{k \neq i} \{ (H_{i,k}/\hbar)\sigma_{k,i}(t) - (H_{k,j}/\hbar)\sigma_{i,k}(t) \} \\
&\quad + \sum_{k \neq i} \Gamma_{i,k}\sigma_{k,k}(t) - \Gamma_{i,i}\sigma_{i,i}(t) \\
\Gamma_{i,i} &= \sum_{k \neq i} \Gamma_{i,k},
\end{aligned} \tag{6.27}$$

$$\begin{aligned}
\frac{d}{dt}\sigma_{i,j}(t) &= -i\Delta_{i,j}\sigma_{i,j}(t) - i(H_{i,j}/\hbar) \{ \sigma_{j,j}(t) - \sigma_{i,i}(t) \} \\
&\quad - i \sum_{k \neq j} (H_{i,k}/\hbar)\sigma_{k,j}(t) + i \sum_{k \neq i} (H_{k,j}/\hbar)\sigma_{i,k}(t) \\
&\quad - \left\{ \frac{1}{2} \left(\Gamma_{i,i} + \Gamma_{j,j} + \Gamma_{i,j}^{\text{deph}} \right) \right\} \sigma_{i,j}(t) \\
\Delta_{i,j} &= (E_i - E_j)/\hbar - \omega.
\end{aligned}$$

In the equations above, ω corresponds to the resonance frequency (9.7 GHz), $E_{i(j)}$ are the eigenenergies of $\hat{H}^{\text{Zeeman}} + \hat{H}^{\text{ZFS}}$, and $H_{i,j} = \langle i | \frac{g\beta_e}{2} \vec{B}_1^T \hat{S} | j \rangle$ are half of the off-diagonal matrix elements of the perturbing Hamiltonian $g\beta_e \vec{B}_1^T \hat{S}$. These matrix elements are computed using the EasySpin derived eigenstates in conjunction with experimental parameters. For example, for the case of $\vec{B}_0 || Z$, where $\vec{B}_1 || X$, the matrix elements are equal to $H_{i,j} = \frac{g\beta_e}{2} B_1 \langle i | \hat{S}_X | j \rangle$. We used the routine “resfreqs_matrix” that computes the line intensities $A_{i \rightarrow j}$ associated with the resonance line positions according to $A_{i \rightarrow j} = B_1^2 |\langle i | g\beta_e \hat{S}_X | j \rangle|^2 \left(\tilde{\Pi}_i^{\text{ex}} - \tilde{\Pi}_j^{\text{ex}} \right)$. Using $B_1 = \sqrt{\frac{2\mu_0}{V_C} \frac{\sqrt{P_{\text{inc}}}}{\sqrt{df}}} = 10$ mT and the polarizations $\tilde{\Pi}_{i,(j)}^{\text{ex}}$, we deduced the elements $H_{i,j}$.

The incoherent part of the Liouvillian in eq. 6.27 involves the relaxation rates of populations [$\Gamma_{i,k}$ for $k \rightarrow i$ and of coherences $\Gamma_{i,j}^{\text{coh}} = \frac{1}{2} \left(\Gamma_{i,j} + \Gamma_{j,j} + \Gamma_{i,j}^{\text{deph}} \right)$]. These values are chosen such that the time-dependent polarization signals $\sigma_{i,i}(t) - \sigma_{j,j}(t)$ which gives rise to the time-dependent absorption and emission signals that are of approximately 1-2 μs , as observed to be the gross signal lifetimes in the experiment⁷ (e.g., the values of $\Gamma_{i,i} \approx 0.1$ MHz, $\Gamma_{i,j}^{\text{coh}} \approx 0.4$ MHz give the gross signal lifetimes of discussed in the SI of ref. 7). The population-relaxation rates also satisfy detailed balance at temperature 80 K, i.e., $\Gamma_{i,i}/\Gamma_{j,j} = \exp[-(E_i - E_j)/K_B T]$. The initial density matrix $\vec{\sigma}(t=0)$ is derived from the computed initial populations of $|T_{k,\xi}^{\text{SOC}}\rangle$, $\sum_{\xi} |\langle T_{k,\xi}^{\text{SOC}} | T_{k,i} \rangle|^2$ (we try different initial coherent density matrices consistent with the computed initial polarizations of 0.3-0.7 since we do not know the exact initial state, i.e., the linear superposition of u, c and l). To solve for $\vec{\sigma}(t)$ we compute the eigenstates \vec{V}_k and eigenvalues λ_k of \tilde{L}^{RWA} , which, in Dirac notation give the following time evolutions: $\sigma_{i,j}(t) = \sum_k \langle i, j | V_k \rangle \langle V_k | \sigma(t=0) \rangle \exp(\lambda_k t)$. As expected, one of the eigenvalues is zero (denoted $\lambda_{k=0}$) and the rest have negative real components such that $\exp(\lambda_{k \neq 0} t)$ decays to zero for sufficiently long times. The eigenvector with the zero eigenvalue gives the steady-state (thermal-equilibrium) density matrix, $\sigma_{i,j}(t = \infty) =$

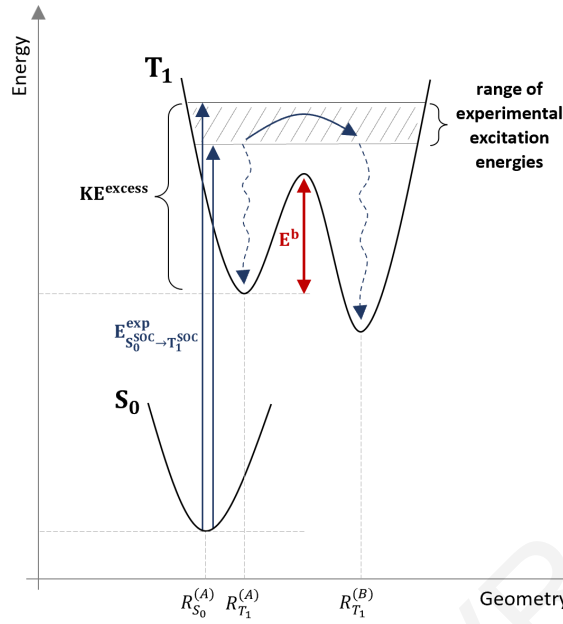


Figure 6.11: Schematic energy diagram for the conformational transitions between two different geometries (A and B) in the T_1 PES. For all the experimental excitation energies ($E_{S_0^{\text{SOC}} \rightarrow T_1^{\text{SOC}}}^{\text{exp}}$), the T_1 manifold is populated with high vibrational kinetic energy. This excess kinetic energy ($\text{KE}^{\text{excess}}$) may be large enough compared to the energy barrier (E^b) for the conformational transition between minimum energy geometries of A and B, so that each excited molecule may change its conformation through motion on the T_1 PES.

$\langle i, j | V_{k=0} \rangle \langle V_{k=0} | \sigma(t=0) \rangle$. We find that $\sigma_{i,i}(t=\infty) - \sigma_{j,j}(t=\infty) \approx 0$ as expected since $\hbar\omega/K_B T \ll 1$. The signal thus, arises from the nonequilibrium populations $\Delta\sigma_{i,i}(t) = \sigma_{i,i}(t) - \sigma_{i,i}(t=0)$. To relate to the experiment we compute the time average of the populations and divide by a microsecond, i.e., $\langle \tilde{\Pi}_i^{\text{ex}}(t) \rangle = (\mu\text{s})^{-1} \int_0^\infty dt \Delta\sigma_{i,i}(t)$, where $\int_0^\infty dt \Delta\sigma_{i,i}(t) = -\sum_{k \neq 0} \langle i, i | V_k \rangle \langle V_k | \sigma(t=0) \rangle / \lambda_k$. This method allows us to approximate $\langle \tilde{\Pi}_i^{\text{ex}}(t) - \tilde{\Pi}_j^{\text{ex}}(t) \rangle$ in terms of the *ab-initio* derived initial polarizations and the eigenvector/eigenvalues of the Bloch Liouvillian, which contain the effect of the spin relaxation time scales, the latter being consistent with the lifetimes of the observed signals. Using these types of computations in conjunction with EasySpin (for the computations of the triplet Hamiltonians for different applied resonant magnetic fields directions, with respect to the D -tensor axis), we find that $\bar{N}_{\text{tot}(\text{ex})}^{\text{min}} \approx 10^9 - 10^{10}$ as before. We emphasize that the above sensitivity analysis is intended to give order of magnitude estimates rather than “exact” numbers.

6.4.5 Excitation-wavelength dependence of the TR-EPR spectrum

Our calculations show that optical excitation within and outside (below) the CT band give measurable TR-EPR signals of similar magnitudes, as observed in the experiment of ref. 7. We now discuss the experimental observation that excitation

in the CT band leads to TR-EPR spectra whose shapes do not change for different excitation wavelengths, while excitation below the CT band, leads to TR-EPR spectra whose shapes differ for each excitation wavelength.

Our computations for optical excitation (section 6.4.1) reveal that photoexcitation below the CT band populates the T_1 manifold because the other triplet manifolds have vertical energies higher than the experimental excitation range (wavelengths 630 nm to 680 nm or energies 1.82 eV to 1.97 eV in figure 6.2). Even inside the CT band, optical excitation for excitation wavelengths below the CT band maximum (wavelengths 530 nm to 580 nm or energies 2.14 eV - 2.34 eV in figure 6.2), populates again the T_1 manifold since the $S_0^{\text{SOC}} \rightarrow T_{2,\xi}^{\text{SOC}}$ vertical excitation energy lies at higher energy values (minimum vertical excitation energy of T_2 manifold at 2.65 eV). For excitation wavelengths above the CT band maximum (wavelengths 430 nm - 480 nm or energies 2.58 eV - 2.89 eV in figure 6.2) the T_2 manifold is energetically accessible and can be populated. These observations suggest that for the optical excitation energy range of 1.82 eV - 2.34 eV the T_1 is excited with successively higher kinetic energies. We propose that the successively higher kinetic energies imparted on the molecule within the T_1 PES increase the conformational disorder on the time scale of the EPR experiment because the imparted kinetic energy is large enough to overcome potential energy barriers of the T_1 PES (as shown schematically in figure 6.11). The increase in disorder causes a wavelength dependence of the TR-EPR spectra that is reflected in the widening of the experimentally fitted Lorentzian widths with decreasing wavelength¹⁴⁸ (as shown in table 6.1).

To check the kinetic energy hypothesis we computed cross sections of the PES of the T_1 manifold along the torsional angles θ_1 and θ_2 (see figure 6.6) in order to examine the energy barrier for the conformational transitions between minimum energy PES geometries (see figure 6.12). Our computations show that the energy barrier in the T_1 manifold for the conformational transition from the anti_2 geometry to the anti-syn_2 geometry is 1.71 eV above the ground-state energy of the anti_2 conformation. Similarly, the energy barrier in the T_1 manifold for the conformational transition from the anti_2 to the syn-anti_2 conformation is about 1.83 eV above the ground-state energy of the anti_2 conformation. Both values are smaller than the experimental optical excitation energy (1.82 eV - 2.34 eV). These results suggest that optical excitation below the CT band, which populates the T_1 manifold PES with very high vibrational kinetic energy, may enable transitions between different minimum-energy conformations of the PES. Similar computations were performed for the other geometric conformations and the conclusions are similar (for further information see section 6.9.2).

We computed the ZFS parameters for the T_1 manifold for each of the above-mentioned minimum energy conformations (table 6.15 in section 6.12). The purpose was to test the quality of the computed T_1 wavefunction for the different minimum energy conformations and to gauge whether the proposed kinetic-energy-induced disorder

gives the same scatter in ZFS parameters as a function of wavelength as observed in experiment. We used the UNO-B3LYP⁹³, as well as the distributed point dipole (DPD) model as proposed by Guigliarelli *et. al.*¹⁴⁹. In the DPD model, the matrix elements ($K, L = x, y, z$) of the \tilde{D} matrix are given by¹³¹

$$D_{KL} = \frac{g^2}{8} \frac{\alpha_f^2}{S(2S-1)} \sum_{AB} P_A^{a-b} P_B^{a-b} \left(\frac{\delta_{KL} R_{AB}^2 - 3R_{AB,K} R_{AB,L}}{R_{AB}^5} \right) \quad (6.28)$$

where α_f is the fine structure constant ($\sim 1/137$ in atomic units) and S is the spin. R_{AB} is the distance between the A th and B th atoms and $R_{AB,K(L)}$ is the $K(L)$ -th coordinate distance between A and B atoms. $R_{A(B)}^{a-b} = \sum_{\mu \in A(B)} P_{\mu\mu}^a - P_{\mu\mu}^b$ is the “gross” spin population on atom $A(B)$. The D values computed with UNO-B3LYP are underestimated compared to the experimental ones ($\sim 40\%$ deviation). However, this is expected since DFT-computed EPR parameters (and especially the ratio E/D) are known to deviate from the experiment in extended - conjugated systems.^{93,150,151} On the other hand, the D values computed using the semiempirical DPD model, are surprisingly much closer to the respective experimental values ($\sim 2\% - 8\%$ deviation). This is may be due to the fact that we used spin densities with Slater-type basis sets for the atomic orbitals (rather than Gaussian-type of UNO-B3LYP). For example, the ratio between the experimental D values derived for the different excitation wavelengths below the CT band (630 nm - 680 nm) is about 0.96-0.98. The ratio between the calculated D values for the different geometric conformations are of the same order as the experimental ones. Both computational methods give approximately the same scatter in D values as a function of conformation as that observed in experiment ($\Delta D = 25$ -50 MHz) but overestimate the E scatter.

In ref. 7 the TR-EPR spectra were fitted without D and E strains. The fitted Lorentzian lineshape (of absorption and emission) was shown to grow with increasing wavelength (see table 6.1). We claim that this increase of width could be re-interpreted as an increase in conformational disorder. We can refit the experimental spectra given all of the parameters derived in table 6.1, but with a fixed Lorentzian width, (value 1.54 mT at the lowest excitation energy of table 6.1, $\lambda_{\text{wav}} = 680$ nm), and wavelength dependent D and E strains (dD and dE) which reflect static disorder. Our results show that the D and E strains increase with decreasing wavelength (e.g., setting at $\lambda_{\text{wav}} = 680$ nm, $dD = 0$, $dE = 0$; $\lambda_{\text{wav}} = 650$ nm, $dD = 40$ MHz, $dE = 15$ MHz; $\lambda_{\text{wav}} = 630$ nm, $dD = 50$ MHz, $dE = 20$ MHz; see section 6.12). This result is consistent with a rise in static disorder with increasing kinetic energy imparted on the T_1 manifold. We cannot interpret, however, the independence of the TR-EPR spectra on wavelength for excitation at the highest energies within the CT band. The T_2 excited state PES is very difficult to predict because as a function of conformation, the excited state cannot be always described by a single determinant wavefunction.

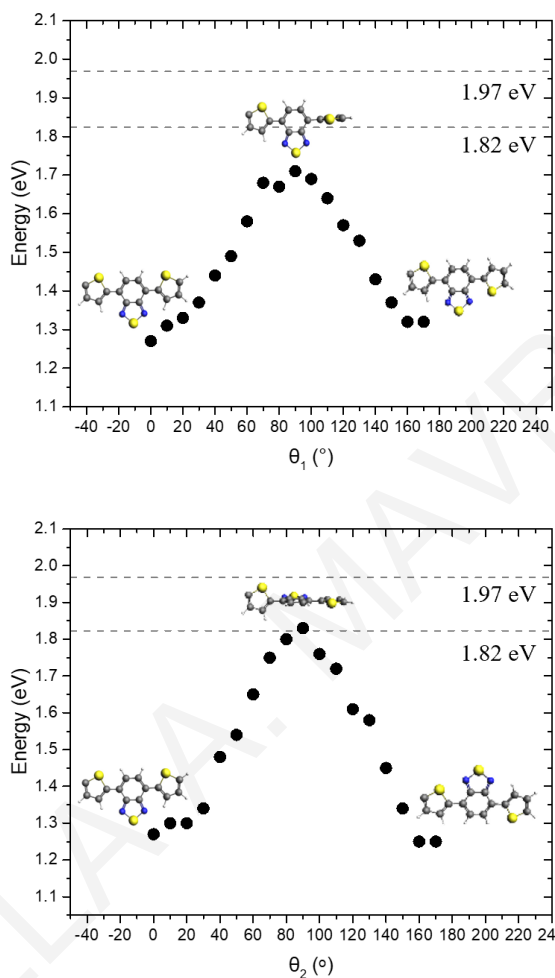


Figure 6.12: PES of the T_1 manifold along the torsional angles θ_1 (above) and θ_2 (below) computed at TDA/BHandHLYP/TZ2P level of theory for anti_2 geometric conformation. The two gray-dashed lines refer to the lowest and maximum experimental wavelengths used for excitation below the CT band (1.82 eV - 1.97 eV). *Above:* The barrier refers to a thiophene unit rotation that brings the Cbz-TBT molecule from anti_2 to anti-syn_2 (see figure 6.7). At $\theta_1 = 0^\circ$ the energy refers to the minimum energy conformation of the T_1 manifold of anti_2. *Below:* The barrier refers to the energy required for a BT-thiophene unit rotation that brings the Cbz-TBT molecule from anti_2 to syn-anti_2 (see figure 6.7). At $\theta_1 = 0^\circ$ the energy refers to the minimum energy conformation of the T_1 manifold of anti_2. In the picture of the molecule, the Cbz unit is excluded for simplicity.

6.5 Conclusions

The TR-EPR experiment in ref. 7 showed that the TR-EPR spectra of Cbz-TBT obtained from optical excitation within the CT band of the molecule are of similar intensity as the TR-EPR spectra obtained from optical excitation below the CT band. This result is quite surprising and counter-intuitive given that: 1) the optical absorbance of the molecule below the CT band is practically zero as compared to the absorbance within the CT band, 2) the molecule is organic with very weak SOC interactions. Using detailed computations and modelling we have explained that the observation is due to an initial-state preparation effect and to very low ISC rates. Because of the weak spin-orbit mixing of singlet and triplet states, upon photoexcitation within and below the CT band a small number of molecules in the ensemble is excited directly from the ground state to states that are predominantly of triplet character. It turns out that these initial triplet populations created for the two optical-excitation regions are similar and detectable by EPR. Further, as a function of time after optical excitation, these initial triplet populations are not substantially perturbed on the time scale of the TR-EPR experiment because the singlet to triplet ISC rates are very slow. Thus, the TR-EPR spectra from the different optical excitation regions are of similar magnitudes as observed in the experiment. This mechanism can be tested by measuring cw-EPR spectra of the ground state ensemble.

Another observation in ref. 7 is that the shapes of the TR-EPR spectra obtained for excitation within the CT band are independent of the optical excitation wavelength, whereas the shapes of the TR-EPR spectra obtained for excitation below the CT band are wavelength-dependent. Excitation below the CT band accesses only the lowest triplet state but at a very high vibrational energy. Thus, increasing the excitation energy below the CT region, increases the vibrational kinetic energy of the lowest triplet and may lead to conformational disorder and additional inhomogeneous broadening of the spectra. This is a plausibility argument and we cannot offer an explanation for the wavelength-independence of the shapes for excitation within the CT band. At these energies the second triplet state becomes accessible.

Initial-state preparation effects analogous to the ones described in this work may also occur in molecular electron transfer, where the observed long-time transfer dynamics is determined by a fast channel with a small initial population that out-competes a slower transfer channel with large initial population.^{152,153} For the case of TR-EPR spectroscopy, such effects are likely to occur in systems where the spin-orbit interactions are sufficiently large to initiate a TR-EPR-measurable triplet population upon photoexcitation, but not large enough to induce fast ISC rates that would perturb the initial triplet populations on the time scale of the experiment.

Supplementary material

6.6 Computation of the lowest singlet and triplet excited states of Cbz-TBT molecule

The aim is to compute the lowest singlet-singlet (S_1) and singlet-triplet excitations (T_1, T_2 manifolds) of Cbz-TBT molecule using TD-DFT theory. Our main purpose is to select a reliable TD-DFT method to accurately describe the excited state energies and wavefunction properties. Therefore, we performed numerical computations to examine the nature of the computed transitions e.g., valence or charge transfer (CT), in order to select the appropriate method to properly describe the excitations.^{154,155}

6.6.1 Calculation of the metric of CT molecular excitations and overcoming triplet instability problems in TD-DFT

To examine the CT character of the lowest-lying excited states of Cbz-TBT molecule, we computed the metric of the electronic excited states. This includes the calculation of: (i) the Λ -index developed by D. Tozer, which is based on the degree of spatial overlap between the occupied and virtual orbitals involved in an excitation,¹²⁰ (ii) the Δr -index developed by C. Adamo which is based on the measure of the average hole-electron distance upon excitation.¹²¹ The combination of these two diagnostic

	PBE		PBE0		CAMY-B3LYP	
	Λ	Δr (Å)	Λ	Δr (Å)	Λ	Δr (Å)
S_1	0.66	2.76	0.66	2.85	0.65	2.99
T_1	0.67	2.88	0.67	2.98	0.64	3.08
T_2	0.18	10.27	0.61	1.70	0.62	0.75

Table 6.2: TD-DFT/TDA diagnostic indexes Λ and Δr computed using three different methods, for the Cbz-TBT molecule in its anti_2 conformation.

	PBE		PBE0		CAMY-B3LYP	
	energy (eV)	contribution	energy (eV)	contribution	energy (eV)	contribution
S_1	1.82	H→L 83%	2.45	H→L 96%	2.76	H→L 92%
T_1	1.33	H→L 99%	1.67	H→L 89%	1.84	H→L 80% H-2→L 11%
T_2	1.89	H-1→L+1 100%	2.64	H-2→L 46% H→L+1 33%	2.84	H→L+1 40% H-2→L 25%

Table 6.3: TD-DFT/TDA vertical excitation energies in eV and the relative molecular orbital contributions computed using three different methods, for the Cbz-TBT molecule in its anti_2 conformation (H refers to HOMO and L refers to LUMO).

quantities determines the type of the transition (e.g., local or CT) and their values are associated with the choice of an appropriate functional.

The diagnostic test suggests that for $0.1 \leq \Lambda \leq 0.8$ given by Generalized Gradient approximation (GGA) or Global Hybrids (GH) or Range-separated (RS) methods, and $\Delta r > 2.0 \text{ \AA}$ given by GH or RS calculation (or $\Delta r > 1.5 \text{ \AA}$ given by GGA) the use of RS or GH with high (>33%) Hartree Fock (HF) exchange percentage is mandatory. Local excitations with $0.3 \leq \Lambda \leq 0.8$ given by GH or RS (or $0.4 \leq \Lambda \leq 0.8$ given by GGA) and $\Delta r < 2.0 \text{ \AA}$ given by GH/RS calculation (or $\Delta r < 1.5 \text{ \AA}$ given by GGA) can be successfully described by GGA and GH (with low HF percentage) methods.^{121,156}

The diagnostic tool Λ and Δr , is also readily generalized to triplet states.¹⁵⁷ However, in the case of triplet excitations, sometimes the TD-DFT inaccuracies are also related to triplet instability problems.^{158,159} It has been shown that application of the Tamm-Dancoff approximation (TDA)¹⁰⁵ dramatically reduces these errors, especially in the case of high-overlap excitations, and further improves the average accuracy of low-overlap excitations¹⁶⁰. Therefore, depending on the type of the excitation, only a combination between appropriate exact-exchange (low for local and high for CT excitations) and Tamm-Dancoff approach guarantees the success of TD-DFT method for calculating triplet excitations.

We used the Amsterdam Density Functional (ADF) program package (version 2018) where the diagnostic indices Λ and Δr are implemented in⁹⁴. All DFT and TD-DFT calculations have been carried out with the anti_2 molecular conformation, as the most probable geometry (see figure 6.7). Three particular functionals have been selected for the calculation of the excited-state properties and the indices,¹⁵⁶ which span over different exchange-correlation (xc) potentials and include a GGA (PBE),^{161,162} a GH (PBE0)¹⁶³ and a RS (CAMY-B3LYP).^{112,119} PBE contains no exact exchange, PBE0 contains 25% exact exchange and CAMY-B3LP contains 19% at small inter-electronic distances increasing up to 65% at large distance. The functionals were used with the TZ2P basic set¹⁰³ in combination with the TDA approximation. The ground-state geometry was optimized using the same functionals as the calculation of the

electronic transitions. SOC interactions are not included in the computations of the excited states because in organic molecules such contributions are relatively small, and the results are not significantly affected. The long alkyl chains attached to the nitrogen atom of carbazole (Cbz) moiety have been replaced by a hydrogen atom to reduce computational cost.

Table 6.2 shows the diagnostic indices Λ and Δr for the excitations. Results indicate that for the first singlet excitation and the first triplet excited state manifold, the Λ -index is greater than 0.6 and the Δr -index is greater than 2\AA . According to the diagnostic tool, these types of excitations are CT and a RS functional or a GH with high HF percentage should be used for their description. The relative excited-state energies and the main molecular orbital contributions for each excitation are shown in table 6.3. The first singlet excited state is mainly attributed to the transition H \rightarrow L (H for HOMO and L for LUMO). For the first triplet excitation manifold, the contribution to molecular orbital transitions calculated with PBE and PBE0 is very similar. For both functionals the excitation is characterized by the same main occupied-to-virtual (H \rightarrow L) transition with comparable percentages. On the other hand, in the case of CAMY-B3LYP method, the first triplet excitation is attributed to two different main contributions of molecular orbital transitions, H \rightarrow L and H-2 \rightarrow L.

In the case of the second triplet excited state manifold, the values of the diagnostic indices and the orbital contributions given by PBE, are different to those given by PBE0 and CAMY-B3LYP. This is because PBE predicts different absolute positions and ordering of the triplet excited states compared to the other two functionals which correct and improve them. The large Λ value in combination with the small Δr value predicted by PBE0 and CAMY-B3LYP methods, show that the second triplet excitation is local. Therefore, it is not necessary to use RS functionals for its description.

Figure 6.13 shows the dominant orbital transitions for each excitation calculated with CAMY-B3LYP method. The orbitals computed with the other two methods give exactly the same results as CAMY-B3LYP. The first singlet excitation $S_0 \rightarrow S_1$ is 92% attributed to the transition H \rightarrow L, where both H and L orbitals are of π -character. The electron density of the H orbital is delocalized over the backbone (excluding the “external” thiadiazole ring - mainly no charge density on the sulfur atom), while the electron density of L orbital is localized on the “inner part” of the molecule, namely the thiadiazole ring. Much less charge density is located on the thiophenes. Therefore, the $S_0 \rightarrow S_1$ transition implies some redistribution of electron density from the conjugated backbone of the molecule toward the central benzothiadiazole (BT) unit (CT character).

The above observations are the same for the first triplet excited state manifold. On the other hand, for the second triplet excited state manifold the major contribution stems from the transition H \rightarrow L+1 where the electron density is delocalized approximately over the whole backbone with a very small redistribution of charge density

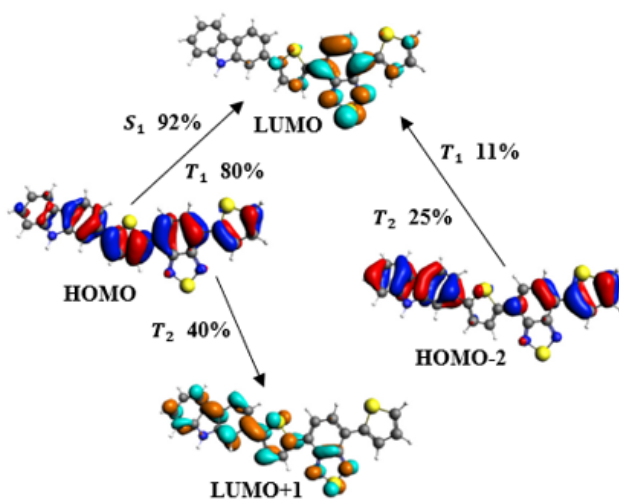


Figure 6.13: Singlet-singlet and singlet-triplet vertical excitation energies of Cbz-TBT in its anti₂ conformation calculated with CAMY-B3LYP method. The percentage value on the right-hand side of each excitation is the contribution to the excitation.

towards the thiophene ring on BT moiety. This is the reason why the Λ -parameter takes values greater than the CT threshold of 0.3/0.4 and the Δr -index does not exceed the value of 1.5/2.0 Å that describes local excitations. Hence, the second triplet excited state manifold will be properly described by conventional DFT functionals with low HF percentage.

6.6.2 The choice of the appropriate functional

The results in subsection 6.6.1 indicate that for the description of the lowest-lying singlet and triplet excitations (S_1 and T_1 manifold) the usage of RS functionals or GH with high HF exchange is required. In this section, we tried to examine the performance of different GH and RS methods for the computation of the excitation energies of Cbz-TBT molecule. We chose two GH with high HF exchange: M062X^{110,111} (54%) and BHandHLYP¹⁰⁴ (50%), and five long-range corrected (LRC) hybrid functionals: LCY-BLYP,^{113,114} wB97,¹¹⁵ wB97X,¹¹⁵ wB97X-D¹¹⁶⁻¹¹⁸ and CAMY-B3LYP in combination with the TZ2P basis set and TDA approximation. SOC was included perturbatively in TD-DFT/TDA calculations of the excitation energies (pSOC-TDA).¹⁰⁹ The relativistic excited-state computations were performed on the optimized B3LYP¹⁰²/TZ2P ground state geometry of anti₂ molecular conformation.

The singlet and triplet electronic states calculated with the different methods are shown in figure 6.14. The results suggest that the first triplet excited state manifold $\{|T_{1,\xi}^{\text{SOC}}\rangle\}$ has very low energy compared to the first singlet $|S_1^{\text{SOC}}\rangle$ excited state and the second triplet excited state manifold $\{|T_{2,\xi}^{\text{SOC}}\rangle\}$, regardless of the method. In addition, most of the functionals show that the $\{|T_{2,\xi}^{\text{SOC}}\rangle\}$ manifold lies below the $|S_1^{\text{SOC}}\rangle$. The opposite is shown by the CAMY-B3LYP method.

In general, the agreement between the different methods is obvious if one considers the energy differences between the singlet and triplet energies. All methods result in approximately the same energy gap values between $|S_1^{\text{SOC}}\rangle$ and $|T_{1,\xi}^{\text{SOC}}\rangle$ ($\Delta E_{S_1^{\text{SOC}},T_{1,\xi}^{\text{SOC}}}$) and between $|S_1^{\text{SOC}}\rangle$ and $|T_{2,\xi}^{\text{SOC}}\rangle$ ($\Delta E_{S_1^{\text{SOC}},T_{2,\xi}^{\text{SOC}}}$). The molecular orbital contributions to the excited states, given by each method are similar, as shown in table 6.4. What changes is the absolute vertical excitation energies for singlet-singlet and singlet-triplet transitions. For example, LRC methods are known to overestimate the excitation energies of CT states especially when the default value of the range-separation parameter is used.¹⁶⁴ Namely, compared to the experimental absorption spectrum, LCY-BLYP, wB97, wB97X and wB97X-D methods overestimate the energy of the lowest absorption band (experimentally centered at 2.52 eV⁷) in contrast to M062X, BHandHLYP and CAMY-B3LYP.

CAMY-B3LYP reproduces well the experimental results for the first absorption band, however, it is the only method which predicts that the second triplet excited state manifold lies above the first singlet one ($\Delta E_{S_1^{\text{SOC}},T_{2,\xi}^{\text{SOC}}} = -0.07$ eV). This indicates that CAMY-B3LYP may not be a suitable functional to accurately describe our system. In addition, LCY-BLYP, wB97, wB97X and wB97X-D functionals give blue-shifted absorption energies but this is overcome if the range-separation parameter is optimized. However, the experimental absorption spectrum is well reproduced by M06-2X and BHandHLYP methods, hence, it is not necessary to use LRC functionals and further optimize their parameters. Since BHandHLYP method is faster than M06-2X, we chose BHandHLYP to perform our computations, to further reduce computational cost.

Summary: Our results in subsection 6.6.1 prove that RS functionals or GH with high HF exchange are required for the description of the excited state energies and wavefunction properties of the lowest-lying singlet-singlet and singlet-triplet transitions of the Cbz-TBT molecule. In subsection 6.6.2 we proved the consistency between the transition energies computed using different RS and GH (large HF%) functionals. The BHandHLYP method accurately reproduces the experimental spectrum compared to the other methods.

	M06-2X	BHandHLYP	LCY-BLYP	wB97	wB97X	wB97X-D	CAMY-B3LYP
SINGLETS							
S_1	2.76 (H→ L 91%)	2.76 (H→ L 93%)	3.14 (H→ L 82%)	3.19 (H→ L 82%)	3.10 (H→ L 84%)	2.91 (H→ L 87%)	2.67 (H→ L 82%)
S_2	3.82	3.83	4.26	4.30	4.20	4.00	3.69
S_3	3.98	3.97	4.56	4.53	4.44	4.24	3.83
S_4	3.99	4.01	4.68	4.68	4.59	4.30	3.84
TRIPLETS							
T_1	1.56 (H→ L 73% H-2→ L 11%)	1.65 (H→ L 75% H-2→ L 11%)	1.85 (H→ L 66% H-2→ L 15%)	1.94 (H→ L 67% H-2→ L 15%)	1.89 (H→ L 69% H-2→ L 14%)	1.83 (H→ L 74% H-2→ L 13%)	1.74 (H→ L 81% H-2→ L 10%)
T_2	2.50 (H→ L+1 38% H-2→ L 20%)	2.65 (H→ L+1 40% H-2→ L 22%)	2.82 (H→ L+1 37% H-2→ L 15%)	2.91 (H→ L+1 37% H-2→ L 16%)	2.87 (H→ L+1 39% H-2→ L 17%)	2.82 (H→ L+1 41% H-2→ L 19%)	2.73 (H→ L+1 42% H-2→ L 26%)
T_3	2.96	3.12	3.25	3.30	3.29	3.29	3.20
T_4	3.10	3.23	3.33	3.42	3.37	3.32	3.27

Table 6.4: pSOC-TDA vertical excitation energies in eV computed using different methods for the Cbz-TBT molecule in its anti_2 conformation. The molecular orbital contributions to the excitations, are shown for the singlet and triplet excited states of interest (H refers to HOMO and L refers to LUMO).

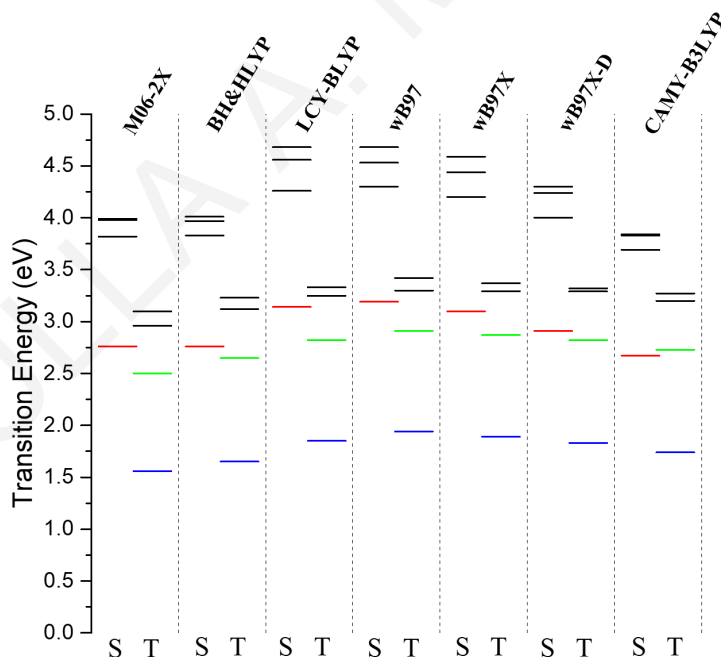


Figure 6.14: Singlet-singlet and singlet-triplet vertical excitation energies of Cbz-TBT in its anti_2 conformation calculated using different GH and RS methods. The electronic state at zero-energy is the ground state $|S_0^{\text{SOC}}\rangle$. The $|S_1^{\text{SOC}}\rangle$ state is colored in red, the $\{|T_{1,\xi}^{\text{SOC}}\rangle\}$ manifold is colored in blue and the $\{|T_{2,\xi}^{\text{SOC}}\rangle\}$ manifold is colored in green. Left column of each method refers to the singlet states (S) and right column to the triplet states (T).

6.6.3 Excited-state computations performed with CIS

The configuration interaction with single-excitations (CIS) method¹²⁴ was used to compute the lowest singlet-singlet ($|S_n^{\text{SOC}}\rangle$) and singlet-triplet ($\{|T_{k,\xi}^{\text{SOC}}\rangle\}$) excitations of the Cbz-TBT molecule in its anti_2 conformation. We used the ORCA program package¹²² and the def2-TZVP basis set,¹²³ and the SOC effects were included in the computations. The figure below (figure 6.15), show the excited-state energies computed with SOC-CIS/def2-TZVP and pSOC-TDA/BHandHLYP/TZ2P methods. The absolute triplet energies given by these different methods are close, but the singlet states computed with CIS are blue shifted compared to those computed with TDA. The energy difference between the two lowest triplet excited states (T_1 and T_2) computed with the TDA and CIS is approximately the same (~ 1 eV).

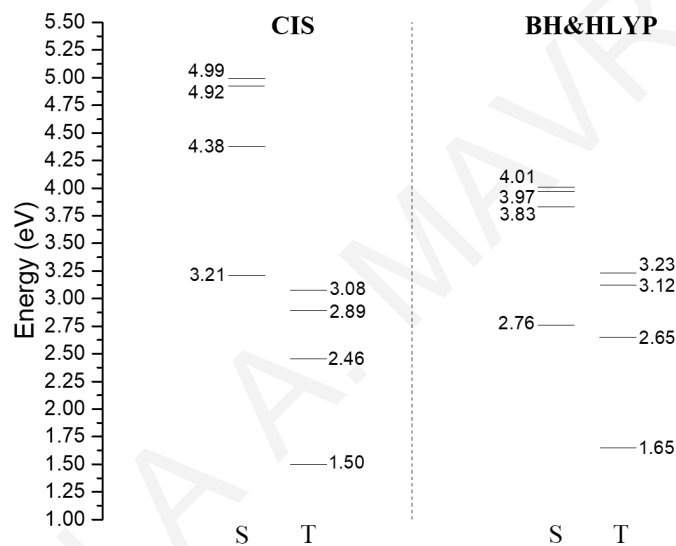


Figure 6.15: Singlet-singlet and singlet-triplet vertical excitation energies of Cbz-TBT in its anti_2 conformation calculated using SOC-CIS/def2-TZVP and pSOC-TDA/BHandHLYP/TZ2P methods. Left column for each method refers to the singlet states (S) and right column to the triplet states (T).

6.7 Spin-Orbit Coupling effects

6.7.1 The SOC Hamiltonian in the framework of the zeroth-order approximation

Within the zeroth-order regular approximation (ZORA), the relativistic Hamiltonian is written as¹⁰⁶

$$\hat{H}^{\text{ZORA}} = V + \vec{\sigma} \cdot \hat{\vec{p}} \frac{c^2}{2c^2 - V} \vec{\sigma} \cdot \hat{\vec{p}}, \quad (6.29)$$

where V is the static Coulomb potential provided by the nuclei (Kohn-Sham potential), $\vec{\sigma}$ is the Pauli spin matrix vector, c is the speed of light and $\hat{\vec{p}}$ is the linear momentum operator. This equation may be further developed to yield⁵²

$$\hat{H}^{\text{ZORA}} = V + \hat{\vec{p}} \frac{c^2}{2c^2 - V} \hat{\vec{p}} + \frac{c^2}{(2c^2 - V)^2} \vec{\sigma} \cdot (\vec{\nabla} V \times \hat{\vec{p}}). \quad (6.30)$$

The first two terms in the right-hand side of eq. 6.30 define the zeroth-order regular approximate scalar relativistic (SR) equation (ZORA SR)¹⁰⁷

$$\hat{H}^{\text{ZORA SR}} = V + \hat{\vec{p}} \frac{c^2}{2c^2 - V} \hat{\vec{p}}, \quad (6.31)$$

while the last term in eq. 6.30 is the spin-orbit term (ZORA SOC)¹⁰⁰

$$\hat{H}^{\text{ZORA SOC}} = \frac{c^2}{(2c^2 - V)^2} \vec{\sigma} \cdot (\vec{\nabla} V \times \hat{\vec{p}}). \quad (6.32)$$

In the present calculations, the “spin-pure” singlet and triplet states ($|S_n\rangle$ and $\{|T_{k,m_s}\rangle\}$) are calculated by means of the ZORA Hamiltonian in its scalar approach (eq. 6.31) and SOC is treated as a perturbation based on the SR states (pSOC) (eq. 6.32) to compute the “spin-mixed” excited states ($|S_n^{\text{SOC}}\rangle$ and $|T_{k,\xi}^{\text{SOC}}\rangle$) as linear combinations of the pure states.¹⁰⁹

6.7.2 SOC integrals between singlet-triplet and triplet-triplet states for the different geometric conformations of the Cbz-TBT molecule

To calculate the SOC matrix elements between pure singlet $|S_n\rangle$ and triplet $|T_{k,m_s}\rangle$ states ($\langle S_n | \hat{H}^{\text{SOC}} | T_{k,m_s} \rangle$), we performed relativistic TD-DFT calculations (pSOC) with the ADF program, employing the BHandHLYP functional with the TZ2P basis set, and using the TDA approximation with no frozen cores and without symmetry constraints. Table 6.5 shows the SOC constants between $|S_1\rangle$, $|T_{1,m_s}\rangle$, $|T_{2,m_s}\rangle$ with $m_s = 0, \pm 1$.

anti_2 (58%)		anti_1 (15%)	
I/J	$\langle I \hat{H}^{\text{SOC}} J\rangle$	I/J	$\langle I \hat{H}^{\text{SOC}} J\rangle$
$S_1/T_{2,0}$	$(6.47i) \times 10^{-7}$	$S_1/T_{2,0}$	$(5.56i) \times 10^{-7}$
$S_1/T_{2,\pm 1}$	$(-1.93 \mp 2.21i) \times 10^{-6}$	$S_1/T_{2,\pm 1}$	$(-1.77 \mp 2.08i) \times 10^{-6}$
$S_1/T_{1,0}$	$(3.62i) \times 10^{-7}$	$S_1/T_{1,0}$	$(-2.92i) \times 10^{-7}$
$S_1/T_{1,\pm 1}$	$(-0.25 \mp 1.09i) \times 10^{-6}$	$S_1/T_{1,\pm 1}$	$(0.34 \pm 1.02i) \times 10^{-6}$
$T_{2,0}/T_{1,0}$	0.00	$T_{2,0}/T_{1,0}$	0.00
$T_{2,0}/T_{1,\pm 1}$	$(\mp 1.22 + 1.39i) \times 10^{-5}$	$T_{2,0}/T_{1,\pm 1}$	$(\pm 0.07 - 2.91i) \times 10^{-6}$
$T_{2,\pm 1}/T_{1,0}$	$(\pm 1.22 + 1.39i) \times 10^{-5}$	$T_{2,\pm 1}/T_{1,0}$	$(\mp 0.07 - 2.91i) \times 10^{-6}$
$T_{2,\pm 1}/T_{1,\pm 1}$	$(\pm 7.21i) \times 10^{-6}$	$T_{2,\pm 1}/T_{1,\pm 1}$	$(\mp 1.03i) \times 10^{-6}$
$T_{2,\pm 1}/T_{1,\mp 1}$	0.00	$T_{2,\pm 1}/T_{1,\mp 1}$	0.00
syn-anti_2 (13%)		anti-syn_1 (12%)	
I/J	$\langle I \hat{H}^{\text{SOC}} J\rangle$	I/J	$\langle I \hat{H}^{\text{SOC}} J\rangle$
$S_1/T_{2,0}$	$(4.66i) \times 10^{-6}$	$S_1/T_{2,0}$	$(-1.95i) \times 10^{-6}$
$S_1/T_{2,\pm 1}$	$(-3.65 \mp 3.26i) \times 10^{-6}$	$S_1/T_{2,\pm 1}$	$(5.43 \pm 2.71i) \times 10^{-6}$
$S_1/T_{1,0}$	$(5.83i) \times 10^{-7}$	$S_1/T_{1,0}$	$(7.16i) \times 10^{-7}$
$S_1/T_{1,\pm 1}$	$(-1.51 \mp 0.85i) \times 10^{-6}$	$S_1/T_{1,\pm 1}$	$(-1.73 \pm 0.19i) \times 10^{-6}$
$T_{2,0}/T_{1,0}$	0.00	$T_{2,0}/T_{1,0}$	0.00
$T_{2,0}/T_{1,\pm 1}$	$(\pm 2.41 - 1.70i) \times 10^{-4}$	$T_{2,0}/T_{1,\pm 1}$	$(\pm 6.76 - 3.31i) \times 10^{-5}$
$T_{2,\pm 1}/T_{1,0}$	$(\mp 2.41 - 1.70i) \times 10^{-4}$	$T_{2,\pm 1}/T_{1,0}$	$(\mp 6.76 - 3.31i) \times 10^{-5}$
$T_{2,\pm 1}/T_{1,\pm 1}$	$(\mp 1.20i) \times 10^{-4}$	$T_{2,\pm 1}/T_{1,\pm 1}$	$(\mp 2.74i) \times 10^{-5}$
$T_{2,\pm 1}/T_{1,\mp 1}$	0.00	$T_{2,\pm 1}/T_{1,\mp 1}$	0.00
anti-syn_2 (13%)		syn_2 (12%)	
I/J	$\langle I \hat{H}^{\text{SOC}} J\rangle$	I/J	$\langle I \hat{H}^{\text{SOC}} J\rangle$
$S_1/T_{2,0}$	$(-7.81i) \times 10^{-7}$	$S_1/T_{2,0}$	$(1.14i) \times 10^{-6}$
$S_1/T_{2,\pm 1}$	$(3.63 \mp 3.41i) \times 10^{-7}$	$S_1/T_{2,\pm 1}$	$(3.49 \pm 3.27i) \times 10^{-6}$
$S_1/T_{1,0}$	$(-3.53i) \times 10^{-7}$	$S_1/T_{1,0}$	$(2.17i) \times 10^{-7}$
$S_1/T_{1,\pm 1}$	$(-0.24 \mp 3.15i) \times 10^{-7}$	$S_1/T_{1,\pm 1}$	$(-4.89 \mp 8.11i) \times 10^{-7}$
$T_{2,0}/T_{1,0}$	0.00	$T_{2,0}/T_{1,0}$	0.00
$T_{2,0}/T_{1,\pm 1}$	$(\mp 9.35 - 2.31i) \times 10^{-7}$	$T_{2,0}/T_{1,\pm 1}$	$(\mp 2.37 + 1.63i) \times 10^{-4}$
$T_{2,\pm 1}/T_{1,0}$	$(\pm 9.35 - 2.31i) \times 10^{-7}$	$T_{2,\pm 1}/T_{1,0}$	$(\pm 2.37 + 1.63i) \times 10^{-4}$
$T_{2,\pm 1}/T_{1,\pm 1}$	$(\pm 9.77i) \times 10^{-7}$	$T_{2,\pm 1}/T_{1,\pm 1}$	$(\pm 1.10i) \times 10^{-4}$
$T_{2,\pm 1}/T_{1,\mp 1}$	0.00	$T_{2,\pm 1}/T_{1,\mp 1}$	0.00

Table 6.5: SOC constants between singlet and triplet excited states in eV, computed at pSOC-TDA/BHandHLYP/TZ2P level of theory for the most probable geometric conformations. The coupling between $|S_1\rangle$ and $|T_{1,m_s}\rangle$ and between $|S_1\rangle$ and $|T_{2,m_s}\rangle$ was computed at the minimum-energy conformation of S_1 and the coupling between $|T_{1,m_s}\rangle$ and $|T_{2,m'_s}\rangle$ computed at the minimum-energy conformation of T_2 .

6.8 Optical properties of the Cbz-TBT molecule for the different geometric conformations

6.8.1 Energy level diagram with the lowest singlet and triplet excitations of the Cbz-TBT molecule computed for the different geometric conformations

Figure 6.16 shows the energy level diagram with the singlet excited states $|S_n^{\text{SOC}}\rangle$ and the triplet excited state manifolds $\{|T_{k,\xi}^{\text{SOC}}\rangle\}$ ($k = 1, 2$) of the molecule for the different geometric conformations, computed at the pSOC-TDA/BHandHLYP/TZ2P level of theory. The similarities between the energy level diagrams computed for each geometric conformation are obvious.

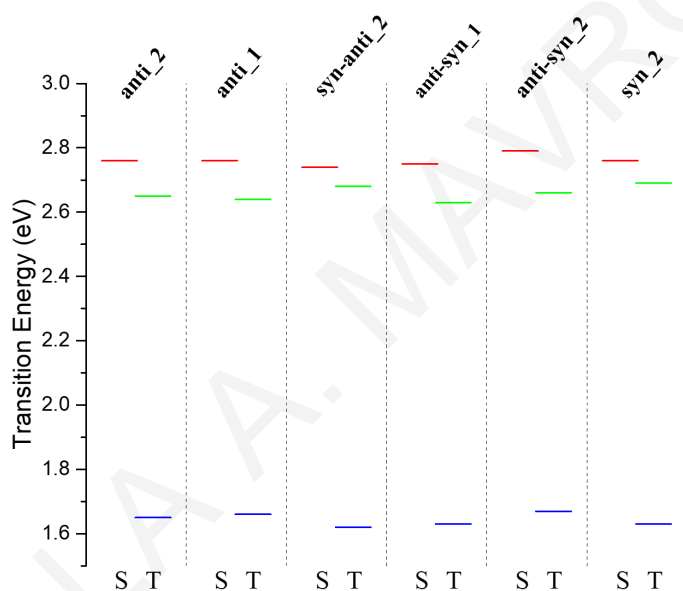


Figure 6.16: Energy level diagram of the Cbz-TBT molecule computed for different geometric conformations at pSOC-TDA/BHandHLYP/TZ2P level of theory. The $|S_1^{\text{SOC}}\rangle$ state is colored in red, the $\{|T_{1,\xi}^{\text{SOC}}\rangle\}$ manifold is colored in blue and the $\{|T_{2,\xi}^{\text{SOC}}\rangle\}$ manifold is colored in green. Left column of each geometric conformation refers to the singlet states (S) and right column to the triplet states (T).

6.8.2 Derivation of the molar extinction coefficient equation

The molar extinction coefficient is related to the oscillator strength of a transition via eq. 6.33, where N_A is the Avogadro constant, e is the electron charge, m_e is the electron mass, c is the speed of light, ε_0 is the vacuum permittivity and \hbar is the Planck constant. σ is the standard deviation of the Gaussian distribution. ΔE_J is the excitation energy (of the transition $S_0^{\text{SOC}} \rightarrow J$) with f_J the corresponding oscillator strength. To simulate the entire spectra, the contributions from all the transitions are added according to^{32,137}

$$\varepsilon(E) = \frac{\pi}{2\ln(10)} \frac{N_A e^2 \hbar}{m_e c \varepsilon_0} \frac{1}{\sigma \sqrt{2\pi}} \sum_J f_J e^{-\frac{1}{2} \left(\frac{E - \Delta E_J}{\sigma} \right)^2}. \quad (6.33)$$

In most computational program packages, the full width at half maximum (FWHM) broadening is set, instead of the standard deviation σ (FWHM = $2\sqrt{2\ln(2)} \sigma$). Therefore, 6.33 reduces to

$$\varepsilon(E) = \frac{\pi}{2\ln(10)} \frac{N_A e^2 \hbar}{m_e c \varepsilon_0} 2\sqrt{\frac{\ln(2)}{\pi}} \frac{1}{\text{FWHM}} \sum_J f_J e^{-2.77 \left(\frac{E - \Delta E_J}{\text{FWHM}} \right)^2}. \quad (6.34)$$

In SI units 6.34 yields

$$\varepsilon(E) = \frac{4.32 \times 10^{-15} \text{Lmol}^{-1} \text{cm}^{-1} j}{\text{FWHM}} \sum_J f_J e^{-2.77 \left(\frac{E - \Delta E_J}{\text{FWHM}} \right)^2} \quad (6.35)$$

with FWHM and E (and ΔE_J) in Joule (j). Equivalently,

$$\varepsilon(E) = \frac{2.18 \times 10^8 \text{Lmol}^{-1} \text{cm}^{-2}}{\text{FWHM}} \sum_J f_J e^{-2.77 \left(\frac{E - \Delta E_J}{\text{FWHM}} \right)^2} \quad (6.36)$$

with FWHM and E (and ΔE_J) in wavenumbers (cm^{-1}). Equivalently,

$$\varepsilon(E) = \frac{2.70 \times 10^4 \text{Lmol}^{-1} \text{cm}^{-1} \text{eV}}{\text{FWHM}} \sum_J f_J e^{-2.77 \left(\frac{E - \Delta E_J}{\text{FWHM}} \right)^2} \quad (6.37)$$

with FWHM and E (and ΔE_J) in eV.

6.8.3 Absorption spectrum of the Cbz-TBT molecule computed for the different geometries

Figure 6.17 shows the optical spectrum calculated with pSOC-TDA/BHandHLYP/TZ2P method for each geometric conformation. For all the geometric conformations, the first absorption band (centered at ~ 2.8 eV) is attributed to the transition $S_0^{\text{SOC}} \rightarrow S_1^{\text{SOC}}$ (or similarly $S_0 \rightarrow S_1$) which is predominantly assigned to H \rightarrow L transition (H for HOMO and L for LUMO).

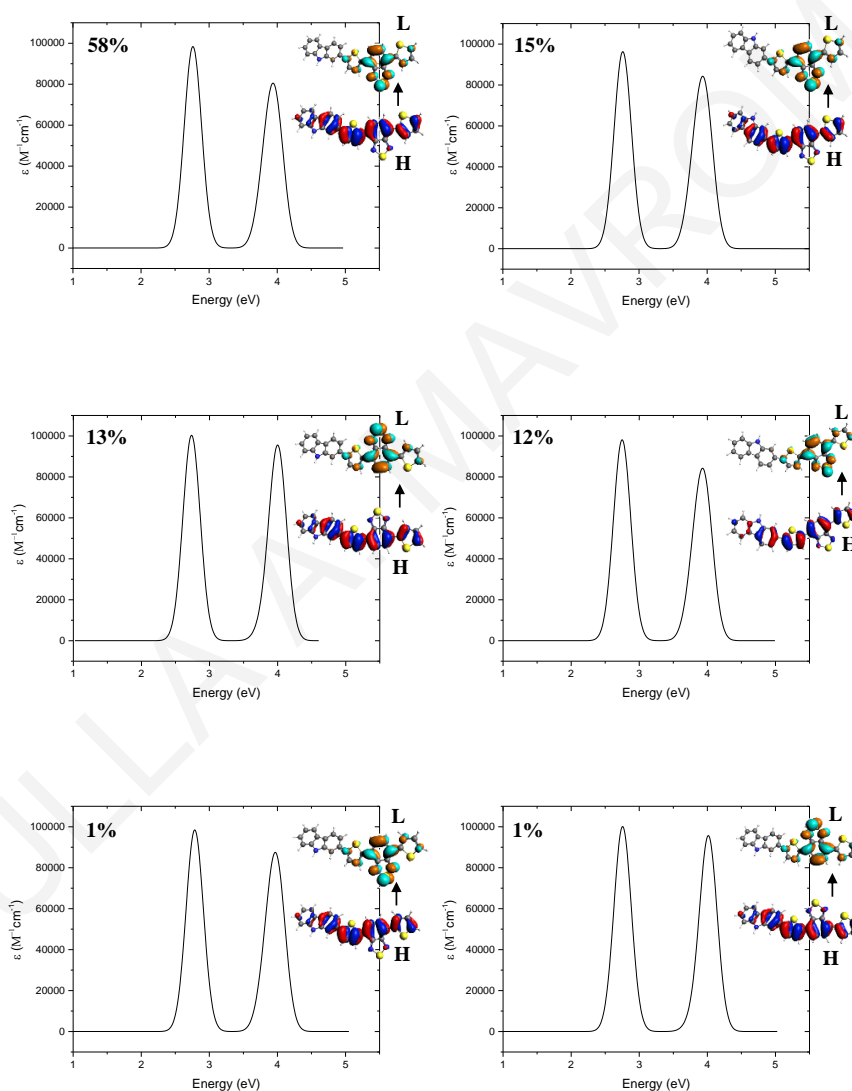


Figure 6.17: Absorption spectrum of the different Cbz-TBT molecular conformations calculated at the optimized B3LYP/TZ2P ground-state geometries using pSOC-TDA/BHandHLYP/TZ2P level of theory (based on a 0.30 eV FWHM Gaussian broadening of the vertical transition energies and associated oscillator strength). On the inset, the frontier orbitals H (HOMO) and L (LUMO) are shown for each conformation. (a) anti_2 (b) anti_1 (c) syn-anti_2 (d) anti-syn_1 (e) anti-syn_2 (f) syn_2.

6.9 Geometric structures of the Cbz-TBT molecule

6.9.1 Geometric structures of ground and excited states of Cbz-TBT

Table 6.6 shows the torsional angles ($\theta_1, \theta_2, \theta_3$) of the optimized ground state, first singlet excited state (S_1) and first and second triplet excited state manifolds (T_1 and T_2) for all the geometric conformations (see figure 6.6). The ground state molecular structures were optimized using the ADF program at the B3LYP¹⁰²/TZ2P level of theory. The results show that the structures are not strictly planar, the torsional angles between the thiophenes and BT moiety in TBT unit (θ_1, θ_2) was found in the range of $0^\circ - 20^\circ$ while the torsional angles between the TBT moiety and the adjacent Cbz unit (θ_3) is about $24^\circ - 27^\circ$ (positive or negative). This is consistent with previous results that report dihedral angles between TBT and carbazole moiety up to 26° .^{8,135,165}

The excited state molecular structures (S_1, T_1, T_2) were optimized using the TDA/BHandHLYP/TZ2P method. Results show that in the first singlet excited state and the first triplet excited state manifolds, the dihedral angles in TBT unit (θ_1, θ_2) as well as the dihedral angle between TBT and the adjacent Cbz moiety (θ_3) are close to zero, in agreement with the literature.^{132,133} The second triplet excited state is not strictly planar and different angles between 0° and 25° are found.

		anti_2 (58%)	anti_1 (15%)	syn-anti_2 (13%)	syn-anti_1 (12%)	anti-syn_2 (1%)	syn_2 (1%)
S_0	$\theta_1(^\circ)$	356	353	353	188	195	170
	$\theta_2(^\circ)$	10	356	180	358	4	190
	$\theta_3(^\circ)$	336	205	26	204	27	27
S_1	$\theta_1(^\circ)$	0	359	1	180	179	180
	$\theta_2(^\circ)$	0	0	180	1	360	180
	$\theta_3(^\circ)$	1	180	1	185	0	1
T_1	$\theta_1(^\circ)$	0	360	360	181	180	180
	$\theta_2(^\circ)$	0	360	179	0	0	180
	$\theta_3(^\circ)$	17	186	12	196	17	15
T_2	$\theta_1(^\circ)$	0	359	359	182	179	181
	$\theta_2(^\circ)$	2	1	152	11	0	153
	$\theta_3(^\circ)$	0	180	0	181	0	0

Table 6.6: Torsional angles θ_1, θ_2 and θ_3 for the optimized ground state, first singlet excited state and first triplet and second triplet excited state manifolds of all Cbz-TBT molecular conformations. The ground state was optimized at the B3LYP/TZ2P level of theory and the excited states were optimized at the TDA/BHandHLYP/TZ2P level.

6.9.2 Energy barrier for the conformational transitions between minimum energy PES of the T_1 manifold along the torsional angles θ_1 and θ_2 .

We computed the energy barrier for the conformational transitions between minimum energy T_1 geometries, to check the hypothesis that upon photoexcitation below the CT band, the kinetic energy is relatively large, so the excited state molecule changes its conformation through motion on the T_1 PES. The energy barrier was computed along the torsional angles θ_1 and θ_2 (as defined in figure 6.6) with respect to the ground state minimum energy of the initial geometric conformation as shown in figure 6.18. We used the ADF program and the TDA/BHandHLYP/TZ2P level of theory via geometry optimizations on the constrained values of θ_1 and θ_2 in the range $0^\circ \leq \theta_n \leq 180^\circ$ (or equivalently $360^\circ \geq \theta_n \geq 180^\circ$ for some conformations) with $n = 1, 2$. All the different molecular conformations show that the one-dimensional T_1 PES has a maximum at $\theta_n = 80^\circ - 90^\circ$ (and $\theta_n = 260^\circ - 270^\circ$) and two minima at $\theta_n = 0^\circ$ (360°), 180° ($n = 1, 2$).

Table 6.7 shows the energy barrier for the conformational transition between minimum energy T_1 geometries. We conclude that the energy barriers are smaller than the experimental optical excitation energy (1.82 eV – 2.34 eV), suggesting that upon photoexcitation the first triplet manifold is populated with high vibrational kinetic energy which enables conformational transitions between different geometric conformations (see section 6.4.5).

Conformation		Energy Barrier (eV)
From (A)	To (B)	
anti_2	(θ_1) anti-syn_2	1.71
anti_2	(θ_2) syn-anti_2	1.83
anti_1	(θ_1) anti-syn_1	1.70
syn-anti_2	(θ_1) syn_2	1.68

Table 6.7: Energy barrier in eV, in the first triplet excited state T_1 along the torsional angles θ_1 and θ_2 (as shown in the brackets) computed at TDA-BHandHLYP-TZ2P level of theory for the different geometric conformations.

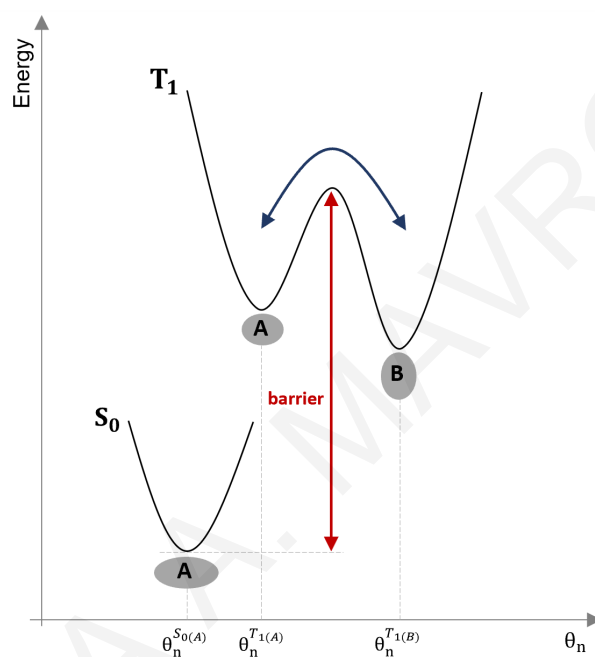


Figure 6.18: Schematic energy diagram for the conformational transitions between two different geometries (A and B) in the T_1 PES along the torsional angles θ_n ($n = 1, 2$). $\theta_n^{S_0(A)}$ refers to the angle θ_n of the ground state minimum energy conformation (S_0) of the initial geometry A. $\theta_n^{T_1(A)}$ refers to the angle θ_n of the minimum energy conformation of T_1 excited state of the initial geometry A. $\theta_n^{T_1(B)}$ refers to the angle θ_n of the minimum energy conformation of T_1 excited state of the final geometry B. The energy barrier was computed with respect to the ground state energy of the initial geometric conformation (A).

6.10 Populations of the Cbz-TBT molecules in the sample

To estimate the number of molecules in the ground state and in the photoexcited singlet and triplet excited state manifolds for each low-energy molecular conformation, we used the relevant experimental parameters,⁷ and computed parameters derived from *ab-initio* computations.

6.10.1 Number of Cbz-TBT molecules in the ground state

In the experiment, the concentration of Cbz-TBT molecules used, was 10 mg/ml and from those, about 150 μ l were placed in the sample tube to perform the measurements.⁷ This indicates that for the Cbz-TBT molecule (465 g molecular mass), the 150 μ l corresponds to 3.23×10^{-6} mol which means that in the ground state there are approximately 1.94×10^{18} molecules in total.

For each conformation s , we estimated the fraction of molecules in the ground state ensemble using Boltzmann equilibrium statistics given by, $\frac{P_s}{P} = \frac{e^{-\frac{\varepsilon_s}{K_B T}}}{P}$ where $P = \sum_{j=1}^N e^{-\varepsilon_j/K_B T}$ with N the total number of minimum energy conformations, $K_B T$ the thermal energy at room temperature ($T = 300$ K), and ε_s the energy gap between the lowest energy ground state conformation and conformation s . In table 6.8 the absolute ground state total energies were computed by *ab-initio* using the ADF program, where the ground state molecular structures were optimized at the B3LYP/TZ2P level of theory, and the minimum geometries were subsequently used in single-point energy calculations using BHandHLYP/TZ2P method.

Using the fraction of molecules in each conformation we estimated the number of molecules in the ground state for each conformation (P_s) and the relative concentration c in molL^{-1} . Table 6.8 shows the most probable geometries that are found in the ensemble.

Conformation (s)	Total Energy (eV)	$\frac{P_s}{P}$ (%)	P_s	Concentration (M)
anti_2	-64173.400	58	1.1×10^{18}	1.3×10^{-2}
anti_1	-64173.365	15	2.9×10^{17}	3.2×10^{-3}
syn-anti_2	-64173.362	13	2.5×10^{17}	2.8×10^{-3}
anti-syn_1	-64173.359	12	2.3×10^{17}	2.6×10^{-3}
anti-syn_2	-64173.305	1	1.9×10^{16}	2.2×10^{-4}
syn_2	-64173.282	1	1.9×10^{16}	2.2×10^{-4}

Table 6.8: Total energy of the ground state geometries computed at the BHandHLYP-TZ2P level of theory on the optimized B3LYP/TZVP minimum energy conformations, the fraction of molecules in each conformation given by Boltzmann statistical mechanics at $T = 300$ K ($\frac{P_s}{P}$), the number of molecules in each conformation in the ground state (P_s) and the relative concentration in $M = \text{molL}^{-1}$.

6.10.2 Calculation of the population transfer to the T_1 manifold upon direct photoexcitation below the CT band

To compute the absorption coefficient for the transition to the first triplet manifold ($a_{S_0^{\text{SOC}} \rightarrow T_{1,\xi}^{\text{SOC}}}(E_{S_0^{\text{SOC}} \rightarrow T_{1,\xi}^{\text{SOC}}})$), we used the eq. 6.9 with the experimental value of the optical path length $l = 3 \text{ mm}^7$ and the relative concentration of molecules c that we have in each conformation (table 6.8). The molar extinction coefficient $\varepsilon_{S_0^{\text{SOC}} \rightarrow T_{1,\xi}^{\text{SOC}}}$ was evaluated using the relative oscillator strengths for the transitions $S_0^{\text{SOC}} \rightarrow T_{1,\xi}^{\text{SOC}}$, computed at pSOC-TDA/BHandHLYP/TZ2P level of the theory using the ADF program. We used the equation

$$\varepsilon_{S_0^{\text{SOC}} \rightarrow T_{1,\xi}^{\text{SOC}}}(E_{S_0^{\text{SOC}} \rightarrow T_{1,\xi}^{\text{SOC}}}) = \frac{2.70 \times 10^4 \text{ Lmol}^{-1} \text{ cm}^{-1} \text{ eV}}{\text{FWHM}} f_{S_0^{\text{SOC}} \rightarrow T_{1,\xi}^{\text{SOC}}} \quad (6.38)$$

(e.g., see eq. 6.37) with broadening parameters $\text{FWHM} = (0.1 - 0.5) \text{ eV}$. To compute the number of molecules that populate the first triplet excited state manifold ($P_{T_1^{\text{SOC}}}$) we used the formula

$$P_{T_1^{\text{SOC}}} = \frac{I_0}{hc/\lambda_{\text{wav}}} \times \sum_{\xi} \left\{ 1 - 10^{-a_{S_0^{\text{SOC}} \rightarrow T_{1,\xi}^{\text{SOC}}}(E_{S_0^{\text{SOC}} \rightarrow T_{1,\xi}^{\text{SOC}}})} \right\} \quad (6.39)$$

(e.g., eqs. 6.8 and 6.10) with I_0 the experimental incident energy ($I_0 = 6.24 \times 10^{15} \text{ eV}^7$), c the speed of light and λ_{wav} the excitation wavelength of the transition $S_0^{\text{SOC}} \rightarrow T_{1,\xi}^{\text{SOC}}$ (we assumed that the ξ energy levels of the first triplet excited state ($T_{1,\xi}^{\text{SOC}}$) have the same energy).

6.10.3 Calculation of the population transfer to the T_2 manifold upon direct photoexcitation inside the CT band

For the computation of the absorbance to the second triplet excited state manifold at the excitation energy of the maximum of the CT band ($E_{S_0^{\text{SOC}} \rightarrow S_1^{\text{SOC}}}$) as well as at the excitation energy of the triplet manifold ($E_{S_0^{\text{SOC}} \rightarrow T_{2,\xi}^{\text{SOC}}}$), we used the equations 6.11 and 6.12 with $l = 3 \text{ mm}^7$ (the experimental value of the optical path length) and c the relative concentration of molecules that we have in each conformation (see table 6.8). The molar extinction coefficient at the energy E , $\varepsilon_{S_0^{\text{SOC}} \rightarrow T_{2,\xi}^{\text{SOC}}}(E)$ (where E denotes $E_{S_0^{\text{SOC}} \rightarrow S_1^{\text{SOC}}}$ and $E_{S_0^{\text{SOC}} \rightarrow T_{2,\xi}^{\text{SOC}}}$) was evaluated using the relative oscillator strengths for the transitions $S_0^{\text{SOC}} \rightarrow T_{2,\xi}^{\text{SOC}}$ computed at pSOC-TDA/BHandHLYP/TZ2P level of the theory using the ADF program. We used the equation

$$\varepsilon_{S_0^{\text{SOC}} \rightarrow T_{2,\xi}^{\text{SOC}}}(E_{S_0^{\text{SOC}} \rightarrow S_1^{\text{SOC}}}) = \frac{2.70 \times 10^4 \text{ Lmol}^{-1} \text{ cm}^{-1} \text{ eV}}{\text{FWHM}} f_{S_0^{\text{SOC}} \rightarrow T_{2,\xi}^{\text{SOC}}} \times \exp \left[-2.77 \left(\frac{E_{S_0^{\text{SOC}} \rightarrow S_1^{\text{SOC}}} - \Delta E_{S_0^{\text{SOC}} \rightarrow T_{2,\xi}^{\text{SOC}}}}{\text{FWHM}} \right)^2 \right] \quad (6.40)$$

	$f_{S_0^{\text{SOC}} \rightarrow T_{1,\xi}^{\text{SOC}}}$	$E_{S_0^{\text{SOC}} \rightarrow T_{1,\xi}^{\text{SOC}}}$ (eV)	$P_{T_1^{\text{SOC}}}$
anti_2	3.65×10^{-10}		
(58%)	4.70×10^{-10}	1.65	$(1.0 - 4.8) \times 10^{10}$
	4.59×10^{-9}		
anti_1	5.40×10^{-9}		
(15%)	2.33×10^{-10}	1.66	$(0.3 - 1.3) \times 10^{10}$
	3.67×10^{-11}		
syn-anti_2	6.77×10^{-9}		
(13%)	2.41×10^{-12}	1.62	$(0.3 - 1.4) \times 10^{10}$
	1.84×10^{-11}		
anti-syn_1	7.67×10^{-10}		
(12%)	1.58×10^{-10}	1.63	$(0.3 - 1.2) \times 10^{10}$
	5.83×10^{-9}		
anti-syn_2	6.49×10^{-10}		
(1%)	3.11×10^{-9}	1.67	$(1.8 - 8.9) \times 10^8$
	2.14×10^{-9}		
syn_2	8.96×10^{-10}		
(1%)	4.62×10^{-9}	1.63	$(1.9 - 9.3) \times 10^8$
	5.65×10^{-10}		

Table 6.9: Oscillator strength for the transition $S_0^{\text{SOC}} \rightarrow T_{1,\xi}^{\text{SOC}}$ ($f_{S_0^{\text{SOC}} \rightarrow T_{1,\xi}^{\text{SOC}}}$) and the relative excitation energies of the direct photo-excitation from S_0^{SOC} to $T_{1,\xi}^{\text{SOC}}$ ($E_{S_0^{\text{SOC}} \rightarrow T_{1,\xi}^{\text{SOC}}}$) for the different conformations, both computed at pSOC-TDA/BHandHLYP/TZ2P level of theory. The last column refers to the population of the first triplet excited state manifold (the range arising from FWHM = 0.1 eV - 0.5 eV).

for the extinction coefficient computed at the energy of the $S_0^{\text{SOC}} \rightarrow S_1^{\text{SOC}}$ excitation, and equation

$$\varepsilon_{S_0^{\text{SOC}} \rightarrow T_{2,\xi}^{\text{SOC}}}(E_{S_0^{\text{SOC}} \rightarrow T_{2,\xi}^{\text{SOC}}}) = \frac{2.70 \times 10^4 \text{ Lmol}^{-1} \text{ cm}^{-1} \text{ eV}}{\text{FWHM}} f_{S_0^{\text{SOC}} \rightarrow T_{2,\xi}^{\text{SOC}}} \quad (6.41)$$

for the extinction coefficient computed at the energy of the $S_0^{\text{SOC}} \rightarrow T_{2,\xi}^{\text{SOC}}$ excitation. We used broadening parameters FWHM = (0.1 - 0.5) eV. To compute the number of molecules that populate the second triplet excited state manifold ($P_{T_2^{\text{SOC}}}$) we used the formula,

$$P_{T_2^{\text{SOC}}}(E) = \frac{I_0}{hc/\lambda_{\text{wav}}} \times \sum_{\xi} \left\{ 1 - 10^{-a_{S_0^{\text{SOC}} \rightarrow T_{2,\xi}^{\text{SOC}}}(E)} \right\} \quad (6.42)$$

	$f_{S_0^{\text{SOC}} \rightarrow T_{2,\xi}^{\text{SOC}}}$	$E_{S_0^{\text{SOC}} \rightarrow T_{2,\xi}^{\text{SOC}}} \text{ (eV)}$	$E_{S_0^{\text{SOC}} \rightarrow S_1^{\text{SOC}}} \text{ (eV)}$	$P_{T_2^{\text{SOC}}}(E_{S_0^{\text{SOC}} \rightarrow S_1^{\text{SOC}}})$	$P_{T_2^{\text{SOC}}}(E_{S_0^{\text{SOC}} \rightarrow T_{2,\xi}^{\text{SOC}}})$
anti_2	3.66×10^{-8}				
(58%)	7.45×10^{-11}	2.65	2.76	$(0.6 - 5.3) \times 10^{10}$	$(0.5 - 2.5) \times 10^{11}$
	8.73×10^{-9}				
anti_1	1.61×10^{-7}				
(15%)	1.96×10^{-8}	2.64	2.76	$(0.4 - 5.2) \times 10^{10}$	$(0.5 - 2.6) \times 10^{11}$
	5.49×10^{-10}				
syn-anti_2	9.87×10^{-8}				
(13%)	5.22×10^{-8}	2.68	2.74	$(3.5 - 8.4) \times 10^{10}$	$(0.4 - 1.9) \times 10^{11}$
	1.59×10^{-9}				
anti-syn_1	4.05×10^{-8}				
(12%)	3.44×10^{-9}	2.63	2.75	$(0.1 - 1.1) \times 10^{10}$	$(1.1 - 5.7) \times 10^{10}$
	5.74×10^{-9}				
anti-syn_2	2.73×10^{-7}				
(1%)	6.35×10^{-8}	2.66	2.77	$(1.8 - 7.5) \times 10^9$	$(0.6 - 3.2) \times 10^{10}$
	2.32×10^{-11}				
syn_2	4.32×10^{-6}				
(1%)	1.09×10^{-8}	2.69	2.76	$(0.8 - 1.4) \times 10^{11}$	$(0.8 - 4.0) \times 10^{11}$
	9.18×10^{-11}				

Table 6.10: Oscillator strength for the transition $S_0^{\text{SOC}} \rightarrow T_{2,\xi}^{\text{SOC}}$ ($f_{S_0^{\text{SOC}} \rightarrow T_{2,\xi}^{\text{SOC}}}$) and the energies of the second triplet excited state manifold ($E_{S_0^{\text{SOC}} \rightarrow T_{2,\xi}^{\text{SOC}}}$) and the first singlet excited state ($E_{S_0^{\text{SOC}} \rightarrow S_1^{\text{SOC}}}$) for the different conformations, both computed at pSOC-TDA/BHandHLYP/TZ2P level of theory. The last two columns refer to the population of the second triplet excited state manifold at the energies $E_{S_0^{\text{SOC}} \rightarrow S_1^{\text{SOC}}}$ and $E_{S_0^{\text{SOC}} \rightarrow T_{2,\xi}^{\text{SOC}}}$ respectively (given the range FWHM = 0.1 eV - 0.5 eV).

with I_0 the experimental incident energy ($I_0 = 6.24 \times 10^{15} \text{ eV}$)⁷, c the speed of light and λ_{wav} the excitation wavelength of the transition $S_0^{\text{SOC}} \rightarrow T_{2,\xi}^{\text{SOC}}$.

6.10.4 Number of photoexcited Cbz-TBT molecules in the S_1^{SOC} state

To compute the number of molecules that populate the first singlet excited state upon photoexcitation, we used the formula in eq. 6.13, with I_0 the experimental incident energy ($I_0 = 6.24 \times 10^{15}$ eV),⁷ and λ_{wav} the excitation wavelength of the transition $S_0^{\text{SOC}} \rightarrow S_1^{\text{SOC}}$. The absorption coefficient for the excitation at the maximum of the CT band is given by the formula

$$a_{S_0^{\text{SOC}} \rightarrow S_1^{\text{SOC}}} \left(E_{S_0^{\text{SOC}} \rightarrow S_1^{\text{SOC}}} \right) = \varepsilon_{S_0^{\text{SOC}} \rightarrow S_1^{\text{SOC}}} \left(E_{S_0^{\text{SOC}} \rightarrow S_1^{\text{SOC}}} \right) cl \quad (6.43)$$

with $l = 3 \text{ mm}^7$ (the experimental value of the optical path length) and c the relative concentration of molecules that we have in each conformation (see table 6.8). The term $1 - 10^{-a_{S_0^{\text{SOC}} \rightarrow S_1^{\text{SOC}}} \left(E_{S_0^{\text{SOC}} \rightarrow S_1^{\text{SOC}}} \right)}$ equals to unity, since the absorbance of the transition $S_0^{\text{SOC}} \rightarrow S_1^{\text{SOC}}$ ($a_{S_0^{\text{SOC}} \rightarrow S_1^{\text{SOC}}}$) is sufficiently large. However, the molar extinction coefficient as well as the excitation energy at the maximum of the CT band calculated for the different geometric conformations, are very similar (see figure 6.17 and table 6.10), e.g., $\varepsilon_{S_0^{\text{SOC}} \rightarrow S_1^{\text{SOC}}} \approx 1 \times 10^5 M^{-1} \text{cm}^{-1}$ (computed with FWHM= 0.3 eV) and $E_{S_0^{\text{SOC}} \rightarrow S_1^{\text{SOC}}} \approx 2.8 \text{ eV}$. Hence, to compute the photo-excited molecules to the first singlet excited state in each conformation, we used $\frac{hc}{\lambda_{\text{wav}}} = 2.8 \text{ eV}$ multiplied by I_0 and the relative percentage of molecules in the ground state (table 6.8). Results are shown in table 6.11.

Conformation (s)	$\frac{P_s}{P}$ (%)	$P_{S_1^{\text{SOC}}}$
anti_2	58	1.3×10^{15}
anti_1	15	3.3×10^{14}
syn-anti_2	13	2.9×10^{14}
anti-syn_1	12	2.7×10^{14}
anti-syn_2	1	2.2×10^{13}
syn_2	1	2.2×10^{13}

Table 6.11: Number of molecules that populate the first singlet excited state ($P_{S_1^{\text{SOC}}}$) upon photoexcitation in each geometric conformation.

6.10.5 Calculation of the initial spin polarizations of the T_1 manifold in the presence of the external magnetic field B_0

The eigenstates of the spin Hamiltonian $\hat{H}^{\text{ZFS}} + \hat{H}^{\text{Zeeman}} = \hat{S}^T \tilde{D} \hat{S} + \beta_e \vec{B}_0^T \tilde{g} \hat{S}$ are not the eigenfunctions of the ZFS Hamiltonian (\hat{H}^{ZFS}). Instead, the Hamiltonian matrix $\tilde{H}^{\text{ZFS}} + \tilde{H}^{\text{Zeeman}}$ should be diagonalized in order to find the correct eigenstates. In the principal axis system X, Y, Z (where the D -tensor matrix is diagonal), the spin Hamiltonian is simplified as follows

$$\hat{H}^{\text{ZFS}} + \hat{H}^{\text{Zeeman}} = g\beta_e \left(B_X \hat{S}_X + B_Y \hat{S}_Y + B_Z \hat{S}_Z \right) + D_X \hat{S}_X^2 + D_Y \hat{S}_Y^2 + D_Z \hat{S}_Z^2 \quad (6.44)$$

where it is assumed that the g -value is fully isotropic. The $\hat{S}_X, \hat{S}_Y, \hat{S}_Z$ operators are quantized along the principal axes X, Y, Z respectively. It is always convenient to write the Hamiltonian matrix $\tilde{H}^{\text{ZFS}} + \tilde{H}^{\text{Zeeman}}$ in the basis of the eigenstates of \hat{S}_Z : $\{|T_{k, M_s}\rangle\}$, $M_s = 0, \pm 1$. To find the eigenstates of \hat{S}_Z we should first diagonalize the D -tensor matrix to determine the orientation of the principal axes X, Y, Z with respect to the molecular axis system (x, y, z) , $[R = \sum_r |r\rangle\langle r|R]$ where $r = x, y, z$ and $R = X, Y, Z$, namely, the orientation of \hat{S}_R with respect to the operators \hat{S}_r which are quantized along the molecular axes x, y, z (see figure 6.19). Thus, the \hat{S}_Z -operator matrix is written as a linear combination of the $\hat{S}_x, \hat{S}_y, \hat{S}_z$ operators. In the matrix form, the spin matrix \tilde{S}_Z is then written in the basis of the eigenstates of \hat{S}_z : $\{|T_{k, m_s}\rangle\}$, $m_s = 0, \pm 1$. Diagonalization of the \tilde{S}_Z matrix gives its eigenvalues $\{|T_{k, M_s}\rangle\}$ written as linear combinations of the triplet sublevels $\{|T_{k, m_s}\rangle\}$.

It is much convenient to choose the external magnetic field to be aligned in a

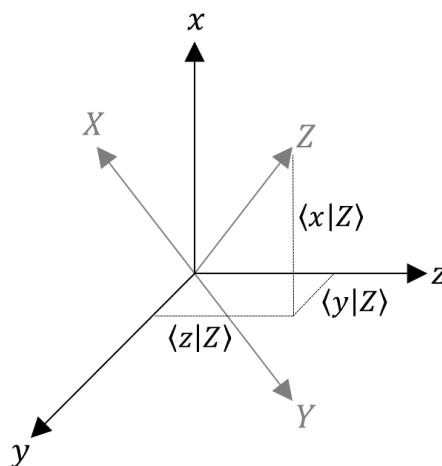


Figure 6.19: The principal axes X, Y, Z are derived from the molecular axes x, y, z . For example, the Z -axis behaves like a vector in the x, y, z plane. The magnitude of its components is given by $\langle r|Z\rangle$ with $r = x, y, z$ respectively.

direction parallel to one of the three D -tensor axes (X, Y and Z) e.g., only consider the molecules with their X, Y, Z axes aligned parallel to the external magnetic field

($\vec{B}_0||X, \vec{B}_0||Y, \vec{B}_0||Z$). We used the EasySpin software package¹⁴⁷ available for MATLAB (MathWorks) to compute the TR-EPR resonance field positions for absorption and emission with the field vector aligned with the tensor axes X, Y, Z respectively. We used the routine ‘eigfields’. Parameters included were the isotropic g -value ($g = 2$) and the D -tensor. We used the experimental ZFS parameters for the excitation wavelength $\lambda_{\text{wav}} = 630$ nm (below the CT band) ($D = 1345$ MHz, $E = 78$ MHz). For each value of the computed resonance fields ($\vec{B}_0||X, \vec{B}_0||Y, \vec{B}_0||Z$), we calculated the matrix elements of the Hamiltonian $\hat{H}^{\text{ZFS}} + \hat{H}^{\text{Zeeman}}$ using the routine ‘sham’. Parameters included were the g -value, the experimental D -tensor values and the magnetic field value at resonance in the X, Y and Z direction respectively. Diagonalization of the Hamiltonian $\hat{H}^{\text{ZFS}} + \hat{H}^{\text{Zeeman}}$ matrix gives the eigenstates of the k th triplet manifold $|T_{k,l}\rangle$, $|T_{k,c}\rangle$, and $|T_{k,u}\rangle$, where l refers to the lowest-in-energy eigenstate, c to the center-in-energy eigenstate and u to the upper-in-energy eigenstate.

To estimate the population transfer to the first triplet excited state sublevels $\{|T_{1,i}\rangle\}$, $i = l, c, u$ we should first calculate the oscillator strengths for the transitions $S_0^{\text{SOC}} \rightarrow T_{1,i}$, following the procedure described in section 6.4.1. To this end, we write the eigenstates $|T_{1,i}\rangle$ in the basis of $\{|T_{1,\xi}^{\text{SOC}}\rangle\}$ manifold, as $|T_{1,i}\rangle = \sum_{\xi} |T_{1,\xi}^{\text{SOC}}\rangle \langle T_{1,\xi}^{\text{SOC}}|T_{1,i}\rangle$. Since the oscillator strength for the transition $S_0^{\text{SOC}} \rightarrow T_{1,i}$ is related to the squared transition dipole moment

$|\langle S_0^{\text{SOC}}|\hat{\mu}|T_{1,i}\rangle|^2 = \sum_{\xi} |\langle T_{1,\xi}^{\text{SOC}}|T_{1,i}\rangle|^2 |\langle S_0^{\text{SOC}}|\hat{\mu}|T_{1,\xi}^{\text{SOC}}\rangle|^2$, its value can be approximated using the calculated oscillator strengths of the transitions $S_0^{\text{SOC}} \rightarrow T_{1,\xi}^{\text{SOC}}$ ($f_{S_0^{\text{SOC}} \rightarrow T_{1,\xi}^{\text{SOC}}}$) via $f_{S_0^{\text{SOC}} \rightarrow T_{1,i}} = \sum_{\xi} |\langle T_{1,\xi}^{\text{SOC}}|T_{1,i}\rangle|^2 f_{S_0^{\text{SOC}} \rightarrow T_{1,\xi}^{\text{SOC}}}$.

The population transfer to the $\{|T_{1,i}\rangle\}$ manifold was calculated according to eq. 6.39, since the extinction coefficient was computed by substituting the oscillator strength $f_{S_0^{\text{SOC}} \rightarrow T_{1,i}}$ in 6.38. Table 6.12 shows the absolute populations computed for the most probable geometry (anti_2) in the cases where the external magnetic field is aligned parallel to the axes X, Y and Z respectively. The relative populations $\tilde{\Pi}_i^{\text{ex}} = \frac{P_{S_0^{\text{SOC}} \rightarrow T_{1,i}}}{\sum_{i=l,c,u} P_{S_0^{\text{SOC}} \rightarrow T_{1,i}}}$, $i = l, c, u$ are also shown in the table.

The polarization p is defined as the population difference between the two states that the TR-EPR absorption and emission occur, $p_{i \rightarrow j} = |\tilde{\Pi}_i^{\text{ex}} - \tilde{\Pi}_j^{\text{ex}}|$, $i = c, j = l/u$. We used the routine ‘levelsplot’ of the EasySpin software to compute the energy level diagram with the relative transitions at resonances for our spin system (see the first row of figure 6.20). Parameters included were the isotropic g -value and the experimental D -tensor ($D = 1345$ MHz, $E = 78$ MHz). Our results show that the transitions occur between $|T_{1,l}\rangle$ and $|T_{1,c}\rangle$ states, and between $|T_{1,u}\rangle$ and $|T_{1,c}\rangle$ states. The polarizations for the relative transitions are shown in figure 6.20. The EPR spectra for each case of magnetic field position ($\vec{B}_0||X, \vec{B}_0||Y, \vec{B}_0||Z$) were computed using the routine ‘pepper’(see the second row of figure 6.20). In addition to the parameters g and D , we also include the computed triplet sublevel populations (p_1, p_2, p_3) in zero-field ($|T_{1,X}\rangle, |T_{1,Y}\rangle$ and $|T_{1,Z}\rangle$) (see section 6.10.6 below) as well as Lorentzian lineshapes of

	$\vec{B}_0 X$	$\vec{B}_0 Y$	$\vec{B}_0 Z$
$f_{S_0^{\text{SOC}} \rightarrow T_{1,l}}$	2.26×10^{-9}	5.29×10^{-10}	2.49×10^{-9}
$f_{S_0^{\text{SOC}} \rightarrow T_{1,c}}$	6.31×10^{-10}	4.36×10^{-9}	4.39×10^{-10}
$f_{S_0^{\text{SOC}} \rightarrow T_{1,u}}$	2.53×10^{-9}	5.41×10^{-10}	2.50×10^{-9}
$P_{S_0^{\text{SOC}} \rightarrow T_{1,l}}$	$(0.4 - 2.0) \times 10^{10}$	$(0.9 - 4.6) \times 10^9$	$(0.4 - 2.2) \times 10^{10}$
$P_{S_0^{\text{SOC}} \rightarrow T_{1,c}}$	$(1.1 - 5.5) \times 10^9$	$(0.8 - 3.8) \times 10^{10}$	$(0.8 - 3.8) \times 10^9$
$P_{S_0^{\text{SOC}} \rightarrow T_{1,u}}$	$(0.4 - 2.2) \times 10^{10}$	$(0.9 - 4.7) \times 10^9$	$(0.4 - 2.2) \times 10^{10}$
$\tilde{\Pi}_l^{ex}$	0.42	0.10	0.46
$\tilde{\Pi}_c^{ex}$	0.12	0.80	0.08
$\tilde{\Pi}_u^{ex}$	0.47	0.10	0.46

Table 6.12: Oscillator strengths for the transitions $S_0^{\text{SOC}} \rightarrow T_{1,i}$, $i = l, c, u$ together with the number of molecules that populate the first triplet excited state manifold $\{|T_{1,i}\rangle\}$, $i = l, c, u$ upon photoexcitation from the singlet ground state (given the range FWHM = 0.1 eV - 0.5 eV). The relative populations $\tilde{\Pi}_i^{ex}$ are also shown.

2.08 mT width (see ref. 7). Finally, the powder spectrum was also computed (third row of figure 6.20). We conclude that our theoretical parameters (e.g., $p_{i \rightarrow j}$) well reproduce the experimental spectra.

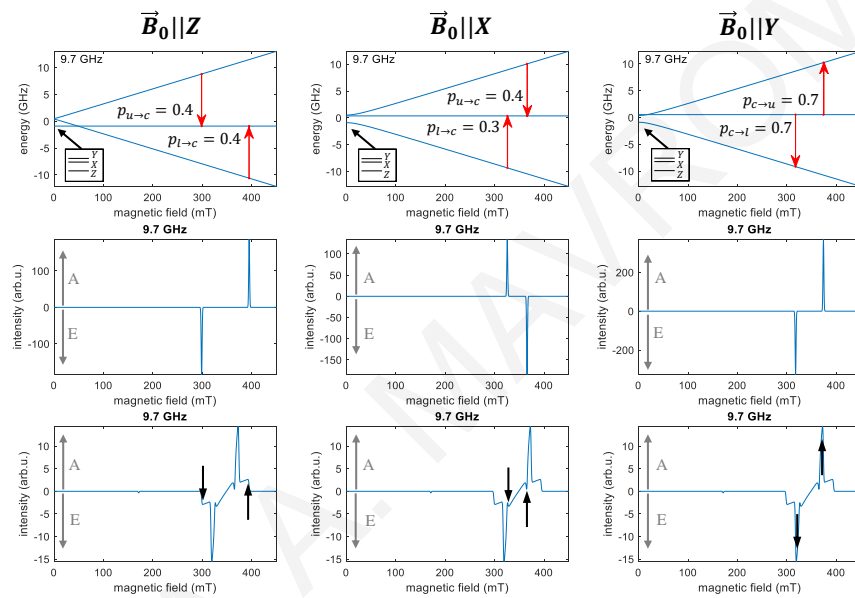


Figure 6.20: *First row:* Energy level diagram of the first triplet excited state sublevels as a function of the static magnetic field \vec{B}_0 aligned with the dipolar axes X, Y, Z respectively. Transitions occur at the resonance fields (down arrows correspond to emissive lines and up arrows to absorptive lines). The inset shows the ZFS triplet states ($|T_{1,X}\rangle, |T_{1,Y}\rangle, |T_{1,Z}\rangle$). *Second row:* TR-EPR spectra computed in the cases where the magnetic field \vec{B}_0 is aligned with the molecular X, Y or Z axis. *Third row:* The full powder TR-EPR spectra. Here, the transitions corresponding to the canonical field orientations (X, Y, Z) are shown as picks in the powder spectrum as indicated by the dark arrows. Lorentzian lineshape was set to 2.08 mT. The transitions can be either absorptive (A) or emissive (E).

6.10.6 Calculation of the ZFS polarizations of the T_1 manifold

The matrix elements of the ZFS Hamiltonian $\hat{H}^{\text{ZFS}} = \hat{S}^T \hat{D} \hat{S}$ were computed using the routine ‘zfield’ of the EasySpin software. Parameters included were the isotropic g -value and the D -tensor. We used the experimental ZFS parameters for the excitation wavelength $\lambda_{\text{wav}} = 630$ nm (below the CT band) ($D = 1345$ MHz, $E = 78$ MHz). Diagonalization of the ZFS Hamiltonian matrix gives the eigenstates of the k th triplet manifold $|T_{k,X}\rangle$, $|T_{k,Y}\rangle$, and $|T_{k,Z}\rangle$, where X, Y and Z is the principal axis system of the D -tensor.

To estimate the population transfer to first triplet excited state sublevels $\{|T_{1,R}\rangle\}$, $R = X, Y, Z$ we should first calculate the oscillator strengths for the transitions $S_0^{\text{SOC}} \rightarrow T_{1,R}$, following the procedure described in previous sections. To this end, we write the eigenstates $|T_{1,R}\rangle$ in the basis of $\{|T_{1,\xi}^{\text{SOC}}\rangle\}$ manifold, as $|T_{1,R}\rangle = \sum_{\xi} |T_{1,\xi}^{\text{SOC}}\rangle \langle T_{1,\xi}^{\text{SOC}} | T_{1,R}\rangle$. Since the oscillator strength for the transition $S_0^{\text{SOC}} \rightarrow T_{1,R}$ is related to the squared transition dipole moment $|\langle S_0^{\text{SOC}} | \hat{\mu} | T_{1,R}\rangle|^2 = \sum_{\xi} |\langle T_{1,\xi}^{\text{SOC}} | T_{1,R}\rangle|^2 |\langle S_0^{\text{SOC}} | \hat{\mu} | T_{1,\xi}^{\text{SOC}}\rangle|^2$, its value can be given using the calculated oscillator strengths of the transitions $S_0^{\text{SOC}} \rightarrow T_{1,\xi}^{\text{SOC}}$ ($f_{S_0^{\text{SOC}} \rightarrow T_{1,\xi}^{\text{SOC}}}$) via $f_{S_0^{\text{SOC}} \rightarrow T_{1,R}} \approx \sum_{\xi} |\langle T_{1,\xi}^{\text{SOC}} | T_{1,R}\rangle|^2 f_{S_0^{\text{SOC}} \rightarrow T_{1,\xi}^{\text{SOC}}}$.

Having calculated the oscillator strengths $f_{S_0^{\text{SOC}} \rightarrow T_{1,R}}$, we used eq. 6.38 to estimate the extinction coefficient $\varepsilon_{S_0^{\text{SOC}} \rightarrow T_{1,R}}$ and then the population transfer to the $\{|T_{1,R}\rangle\}$ manifold according to eq. 6.39. The table below, show the absolute populations computed for the most probable geometry (anti_2). The relative populations $\tilde{\Pi}_R^{\text{ZFS}} = \frac{P_{S_0^{\text{SOC}} \rightarrow T_{1,R}}}{\sum_{R=X,Y,Z} P_{S_0^{\text{SOC}} \rightarrow T_{1,R}}}$, $R = X, Y, Z$ are also shown in the table 6.13.

	$R = X$	$R = Y$	$R = Z$
$f_{S_0^{\text{SOC}} \rightarrow T_{1,R}}$	6.31×10^{-10}	4.36×10^{-9}	4.39×10^{-10}
$P_{S_0^{\text{SOC}} \rightarrow T_{1,R}}$	$(1.1 - 5.5) \times 10^9$	$(0.8 - 3.8) \times 10^{10}$	$(0.8 - 3.8) \times 10^9$
$\tilde{\Pi}_R^{\text{ZFS}}$	0.12	0.80	0.08

Table 6.13: Number of molecules that populate the first triplet excited state manifold $\{|T_{1,R}\rangle\}$, $R = X, Y, Z$ upon photoexcitation from the singlet ground state together with the relative oscillator strengths $f_{S_0^{\text{SOC}} \rightarrow T_{1,R}}$ (given the range FWHM = 0.1 eV - 0.5 eV). The relative populations $\tilde{\Pi}_R^{\text{ZFS}}$ are also shown.

6.11 Computation of singlet-to-triplet and triplet-to-triplet transition rates

The rate constant for the ISC transition between singlet and triplet states is given by eq. 6.16. The simulations were performed using the fft integration method available in MATLAB. fft computes the Discrete Fourier Transform (DFT) of a function using a Fast Fourier Transform (FFT) algorithm. The integration region was set equals to $-10 - 10$ psec with 262144 integration points. Line broadening was included using Lorentzian lines for homogeneous broadening equals to $\Gamma = 10^{12} \text{ sec}^{-1}$. The temperature was set to $T = 80$ K (TR-EPR experimental temperature⁷) (see details in chapter 7 and appendices A and C).

Table 6.14 shows the total rate constants for the transitions $S_1 \rightarrow T_2$ ($k_{S_1 \rightarrow T_2} = \sum_{m_s} k_{S_1 \rightarrow T_{2,m_s}}$), $S_1 \rightarrow T_1$ ($k_{S_1 \rightarrow T_1} = \sum_{m_s} k_{S_1 \rightarrow T_{1,m_s}}$) and $T_2 \rightarrow T_1$ ($k_{T_2 \rightarrow T_1} = \sum_{m_{s'}} \sum_{m_s} k_{T_{2,m_s} \rightarrow T_{1,m_{s'}}$), as well as the fluorescence and phosphorescence rates ($k_{S_1 \rightarrow S_0}$, $k_{T_1 \rightarrow S_0} = \sum_{m_s} k_{T_{1,m_s} \rightarrow S_0}$ and $k_{T_2 \rightarrow S_0} = \sum_{m_s} k_{T_{2,m_s} \rightarrow S_0}$) together with the corresponding energy differences (ΔE_{IJ} as shown in figure 6.9).

Figure 6.21 shows the population transfer to the first and second triplet excited states as a function of time computed for anti-syn_1 (12%) geometric conformation by solving the approximate kinetic equations for the populations (e.g., see eq. 6.18). Results are similar to those computed for the most probable geometry (anti_2) (see section 6.4.2), namely on the time scale of the TR-EPR experiment ($0.5 \mu\text{sec}$), there is no substantial increase in the total second triplet excited state population that arises from the lowest singlet state following the excitation in the CT band. Even though the population transfer to the second triplet excited state and the first triplet excited state is faster in the case of anti-syn_1 compared to anti_2, (T_2 retains measurable values for $6 \mu\text{sec}$ and T_1 gets measurable values after $4 \mu\text{sec}$) the time scale is still longer than the experimental time between optical excitation and TR-EPR signal detection (which is approximately $0.5 \mu\text{sec}$ ⁷).

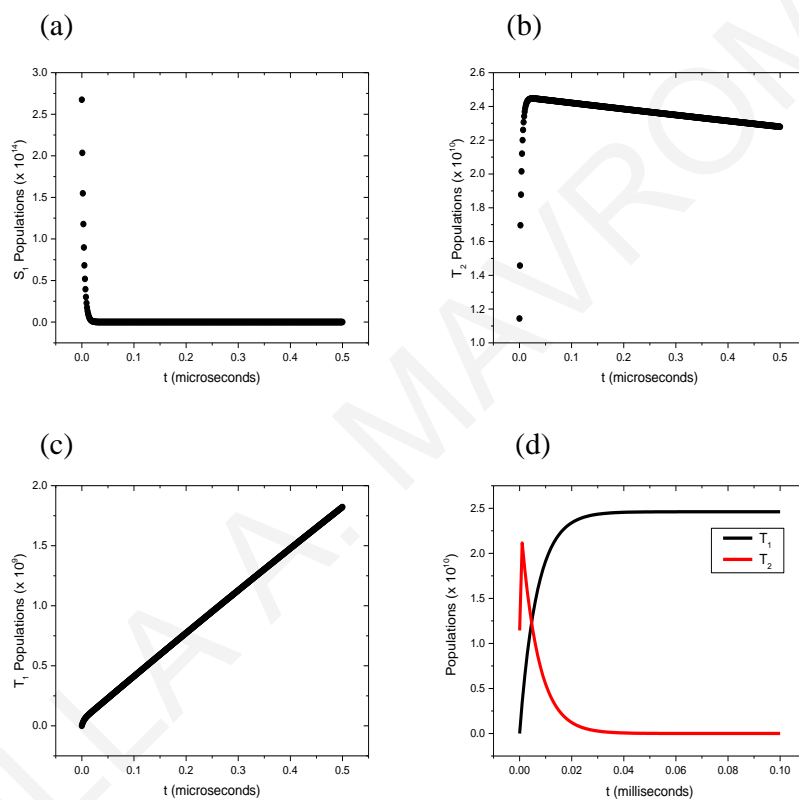


Figure 6.21: Population transfer to the first and second triplet excited states as a function of time computed for anti-syn₁ (12%) geometric conformation. (a) Population of S_1 from 0 to 0.5 μsec . (b) Population transfer to T_2 from 0 to 0.5 μsec . (c) Population transfer to T_1 from 0 to 0.5 μsec and (d) population transfer to T_2 and T_1 for larger time scales than 0.5 μsec , namely from 0 to 0.1 msec. Initial condition for T_2 : $P_{T_2}(t = 0) = 1.1 \times 10^{10}$.

	I/J	ΔE_{IJ} (eV)	$k_{I \rightarrow J}$ (1/sec)	$k_{S_1 \rightarrow S_0}$ (1/sec)	$k_{T_1 \rightarrow S_0}$ (1/sec)	$k_{T_2 \rightarrow S_0}$ (1/sec)
anti_2	S_1/T_2	0.16	4.00×10^3			
(58%)	S_1/T_1	1.23	1.77×10^1	2.78×10^8	6.41×10^{-2}	2.47×10^0
	T_2/T_1	1.07	7.63×10^3			
anti_1	S_1/T_2	0.15	3.97×10^3			
(15%)	S_1/T_1	1.20	2.00×10^1	2.74×10^8	0.00	1.09×10^{-1}
	T_2/T_1	1.05	2.60×10^2			
syn-anti_2	S_1/T_2	0.08	1.24×10^1			
(13%)	S_1/T_1	1.26	4.60×10^1	2.75×10^8	0.00	2.19×10^2
	T_2/T_1	1.17	3.46×10^5			
anti-syn_1	S_1/T_2	0.17	1.34×10^4			
(12%)	S_1/T_1	1.19	5.42×10^1	2.73×10^8	0.00	3.44×10^1
	T_2/T_1	1.02	1.50×10^5			
anti-syn_2	S_1/T_2	0.16	2.46×10^2			
(1%)	S_1/T_1	1.26	1.93×10^0	2.78×10^8	6.04×10^{-2}	0.00
	T_2/T_1	1.10	2.56×10^1			
syn_2	S_1/T_2	0.08	1.61×10^2			
(1%)	S_1/T_1	1.27	1.28×10^1	2.75×10^8	0.00	2.14×10^2
	T_2/T_1	1.19	3.12×10^5			

Table 6.14: Total rate constants for the transitions $S_1 \rightarrow T_2$, $S_1 \rightarrow T_1$ and $T_2 \rightarrow T_1$ and the corresponding energy differences $\Delta E_{S_1, T_1}$ (or equivalently $\Delta E_{S_1, T_1, m_s}$), $\Delta E_{S_1, T_2}$ (or equivalently $\Delta E_{S_1, T_2, m_s}$), $\Delta E_{T_2, T_1}$ (or equivalently $\Delta E_{T_2, m_s, T_1, m_s}$) computed for the most probable geometric conformations of the Cbz-TBT molecule.

6.12 Theoretical calculations of the EPR parameters

6.12.1 Zero-field splitting parameters

The EPR-ZFS parameters of the first triplet excited state (T_1) of the molecule in its different molecular conformations were calculated using the ORCA program package at the DFT level of theory, where only the spin-spin contribution to the ZFS parameter D was considered.¹³⁰ We used the spin-unrestricted natural orbital (UNO) approach⁹³ in combination with the B3LYP functional¹⁰⁴ and the def2-TZVP basis set without symmetry constraints.

Additional computations were performed using the distributed point-dipole (DPD) approximation.¹⁴⁹ (see eq. D.1 and appendix D for further information). The ZFS parameters for each conformation computed with UNO-B3LYP and DPD methods are summarized in table 6.15. Figure 6.22 shows the canonical orientations of the ZFS tensors (principal axis system X, Y and Z) for each conformation computed with UNO-B3LYP/def2-TZVP method. Below, we also show the optimized atomic coordinates of T_1 excited state of the six different conformations computed at BHandHLYP/TZ2P level of theory.

Geometry	DPD Model		UNO-B3LYP	
	D (MHz)	E (MHz)	D (MHz)	E (MHz)
anti_2	1319	180	825	192
anti_1	1229	210	809	194
syn-anti_2	1349	210	798	186
anti-syn_1	1289	180	810	190
anti-syn_2	1319	119	816	189
syn_2	1379	180	792	181

Table 6.15: ZFS parameters in MHz calculated at the minimum energy conformation of the T_1 manifold excited state for each geometric conformation at UNO-B3LYP/def2-TZVP level of theory and using the distributed Point-Dipole (DPD) approximation.

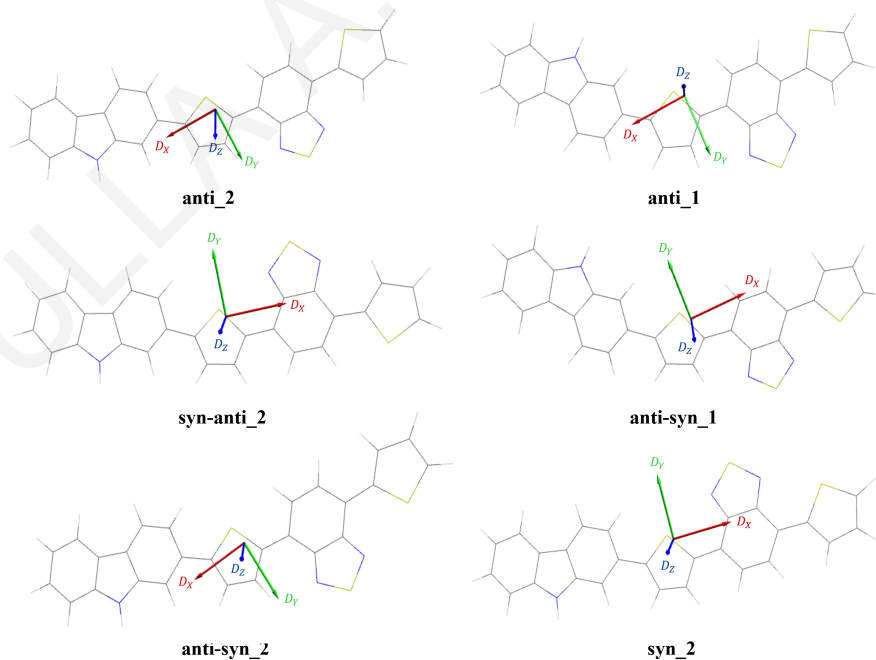


Figure 6.22: Orientation of the principal axes of the ZFS tensor computed at UNO-B3LYP/def2-TZVP level of theory for the different geometric conformations. To visualize the tensor, we used the Avogadro software package.

1) anti_2 T₁

C	-1.3896	0.5553	-1.5268
C	1.1773	0.7247	-0.5285
C	-0.8326	-0.5732	-0.9686
C	-0.6867	1.7557	-1.5914
C	0.5932	1.8469	-1.0957
C	0.4541	-0.4756	-0.4721
H	-2.3880	0.5083	-1.9206
H	-1.1518	2.6165	-2.0337
H	1.1310	2.7757	-1.1483
H	3.4892	-2.5029	1.3911
H	5.5500	1.2333	1.1015
H	-1.3816	-1.4957	-0.9223
C	2.4570	0.4600	0.0715
C	4.6627	-0.7066	1.3176
C	2.4500	-0.8880	0.4611
C	3.5881	1.2212	0.3175
C	4.6701	0.6429	0.9304
C	3.5300	-1.4766	1.0797
H	0.9633	-2.3755	0.2918
H	3.6262	2.2553	0.0286
N	1.2353	-1.4332	0.1274
H	9.1887	0.5596	3.8416
S	10.9025	-4.8725	4.7439
H	11.2308	0.8761	4.9847
C	7.9844	-1.7334	3.1565
C	7.3054	-2.8879	2.7711
C	6.1132	-2.6358	2.1134
C	5.8198	-1.3001	1.9586
S	7.0639	-0.3363	2.6604
C	9.2028	-1.6018	3.8332
H	7.6949	-3.8631	2.9696
H	5.4840	-3.4158	1.7323
C	14.8889	0.1201	7.0355
C	14.9619	-1.2358	7.0564
C	13.8686	-1.8531	6.4354
C	12.9443	-0.9570	5.9311
S	13.4796	0.6706	6.2550
H	15.5896	0.8217	7.4380
H	15.7747	-1.7740	7.5033
H	13.7385	-2.9100	6.3470
C	11.7309	-1.2056	5.2476
C	9.9945	-2.7216	4.2636
C	11.2443	-2.5236	4.9612
C	9.7411	-0.3097	4.1433
C	10.9069	-0.1296	4.7960
N	9.7080	-3.9862	4.0906
N	11.8308	-3.6523	5.2745

2) anti_1 T₁

C	-0.6688	2.0601	-1.4026
C	0.9995	0.0869	-0.4338
C	0.5254	2.4397	-0.8326
C	-1.0361	0.7197	-1.4938
C	-0.2093	-0.2686	-1.0130
C	1.3527	1.4419	-0.3512
H	-1.3312	2.8143	-1.7853
H	-1.9751	0.4594	-1.9448
H	-0.4979	-1.3011	-1.0860
H	4.9329	0.6520	1.4718
H	3.6754	-3.4264	1.1495
H	0.8015	3.4759	-0.7663
C	2.0806	-0.6542	0.1558
C	4.4593	-1.4417	1.3877
C	3.0373	0.2845	0.5675
C	2.3302	-2.0012	0.3727
C	3.4980	-2.3832	0.9783
C	4.2149	-0.0900	1.1756
H	3.0653	2.3899	0.4373
H	1.6155	-2.7453	0.0729
N	2.5818	1.5403	0.2539
H	8.8529	0.3982	3.7838
S	11.1927	-4.7723	4.8039
H	10.8708	0.9800	4.8631
C	7.9076	-2.0352	3.1881
C	7.3567	-3.2697	2.8446
C	6.1343	-3.1735	2.2039
C	5.6841	-1.8841	2.0212
S	6.8247	-0.7660	2.6742
C	9.1135	-1.7465	3.8344
H	7.8552	-4.1890	3.0647
H	5.5893	-4.0330	1.8688
C	14.6483	0.7091	6.8200
C	14.8593	-0.6292	6.9076
C	13.8249	-1.3856	6.3408
C	12.8060	-0.6155	5.8132
S	13.1780	1.0725	6.0423
H	15.2798	1.4980	7.1718
H	15.7294	-1.0585	7.3643
H	13.8024	-2.4535	6.3081
C	11.6111	-1.0213	5.1718
C	10.0365	-2.7554	4.2792
C	11.2695	-2.3944	4.9403
C	9.5077	-0.3932	4.0946
C	10.6607	-0.0615	4.7108
N	9.8928	-4.0493	4.1517
N	11.9865	-3.4389	5.2741

3) syn-anti_2 T₁

C	-1.4222	0.4457	-1.5634
C	1.1256	0.6890	-0.5328
C	-0.8207	-0.6780	-1.0427
C	-0.7725	1.6774	-1.5751
C	0.4977	1.8055	-1.0632
C	0.4557	-0.5432	-0.5288
H	-2.4142	0.3702	-1.9689
H	-1.2716	2.5337	-1.9884
H	0.9944	2.7583	-1.0740
H	3.5547	-2.4996	1.3007
H	5.4468	1.3363	1.1769
H	-1.3292	-1.6245	-1.0370
C	2.4089	0.4593	0.0726
C	4.6482	-0.6501	1.3135
C	2.4578	-0.9005	0.4151
C	3.5021	1.2609	0.3592
C	4.5999	0.7109	0.9683
C	3.5545	-1.4612	1.0295
H	1.0393	-2.4447	0.1751
H	3.4971	2.3053	0.1073
N	1.2727	-1.4869	0.0445
H	9.4774	-3.5688	4.1249
S	10.4175	2.1115	4.3499
H	11.5189	-3.4613	5.3035
C	7.9837	-1.5478	3.1725
C	7.3140	-2.7312	2.8411
C	6.1210	-2.5319	2.1767
C	5.8177	-1.2039	1.9654
S	7.0551	-0.1894	2.6111
C	9.2003	-1.4384	3.8547
H	7.6954	-3.7037	3.0749
H	5.4999	-3.3385	1.8413
C	14.9913	-1.9705	7.2840
C	14.8775	-0.6256	7.1399
C	13.7270	-0.2451	6.4356
C	12.9491	-1.3141	6.0353
S	13.6919	-2.8005	6.5612
H	15.7697	-2.5149	7.7768
H	15.5961	0.0702	7.5268
H	13.4562	0.7655	6.2173
C	11.7298	-1.3172	5.3150
C	9.8318	-0.1875	4.1477
C	11.0802	-0.1210	4.8663
C	9.8991	-2.6030	4.3177
C	11.0663	-2.5392	4.9920
N	9.3720	0.9892	3.8127
N	11.4972	1.1097	5.0345

4) anti-syn_1 T₁

C	-1.4152	-0.0834	0.1363
C	0.7338	1.6235	0.1333
C	-1.5561	1.2363	0.5583
C	-0.1966	-0.5575	-0.2906
C	0.8948	0.2977	-0.2956
C	-0.4886	2.1055	0.5633
C	2.2763	0.1525	-0.6664
C	4.9843	0.5603	-1.2004
C	2.8870	1.3947	-0.4432
C	3.0449	-0.8911	-1.1596
C	4.3751	-0.6870	-1.4195
C	4.2227	1.6100	-0.7027
S	14.9718	4.5906	-1.9210
N	13.3644	2.3464	-2.7356
N	1.9432	2.2673	0.0368
N	11.3788	0.9208	-2.9553
C	15.6208	6.0115	-1.2445
C	14.7178	6.6885	-0.4861
C	13.4751	6.0534	-0.4473
C	13.4243	4.8775	-1.1821
C	9.9242	2.3466	-1.5833
C	9.9591	3.5637	-0.8264
C	11.0560	4.3390	-0.7075
C	12.3049	4.0256	-1.3299
C	12.3269	2.8174	-2.0920
C	11.1590	1.9806	-2.2208
H	9.0626	3.8769	-0.3263
S	12.9268	0.9580	-3.4533
H	-0.6054	3.1224	0.8902
H	-2.5180	1.5840	0.8869
H	4.6606	2.5775	-0.5413
H	2.6084	-1.8574	-1.3332
H	16.6391	6.2798	-1.4372
H	14.9375	7.6058	0.0240
H	-2.2692	-0.7343	0.1454
H	-0.0941	-1.5767	-0.6154
H	4.9673	-1.5047	-1.7808
H	2.1090	3.2175	0.2792
H	12.6407	6.4394	0.1013
H	10.9823	5.2322	-0.1205
C	8.7495	1.5912	-1.6836
C	8.5181	0.3975	-2.3628
C	7.2155	-0.0625	-2.2498
C	6.3922	0.7409	-1.4953
S	7.2745	2.0972	-0.9003
H	6.8712	-0.9557	-2.7320
H	9.2884	-0.0925	-2.9188

5) anti-syn_2 T₁

C	-1.3781	0.5897	-1.5182
C	1.1906	0.7392	-0.5215
C	-0.8285	-0.5438	-0.9627
C	-0.6669	1.7853	-1.5809
C	0.6139	1.8666	-1.0860
C	0.4592	-0.4561	-0.4669
H	-2.3771	0.5504	-1.9114
H	-1.1263	2.6502	-2.0212
H	1.1581	2.7918	-1.1371
H	3.4817	-2.5074	1.3919
H	5.5680	1.2144	1.1059
H	-1.3839	-1.4624	-0.9179
C	2.4690	0.4645	0.0770
C	4.6670	-0.7192	1.3201
C	2.4529	-0.8841	0.4643
C	3.6053	1.2175	0.3234
C	4.6837	0.6305	0.9347
C	3.5293	-1.4810	1.0817
H	0.9559	-2.3610	0.2927
H	3.6504	2.2517	0.0360
N	1.2343	-1.4202	0.1303
H	9.1894	0.5192	3.8643
S	10.9068	-4.9138	4.7418
H	11.2275	0.8299	5.0112
C	7.9812	-1.7651	3.1610
C	7.3023	-2.9153	2.7675
C	6.1112	-2.6572	2.1074
C	5.8210	-1.3209	1.9604
S	7.0647	-0.3639	2.6719
C	9.1994	-1.6405	3.8416
H	7.6897	-3.8924	2.9611
H	5.4819	-3.4337	1.7194
C	15.0906	-1.1293	7.1621
C	14.6872	0.1528	6.9556
C	13.4723	0.2232	6.2714
C	12.9383	-1.0167	5.9498
S	13.9976	-2.2693	6.5268
H	15.9800	-1.4588	7.6585
H	15.2410	1.0112	7.2820
H	12.9986	1.1496	6.0196
C	11.7259	-1.2577	5.2629
C	9.9875	-2.7646	4.2655
C	11.2332	-2.5652	4.9650
C	9.7410	-0.3522	4.1618
C	10.9056	-0.1733	4.8173
N	9.7078	-4.0300	4.0881
N	11.8274	-3.6884	5.2776

6) syn_2 T₁

C	-1.4321	0.4175	-1.5440
C	1.1278	0.6708	-0.5461
C	-0.8353	-0.6943	-0.9930
C	-0.7718	1.6421	-1.6018
C	0.5044	1.7752	-1.1062
C	0.4473	-0.5546	-0.4963
H	-2.4286	0.3379	-1.9372
H	-1.2673	2.4890	-2.0380
H	1.0093	2.7226	-1.1526
H	3.5481	-2.4789	1.3668
H	5.4726	1.3323	1.0997
H	-1.3518	-1.6355	-0.9518
C	2.4151	0.4491	0.0542
C	4.6569	-0.6405	1.3063
C	2.4557	-0.8996	0.4387
C	3.5174	1.2499	0.3055
C	4.6170	0.7094	0.9207
C	3.5539	-1.4504	1.0599
H	1.0213	-2.4377	0.2628
H	3.5189	2.2858	0.0207
N	1.2618	-1.4868	0.0990
H	9.5229	-3.5269	4.0893
S	10.3896	2.1586	4.4133
H	11.5662	-3.4122	5.2597
C	7.9965	-1.5177	3.1682
C	7.3432	-2.7042	2.8229
C	6.1481	-2.5123	2.1575
C	5.8302	-1.1868	1.9599
S	7.0513	-0.1649	2.6220
C	9.2131	-1.3987	3.8516
H	7.7367	-3.6746	3.0458
H	5.5385	-3.3219	1.8082
C	15.0538	-0.6956	7.2264
C	14.8560	-2.0378	7.1387
C	13.6798	-2.3577	6.4567
C	12.9699	-1.2511	6.0168
S	13.8124	0.1978	6.4791
H	15.8717	-0.1880	7.6948
H	15.5280	-2.7666	7.5478
H	13.3589	-3.3654	6.2899
C	11.7468	-1.2616	5.3042
C	9.8250	-0.1430	4.1627
C	11.0728	-0.0770	4.8776
C	9.9324	-2.5585	4.2958
C	11.1017	-2.4924	4.9659
N	9.3528	1.0360	3.8541
N	11.4812	1.1511	5.0728

6.12.2 EPR g-tensor

The g-tensor was computed at the optimized first triplet excited state (T_1) of the molecule using spin-unrestricted DFT and the ‘eprnmr’ module of ORCA program package. We used the B3LYP functional in combination with the def2-TZVP basis set without symmetry constraints. The computations show that the g-value is approximately isotropic for each geometric conformation (principal values are approximately the same) with a value of $g \approx 2$.⁶⁸

geometry	g_x	g_y	g_z
anti_2	2.002	2.003	2.004
anti_1	2.002	2.004	2.004
syn-anti_2	2.002	2.003	2.005
anti-syn_1	2.002	2.003	2.005
anti-syn_2	2.002	2.003	2.005
syn_2	2.002	2.003	2.004

Table 6.16: Principal values of the g-tensor computed at the minimum energy conformation of the T_1 manifold excited state for each geometric conformation using B3LYP/def2-TZVP method.

6.12.3 Anisotropic spectra broadenings - D-strains

The simulations of the TR-EPR spectra were performed using the EasySpin software and the routine ‘pepper’. Parameters included were the g-tensor ($g \approx 2$), the experimental ZFS parameters (D and E) and the experimental triplet sublevel populations (p_1, p_2, p_3) [see table 6.2 in the main text]. Line broadening was included using a fixed Lorentzian line width (1.54 mT) and D and E strains (dD^{simul} and dE^{simul}) that change as a function of the wavelength.

λ_{wav} (nm)	D^{exp} (MHz)	E^{exp} (MHz)	Γ^{exp} (mT)	Γ^{simul} (mT)	Strains			
					dD^{simul} (MHz)	dE^{simul} (MHz)		
630	1344.7	1.5	77.7	0.7	2.08	1.54	50	20
650	1317.2	1.4	75.0	0.7	1.83	1.54	40	15
680	1288.5	1.3	73.7	0.6	1.54	1.54	0	0

Table 6.17: Experimentally derived ZFS parameters together with the Lorentzian lineshapes obtained for the different excitation wavelengths (λ_{wav}) below (630-680 nm) the CT band.⁸ The last two columns show the D and E strains computed by fitting on the experimental spectrum.

CHAPTER 7

Computation of the non-adiabatic transition rates

In this chapter, we explain in detail how we incorporated the multi-mode rate equations that we discussed in section 2.2, in a MATLAB code to compute the intersystem crossing (ISC) rates and the electron/hole transfer rates in molecular systems. The chapter is divided into two main parts. In the first one, we describe the procedure that we followed to write the code in MATLAB that computes the Fourier Transform (FT) of the correlation function, based on eqs. 2.41 and 2.30. We show how we can extract all the required parameters of eq. 2.41, using the Amsterdam density functional (ADF) program package. Such parameters are the energy gap, the normal mode frequencies and reorganization energies, the spin-orbit coupling (SOC) interaction matrix elements and the charge transfer interaction matrix elements. In the second part, we show results related to the computation of the hole transfer rate between two guanine molecules and, and we discuss its dependence on temperature and its relation to the classical Marcus limit.

7.1 MATLAB coding for the ISC rates using the ADF program for normal mode computations

To compute the ISC rate parameters, the singlet excited state ($|S_n\rangle$) and the triplet excited state ($|T_{k,m_s}\rangle$) involved in the transition should be optimized to extract the optimal geometries and their minimum energies (i.e., $E_{S_n}^{min}$ and $E_{T_{k,m_s}}^{min}$). These minimum energy molecular geometries are also used to compute the normal modes α and their frequencies (ω_α). The normal mode frequency calculation in ADF generates two binary TAPE21 output files (one for the singlet computation and one for the triplet) with extension .t21, which contain important information and are used to calculate the required parameters that characterize a vibronic transition (i.e., electron-phonon couplings and reorganization energies, see below and appendix A).^{101,125,126,128} These two vibrational mode output files are used as input files in the FCF (Franck Condon

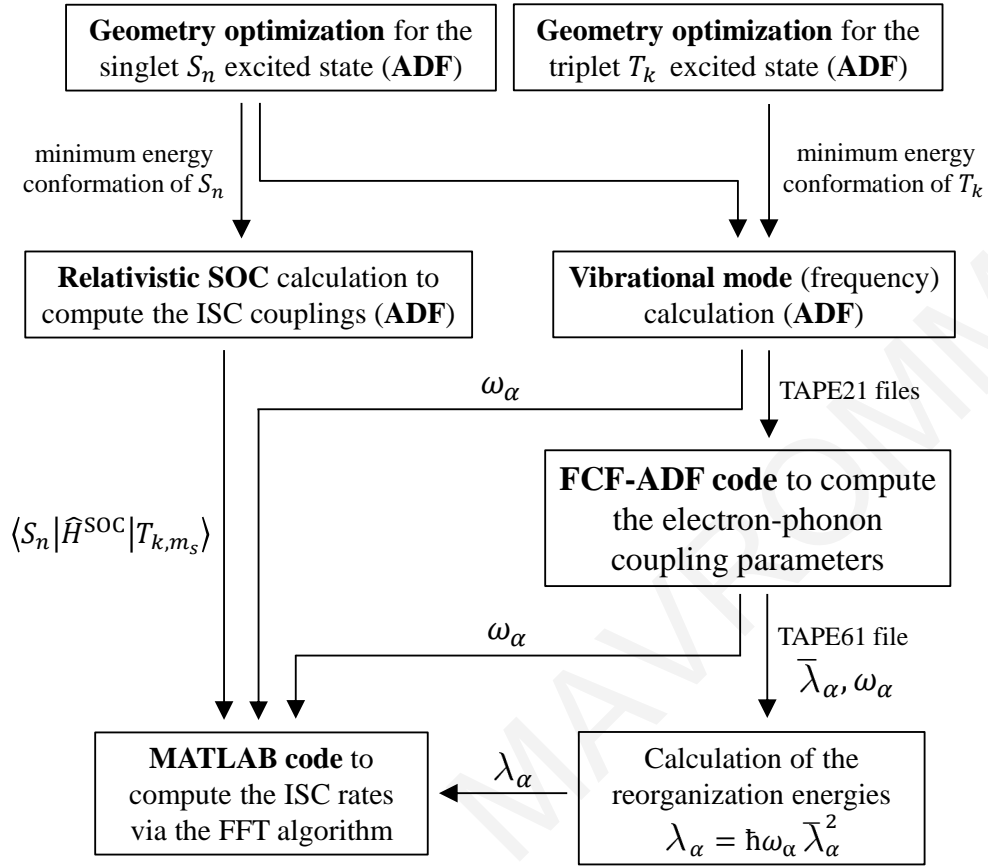


Figure 7.1: Flowchart showing the computational procedure we followed to compute the ISC transition rates $S_n \rightarrow T_{k,m_s}$ using the ADF program package in combination with MATLAB programming.

factor) auxiliary program, implemented in the ADF package which calculates the FCFs between the two states.^{127,128} The specific module computes the displacement of the atoms from their equilibrium positions during the transition from the initial electronic state to the final electronic state. The displacement vector \vec{k}_α is related to the electron-phonon coupling parameters $\bar{\lambda}_\alpha$ via¹⁰¹

$$\bar{\lambda}_\alpha = \left(\frac{\vec{\omega}_\alpha}{2\hbar} \right)^{1/2} \vec{k}_\alpha \quad (7.1)$$

where $\vec{\omega}_\alpha$ is a vector containing the reduced frequencies. The electron-phonon couplings $\bar{\lambda}_\alpha$ are used to calculate the reorganization energy per mode λ_α via

$$\lambda_\alpha = \hbar\omega_\alpha \bar{\lambda}_\alpha^2. \quad (7.2)$$

The SOC matrix elements for the ISC transition $S_n \rightarrow T_{k,m_s}$ are computed at the minimum energy molecular geometry of the singlet excited state of interest

(S_n). We compute the singlet and triplet excited states by solving the linear response equations that are based on the relativistic ZORA (zeroth-order regular approximation) Hamiltonian in its scalar approximation (see eq. 6.31). Then, the SOC interaction is applied as a perturbation (see eq. 6.32) to compute the SOC matrix in the basis of the spin-pure singlet and triplet excited states.

To compute the ISC rates I wrote a code in MATLAB applying eq. 6.16 with the inputs from the previous computations i.e., the mode reorganization energies λ_α , the corresponding frequencies ω_α and the SOC parameters $\langle S_n | \hat{H}^{\text{SOC}} | T_{k,m_s} \rangle$. As a first step, the code computes the time correlation function $e^{G(t)-G(0)}$ according to equation 6.17 using the computed mode frequencies ω_α and mode reorganization energies λ_α (lines 33-52 in the code). Then, it computes the FT of the correlation function (lines 74-85 in the code), which is used to estimate the ISC rate at frequency $\Delta E_{S_n, T_{k,m_s}} / \hbar$ ($\Delta E_{S_n, T_{k,m_s}} = E_{S_n}^{\text{min}} - E_{T_{k,m_s}}^{\text{min}}$) according to the equation (see eq. 6.16)

$$k_{S_n \rightarrow T_{k,m_s}} \left(\frac{\Delta E_{S_n, T_{k,m_s}}}{\hbar} \right) = \frac{|\langle S_n | \hat{H}^{\text{SOC}} | T_{k,m_s} \rangle|^2}{\hbar^2} \text{FT} (e^{G(t)-G(0)-\Gamma|t|}). \quad (7.3)$$

The methodology used to compute the FT of the correlation function is called Discrete Fourier Transform (DFT). The DFT is commonly used in the field of digital signal processing because it converts a signal (= a quantity that varies over time) of finite length, into a complex-valued function over some finite frequency range (spectrum of the signal). Therefore, a signal can be viewed from two different standpoints, the time domain and the frequency domain (see figure 7.2(a)). In general, the DFT involves two steps: (1) the sampling of the time signal, (2) the transformation of the sample to the frequency domain (spectrum) by using FT.

As an example, lets consider the following equations, where $x(t)$ is a general analog time signal and $X(f)$ is its FT spectrum

$$x(t) = \int_{-\infty}^{\infty} X(f) e^{i2\pi ft} df \quad (7.4a)$$

$$X(f) = \int_{-\infty}^{\infty} x(t) e^{-i2\pi ft} dt. \quad (7.4b)$$

The continuous-time signal $x(t)$ is sampled at discrete number of points (the samples) (see figure 7.2(b)). Suppose that this discrete-time signal $x(n)$ is created by taking N samples of the original signal $x(t)$ over some finite duration of time τ , and that the sampling interval equals $t_s = \tau/N$ (see figure 7.3). Then, $x(n)$ is related to its discrete

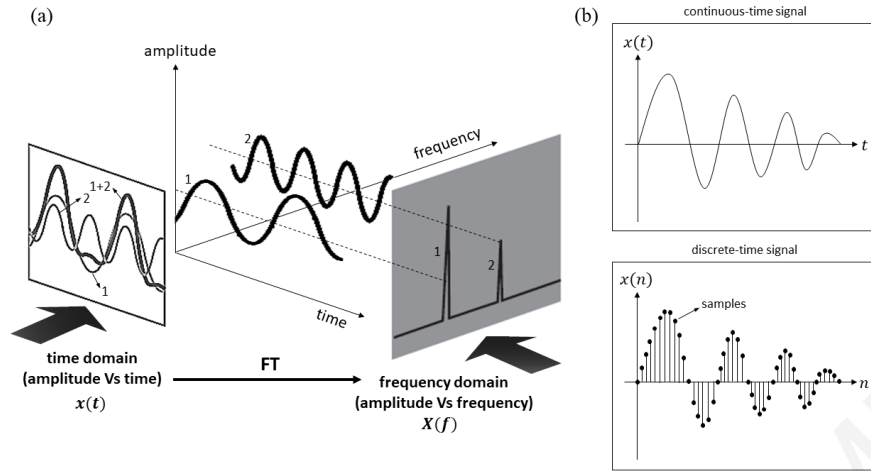


Figure 7.2: (a) Example of a signal in time domain ($x(t)$) and its spectrum in the frequency domain ($X(f)$). Two sinusoidal waves (1 and 2) of different frequencies are superimposed and form a signal (1+2) in the time domain. The frequency spectrum of the signal is computed from the FT of $x(t)$. It is represented by delta functions entirely localized at the two frequency components of the sinusoidal waves 1 and 2. (b) A signal is classified as continuous-time signal (above) and discrete-time signal (below). The discrete-time signal is a time sequence that has been sampled from a continuous-time signal. It takes on only a discrete set of values (samples).

Fourier spectrum via DFT as follows

$$\begin{aligned}
 x(n) &= \left(\frac{1}{N}\right) \sum_{k=0}^{N-1} X(k) e^{i2\pi nk/N} \\
 X(k) &= \sum_{n=0}^{N-1} x(n) e^{-i2\pi nk/N},
 \end{aligned} \tag{7.5}$$

where $X(k)$ is the spectrum of $x(n)$. $X(k)$ has (at least) N values spaced apart in the frequency domain by $1/\tau$. The reciprocal of t_s is the sampling rate or frequency ($F_s = 1/t_s$) (see figure 7.3). The spectrum is periodic with period being equal to $1/t_s$ and the signal is periodic with period that equals to F_s . Since one period extends from 0 to F_s , the DFT is only defined in the region between 0 and F_s (see figure 7.3). For any sampling interval t_s there is a critical sampling frequency ω_c which is one-half of the highest sampling frequency component (bandwidth) and it is called Nyquist frequency

$$\omega_c = \frac{1}{2t_s} = 0.5F_s^{max}. \tag{7.6}$$

The sampling frequency F_s should be at least the critical sampling frequency to avoid aliasing (difference between the reconstructed signal from the samples and the original signal, when the resolution is too low). Typically, F_s is always chosen to be much greater than the critical sampling frequency, so that the signal is sufficiently sampled. In addition, the signal is always sampled for a long enough duration of time, so that

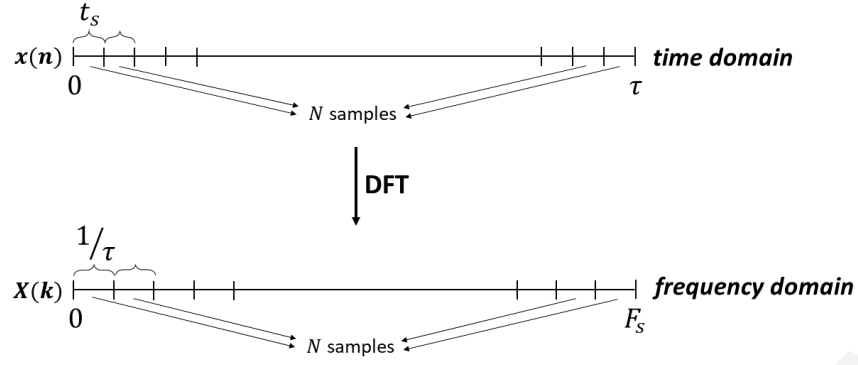


Figure 7.3: Schematic diagram of a DFT pair showing that the discrete signal $x(n)$ and the discrete frequency spectrum $X(k)$ are sampled in equal intervals. In the figure, $F_s = 1/t_s$ and $t_s = \tau/N$.

the resolution of the DFT will not be poor with respect to the original spectrum.

The DFT is efficiently computed using the Fast Fourier Transform (FFT) algorithm. It is implemented in many programming softwares such as MATLAB, Python, Mathematica, Fortran etc. Regardless of the preferred software, FFT is an algorithm that determines the DFT of a sequence significantly faster compared to the direct implementation. The time taken to evaluate the standard DFT of a N -sized signal scales as N^2 . In contrast, FFT scales as $N \log_2(N)$. The advantage of this approach is that the DFT of a sequence of N points can be written in terms of two separated DFTs of length $N/2$ that involve even and odd indexed subsequences, i.e.,

$$X(k)_{FFT} = \underbrace{\sum_{r=0}^{\frac{N}{2}-1} x(2r) e^{-i2\pi k(2r)/N}}_{\text{even}} + \underbrace{\sum_{r=0}^{\frac{N}{2}-1} x(2r+1) e^{-i2\pi k(2r+1)/N}}_{\text{odd}} \quad (7.7)$$

which results in

$$X(k)_{FFT} = \sum_{r=0}^{\frac{N}{2}-1} x(2r) e^{-\frac{i2\pi kr}{N/2}} + e^{-\frac{i2\pi k}{N}} \sum_{r=0}^{\frac{N}{2}-1} x(2r+1) e^{-\frac{i2\pi kr}{N/2}}. \quad (7.8)$$

Equation 7.8 implies that the N -point DFT can be obtained from two $N/2$ -point transforms, one on even input data and one on odd input data that are computed simultaneously. This decomposition makes the FFT algorithm much faster than direct computation.

Figure 7.7 shows our MATLAB code for the computation of the DFT of the correlation function $e^{G(t)-G(0)-\Gamma|t|}$ that involves frequencies and reorganization energies for the transition $S_1 \rightarrow T_1$ in Cbz-TBT molecule (see chapter 6). First, we set the sampling frequency $F_s = 100000 \text{ cm}^{-1}$. This value is much greater than the highest

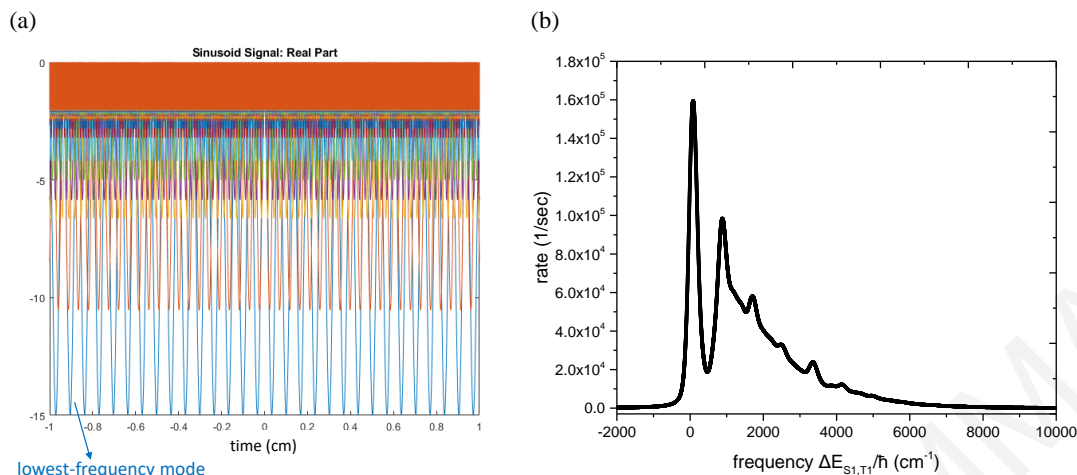


Figure 7.4: (a) Real part of the $G(t)$ function (with cosine, see eq. 6.17). The plot shows the 135 cosine waves in the time domain, one for each normal mode of frequency ω_α . The lowest-frequency mode has the greater period of oscillation (~ 0.07 cm) (with light blue color). The time duration of the signal is chosen to be much greater than the period of oscillation of the lowest-frequency mode (i.e., $\tau = 2$ cm). (b) The ISC rate (in sec^{-1}) as a function of the frequency $\Delta E_{S_1, T_1}/\hbar$ (in cm^{-1}) for the transition $S_1 \rightarrow T_1$ in Cbz-TBT molecule. The rate at $\Delta E_{S_1, T_1}/\hbar = 9910.28 \text{ cm}^{-1}$ equals to 17.67 sec^{-1} .

frequency component of our system, which equals to $\omega_\alpha^{max} = 3791.33 \text{ cm}^{-1}$ (line 23 in the code). Then, we define the time duration of the signal $\tau = 2$ cm to be greater than the period of the lowest-frequency mode (~ 0.07 cm), so that the sinusoidal signal that comes from this particular frequency is well resolved (see figure 7.4(a)). The time domain is a column vector of $1 \times N$ dimensions where $N = \tau F_S$ (line 27 in the code). Therefore, the correlation function is a column vector of $1 \times N$ dimensions in the time domain (lines 32-52 in the code). The DFT is equally sampled with $nfft = N$ number of points in the frequency domain (line 74 in the code). To increase the frequency resolution (and the accuracy of the DFT amplitudes) the DFT is further sampled at $nfft2 > nfft (=N)$ intervals (line 76 in the code). The extra spaces from N to $nfft2$ are filled with zeros (zero-padding) [line 78 in the code]. The function `fft` returns the DFT of the correlation function as a column vector of $1 \times nfft2$ dimensions (lines 83-85 in the code), and the frequency domain has the same dimensions $1 \times nfft2$ (line 88 in the code). The computed DFT vector is multiplied by the relative SOC matrix elements according to equation 7.3 to produce the ISC rate constants (line 94 in the code). The rates are now plotted in the frequency space, and from this plot we extract the rate constant at $\Delta E_{S_n, T_{k, m_s}}/\hbar$ (lines 109-112 in the code) (see figure 7.4(b)).

7.2 Effects of temperature on hole transfer rates between two guanine molecules and the transition from the quantum to the classical rate limit

It has been suggested that for some organic molecules the fully quantum model for non-adiabatic rates (eq. 2.41) yields charge transfer rates that are lower than the classical Marcus formula for the rate and more robust to temperature changes (even up to 300 K).^{166–169} This phenomenon can be explained by the nuclear tunneling effect associated with the high-frequency modes that exhibit strong electron-phonon couplings. In this section, we examine the hole transfer rate between two unsolvated guanine molecules in order to explore further, deviations of the hole transfer rate from the classical Marcus theory.

We compute the transition rate for hole transfer between two guanine (G) molecules ($k_{|G+G\rangle\rightarrow|GG^+\rangle}$) as shown in figure 7.5(a). The MATLAB code that we introduced in the previous section (see figure 7.7) is now modified according to eq. 2.34 for the case of inter-molecular charge transport characterized by different sets of vibrational coordinates for the donor and the acceptor. The rate is computed at different temperatures and the results are summarized in figure 7.5(b). These results show that the transition rate does not change much with the temperature for temperatures lower than the room (300 K). The temperature-induced broadening at $T = 300$ K is negligible and the maximum rate (at the peak) slightly decreases from 7.81 psec ($T = 10$ K) to 7.65 psec ($T = 300$ K) when increasing the temperature. Further, the rate as a function of ΔE is not given by the classical Marcus form (see eq. 2.31). In table 7.1, the hole-transfer rate computed using the classical Marcus formula (eq. 2.31) at different temperatures, is compared to the rate computed using the quantum formula (eq. 2.41). The results indicate strong dependence of the classical Marcus rate on temperature. In addition, the classical Marcus rate is much greater than the quantum rate, even at $T = 300$ K (the classical Marcus rate is approximately 2 to 3 orders of magnitude greater than the quantum rate).

T (K)	Quantum Rate (eq. 2.34)	Marcus rate (eq. 2.31)
10	8.94×10^{11}	0
100	8.85×10^{11}	5.74×10^1
200	8.15×10^{11}	2.79×10^7
300	7.40×10^{11}	2.01×10^9

Table 7.1: Rate computed with the Fermi’s Golden rule formula Vs rate computed with the Marcus formula for the hole transfer process $|G^+G\rangle \rightarrow |GG^+\rangle$. The rate is given at $\Delta E = 0$.

Further analysis of the results using the normal mode computations, reveals that for the states $|G^+\rangle$ and $|G\rangle$, only the first 3 normal modes (those with the lowest

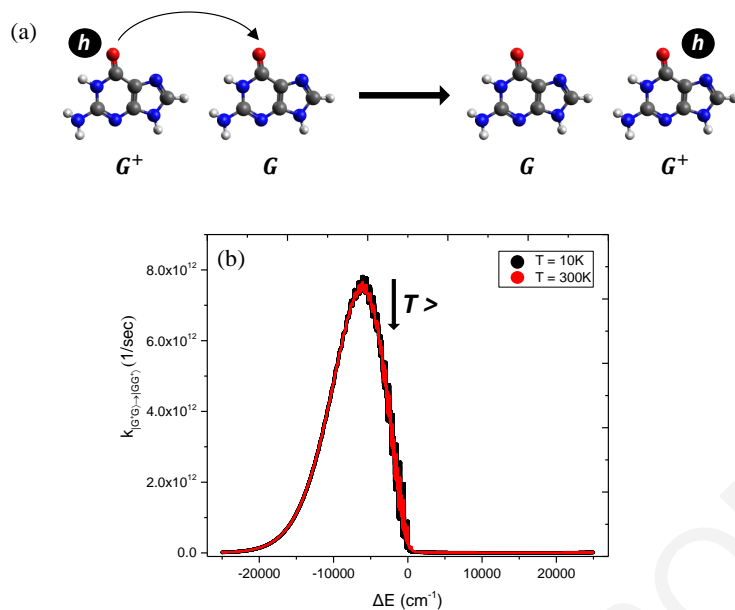


Figure 7.5: (a) Two guanine molecules take part in a hole transfer transition. The driving force is zero ($\Delta E = 0$) and the electronic coupling is $\langle G^+G | \hat{V} | GG^+ \rangle = 0.03$ eV. (b) Hole transfer rate for the transition $|G^+G\rangle \rightarrow |GG^+\rangle$, as a function of ΔE at different temperatures.

frequencies) can be considered as “classical” modes (i.e., $\hbar\omega_\alpha < K_B T$) at 300 K. The other 39 higher frequency modes are all “quantum” (i.e., $\hbar\omega_\alpha \gg K_B T$) [Note that guanine has 42 normal modes at total]. Therefore, it is not surprising that the temperature and ΔE dependence of the rate does not follow the classical Marcus expression (see appendix B for detailed explanation). In order to get a hole transfer rate that follows the classical Marcus formula, we convert the high-frequency quantum modes to low frequency classical ones ($\hbar\omega_\alpha < K_B T$). We rescale $\hbar\omega_\alpha$ by 10 (i.e., $\hbar\omega_\alpha^{(\text{new})} = \hbar\omega_\alpha/10$) and $\bar{\lambda}_\alpha$ by $\sqrt{10}$ (i.e., $\bar{\lambda}_\alpha^{(\text{new})} = \bar{\lambda}_\alpha\sqrt{10}$). In this way, the total reorganization energy of the system is unchanged, and 90% of the modes become classical at $T = 300$ K. With the new parameters we compute the hole transfer rate using our MATLAB code at $T = 300$ K. The rate as a function of ΔE is shown in figure 7.6(a), together with the rate computed using the unscaled parameters at $T = 300$ K (i.e., the same as figure 7.5(b)). We see that the new rate follows the classical Marcus distribution e.g., the simulated spectrum fits to Gaussian and we get $\sigma = 2.3 \times 10^{-1} \pm 8.2 \times 10^{-6}$ eV. The total reorganization energy is related to σ by $\sigma = \sqrt{2K_B T \lambda}$ and gives 1.01 eV while the computed inner-sphere reorganization energy (see eq. 7.2) is $\lambda_G + \lambda_{G^+} = 0.93$ eV.

Using the scaled normal mode parameters we decrease the temperature ($T = 10$ K) such that all modes can be considered “quantum” at this temperature. In this case, as expected, the exact quantum rate is not described by the classical Marcus theory. The exact rate is shown in figure 7.6(b) (in red). It is not described by a Gaussian distribution (not symmetric around the mean ΔE value). The rate at $T = 10$ K and for $\lambda = 0.93$ eV computed using the Marcus formula, is also shown in the same plot

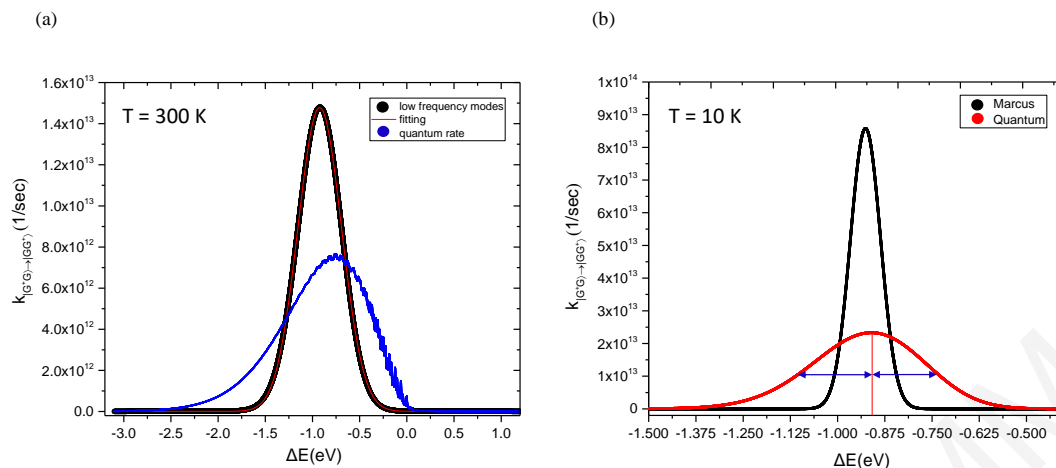


Figure 7.6: (a) Hole transfer rate computed using the scaled normal mode parameters at $T = 300$ K (black line). The fitting into Gaussian distribution (red line) reveals the rate can be described by the classical Marcus formula. The plot also shows the hole transfer rate that was computed using the unscaled frequencies and electron-phonon couplings at $T = 300$ K. In this case, the spectrum can not be described by a Gaussian distribution. (b) Hole transfer rate computed using the scaled normal mode parameters at $T = 10$ K. The spectrum is computed using eq. 2.29 and it is shown in red. The rate is also computed using the classical Marcus formula eq. 2.31 at $T = 10$ K and it is shown in black for comparison.

(in black). It shows large deviations from the exact rate. Therefore, as expected, at $T = 10$ K the rate cannot be described by the classical Marcus formula.

The above results show that the classical Marcus formula does not accurately describe the transition rate in electron/hole or exciton transfer transitions in small organic molecules that have a majority of high frequency modes that remain quantum for a large range of temperatures. This point must be taken in to account in transport computations in dry environments that favor high frequency modes.

```

1 clear
2 clc
3 format long
4 %
5 syms t
6 %
7 %%%%%%%%%%%%%%%%%%%%%%%%%%%%%%%%%%%%%%%%%%%%%%%%%%%%%%%%%%%%%%%%%%%%%%%%%
8 % CONSTANT VALUES
9 c_vel = 2.997925*10^10;           % light velocity in vacuum (cm/sec)
10 h_bar = 5.308837*10^(-12);      % Planck constant (cm**-.1.sec)
11 kbT = 55.564312;                % thermal energy (cm**-.1) [for T = 80K]
12 %
13 % INPUT PARAMETERS
14 V = 0.013083;                   % electronic coupling between S1 and T1 states (cm**-.1)
15 nm=135;                          % number of modes
16 gamma = 33.3565*2*pi;           % homogeneous broadening (cm**-.1) [gamma = 1 psec]
17 data = readmatrix('S1T1parametres'); % nm X 2 matrix: 1st column --> frequencies per mode (cm**-.1)
18 %                               2nd column --> reorganization energy per mode (cm**-.1)
19 Er = 1590.436074;               % total reorganization energy (cm**-.1)
20 DE = 9910.284966;               % energy difference at the minimum-energy conformations (cm**-.1)
21 %
22 % PARAMETERS FOR THE FFT INTEGRATION
23 Fs = 100000;                    % sampling frequency (cm**-.1)
24 T = 1/Fs;                        % sampling period/time increment (cm)
25 %
26 % TIME DOMAIN
27 t = -1:T:1;                      % time vector (cm)
28 %
29 %%%%%%%%%%%%%%%%%%%%%%%%%%%%%%%%%%%%%%%%%%%%%%%%%%%%%%%%%%%%%%%%%%%%%%%%%
30 % CONSTRUCTION OF THE CORRELATION FUNCTION
31 %%%%%%%%%%%%%%%%%%%%%%%%%%%%%%%%%%%%%%%%%%%%%%%%%%%%%%%%%%%%%%%%%%%%%%%%%
32 sum = zeros(1,length(t));
33 for j=1:nm
34     occup_num = (exp(data(j,1)/kbT) - 1)^(-1); % thermal boson occupation number
35     real_part = ((2*occup_num)+1)*cos(data(j,1)*2*pi*t)-1;
36     imaginary_part = sin(data(j,1)*2*pi*t);
37     G = (data(j,2)/data(j,1))*(real_part-1i*imaginary_part); % G(t)-G(0)
38     sum = sum + G;
39     % plots: real and imaginary part of G(t)
40     figure(1);
41     plot(t,real_part);
42     title('Sinusoid Signal: Real Part');
43     xlabel('time');
44     ylabel('Amplitude');
45     hold on;
46     figure(2);
47     plot(t,imaginary_part);
48     title('Sinusoid Signal: Imaginary part');
49     xlabel('time');
50     ylabel('Amplitude');
51     hold on;
52 end
53 % plot of G(t)
54 figure(3);
55 plot(t,sum);
56 title('Sinusoid Signal: G(t) with real parts');
57 xlabel('time');
58 ylabel('Amplitude');
59 hold on;
60 %
61 corr=exp(sum).*exp(-gamma*abs(t)); % exponential G(t) (correlation function)
62 % plot of the correlation function
63 figure(4);
64 plot(t,corr);
65 title('Exp(G(t))');
66 xlabel('time');
67 ylabel('Amplitude');
68 %

```

```

69 %%%%%%%%%%%%%%%%%%%%%%%%%%%%%%%%%%%%%%%%%%%%%%%%%%%%%%%%%%%%%%%%%%%%%%%%%
70 % FOURIER TRANSFORM OF THE CORRELATION FUNCTION
71 %%%%%%%%%%%%%%%%%%%%%%%%%%%%%%%%%%%%%%%%%%%%%%%%%%%%%%%%%%%%%%%%%%%%%%%%%
72 %
73 % DFT sampling
74 nfft = length(corr);           % number of points in the frequency domain
75 %                               (equals the number of points in time domain)
76 nfft2 = 2^nextpow2(nfft);     % signal length becomes exact power of 2
77 %
78 corr(nfft2) = 0;              % padding with zeros the correlation function
79 %                               so that length(corr) equals to nfft2.
80 corr = circshift(corr,[0,-(nfft-1)/2]); % circular shift of correlation function for symmetry
81 %
82 % DFT (FFT)
83 X=fft(corr);
84 X=fftshift(X);                % shift the center of FFT at zero-frequency
85 mx=abs(X)/Fs;                 % FFT amplitude
86 %
87 % FREQUENCY DOMAIN
88 f = -(nfft2/2:nfft2/2-1)*(Fs/nfft2); % frequency (cm**-1)
89 %
90 %%%%%%%%%%%%%%%%%%%%%%%%%%%%%%%%%%%%%%%%%%%%%%%%%%%%%%%%%%%%%%%%%%%%%%%%%
91 % CALCULATION OF THE TRANSITION RATE
92 %%%%%%%%%%%%%%%%%%%%%%%%%%%%%%%%%%%%%%%%%%%%%%%%%%%%%%%%%%%%%%%%%%%%%%%%%
93 %
94 rate=(V^2)/(h_bar^2).*mx/c_vel; % rate (Hz)
95 writematrix([f.' , rate.'],'RATE_Vs_Freq.xlsx');
96 %
97 % CLASSICAL MARCUS RATE
98 rate_Marcus = ((V^2)/h_bar)*sqrt(pi/(kB*Er))*exp(-(f-Er).^2/(4*kB*Er));
99 %
100 %%%%%%%%%%%%%%%%%%%%%%%%%%%%%%%%%%%%%%%%%%%%%%%%%%%%%%%%%%%%%%%%%%%%%%%%%
101 % PLOTS
102 figure(5);
103 plot(f,mx);
104 title('FFT');
105 xlabel('DE');
106 ylabel('Power');
107 figure(6);
108 %
109 plot(f,rate,f, rate_Marcus);
110 title('Rate Spectrum of the Sinusoid Signal');
111 xlabel('DE');
112 ylabel('Power');
113 %

```

Figure 7.7: MATLAB code for the computation of the ISC rates according to equation 7.3.

CHAPTER 8

Molecular wires for efficient long-distance triplet exciton transfer

In this chapter, we propose design rules for building organic molecular bridges that enable coherent long-distance triplet-exciton transfer (TET). Using these rules we describe example polychromophoric structures with low inner-sphere exciton reorganization energies, low static and dynamic disorder and enhanced π -stacking interactions between nearest-neighbor chromophores. These features lead to triplet-exciton eigenstates that are delocalized over several units at room temperature. The use of such bridges in donor-bridge-acceptor assemblies enables fast triplet-exciton transport over very long distances that is rate-limited by the donor-bridge injection and bridge-acceptor trapping rates.

8.1 Introduction

Triplet exciton transfer (TET) is an important process in photosynthetic photoprotection and is central to the harvesting of triplet excitons (TE's) in a variety of contexts such as catalysis, photovoltaics, and energy conversion (e.g., singlet fission (SF) and triplet-triplet annihilation).^{26,87,170–176} For many applications it is desirable to achieve fast, directed, and long-distance TET. For example, in SF reactions that produce a correlated TE pair, it is important to separate the two TE products via fast TET to distinct locations, in order to avoid the backreaction.^{23,177–180}

Implementing directed long-distance TET on the single-molecule scale requires building molecular linkers (bridges) that connect TE donors (D) to acceptors (A).^{25,82,87,181–187} It is known that the speed of bridge-mediated D-to-A singlet-exciton transfer (SET) may be improved by enhanced π -stacking interactions between nearest-neighbor molecular bridge (B) units linking D and A.^{188,189} The π -stacking amplifies the nearest-neighbor SET couplings (V^{SET}), leading to delocalized bridge singlet excitons (SE's) that channel D-to-A SET.^{10,14,28,190–193} There are many examples of molecular assem-

blies with enhanced π -stacking interactions.^{3,194–198}

However, a bridge with large V^{SET} that supports fast SET, will not support equally fast TET because the TET coupling between adjacent bridging units (V^{TET}) is generally much weaker than V^{SET} for inter-unit distances (ΔR) that are greater than Van der Waals (VdW) (V^{TET} decays approximately as $e^{-\beta\Delta R}$ whereas V^{SET} decays as $1/\Delta R^3$).^{9,10,13,14,21} To illustrate this point, we computed both V^{SET} and V^{TET} for some of the π -stacked systems mentioned above^{2–5} (see section 8.9). Even for geometries with π -stacking distances slightly greater than VdW and with $V^{\text{SET}} \approx 0.1$ eV, $V^{\text{TET}} \approx 0.01$ eV (see figure 8.13).

This known behaviour explains why long-distance TET is an incoherent hopping process, characterized by slow and short hopping steps, in contrast to SET that may involve quasi-coherent or fully coherent transfer mechanisms with faster and longer steps (especially for π -stacked assemblies). Although TE's have much longer lifetimes compared to SE's, the slow speed of TET constrains the transport distance that can be achieved within these lifetimes. Thus, an improvement of the speed of TET in organic bridges, in conjunction with the long TE lifetimes, could greatly enhance the maximum distance of TET. Our goal is to show how to modify existing organic π -stacked bridges in order to transform them to molecular wires that enable fast and coherent TET over long distances. Given the importance of purely organic electronic devices, we focus on organic (rather than metal-organic) molecules. Further, we consider bridge architectures with a π -stacking core that support excitonic states that are largely localized within the core. This characteristic makes it easier to protect the excitons from solvent and environmental effects.

We suggest that a molecular bridge that could support delocalized TE's and enable coherent TET, should be designed to: (i) be homopolymeric, (ii) have very tight π -stacking between units (maximum inter-unit distance should be VdW), (iii) maintain the tight π -stacking in the presence of room-temperature disorder, (iii) have low inner-sphere reorganization energy for TE formation within each monomer unit (the outer sphere reorganization energy depends on the solvent and should also be minimized by use of non-polar solvents). Similar design principles have been discussed in the context of SET in molecular nanocrystals e.g., see refs. 28,190 using results of theoretical studies of transport efficiency (for electrons, holes, or excitons) based on tight-binding (multi-site) models.^{9,10,13,14,16,190,193,199} The important parameters for transport in a model with identical sites and independently-fluctuating site energies are the root-mean-squared coupling (V_{rms}) between nearest-neighbor sites (localized electronic states), the site reorganization energy λ , and the standard deviation of the site energy σ_E induced by dynamic disorder. Several studies show that delocalized eigenstates and coherent or quasi-coherent transport are possible when $V_{\text{rms}} \geq \sigma_E, \frac{\lambda}{2}$ (e.g., see refs. 28,190,192,193,199). This condition is relevant to identical nearest-neighbor sites $i, i+1$ and is derived from the assumption that each site has independent energy fluctu-

ations. The eigenstates of the multi-site system will not localize on each of the sites if the nearest-neighbor coupling satisfies $V_{i,i+1} \geq U^{\text{act}}$, where $U^{\text{act}} = (\lambda_i + \lambda_{i+1})/4 = \lambda/2$, (since $\lambda_i = \lambda_{i+1} = \lambda$). Therefore, $V_{\text{rms}} \geq \frac{\lambda}{2}$ is an approximate condition that needs to be satisfied to allow for the possibility of delocalized TE eigenstates. It does not always guarantee the existence of delocalized eigenstates, i.e., it is a necessary but not a sufficient condition for localization, because the total reorganization energy in U^{act} may be greater than the sum of the inner-sphere monomer contributions due to collective molecular and solvent motions. $V_{\text{rms}} \geq \sigma_E$ is also an approximate condition that characterizes coherent transport ($\sigma_E \approx \sqrt{2K_B T \lambda}$), in addition to $\sigma_V < V_{\text{ave}}$. We use the criterion $V_{\text{rms}} \geq \sigma_E, \frac{\lambda}{2}$ to screen for molecular architectures that may support coherent long-distance TET. The criterion is combined with electronic structure and molecular dynamics computations and with a model for coherent transport. For each structure we verify that $\sigma_V < V_{\text{ave}}$.

Consider a polymeric wire with identical monomer chromophores and identify the lowest exciton level of each monomer with a site level in a multi-site system (the latter representing a homopolymer). Given that V^{TET} is generally weak, it follows that the primary goals in the design of a polychromophoric molecular wire for coherent TET are the minimization of the site (monomer) reorganization energy λ ($\lambda = \lambda^{\text{mon}}$) and of σ_E ($\sigma_E = \sigma_E^{\text{mon}}$), and the maximization of V_{rms} . Typical minimal values for inner-sphere λ in molecules are of the order of 0.1 eV^{188,191} leading to a room-temperature $\sigma_E \approx 0.1$ eV. Given the condition $V_{\text{rms}} \geq \sigma_E, \frac{\lambda}{2}$, the V_{rms} magnitudes should be at least 0.1 eV. Such magnitudes require at most VdW π -stacking distances that are not destroyed by conformational disorder. Below we explore some potential structures that could fulfill these parameter-value requirements.

Vura-Weis and co-workers probed the dependence of D-to-A TET mechanism on bridge length using benzophenone (Bp) as D, naphthalene (Nap) as A and polyfluorene as B.¹ The fluorene (F) monomers were connected via methylene linkers in face-to-face (approximately π -stacked) geometries and the bridge length was varied from one up to three F units (Fn, n=1-3) (see figure 8.1A,B). The experiment involved transient triplet absorption measurements and showed that through-bridge tunneling mediates transport for the shortest bridge length (one F unit), while for larger bridge lengths the transport mechanism is multi-step thermally activated hopping. The TET times for the dimer and trimer bridges were 100 – 200 psec (minimum bridge lengths of 7 to 10.5 Å, respectively). In these systems the deduced D-to-B injection times and B-to-A trapping times are similar.

Electronic structure and molecular dynamic (MD) simulations of the TET mechanism on the Fn systems showed that the bridge TE's are mostly localized in individual F units due to thermal disorder that involves twisting about the methylene linkers, destroying the F-to-F π -stacking interactions.²⁰⁰ Further, the F-to-F V_{rms} was found to be small compared to the F-monomer TE reorganization energy. This result is consis-

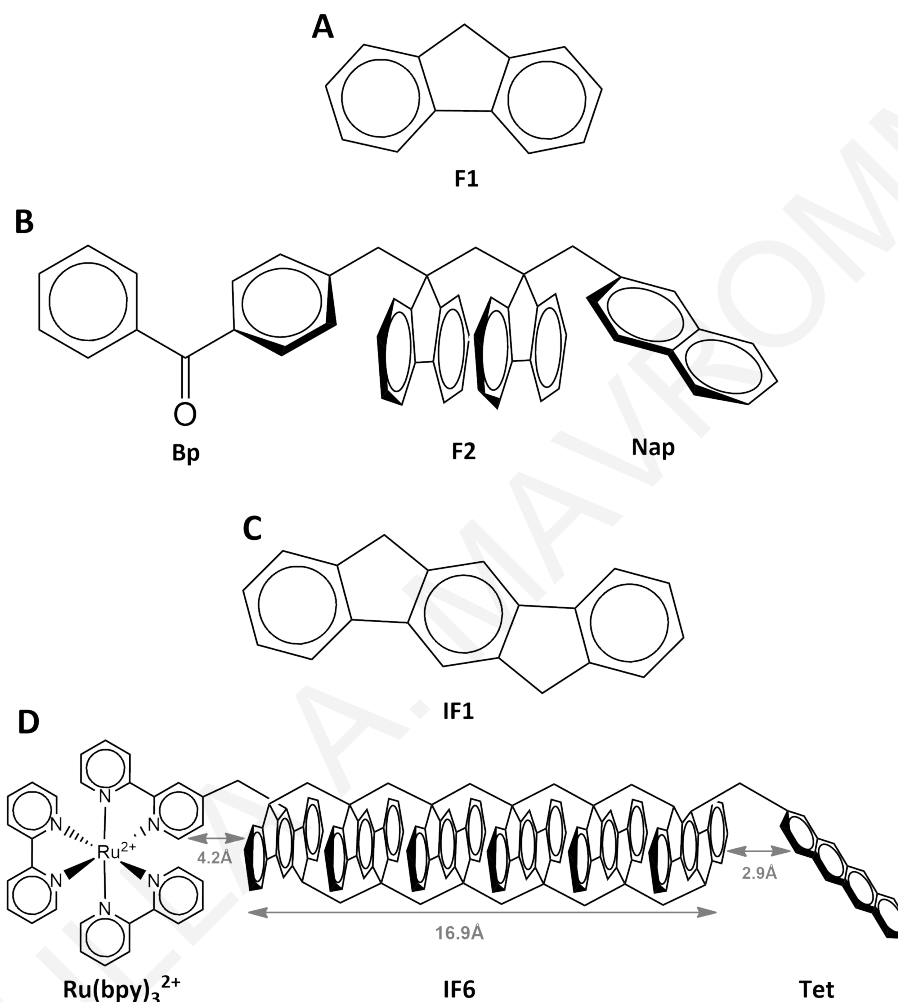


Figure 8.1: (A) Fluorene monomer bridging unit (F1) used in ref. 1. (B) The structure of Bp-Fn-Nap systems used in ref. 1. The bridges contained one up to three F units (Fn, n=1-3). (C) Chemical structure of the proposed indenofluorene (6,12-dihydroindeno[1,2-b]fluorene) bridging monomer (IF1). (D) Molecular structure of the indenofluorene hexamer (IF6) bridge (16.9 Å length). The monomers are constrained to a rigid π -stacked geometry through two methylene linkers and the interchromophore distance is 2.8-3.0 Å. The IF6 bridge is linked to a Ru(bpy)₃²⁺ D and a tetracene (Tet) A in approximately 4.2 Å and 2.9 Å distance respectively.

tent with the incoherent multistep hopping between F units for longer bridge lengths.

We can improve the F-based TE wires of ref. 1 by transforming them to wires that fulfil the abovementioned conditions for coherent TET. Namely, minimize chromophore TE reorganization energy, enable tight π -stacking interactions between chromophores, and remedy the problem of conformational disorder. To this end we propose polymers of indenofluorene (IF)-based monomer units brought to optimal π -stacked geometries by linking them with two methyl groups (see figure 8.1C,D). This linking brings the nearest-neighbor chromophores at an average distance less than 3.4 Å and prevents torsional and slipping motions between the chromophores.

8.2 Results and Discussion

We tested the structural stability of the cofacial geometries and the π -stacking interactions in the dimer and the longer polymers (figure 8.1D) via room-temperature MD simulations. We also performed electronic structure computations to characterize the SE and TE spectra. The electronic structure methods included configuration interaction singles (CIS) and time-dependent density functional theory (TD-DFT) for the monomer and the larger systems, as well as higher-level *ab-initio* approaches for the dimer (see section 8.6). The MD simulation results show that the tight π -stacking is maintained even at room temperature. Figure 8.2(a) shows examples of the TE eigenstates of the monomer (IF1), dimer (IF2) and decamer (IF10) computed with CIS for the minimum-energy conformations. The energy difference between adjacent (in energy) TE eigenstates is high (e.g., 0.2 eV for IF10 to 0.3 eV for IF2), implying that the V^{TET} between neighboring units is large. The TE eigenstates are delocalized over several bridge units (see figure 8.2(b) and section 8.5).

To explore the effects of thermal motion on the nearest-neighbor V^{TET} we first performed room-temperature MD simulations on the dimer. Using the MD-trajectory structures we computed (with CIS) the fluctuations in the energy splitting of the lowest two TE eigenstates, to estimate the nearest-neighbor coupling V^{TET} [$\Delta E = E_{T_2^{(2)}} - E_{T_1^{(2)}} \approx 2V^{\text{TET}}$]. The MD-derived rms V^{TET} is large ($V_{\text{rms}} = 0.13$ eV) with $V_{\text{ave}} = 0.12$ eV, and $\sigma_V = 0.04$ eV. These values indicate that the thermal structural distortions do not significantly reduce the monomer-to-monomer TET coupling.

To investigate the effects of thermal motion on the TE energies of the monomers, we computed, from the MD simulations on the dimer, the standard deviation (σ_E^{mon}) of the lowest TE energy E ($E = E_{T_1^{(1)}}$) of each monomer fragment using CIS. For each MD dimer structure, we removed the methylene bridges that link the two IF units and capped the carbon atoms at the positions 5' and 11' with hydrogens (see figure 8.7). We found that $\sigma_E^{\text{mon}} = 0.12$ eV, i.e., $\sigma_E^{\text{mon}} \approx V_{\text{rms}}$. To test whether localized TE-polaron formation is likely in these polymeric systems, we compared V_{rms} to the activation energy for monomer-to-monomer TET. The activation energy is approximated

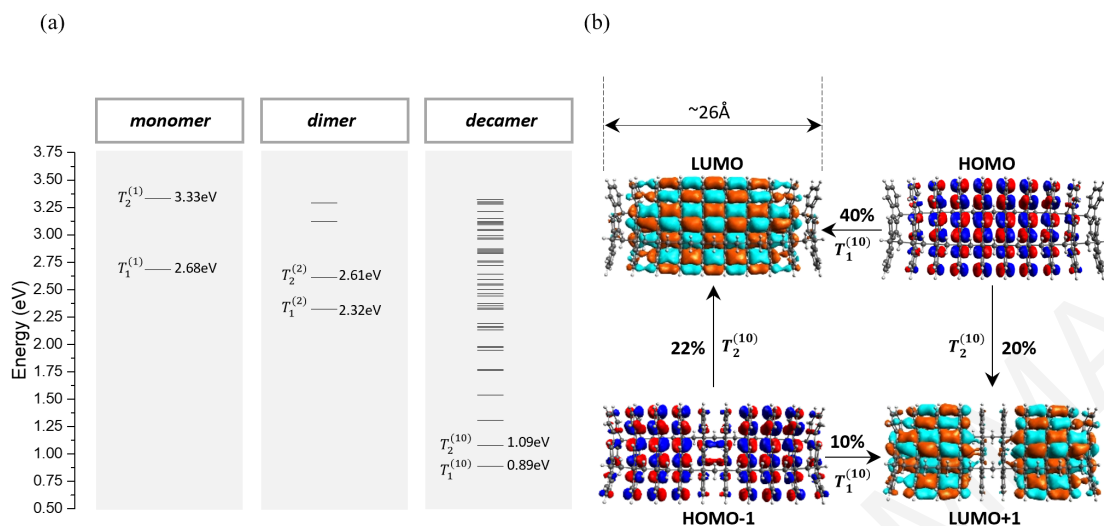


Figure 8.2: (a) TE states of the bridge type shown in figure 8.1 computed at CIS/def2-SVP level of theory. Due to enhanced π -stacking, TE splittings are large (e.g., $\Delta E_{T_2^{(2)}-T_1^{(2)}} = 0.3$ eV for the dimer). For longer polymers the TE band structure is stabilized. (b) Single excitation molecular orbital contribution to the lowest two TE states of the IF10 (computed with isosurface value 0.01). The figure shows only the largest contributions. The notations (1),(2),(10) refer to monomer, dimer and decamer bridges respectively.

by $U^{\text{act}} = (\lambda_D + \lambda_A)/4$, where λ_D and λ_A are the monomer reorganization energies (λ^{mon}) as shown schematically in figure 8.6. This notation implies that one monomer is the TE “donor” (D) and the other monomer the TE “acceptor” (A). We computed $\lambda_{D(A)} = 0.27$ eV, (using TD-DFT and BP86¹¹⁴ functional) such that $U^{\text{act}} = 0.14$ eV, a value that is of the same order of magnitude as V_{rms} . Since $V_{\text{rms}} \approx U^{\text{act}} = \frac{\lambda^{\text{mon}}}{2}$ we do not expect that TE-polaronic states are localized on a single monomer. Further, as expected $\sigma_E^{\text{mon}} \approx \sqrt{2K_B T_{293K} \lambda_{D(A)}}$.

To probe the delocalization of TE’s in the presence of disorder for longer polymers we performed room-temperature MD simulations on the decamer followed by CIS computations on 3000 MD snapshots. From the snapshots we computed averaged values of the HOMO and LUMO inverse participation ratios (IPR’s) (e.g., see refs. 27,28,201). The HOMO and LUMO have high contributions to the lowest TE’s, e.g., $T_1^{(10)}$: 40% HOMO→LUMO (for the other orbital contributions see section 8.8). As reference IPR values we used those computed for the optimized geometry shown in figure 8.2(b). The computations show that the MD IPR values vary approximately by 27% with respect to the reference IPR. The results imply that thermal fluctuations largely preserve the delocalization of the TE’s shown in figure 8.2(b).

In summary, for these types of bridges $V_{\text{rms}} \approx \sigma_E^{\text{mon}}, \frac{\lambda^{\text{mon}}}{2}$. For this parameter regime we estimate the intra-bridge TET rate k_{br} (to be defined below) using a N -site

tight-binding bridge Hamiltonian

$$\hat{H} = \sum_{i=1}^N E|i\rangle\langle i| + \sum_{i=1}^{N-1} (V|i\rangle\langle i+1| + \text{hc}) \quad (8.1)$$

(see figure 2(a)). The index i is the monomer number, and $|i\rangle$ denotes the lowest TE eigenstate of the monomer (E is the TE energy and $V = V_{\text{rms}}$). We solve the Liouville equation for the density matrix

$$i\hbar \frac{d}{dt} \rho_{j,l}(t) = \sum_i H_{j,i} \rho_{i,l}(t) - \rho_{j,i}(t) H_{i,l} - i\hbar \left(\frac{\gamma_i}{2} + \frac{\gamma_j}{2} + \gamma_{i,j} \right) \rho_{j,l}(t) \quad (8.2)$$

where the γ_i terms are monomer TE population-relaxation rates and the $\gamma_{i,j}$ terms are pure dephasing rates for all i, j TE pairs.^{202–206} Each γ_i ($i = 1 - (N - 1)$) describes a phosphorescence decay rate with $\gamma_i = k_B^{(ph)} = (\mu s)^{-1}$ and $\gamma_N = k_B^{(ph)} + k_{B \rightarrow A}^{(\text{TET})}$, where $k_{B \rightarrow A}^{(\text{TET})}$ is the TET rate from the N th monomer to an acceptor. The pure dephasing rates are set equal to $\gamma_{i,j} = \gamma_{\text{deph}} = \hbar^{-1} \sqrt{\sigma_i^2 + \sigma_j^2}$, where $\sigma_{i(j)} = \sigma_E^{\text{mon}}$. This phenomenological model has been used in different contexts to study the transition from incoherent to coherent transport.^{203–205,207} It incorporates both diagonal dynamic disorder and population relaxation (we include approximately off-diagonal dynamic disorder by setting $V = V_{\text{rms}}$). The model allows for analytical solutions of mean first passage times (MFPTs) as a function of its few parameters. These analytical solutions can be used to predict the approximate dependence of the intra-bridge TET rate on bridge length. For our purposes we combine this approximate model with MD and electronic-structure computations of its parameters in order to screen candidate structures according to the estimated k_{br} . The model is not a substitute to high-level non-adiabatic simulations that also include effects such as spontaneous TE localization and back reactions from electronic to nuclear dynamics. These effects may reduce the value of k_{br} as compared to our estimate, but such simulations are very expensive for the purposes of initial screening.

The model allows for a precise definition of k_{br} . If the TE is initially located at the 1st monomer, (probability $P_1(t = 0) = 1$), the overall decay time of the TE is given by $\langle \tau \rangle = \sum_{i=1}^N \int_0^\infty P_i(t) dt$. Using the above model, we compute $\langle \tau \rangle$ numerically as a function of N and γ_N for the parameter regime $V \geq \hbar \gamma_{\text{deph}} \approx 0.1$ eV and for γ_N ranging from $(1 \text{ fsec})^{-1}$ to $(10 \text{ nsec})^{-1}$. We find that $\langle \tau \rangle$ is not affected by the slow phosphorescence rates, i.e., we get identical results if we set $\gamma_{i \neq N} = 0$ and $\gamma_N = k_{B \rightarrow A}^{(\text{TET})}$. Further, $\langle \tau \rangle$ is given by the MFPT to N , i.e., $\langle \tau \rangle = \int_0^\infty t P_N(t) dt / \int_0^\infty P_N(t) dt$. The numerically calculated $\langle \tau \rangle$ values are very close to the approximate formula

$$\langle \tau \rangle \approx \frac{N}{\gamma_N} + \frac{N(N-1)}{2} (k_{i \rightarrow i \pm 1}(V, \gamma_{\text{deph}}))^{-1} + \frac{N-1}{2} (\tilde{k}(V, \gamma_N))^{-1} \quad (8.3)$$

$k_{i \rightarrow i \pm 1}(V, \gamma_{\text{deph}}) = 2(V/\hbar)^2 / \gamma_{\text{deph}}$ is an effective transfer rate between nearest-neighbor

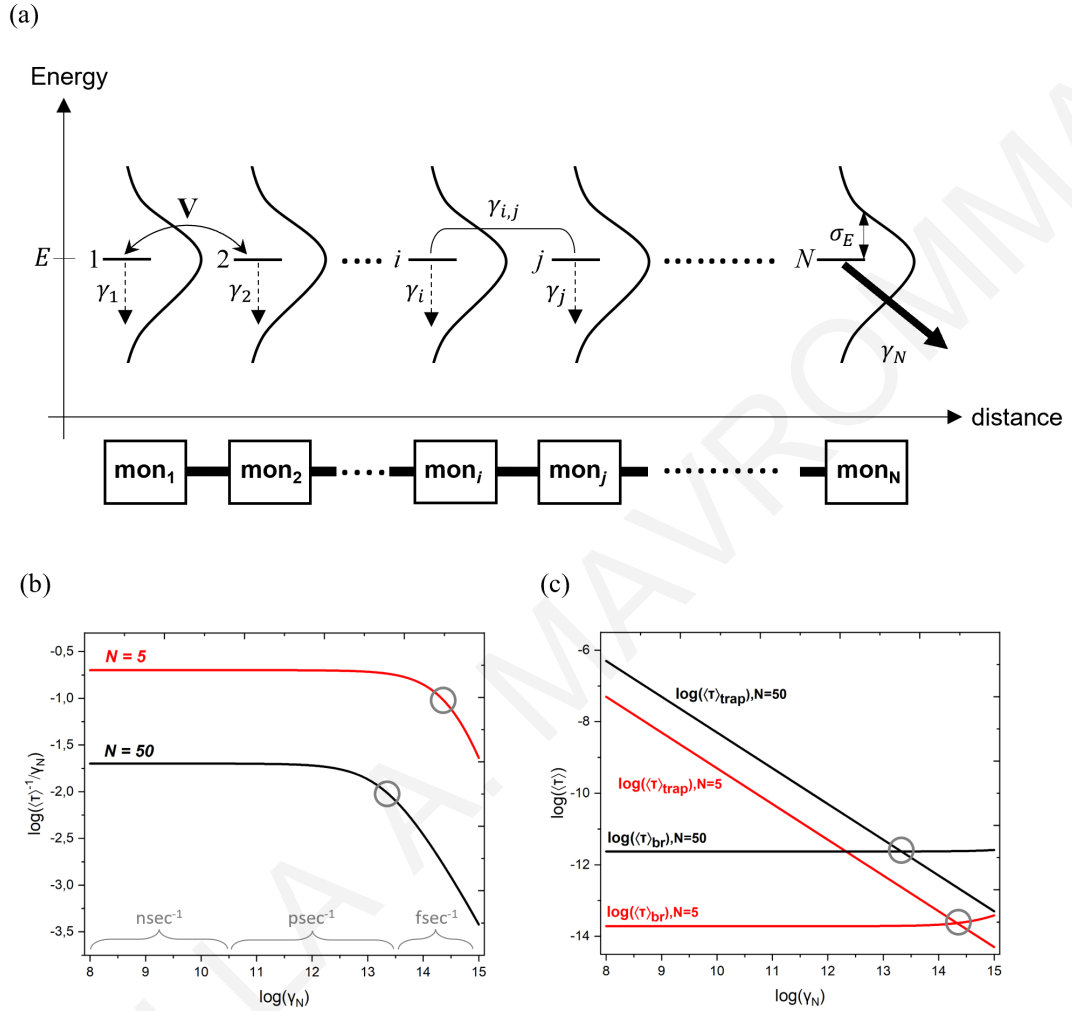


Figure 8.3: (a) Schematic diagram of the tight-binding model used to estimate the intra-bridge TET rates $k_{\text{br}} = \langle \tau \rangle_{\text{br}}^{-1}$ for a bridge with N sites (monomers). E is the monomer TE energy, $V = V_{\text{rms}}$ is the rms nearest-neighbour TET coupling and σ_E is the standard deviation of the energies E arising from dynamic disorder. The γ_i for $i = 1 - (N - 1)$ are the monomer TE population relaxation rates. Each γ_i equals $\gamma_i = k_B^{(\text{ph})}$ (monomer TE phosphorescence decay rate) and γ_N is the TET rate to an acceptor, $\gamma_N \approx k_{B \rightarrow A}^{(\text{TET})}$. The $\gamma_{i,j}$ are pure dephasing rates given by $\gamma_{i,j} = \hbar^{-1} \sqrt{\sigma_{E(i)}^2 + \sigma_{E(j)}^2}$. (b) $\langle \tau \rangle^{-1} / \gamma_N$ versus γ_N (both on a \log_{10} scale) for $N = 5$ (red) and $N = 50$ (black) with $\gamma_i = 1 \mu\text{s}^{-1}$ ($i = 1 - (N - 1)$), $\hbar\gamma_{i,j} = 0.1 \text{ eV}$ and $V = 0.15 \text{ eV}$ ($V > \sigma_E$). (c) Trapping time $\langle \tau \rangle_{\text{trap}}$ and intrinsic bridge TET time $\langle \tau \rangle_{\text{br}}$ versus γ_N , both in logarithmic scale, for $N = 5$ and $N = 50$. The circles indicate the values of γ_N for which $\langle \tau \rangle_{\text{trap}} = \langle \tau \rangle_{\text{br}}$.

TE populations and $\tilde{k}(V, \gamma_N) = 2(V/\hbar)^2/\gamma_N$.²⁰⁴ We re-write the analytical formula for $\langle\tau\rangle$ as $\langle\tau\rangle \approx \langle\tau\rangle_{\text{trap}} + \langle\tau\rangle_{\text{br}}$ where we have separated the trapping time $\langle\tau\rangle_{\text{trap}} = N/\gamma_N$ since it trivially depends on the bridge length and on the final-site population-relaxation rate γ_N . The remaining terms depend on the bridge Hamiltonian and the dephasing parameters and are written as $\langle\tau\rangle_{\text{br}} = \langle\tau\rangle_{\text{br,deph}} + \langle\tau\rangle_{\text{br,relax}}$ with $\langle\tau\rangle_{\text{br,deph}} = \frac{N(N-1)}{2}(k_{i \rightarrow i \pm 1}(V, \gamma_{\text{deph}}))^{-1}$ and $\langle\tau\rangle_{\text{br,relax}} = \frac{N-1}{2}(\tilde{k}(V, \gamma_N))^{-1}$. We see that when $\langle\tau\rangle_{\text{br}} \ll \langle\tau\rangle_{\text{trap}}$ the overall decay rate $\langle\tau\rangle^{-1}$ is independent of V and γ_{deph} because it is rate-limited by $\gamma_N = k_{B \rightarrow A}^{(\text{TET})}$, i.e., $\langle\tau\rangle^{-1} \approx \gamma_N/N$. In the opposite limit, $\langle\tau\rangle_{\text{br}} \gg \langle\tau\rangle_{\text{trap}}$, the overall rate is given by $\langle\tau\rangle^{-1} \approx \langle\tau\rangle_{\text{br}}^{-1}$. The intra-bridge TET rate is given by $k_{\text{br}} = \langle\tau\rangle_{\text{br}}^{-1}$.

Figure 8.3(b) shows the numerically computed $\langle\tau\rangle^{-1}/\gamma_N$ versus γ_N in logarithmic scale for $N = 5$ and $N = 50$ using $V = 0.15$ eV and $\hbar\gamma_{i,j} = 0.1$ eV. Figure 8.3(c) shows $\langle\tau\rangle_{\text{trap}}$ and $\langle\tau\rangle_{\text{br}}$ in logarithmic scale for the systems in figure 8.3(b). From the plots we deduce that $\langle\tau\rangle_{\text{br}} = 20$ fsec and 2 psec for $N = 5$ and $N = 50$ respectively. The circles in both figures show the γ_N values for which $\langle\tau\rangle_{\text{trap}} = \langle\tau\rangle_{\text{br}}$. For lower γ_N values the overall rate $\langle\tau\rangle^{-1}$ becomes rate-limited by the trapping time. The computed values of $\langle\tau\rangle_{\text{br}}$ in figure 8.3(b) suggest very fast TET for bridge lengths of approximately ~ 1 nm ($N = 5$) and ~ 15 nm ($N = 50$), respectively. The ultrafast transfer times for $N = 5$ (20 fsec) should be compared to the much slower TET times of 100-200 psec for the dimer and trimer bridges in ref. 1. The dependence of k_{br} as a function of bridge length N is given by $(\langle\tau\rangle_{\text{br,deph}} + \langle\tau\rangle_{\text{br,relax}})^{-1}$. Further, for $\hbar\gamma_{\text{deph}} \leq V_{\text{rms}}$ and $\hbar\gamma_{\text{deph}} \approx 0.1$ eV, it holds that $\langle\tau\rangle_{\text{br,deph}} \gg \langle\tau\rangle_{\text{br,relax}}$ for $\gamma_N \leq 10$ fsec⁻¹. In this broad regime, the distance dependence of the intra-bridge TET rate is approximately $k_{\text{br}} \approx \frac{1}{N(N-1)} \frac{(V/\hbar)^2}{\gamma_{\text{deph}}}$ (see section 8.11).

Due to the ultrafast k_{br} predicted for such types of bridges, a common situation for different choices of D and A will be that the TET D-to-B injection rate $k_{D \rightarrow B}^{(\text{TET})}$ and the B-to-A trapping rate $k_{B \rightarrow A}^{(\text{TET})}$ are slower than k_{br} . Therefore, the effective (bridge-mediated) D-to-A TET rate $k_{D \rightarrow A}^{(\text{eff,TET})}$ will be rate-limited by the slowest of $k_{D \rightarrow B}^{(\text{TET})}$ and $k_{B \rightarrow A}^{(\text{TET})}$. If the initial D TE states are created by intersystem crossing (ISC) from D SE states produced by D photoexcitation, it is possible that fast D-to-A SET will take place. This is because any bridge architecture with a wide TE band will necessarily have at least an equally wide SE band. Thus, the SET transport channel may out-compete the TET channel. In this case, to enable D-to-A TET as opposed to SET, it is necessary to use donors with fast ISC rates as compared to the D-to-B SE injection rates, $k_D^{(\text{ISC})} > k_{D \rightarrow B}^{(\text{SET})}$.

As a case study of the above constraints we used a Ru(bpy)₃²⁺ complex for D, due to its fast ISC rate (20-40 fsec)^{208,209} and long triplet lifetime (~ 10 μsec).²¹⁰⁻²¹² We connected it to a hexamer (IF6) bridge and a tetracene acceptor^{213,214} (figure 8.1(D)). The D and A moieties are linked to the bridge via methylene groups. Figure 8.4 (left-hand side) shows the TE eigenenergy manifold of the D-B-A system for one of

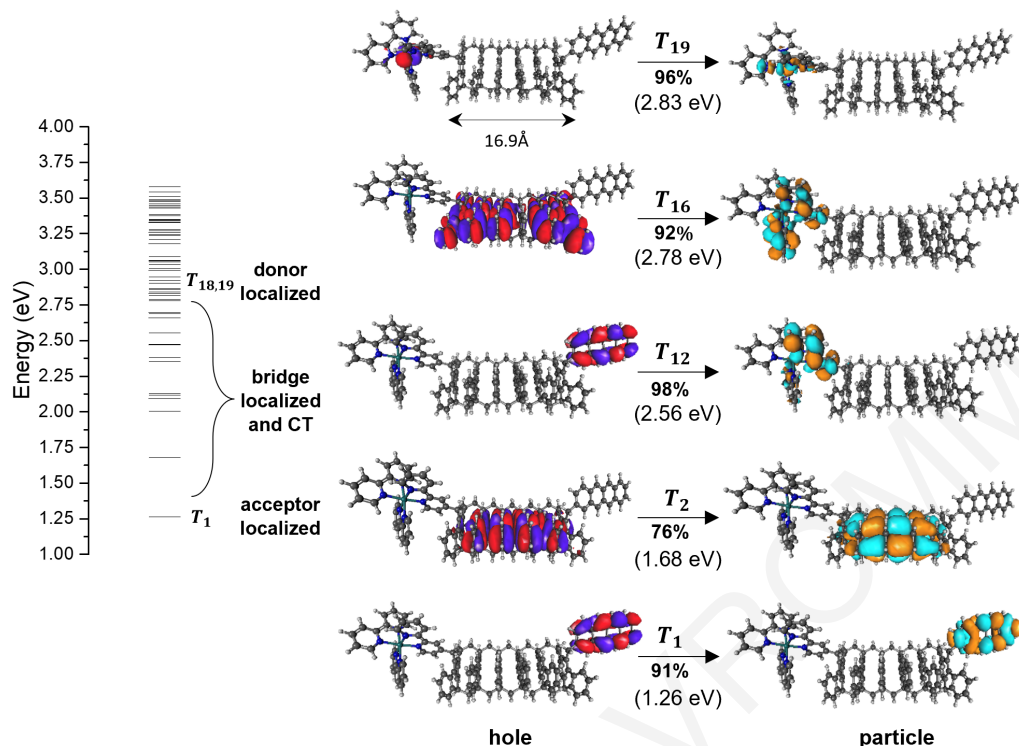


Figure 8.4: *Left:* Energy level diagram of the TE eigenstates of $\text{Ru}(\text{bpy})_3^{2+}$ - IF6 - Tet system computed at wB97/def2-SVP level of theory. *Right:* Hole-particle pairs of the natural transition orbitals (NTOs) of some TE's. T_{19} is localized on D, T_1 on A, T_2 on B and T_{16} , T_{12} are D-B and D-A CT TE's.

the geometries we considered, computed at the gas-phase using TD-DFT (wB97/def2-SVP^{115,215} and see section 8.7 for higher basis set computations). The right-hand side shows representative TE eigenstate of the entire D-B-A systems. The D-localized TE energies are above the lowest B-localized TE energies, the latter being above the lowest A-localized TE. Further, there are no charge transfer (CT) D-B or A-B TE's with energies below the other TE's so that there is no CT state trapping. This is an optimal placement of the TE bands for coherent resonant D-to-A TET. Further, the bridge-localized TE eigenstates have delocalization lengths that cover the entire bridge. For this system, the simulations described in figure 8.3(b) for $N = 6$ predict an ultrafast intra-bridge TET rate over a bridge length of ~ 1.5 nm ($k_{\text{br}} \approx (10\text{fsec})^{-1}$).

The design requirements for proposing the polymeric structure in figure 8.1 could be satisfied for a variety of monomer units. For example, for a perylene diimide (PDI) monomer the inner-sphere reorganization energy of the lowest TE is small, approximately 0.1 eV (see section 8.9). We performed computations on perylene-based polymers in order to explore different candidate structures (see section 8.9). Among our trial systems the best, from the point of view of optimizing coherent TET, are built from polymers with doubly-linked monomers using methyl linkers that bring the monomers to sub-VdW intermonomer distances (see figure 8.5). The necessity of double linkage is illustrated in figures 8.5(a-c). Figure 8.5(a) shows a dimer system with a

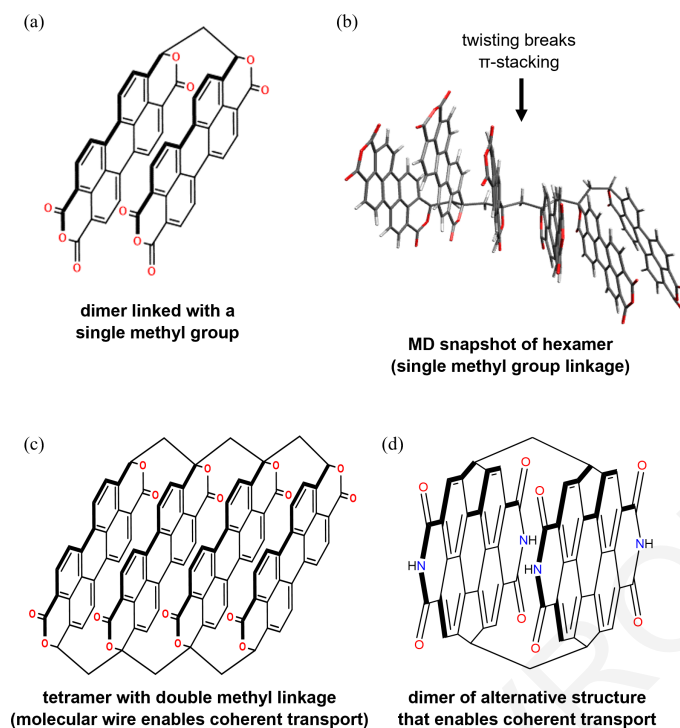


Figure 8.5: (a) Structure of anthra[2,1,9-def:6,5,10-d',e',f']diisochromene-1,3,8(10H)-trione dimer with a single methyl group linkage which enforces sub-VdW π -stacking. (b) Longer polymers with single methyl group linkages between monomers twist at room temperature, breaking the π -stacking and diminishing the interchromophore TET coupling. (c) This problem can be remedied by double methyl linkages between units of anthra[2,1,9-def:6,5,10-d',e',f']diisochromene-1,3,8(3H,10H)-dione monomers. In this case π -stacking is preserved for all pairs of nearest-neighbor monomers and for each pair, $V_{\text{rms}} \geq \frac{\lambda_{\text{mon}}}{2}$. Such a wire supports long-distance coherent ET as in the case of the wires shown in figure 8.1. (d) Structure of two dicyclopenta[ghi,pqr]perylene derivatives linked with two methylene linkers to build a dimer. This type of structure also has strong TET coupling compared to the monomer reorganization energy ($V_{\text{rms}} = 0.2$ eV).

single linker at C=O positions. This C=O to C–C substitution is challenging from a synthetic point of view, but it may be possible.²¹⁶ If a single methyl bridge is used per monomer pair to build a polymer, molecular dynamics simulations show that the π -stacking breaks for a long-enough polymer, diminishing the TET coupling and the TET efficiency (figure 8.5(b)). Such a system can be transformed to a molecular wire that supports coherent TET over long distances if nearest-neighbor monomers are linked by two methyl groups as in figure 8.5(c). In this case we find that $V_{\text{rms}} \approx 0.15$ eV such that $V_{\text{rms}} > \frac{\lambda_{\text{mon}}}{2}$, as in the previous IF example (see section 8.9). Another good system for coherent TET, that might be easier to synthesize compared to the previous one is shown in figure 8.5(d).²¹⁷ For this dimer structure we find that $V_{\text{rms}} = 0.2$ eV such that $V_{\text{rms}} > \frac{\lambda_{\text{mon}}}{2}$.

8.3 Conclusions

In conclusion, we have proposed design principles for building long and rigid molecular bridges with delocalized TE states at room temperature. Such bridges, when placed in non-polarizable solvents, can mediate ultrafast and coherent TE transport from donor to acceptor moieties for distances that are much longer than what is currently possible. We have shown some example theoretical bridge structures that satisfy the design principles and are predicted to support single-molecule ultrafast and coherent TET. These structures are not meant to represent the only solutions to the constraints imposed by the design principles. They are shown because they minimize, at room temperature, intermonomer torsion and slide while simultaneously preserving sub-VdW intermonomer distances (the fluctuations in V^{TET} are at most 30% of the average). Although these three features present a great challenge for synthetic chemistry, they are absolutely necessary for long-distance and ultrafast coherent TET along the molecular wire.

Supplementary material

8.4 Summary of the computational methodologies for the IFn bridges

Ab-initio electronic structure calculations on the proposed bridges. We performed geometry optimizations on the singlet ground state of the indenofluorene (IF) monomer and the polymers (π -stacked dimer to hexamer). We used density functional theory (DFT) and the ORCA program package^{122,218} at the B3LYP^{114,129,219} level of theory in combination with the def2-TZVP¹²³ basis set. We applied the resolution of identity approximation (RI) for the Coulomb integrals and the chain of spheres approximation (COSX) to the exact exchange,^{220,221} in combination with the def2/J auxiliary basis sets²²² without symmetry constraints. Dispersion corrections were included via Grimme's D3 correction^{223,224} using Becke-Johnson (BJ) damping.²²⁵ The B3LYP functional paired with dispersion corrections was selected because it accurately predicts the equilibrium geometries and the interaction energies of van der Waals (VdW) complexes.²²⁶⁻²²⁸ The ground-state geometry of the decamer was relaxed using steepest-descent molecular mechanics with the UFF (Universal Force Field) force field as implemented in the Avogadro software.²²⁹ For these optimized structures we computed the lowest excited states (singlet-to-singlet and singlet-to-triplet transitions) using the Amsterdam Density Functional (ADF) program package,⁹⁴ and time-dependent DFT (TD-DFT) with the Tamm-Dancoff approximation (TDA).¹⁰⁵ We used the M06-2X functional,^{110,111} combined with DZP basis set¹⁰³ without symmetry constraints. Meta-hybrids reliably predict the excitation energies and spectroscopic properties of non-covalent complexes.²³⁰ The singlet-to-triplet transitions were also computed with the Configuration Interaction Singles (CIS) method, as implemented in the ORCA program package, in combination with the def2-SVP basis set.^{123,215}

In section 8.5 we show the energies of the singlet exciton (SE) and triplet exciton (TE) eigenstates of the monomer, dimer, hexamer and decamer bridges. Figure 8.8 shows the SE energies computed at the M06-2X/DZP level of theory while figures

8.9 and 8.10 show the TE energies computed at the M06-2X/DZP and CIS/def2-SVP levels, for comparison. In addition, tables 8.1, 8.2, 8.3 and 8.4 show the delocalization of the molecular orbitals that contribute to the lowest two TE eigenstates, of the monomer, dimer, hexamer and decamer, computed with CIS/def2-SVP (M06-2X/DZP method gives similar delocalization of the orbitals).

Reorganization energy calculations for the monomer. For the computations of the reorganization energies of the monomer, we used ADF to diagonalize the mass-weighted Hessian matrix \tilde{H} by $L^T \tilde{H} L = \omega^2$ on the optimized structures of the monomer for the ground state (S_0) and first TE state (T_1), in order to obtain the normal modes and their frequencies (where L denotes the eigenvectors and ω the eigenvalues).^{125,126} Then we used the FCF (Franck-Condon factors) auxiliary program as implemented in ADF to compute the reorganization energy for each normal mode.^{127,128} The total reorganization energy for the transition $S_0 \rightarrow T_1(T_1 \rightarrow S_0)$ equals to the sum of the normal mode reorganization energies. The geometry optimization and frequency computations employed the BP86 functional¹¹⁴ and the TZ2P basis set¹⁰³ with the TDA. Figure 8.6 shows schematically the monomer reorganization energies (λ_D and λ_A) used to compute the activation energy U^{act} in the main text. In the classical high-temperature limit, the total reorganization energy (λ) for donor (D) to acceptor (A) TET is approximated by (see pages 289-291 in ref. 10)

$$\lambda = \lambda_D + \lambda_A. \quad (8.4)$$

Ab-initio electronic structure calculations on the donor-bridge-acceptor complexes. We performed excited-state computations (with TD-DFT) on the combined donor-bridge-acceptor system using the ORCA program package and with the ω B97 range-separated functional,¹¹⁵ in combination with the TDA and without symmetry constraints. Range-separated functionals reproduce well the optical absorption spectrum and the lowest-lying triplet excited states of heavy-metal systems (such as $\text{Ru}(\text{bpy})_3^{2+}$).²³¹⁻²³³ In addition, range-separated functionals combined with TDA perform well in the calculation of TE energies in long π -conjugated molecules and accurately predict the charge-transfer (CT) donor-bridge and bridge-acceptor excitations.^{159,160,198,234} The def2-SVP basis set was used for all the atoms. In the case of Ru(II), the def2-SVP basis set was used for the outer-core $[(4s)^2(4p)^6]$ and the valence $(4d)^6$ electrons while the inner-core electrons were treated as effective core potential (ECP).²³⁵ We also performed computations with the CIS method and the def2-SVP basis set for comparison. The results were found to be similar to those computed with TDA, i.e., the ordering of the TE exciton eigenenergies and the localization of the TE eigenstates were similar for both methods.

Effects of thermal fluctuations on the polymer structural stability. To test the structural stability of the polymers (dimer up to decamer), we performed classical molecular dynamic (MD) simulations using the AMBER program package.²³⁶ The op-

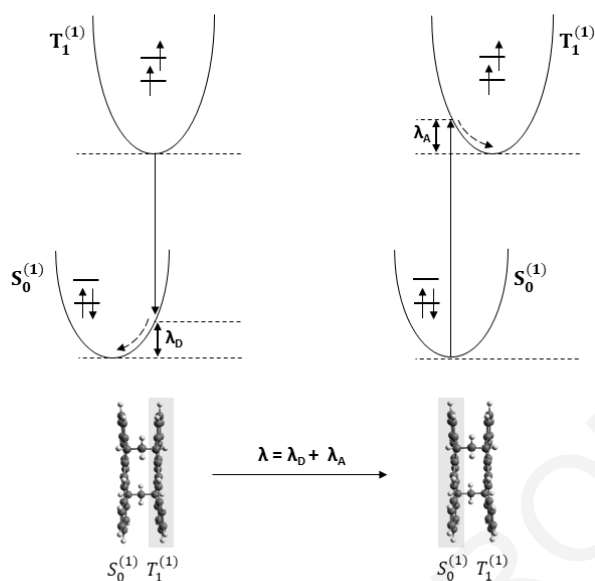


Figure 8.6: Schematic representation of the potential energy surfaces (PES) of the singlet ground state $S_0^{(1)}$ and the first TE state $T_1^{(1)}$ of the donor and acceptor moieties (i.e., IF monomer). The donor-to-acceptor reorganization energy λ , is the sum of the reorganization energies of the donor and acceptor, according to 8.4.

timized structures of the IF bridges were used as the initial structures for the simulations. The atomic charges were calculated with the AM1-BCC model^{237,238} and the simulations were carried out under conditions of constant temperature (298 K) and the GAFF force field,²³⁹ for 10 nsec using 1 fsec integration step and the Langevin thermostat with frequency of collision^{240–242} equal to 5 (ps)^{-1} .

Effects of thermal fluctuations on the nearest-neighbor TE transfer (TET) coupling. The effects of conformational fluctuations on the TET coupling were tested by performing *ab-initio* MD simulations on the dimer structure, using the Q-CHEM program package.²⁴³ For the computations we used the B3LYP functional with the 6-31G* basis set²⁴⁴ in combination with Grimme’s D3BJ dispersion correction. The simulation was carried out with the NVT (constant volume and temperature) ensemble using the white noise Langevin thermostat²⁴⁵ at room temperature (298 K) for a total of 23 psec with 1 fsec time step. The system was equilibrated during the first 3 psec. The 20 psec MD simulation time for the dimer is sufficient for sampling its vibrational motions (we performed normal mode computations on the dimer using ADF and BP86/TZ2P and found that the lowest-frequency normal mode has a period of approximately 1 psec). To compute the fluctuations of the TET coupling we picked 190 MD snapshots separated by 100 fsec and for each snapshot we computed the TE splitting between the lowest two TE states of the dimer ($\Delta E = E_{T_2^{(2)}} - E_{T_1^{(2)}} = 2V^{TET}$) using the ORCA program at CIS/def2-SVP level of theory. From the collection of the MD-derived splittings we

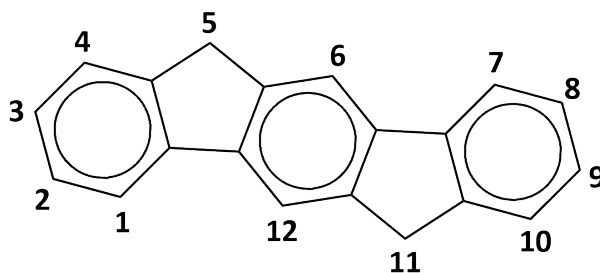


Figure 8.7: The IF monomers are cut off from the dimer and each monomer is capped with hydrogens at positions 5' and 11'.

deduced the root mean square (rms) of the TET coupling (V_{rms} in the main text).

Effects of thermal fluctuations on the monomer TE energies. To compute the fluctuations of the monomer TE energies we used the abovementioned MD-derived dimer structures to create 380 (190×2) monomer structures by cutting the two methylene bridges, and capping the carbons at the positions 5' and 11' with hydrogen atoms (see figure 8.7). We computed the energy of the lowest TE state of each monomer structure at the CIS level (in combination with def2-SVP basis set) using the ORCA program. From the collection of TE energies we estimated the standard deviation σ_E^{mon} of the main text.

Effects of structural fluctuations on the TE delocalization. We studied the effects of thermal fluctuations of the molecular orbitals of the IF decamer (IF10) by performing classical MD simulations and using the MD-derived snapshots for subsequent computations of the frontier molecular orbitals. We used the AMBER and the ORCA program packages to perform the MD simulations and the quantum chemical calculations respectively. First, the system was equilibrated for 1 nsec using the Langevin thermostat (frequency of collision equals to 5 (ps)^{-1}) at a temperature of 298 K with a time step of 1 fsec. After equilibration, we ran MD simulations up to 9 nsec using 1 fsec time step, with the GAFF force field. The atomic charges were calculated using the AM1-BCC charge model. We performed computations of the molecular orbitals on 3000 MD trajectories separated by 3 psec. These calculations were carried out at HF/def2-SVP level of theory and the orbital eigenstates were used to evaluate the inverse participation ratio (IPR) of the orbitals involved in the lowest TE's of the decamer (see section 8.8 for the IPR).

8.5 SE and TE states of the IF_n bridges with n = 1,2,6,10

In this section we show the computed SE and TE eigenenergies of the proposed bridges (monomer, dimer, hexamer, decamer). In figures 8.9 and 8.10 we compare the performance of the M06-2X functional to the CIS method for the computation of TE energies. The results show that the TE energies (especially the lowest-lying TE's) and splittings are similar. Tables 8.1, 8.2, 8.3 and 8.4 show the natural transition orbitals (NTOs)²⁴⁶ of the lowest TE's of the monomer, dimer, hexamer and decamer, computed at the CIS/def2-SVP level of theory. The last column of each table shows the transition amplitudes of particle-hole excitations (in percentages).

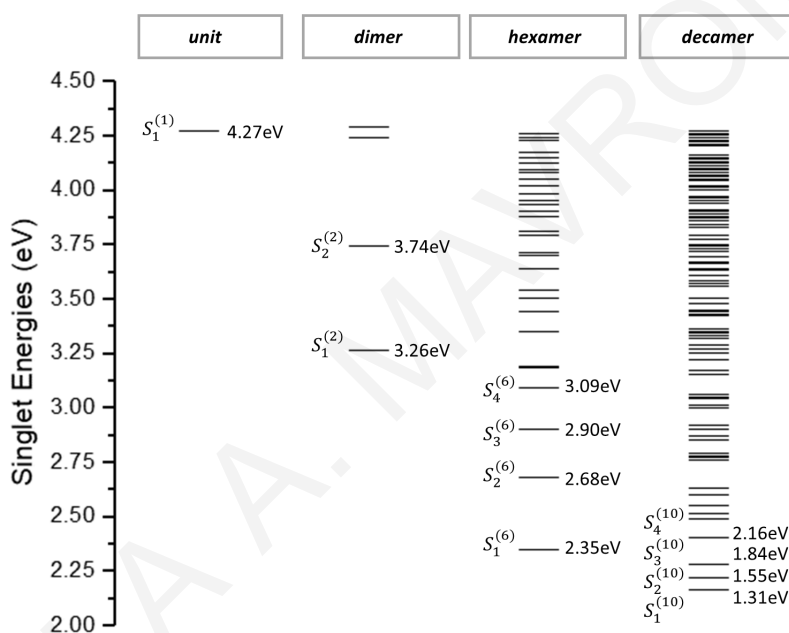


Figure 8.8: SE states ($S^{(n)}$) of the IF_n bridges (n = 1,2,6,10) computed at the M06-2X/DZP level of theory using the ADF program package. The notations (1), (2), (6), (10) denote monomer, dimer, hexamer and decamer systems respectively.

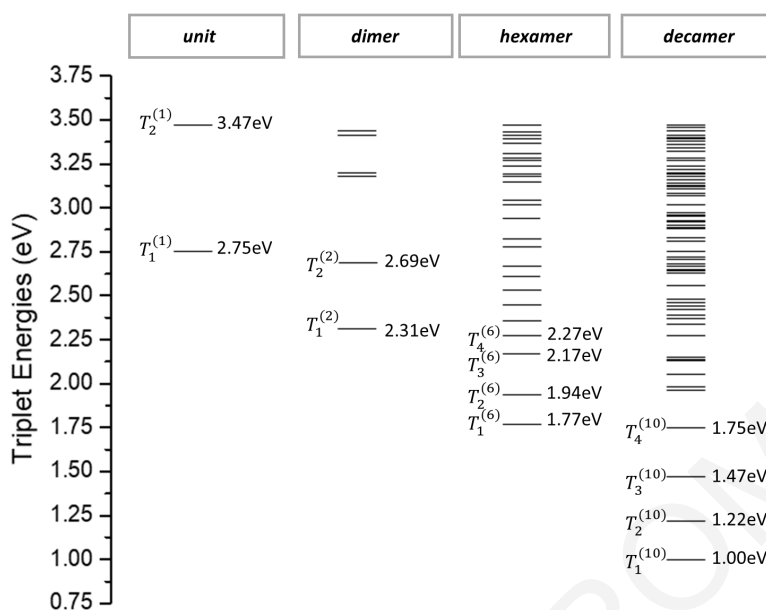


Figure 8.9: TE states ($T^{(n)}$) of the IF_n bridges (n = 1,2,6,10) computed at the M06-2X/DZP level of theory using the ADF program package. The notations (1), (2), (6), (10) denote monomer, dimer, hexamer and decamer systems respectively.

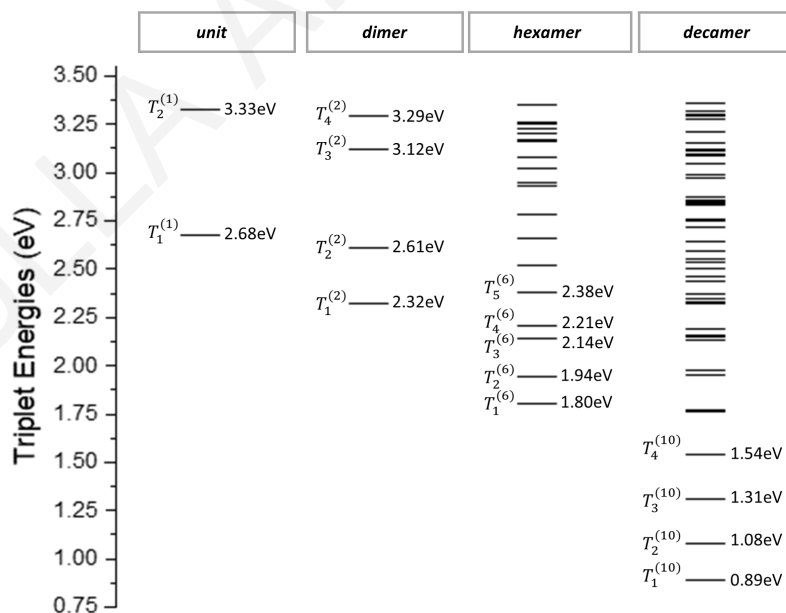


Figure 8.10: TE states ($T^{(n)}$) of the IF_n bridges (n = 1,2,6,10) computed at the CIS/def2-SVP level of theory using the ORCA program package. The notations (1), (2), (6), (10) denote monomer, dimer, hexamer and decamer systems respectively.

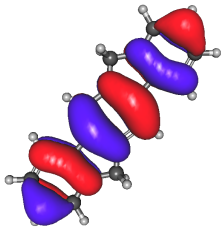
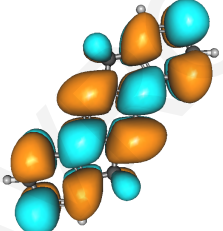
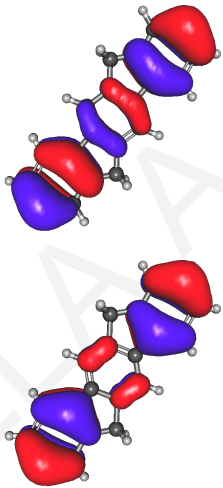
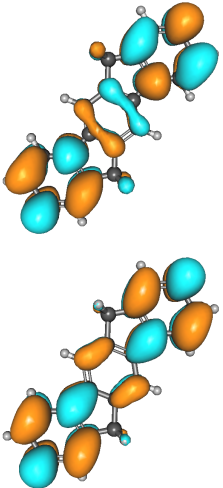
Triplet State	hole	particle	contribution
1			62%
2			27%
			27%

Table 8.1: Hole-particle pairs of NTOs of the lowest two ($T_1^{(1)}$, $T_2^{(1)}$) TE states of the monomer, computed at the CIS/def2-SVP level of theory (based on a 0.02 isosurface value).

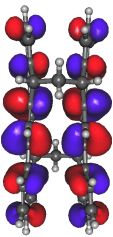
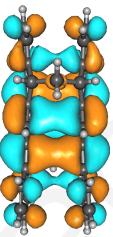
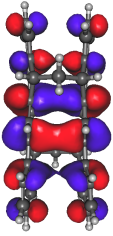
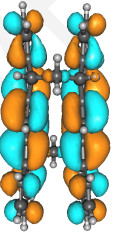
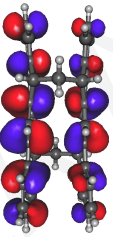
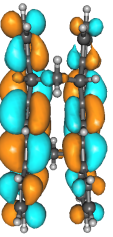
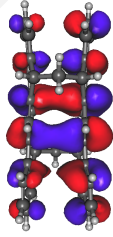
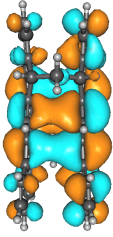
Triplet State	hole	particle	contribution
1			52%
			15%
2			32%
			31%

Table 8.2: Hole-particle pairs of NTOs of the lowest two ($T_1^{(2)}$, $T_2^{(2)}$) TE states of the dimer, computed at the CIS/def2-SVP level of theory (based on a 0.02 isosurface value).

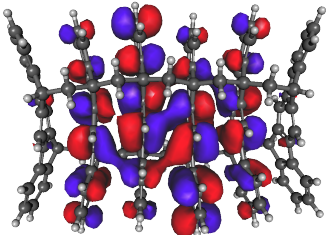
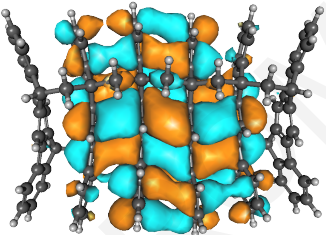
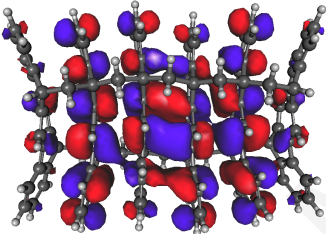
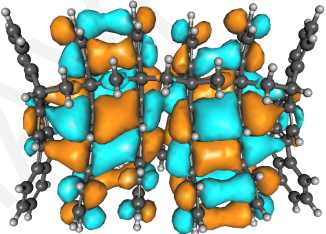
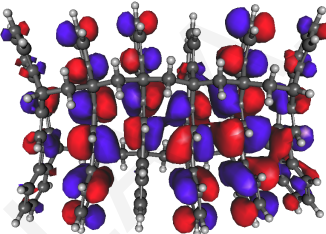
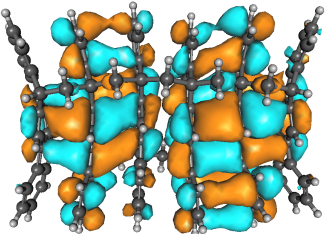
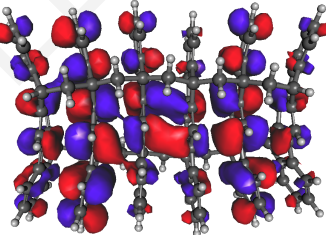
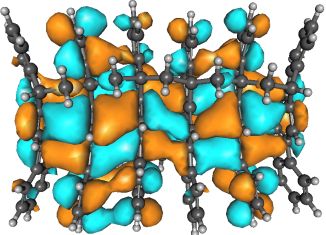
Triplet State	hole	particle	contribution
1			43%
			15%
2			30%
			26%

Table 8.3: Hole-particle pairs of NTOs of the lowest two ($T_1^{(6)}$, $T_2^{(6)}$) TE states of the hexamer, computed at the CIS/def2-SVP level of theory (based on a 0.01 isosurface value).

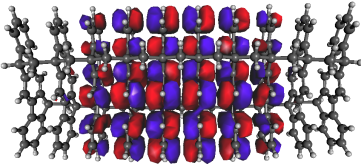
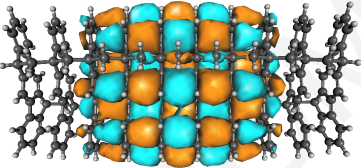
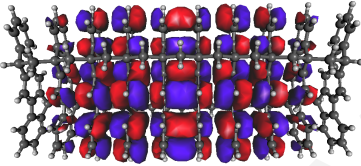
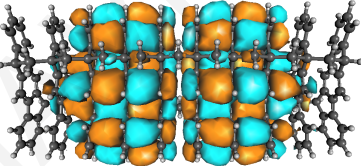
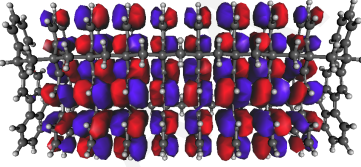
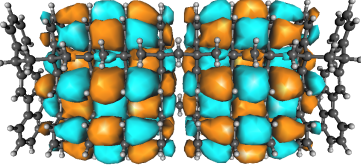
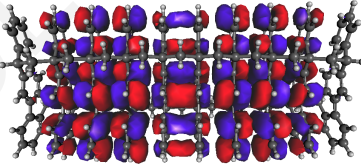
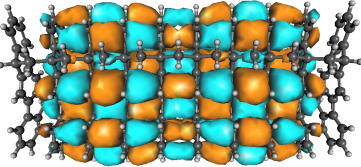
Triplet State	hole	particle	contribution
1			52%
			15%
2			33%
			29%

Table 8.4: Hole-particle pairs of NTOs of the lowest two ($T_1^{(10)}$, $T_2^{(10)}$) triplet states of the decamer, computed at the CIS/def2-SVP level of theory (based on a 0.005 isosurface value).

8.6 Comparison between CIS (TD-DFT) and higher-level methods for the TE energies of the IF dimer

The lowest TE states of the IF dimer were computed using high-level *ab-initio* methods including similarity-transformed equation of motion coupled cluster method (STEOM-CC),²⁴⁷⁻²⁵² perturbative doubles correction for the single excitation configuration interaction method (CIS(D)),²⁵³ and algebraic diagrammatic construction method to second-order (ADC(2)).^{254,255} We computed the lowest two TE states ($T_1^{(2)}, T_2^{(2)}$) of the dimer using these methods and we compared the results with those given by TD-DFT and CIS methods.

The STEOM-DLPNO-CCSD (similarity transformed equation of motion – domain-based local pair natural orbital – coupled cluster with singles and doubles excitations) were carried out using the ORCA program package in combination with def2-SVP basis set. The $T_{\text{CutPNOsingles}}$ keyword was set to $1e - 11$ and the active selection keywords “Othresh” and “Vthresh” were set to 0.005. The CIS(D) and ADC(2) methods were both carried out using the Q-CHEM program package. The CIS(D) method was combined with def2-SVP basis set and the ADC(2) with 6-31G. All the computations were performed at the optimized geometry of the dimer (see section 8.4).

	STEOM-DLPNO-CCSD (eV)	CIS(D) (eV)	ADC(2) (eV)	CIS (eV)	M06-2X (eV)	ω B97 (eV)
$T_1^{(2)}$	2.20	3.12	2.89	2.32	2.34	2.82
$T_2^{(2)}$	2.55	3.52	3.32	2.61	2.70	3.18
ΔE	0.35	0.40	0.43	0.29	0.36	0.36

Table 8.5: TE energies of the IF dimer computed with different *ab-initio* methods. Values are in eV.

Our results show that, although the absolute TE energies vary from 2.2 eV to 3.1 eV across methods, the energy splitting ΔE ($\Delta E = E_{T_2^{(2)}} - E_{T_1^{(2)}}$) that is used to estimate the TET coupling varies much less 0.3 eV to 0.4 eV.

8.7 Testing the accuracy of the TE energies of the donor-bridge-acceptor systems using higher-level basis sets

In this section we test the accuracy of the TD-DFT computations on the donor-bridge-acceptor system, with respect to the chosen basis set. To reduce computational cost we performed our computations on the donor-bridge system where the bridge is the IF2. We used the ω B97 functional in combination with the def2-SVP basis set of double-zeta quality. These results were compared to those performed with the def2-TZVP basis set which is of triple-zeta quality. The results are summarized in table 8.6.

Triplet state	def2-SVP	def2-TZVP	% deviation
1	2.46	2.43	1.15
2	2.51	2.48	1.29
3	2.52	2.49	1.24
4	2.60	2.57	1.25
5	2.64	2.60	1.58
6	2.66	2.61	1.80
7	2.69	2.66	1.13
8	2.99	2.95	1.29
9	3.07	3.04	0.82
10	3.10	3.07	0.85
11	3.16	3.12	1.19
12	3.21	3.19	0.56
13	3.23	3.20	0.97
14	3.31	3.30	0.52
15	3.40	3.35	1.46
16	3.41	3.36	1.31
17	3.43	3.39	1.36
18	3.46	3.40	1.59
19	3.48	3.45	0.78
20	3.51	3.48	0.72

Table 8.6: Comparison of TE energies computed using the ω B97 functional with the def2-SVP and def2-TZVP basis set for the Ru(bpy₃²⁺)-IF2 system. Energy values are in eV.

The results on the lowest 20 triplet excited states show that the TE energies computed with def2-SVP are systematically larger by approximately 2% as compared to those computed with def2-TZVP. Also the ordering of the TE states does not change. Therefore, for our calculations on the donor-bridge-acceptor systems we used the def2-SVP basis set since it provides accurate results with lower computational time.

8.8 Computation of the IPR parameters

The delocalization of molecular wavefunctions is described by the inverse participation ratio (IPR).^{27,28,201,256–258} Consider the k th molecular orbital wavefunction

$$|\chi_k\rangle = \sum_{n=1}^N c_n^k |\varphi_n\rangle \quad \sum_{n=1}^N |c_n^k|^2 = 1 \quad (8.5)$$

expressed in the basis of N atomic (site) orbitals $(\varphi_1, \varphi_2, \dots, \varphi_N)$. The IPR for this molecular orbital is defined as

$$L_k = \left(\sum_{n=1}^N |c_n^k|^4 \right)^{-1} \quad (8.6)$$

where c_n^k is the amplitude of the k th eigenfunction corresponding to the n th site. The IPR can range from a value of 1 for a fully localized molecular orbital (localized at a single φ_n), to a value of N for a fully delocalized molecular orbital.

The TE states ($|\mathcal{Y}_T\rangle$) are linear combinations of singly excited Slater-type determinants that describe the promotion of an electron from an occupied molecular orbital χ_a to a virtual molecular orbital χ_i

$$|\mathcal{Y}_T\rangle = \sum_{a,i} b_{a,i} |\Psi_a^i\rangle. \quad (8.7)$$

The TE delocalization can be estimated from the delocalization length of the occupied and virtual molecular orbitals involved in the excitation (L_a, L_i) .

We computed the IPR's for the HOMO, HOMO-1 and LUMO, LUMO+1 molecular orbitals of the decamer since they contribute to the lowest TE state ($T_1^{(10)}$: 40% HOMO \rightarrow LUMO and 10% HOMO-1 \rightarrow LUMO+1 in figure 1(b) of the main text). The reference values for the IPRs are those computed for the optimized geometric conformation of the decamer (shown in figure 1(b) of the main text). We found that the IPRs for the HOMO and HOMO-1 orbitals (figure 1(b), main text) are equal to 336 and 401 respectively, and those for the LUMO and LUMO+1 orbitals (figure 1(b), main text) are equal to 489 and 462 respectively. These results reveal that, for the decamer bridge, an IPR value of the order of ~ 400 (average value of the four molecular orbitals that contribute to the lowest TE state) describes a fully delocalized TE state. We also computed MD-averaged IPR values \bar{L}_k and standard deviations σ_{L_k} for the relevant molecular orbitals χ_k contributing the TE state (using 3000 MD snapshots). The values $\bar{L}_k \pm \sigma_{L_k}$ for the HOMO, HOMO-1, LUMO and LUMO+1 orbitals are 207 ± 56 , 258 ± 65 , 335 ± 63 and 365 ± 54 , respectively (mean value: 292 ± 60). Thus, the MD-averaged IPR is approximately 73% of the reference IPR value for the optimized geometry of figure 1(b). These results imply that thermal fluctuations do

not affect the delocalization of the TE's on longer polymers.

8.9 SE and TE computations on the perylene-based dyads

Figure 8.11 shows the π -stacked perylene-based dimer structures we used to compute SET and TET couplings. These are: perylene-3,4,9,10-bis(dicarboxyimide) (PDI) ((a) and (b)), perylene-3,4-dicarboximide (PMI) (c) and terrylene-3,4:11,12-bis(dicarboximide) (TDI) (d).

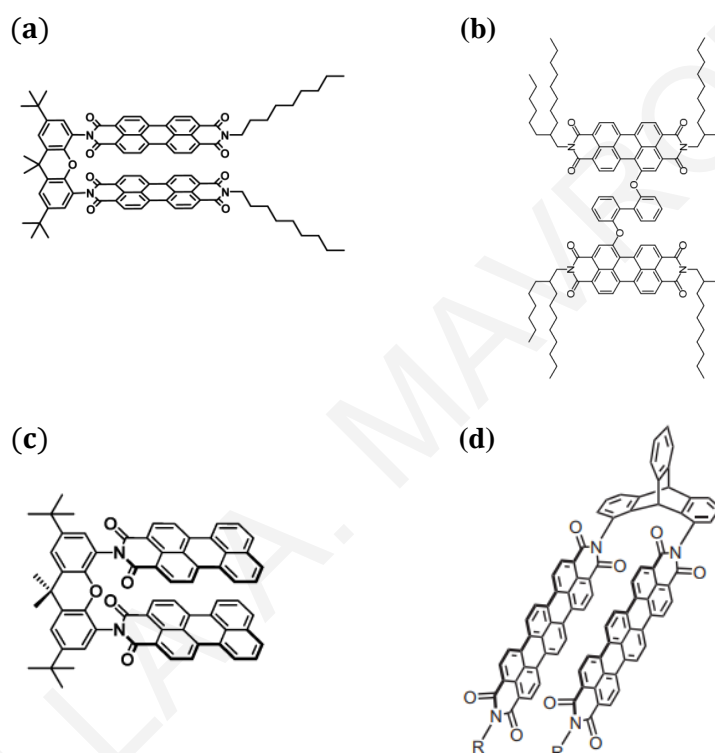


Figure 8.11: Molecular structures of perylene-based dimers. (a) PDI dimer of ref. 2, (b) PDI dimer of ref. 3, (c) PMI dimer of ref. 4 and (d) TDI dimer of ref. 5 with R = Me.

Table 8.7 summarizes the lowest two SE and TE energies of the dimers and the energy splittings: $\Delta E_{SE} = E_{S_2^{(2)}} - E_{S_1^{(2)}} = 2V^{SET}$ and $\Delta E_{TE} = E_{T_2^{(2)}} - E_{T_1^{(2)}} = 2V^{TET}$, where the notation (2) denotes dimer. The excited-state computations were performed using the ORCA program package at the CIS/def2-SVP level and also at the ω B97/def2-SVP level applying the TDA. The geometric structures (a), (c) and (d) (see figure 8.11), were taken from refs. 2, 4 and 5 respectively. The ground-state structure of (b) was built using the Avogadro software, and optimized at the B3LYP/def2-SVP level of theory (including dispersion corrections D3BJ) using the ORCA program.

The experimentally-derived SET couplings (from absorption band widths)¹⁹⁵ are approximately 0.1 eV. Further, SET couplings for several organic π -stacked dimeric systems computed using high-level methods are 0.1 - 0.4 eV.^{3,194,198} Our CIS and DFT

computations on the π -stacked dimeric systems of figure 8.11 give SET coupling values consistent with the abovementioned SET coupling magnitudes (table 8.7). The TET couplings computed by both DFT and CIS methods are similar to each other and are much weaker than the SET couplings (see table 8.7). On the other hand, for the proposed IF dimer the TET coupling is an order of magnitude greater than those predicted for the perylene-based dimers.

	(a)		(b)		(c)		(d)		IF	
	CIS	ω B97	CIS	ω B97	CIS	ω B97	CIS	ω B97	CIS	ω B97
ΔE_{SE}	0.39	0.40	0.20	0.17	0.25	0.26	0.39	0.35	0.74	0.53
ΔE_{TE}	0.02	0.03	0.02	0.03	0.01	0.02	0.05	0.05	0.29	0.35

Table 8.7: SE and TE energy splittings (ΔE_{SE} , ΔE_{TE}) of the perylene-based dimers (shown in figure 8.11) and the IF dimer. Values are in eV.

The inter-chromophore distance between the monomers in the above-mentioned dimers (figure 8.11) is on average greater than VdW ($\sim 4\text{\AA}$). To reduce this distance we tried to link several perylene-based monomers via shorter bridges as shown in figures 8.12 and figure 4 in the main text. Similar monomer structures to the ones shown in the figures have already been synthesized, e.g., see refs. 6,216. We performed MD computations to estimate the V_{rms} in these systems. The results show that the structure in figure 8.12(a) is very rigid (very low torsional and slippage motions), but the intermonomer distance is always greater than $\sim 4\text{\AA}$. This causes weak TET coupling of the order of ~ 0.01 eV. The structure shown in figure 8.12(b) shows large dynamic disorder that diminishes the TET coupling (~ 0.03 eV). On the other hand, the structure shown in figure 4(c) in the main text exhibits large interchromophore TET coupling because it maintains tight π -stacking. The average value of the TET coupling equals to $V_{ave} = 0.14$ with $\sigma_V = 0.05$ eV and the rms coupling equals to $V_{rms} = 0.15$ eV. If the monomers are linked with a single methyl group (see figure 4(a) in the main text), MD simulations on the dimer and longer polymers (i.e., hexamer) show that the π -stacking breaks (figure 4(b)). Therefore, to prevent this breaking it is necessary to link the nearest-neighbor chromophores with methylene bridges in two positions (as shown in figure 4(c) in the main text). We also computed the TE reorganization energy of the perylene-based monomer whose dimer structure is shown in figure 4(a) (λ computed as described in section 8.4). We found that $\lambda_{D(A)} = 0.14$ eV such that $U^{act} = 0.07$ eV. Therefore for these types of doubly-linked bridges, $V_{rms} > \lambda/2$. Another candidate that also looks promising for building molecular wires that support coherent TET is shown in figure 4(d) in the main text. For this system, the MD simulations followed by CIS computations give $V_{rms} = 0.2$ eV, i.e., $V_{rms} > \lambda/2$.

The MD simulations on the dimers and the longer polymers were performed using the AMBER program package for a total of 10 nsec with 1 fsec time step and the NVT ensemble at a temperature of 298 K (Langevin thermostat with frequency of

collision equal to 5 (ps)^{-1}). To estimate the MD-averaged TET coupling, we performed quantum chemical calculations on 2000 MD-snapshot structures at the CIS/def2-SVP level of theory (using ORCA).

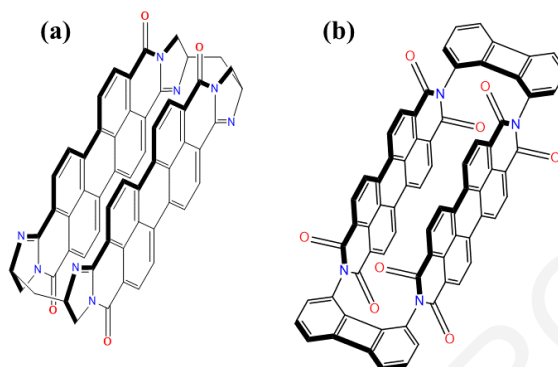


Figure 8.12: Molecular structures of perylene-based chromophore dimers that were tested for coherent TE transport. (a) Bisbenzimidazo[2,1-a:2',1'-a']anthra[2,1,9-def:6,5,10-d'e'f']diisoquinoline-10,21-dione monomers linked with methyl groups, (b) anthra[2,1,9-def:6,5,10-d'e'f']diisoquinoline-1,3,8,10(2H,9H)-tetraone (perylene diimide) monomers linked with biphenylene bridges.⁶

8.10 TET and SET couplings as a function of the inter-chromophore distance

We tested the TET and SET couplings as a function of the inter-chromophore distance between two fluorene monomers and two PDI monomers (3,4,9,10-Perylenetetracarboxylic dianhydride), as shown in figure 8.13. The couplings were computed using the ORCA program package at CIS/def2-SVP level. Our results reveal that the TET coupling becomes two to three orders of magnitude smaller than the SET couplings when the distance between the monomers becomes greater than VdW.

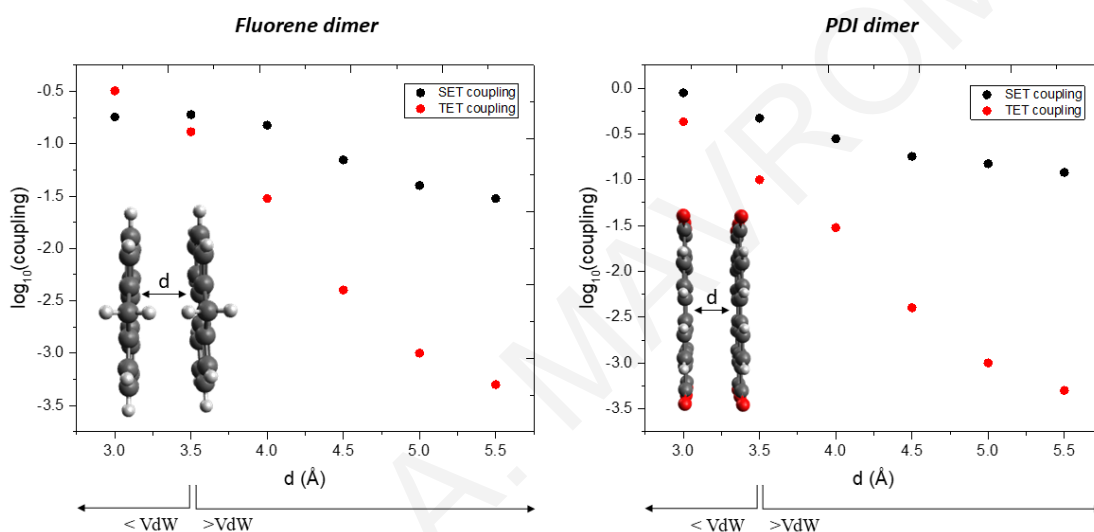


Figure 8.13: SET and TET couplings (in logarithmic scale) versus distance (in Å). The TET coupling drops considerably below 0.10 eV for distances greater than VdW while the SET coupling is much greater. *left.* Computations on the fluorene dimer. *right.* Computations on the PDI dimer.

8.11 Distance dependence of the intra-bridge TET rate

From the analytical solutions to the Mean First Passage Time (MFPT) in the model described in ref. 204, we define the intra-bridge rate as $k_{br} = 1/\langle\tau\rangle_{br}$ where,

$$\langle\tau\rangle_{br} \approx \langle\tau\rangle_{br,deph} + \langle\tau\rangle_{br,relax}$$

$$\langle\tau\rangle_{br,deph} = \frac{N(N-1)}{2} \frac{\gamma_{deph}}{2(V/\hbar)^2} \quad (8.8)$$

$$\langle\tau\rangle_{br,relax} = \frac{N-1}{2} \frac{\gamma_N}{2(V/\hbar)^2}.$$

Figure 8.14 shows the intra-bridge TET rate k_{br} (in logarithmic scale) as a function of the bridge length N , computed for $V = 0.2$ eV, $\hbar\gamma_{deph} = 0.1$ eV and $\gamma_N = (10 \text{ nsec})^{-1}$. In the range of $\gamma_N \leq (10 \text{ fsec})^{-1}$ the behavior of k_{br} is near identical and is dominated by $\langle\tau\rangle_{br,deph}$.

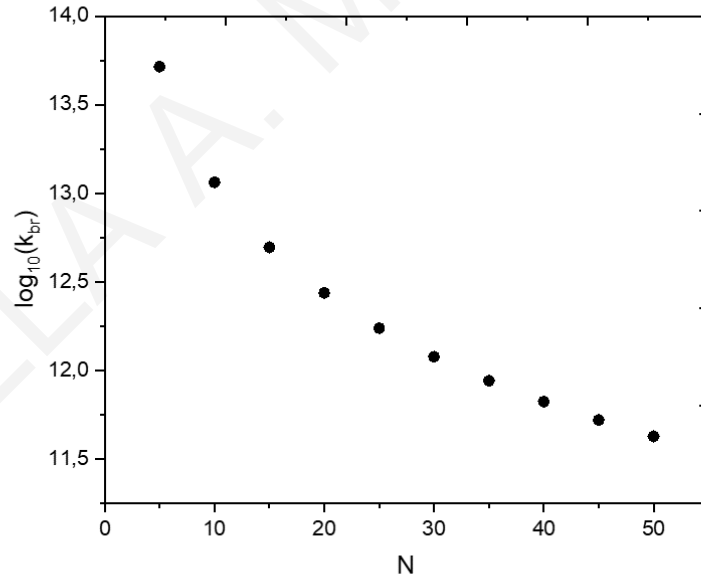


Figure 8.14: Distance dependence of the intra-bridge TET rate (k_{br}) (in logarithmic scale) as a function of the length of the bridge. The simulations were performed for $V = 0.2$ eV, $\hbar\gamma_{deph} = 0.1$ eV and $\gamma_N = (10 \text{ nsec})^{-1}$.

8.12 Ground state structures of the proposed IF bridges

Below are the atomic coordinates of the optimized ground-state structures computed according to section 8.4.

IF dimer:

C	-2.389	1.438	-0.054	C	-10.844	-4.795	4.856
C	-2.498	0.232	-0.743	C	-9.611	-2.786	5.397
C	-3.628	-0.566	-0.599	C	-9.827	-5.213	3.998
C	-3.406	1.860	0.801	H	-9.528	-1.853	5.941
C	-4.526	1.065	0.958	H	-9.927	-6.143	3.451
C	-4.643	-0.142	0.251	C	-8.596	-3.206	4.545
C	-5.760	1.294	1.815	C	-8.710	-4.414	3.838
C	-6.642	0.122	1.418	H	-6.998	-5.575	3.283
C	-5.932	-0.750	0.571	C	-7.310	-2.595	4.222
C	-6.453	-1.995	0.228	C	-7.478	-4.638	2.978
C	-7.706	-2.325	0.704	H	-7.379	-0.645	5.143
C	-7.946	-0.159	1.787	C	-6.791	-1.349	4.565
C	-8.487	-1.384	1.402	C	-6.598	-3.465	3.375
H	-1.505	2.050	-0.180	H	-4.768	0.680	5.186
H	-1.695	-0.087	-1.395	C	-5.538	-1.016	4.090
H	-3.713	-1.499	-1.143	C	-5.295	-3.182	3.006
H	-3.304	2.789	1.348	C	-4.814	0.313	4.155
H	-6.237	2.232	1.507	C	-4.755	-1.956	3.393
H	-5.866	-2.700	-0.348	H	-4.723	-3.870	2.393
H	-8.516	0.530	2.400	C	-3.427	-0.061	3.670
C	-9.816	-3.279	1.131	C	-3.428	-1.376	3.175
C	-9.814	-1.964	1.624	C	-2.266	0.688	3.668
C	-10.971	-1.415	2.163	C	-2.269	-1.923	2.639
C	-12.134	-2.179	2.180	H	-2.259	1.700	4.056
H	-13.042	-1.763	2.597	H	-2.261	-2.931	2.244
C	-12.142	-3.470	1.661	C	-1.099	0.130	3.150
H	-13.057	-4.049	1.672	C	-1.106	-1.160	2.628
C	-10.977	-4.029	1.139	H	-0.184	0.709	3.144
H	-10.986	-5.042	0.754	H	-0.196	-1.576	2.213
H	-10.978	-0.407	2.556	C	-5.502	1.450	3.341
C	-8.432	-3.654	0.641	H	-6.466	1.653	3.816
H	-8.481	-4.020	-0.389	H	-4.902	2.353	3.477
H	-11.539	-3.273	6.199	C	-7.740	-4.792	1.452
H	-11.724	-5.411	4.984	H	-6.778	-4.994	0.974
C	-10.737	-3.588	5.544	H	-8.340	-5.695	1.316

IF hexamer:

C	-4.233	0.386	-1.998	C	-8.970	-4.262	4.423
C	-4.796	-0.785	-2.499	H	-4.114	-0.141	5.098
C	-5.719	-1.495	-1.746	C	-7.173	-2.896	3.969
C	-4.587	0.867	-0.741	C	-8.164	-4.972	3.341
C	-5.517	0.173	0.008	H	-6.414	-1.049	4.724
C	-6.076	-1.007	-0.497	C	-6.293	-1.846	4.002
C	-6.176	0.542	1.339	C	-7.030	-3.959	3.057
C	-7.236	-0.545	1.475	H	-0.536	-4.954	1.243
C	-7.090	-1.470	0.432	C	-5.279	-1.834	3.090
C	-7.885	-2.595	0.370	C	-6.007	-3.927	2.115
C	-8.880	-2.715	1.305	C	-4.279	-0.732	2.969
C	-8.320	-0.608	2.332	C	-5.125	-2.833	2.123
C	-9.184	-1.693	2.211	H	-5.898	-4.715	1.378
H	-3.526	0.939	-2.601	C	-3.460	-1.216	1.778
H	-4.510	-1.139	-3.481	C	-3.989	-2.429	1.281
H	-6.169	-2.400	-2.137	C	-2.405	-0.596	1.144
H	-4.147	1.786	-0.374	C	-3.438	-3.001	0.143
H	-7.724	-3.349	-0.390	H	-2.007	0.340	1.518
H	-8.499	0.162	3.073	H	-3.840	-3.921	-0.261
C	-10.890	-3.278	2.359	C	-1.854	-1.179	0.004
C	-10.472	-2.018	2.829	C	-2.374	-2.368	-0.492
C	-11.299	-1.279	3.663	H	-1.034	-0.693	-0.508
C	-12.546	-1.791	4.004	H	-1.950	-2.807	-1.386
H	-13.206	-1.215	4.640	C	-5.105	0.601	2.558
C	-12.962	-3.027	3.525	H	-5.648	0.936	3.445
H	-13.943	-3.403	3.784	H	-4.389	1.386	2.307
C	-12.127	-3.781	2.702	C	-9.084	-5.164	2.033
H	-12.462	-4.737	2.320	H	-8.458	-5.577	1.237
H	-10.987	-0.311	4.034	H	-9.849	-5.910	2.257
C	-9.842	-3.860	1.415	H	-8.987	-1.630	-2.574
C	-10.432	-4.081	-0.024	H	-11.288	-3.260	-1.813
H	-10.502	-2.010	7.152	C	-11.105	-2.848	-0.816
H	-11.592	-4.129	6.529	H	-7.748	0.162	-4.184
C	-10.061	-2.632	6.384	H	-13.728	-4.063	-0.544
C	-10.679	-3.831	6.033	C	-9.365	-1.029	-1.755
C	-8.890	-2.241	5.759	H	-6.309	1.959	-5.097
C	-10.137	-4.651	5.050	C	-7.431	0.982	-3.551
H	-8.401	-1.314	6.032	C	-13.622	-3.068	-0.127
H	-10.632	-5.578	4.791	C	-10.373	-1.493	-0.918
C	-8.355	-3.065	4.781	C	-12.415	-2.401	-0.189

C	-6.631	1.999	-4.063	C	-0.898	-2.314	3.346
C	-8.791	0.220	-1.478	C	-2.148	-4.722	2.636
C	-7.842	1.049	-2.226	H	-0.402	-1.388	3.606
C	-14.717	-2.441	0.472	H	-2.639	-5.648	2.362
H	-15.672	-2.949	0.511	C	-0.357	-3.134	2.363
C	-10.965	-0.578	-0.019	C	-0.976	-4.332	2.011
C	-12.286	-1.104	0.340	C	-3.454	-0.624	4.373
C	-6.239	3.067	-3.262	C	-7.582	-6.339	4.020
C	-9.104	0.906	-0.285	H	-8.431	-7.009	4.174
C	-7.438	2.125	-1.413	H	-6.922	-6.821	3.295
H	-5.623	3.854	-3.678	H	2.174	-5.743	3.752
C	-14.584	-1.169	1.017	H	-6.518	-5.828	11.874
C	-10.290	0.586	0.364	H	-7.501	-7.906	10.993
C	-13.368	-0.493	0.957	C	-6.232	-6.181	10.892
C	-6.640	3.129	-1.926	C	-6.795	-7.352	10.390
C	-8.061	2.012	-0.029	C	-5.311	-5.469	10.139
H	-15.437	-0.695	1.488	C	-6.442	-7.831	9.132
H	-10.665	1.190	1.182	H	-4.861	-4.565	10.530
H	-13.277	0.503	1.371	H	-6.883	-8.750	8.765
H	-6.329	3.962	-1.305	C	-4.954	-5.956	8.889
H	-9.634	-4.471	-0.659	C	-5.514	-7.135	8.383
C	-6.985	1.878	1.157	C	-3.942	-5.491	7.960
H	-6.288	2.707	1.008	C	-4.855	-7.503	7.051
H	-7.512	2.080	2.093	H	-3.307	-3.615	8.784
H	-11.206	-4.852	0.007	C	-3.147	-4.367	8.023
H	-8.574	2.950	0.207	C	-3.797	-6.415	6.914
H	-9.086	-4.162	9.782	H	2.912	-3.556	4.612
H	-9.999	-6.276	8.904	C	-2.153	-4.245	7.087
C	-8.661	-4.600	8.887	C	-2.714	-6.351	6.057
C	-9.180	-5.789	8.391	C	-1.192	-3.100	6.978
C	-7.600	-3.965	8.251	C	-1.850	-5.266	6.179
C	-8.629	-6.372	7.251	H	-2.535	-7.119	5.315
H	-7.198	-3.044	8.656	C	-0.143	-3.681	6.034
H	-9.026	-7.309	6.877	C	-0.562	-4.940	5.562
C	-7.048	-4.536	7.113	C	1.094	-3.179	5.692
C	-7.575	-5.750	6.617	C	0.265	-5.679	4.728
H	-2.604	0.045	4.219	H	1.430	-2.223	6.076
C	-5.912	-4.130	6.271	H	-0.047	-6.646	4.355
C	-6.756	-6.232	5.424	C	1.930	-3.931	4.869
H	-5.139	-2.248	7.017	C	1.513	-5.167	4.388
C	-5.031	-3.036	6.279	C	-1.951	-1.797	6.361
C	-5.758	-5.128	5.304	C	-5.928	-7.563	5.834
H	0.557	-2.838	1.868	H	-1.187	-1.050	6.136
C	-4.007	-3.003	5.337	H	-2.578	-1.385	7.158
C	-4.745	-5.116	4.392	H	-6.643	-8.349	6.086
C	-2.872	-1.990	5.054	H	-5.386	-7.898	4.946
C	-3.865	-4.065	4.425	H	4.407	-6.258	6.902
H	-4.623	-5.912	3.669	H	-4.715	-8.929	13.485
C	-2.067	-2.701	3.973	H	-5.399	-10.822	12.064
C	-2.683	-3.897	3.614	C	-4.394	-8.967	12.451

C	-4.785	-10.034	11.648
C	-3.595	-7.948	11.940
C	-4.385	-10.094	10.312
H	-3.279	-7.128	12.574
H	-4.695	-10.926	9.690
C	-3.186	-8.012	10.614
C	-3.589	-9.087	9.800
C	-2.238	-7.181	9.867
C	-2.968	-8.972	8.416
H	-2.041	-5.333	10.966
C	-1.665	-5.932	10.145
C	-1.925	-7.865	8.672
H	4.641	-4.006	7.883
C	-0.658	-5.466	9.309
C	-0.740	-7.543	8.023
C	0.074	-4.111	9.208
C	-0.065	-6.380	8.408
H	-0.365	-8.146	7.204
C	1.384	-4.556	8.581
C	1.255	-5.852	8.049
C	2.591	-3.889	8.521
C	2.338	-6.462	7.431
H	2.696	-2.895	8.940
H	2.248	-7.458	7.016
C	3.686	-4.514	7.921
C	3.554	-5.785	7.373
C	-4.045	-8.838	7.231
H	-3.519	-9.039	6.295
H	-4.741	-9.668	7.380
C	-0.601	-2.879	8.417
H	-1.399	-2.490	9.052
H	0.172	-2.107	8.386
H	0.256	-3.699	10.205
H	-2.453	-9.908	8.178

IF decamer:

H	-11.032	-4.198	6.405	C	-6.295	-5.417	7.231
H	-11.220	-6.529	5.565	C	-6.566	-6.698	6.782
C	-10.214	-4.638	5.849	H	-2.471	-0.285	5.602
C	-10.321	-5.959	5.372	C	-5.045	-4.987	6.644
C	-9.054	-3.886	5.604	C	-5.479	-7.197	5.857
C	-9.266	-6.541	4.649	H	-4.676	-3.035	7.512
H	-8.973	-2.866	5.956	C	-4.341	-3.794	6.818
H	-9.345	-7.556	4.282	C	-4.595	-5.987	5.788
C	-8.021	-4.482	4.880	H	1.144	-1.991	2.719
C	-8.117	-5.783	4.412	C	-3.192	-3.620	6.031
H	-3.847	-0.987	6.484	C	-3.476	-5.791	4.963
C	-6.765	-3.914	4.433	C	-2.260	-2.445	6.022
C	-6.880	-6.199	3.658	C	-2.811	-4.570	5.088
H	-6.602	-2.002	5.470	H	-3.154	-6.540	4.253
C	-6.169	-2.672	4.738	C	-1.367	-2.804	4.855
C	-6.163	-4.845	3.585	C	-1.699	-4.040	4.330
H	0.524	-4.206	1.780	C	-0.334	-2.047	4.290
C	-4.972	-2.349	4.074	C	-1.038	-4.572	3.222
C	-5.057	-4.457	2.808	H	-0.072	-1.079	4.695
C	-4.028	-1.160	4.284	H	-1.317	-5.534	2.813
C	-4.513	-3.177	3.048	C	0.347	-2.563	3.174
H	-4.629	-5.123	2.071	C	-0.005	-3.819	2.641
C	-3.183	-1.293	3.044	C	-3.146	-1.166	5.642
C	-3.448	-2.472	2.364	C	-6.081	-7.403	4.388
C	-2.234	-0.390	2.556	H	-6.762	-8.280	4.420
C	-2.783	-2.803	1.184	H	-5.239	-7.684	3.721
H	-2.027	0.533	3.082	H	2.271	-5.823	3.894
H	-3.005	-3.721	0.656	H	-7.187	-5.852	11.491
C	-1.557	-0.701	1.365	H	-7.823	-8.136	10.746
C	-1.828	-1.904	0.684	C	-6.556	-6.386	10.792
H	-0.819	-0.014	0.971	C	-6.917	-7.680	10.370
H	-1.300	-2.134	-0.232	C	-5.381	-5.784	10.312
H	-9.057	-4.863	9.111	C	-6.108	-8.384	9.460
H	-9.552	-7.169	8.327	H	-5.101	-4.789	10.630
C	-8.357	-5.374	8.464	H	-6.387	-9.375	9.129
C	-8.638	-6.680	8.019	C	-4.593	-6.502	9.411
C	-7.173	-4.729	8.070	C	-4.943	-7.772	8.985
C	-7.739	-7.353	7.173	C	-3.366	-6.122	8.748
H	-6.955	-3.723	8.402	C	-3.944	-8.316	7.990
H	-7.956	-8.353	6.823	H	-2.906	-4.151	9.535

C	-2.619	-4.944	8.858	C	3.860	-5.460	7.231
C	-2.994	-7.155	7.890	C	3.447	-6.738	6.805
H	2.962	-3.578	4.706	C	-3.153	-9.614	8.653
C	-1.492	-4.830	8.029	H	-2.414	-9.964	7.900
C	-1.877	-7.034	7.049	H	-3.899	-10.428	8.770
C	-0.534	-3.673	7.938	C	0.339	-3.576	9.344
C	-1.153	-5.839	7.130	H	-0.363	-3.252	10.141
H	-1.601	-7.819	6.358	H	1.076	-2.755	9.215
C	0.363	-4.145	6.817	H	10.969	-12.087	14.699
C	-0.010	-5.398	6.362	H	9.174	-10.978	12.458
C	1.441	-3.470	6.233	H	7.114	-12.012	13.410
C	0.657	-6.029	5.310	H	7.424	-9.799	10.284
H	1.735	-2.490	6.584	H	12.839	-13.075	17.079
H	0.349	-7.004	4.958	H	8.884	-13.151	15.559
C	2.128	-4.086	5.173	H	10.738	-14.216	17.787
C	1.737	-5.359	4.712	H	5.389	-10.830	11.291
C	-1.386	-2.371	7.418	C	10.338	-11.553	15.397
C	-4.684	-8.473	6.534	H	7.630	-16.954	19.703
H	-0.675	-1.524	7.318	H	0.790	-12.328	12.033
H	-2.092	-2.101	8.231	C	8.584	-10.437	13.186
H	-5.410	-9.309	6.614	C	7.424	-11.023	13.718
H	-3.906	-8.795	5.810	H	2.452	-13.512	14.060
H	3.988	-7.244	6.016	C	9.164	-12.156	15.877
H	-5.392	-6.962	13.731	H	5.875	-15.840	17.956
H	-6.097	-9.233	13.010	H	4.145	-14.689	16.046
C	-4.802	-7.503	13.003	C	6.859	-9.260	11.033
C	-5.202	-8.791	12.594	H	8.393	-17.725	21.984
C	-3.642	-6.917	12.471	C	12.139	-12.565	17.726
C	-4.446	-9.504	11.647	H	4.977	-12.633	14.617
H	-3.331	-5.928	12.779	H	-0.670	-12.767	12.954
H	-4.753	-10.491	11.329	H	6.254	-17.657	20.584
C	-2.907	-7.645	11.533	C	10.955	-13.210	18.119
C	-3.294	-8.909	11.122	C	5.714	-9.844	11.597
C	-1.699	-7.285	10.824	H	12.756	-15.073	20.233
C	-2.344	-9.474	10.091	H	8.459	-14.905	18.676
H	-1.195	-5.307	11.571	C	6.929	-16.775	20.545
C	-0.933	-6.114	10.900	C	0.085	-11.966	12.811
C	-1.367	-8.333	9.967	H	10.385	-15.938	20.719
H	4.717	-4.989	6.766	H	3.295	-11.455	12.567
C	0.184	-6.031	10.054	H	1.636	-10.260	10.507
C	-0.254	-8.247	9.117	H	3.692	-9.608	9.184
C	1.160	-4.890	9.929	H	6.688	-13.790	16.653
C	0.500	-7.068	9.178	H	1.001	-13.968	14.988
H	0.002	-9.050	8.438	H	11.605	-9.803	15.445
C	2.060	-5.418	8.836	H	14.814	-13.739	19.785
C	1.664	-6.677	8.414	C	1.751	-13.162	14.847
C	3.166	-4.791	8.253	C	10.698	-10.259	15.820
C	2.338	-7.360	7.400	H	4.458	-16.418	18.869
H	3.479	-3.807	8.579	C	5.169	-15.570	18.770
H	2.015	-8.340	7.077	H	5.811	-18.476	23.104

C	3.443	-14.366	16.844	C	3.336	-7.913	10.481
H	2.706	-15.187	16.972	C	2.157	-8.279	11.235
C	7.811	-16.782	21.903	C	7.076	-9.031	15.067
C	8.984	-9.149	13.595	C	8.725	-10.168	17.205
C	-0.709	-10.651	12.171	C	6.552	-7.265	12.409
H	-3.090	-11.661	13.467	H	2.047	-15.453	19.603
H	5.700	-8.558	8.143	C	5.339	-17.243	24.821
H	9.879	-8.707	13.180	C	14.102	-11.980	20.819
C	12.836	-14.053	20.585	H	4.602	-17.931	25.215
C	4.715	-11.826	15.288	C	11.520	-10.586	19.017
C	8.123	-14.146	19.370	C	5.413	-7.857	12.965
C	7.277	-7.976	11.437	C	0.040	-11.288	15.300
C	9.951	-15.269	21.450	C	10.347	-11.242	19.407
C	6.689	-10.296	14.656	C	5.149	-15.139	21.332
C	4.021	-8.625	9.494	H	0.304	-14.135	17.609
C	3.045	-10.643	13.237	C	-1.084	-11.891	15.874
C	13.996	-13.300	20.341	C	-3.495	-9.965	14.752
C	12.419	-11.258	18.172	C	5.572	-6.748	9.319
C	1.388	-9.449	11.179	H	-4.379	-10.406	15.193
H	8.161	-7.535	10.996	C	4.117	-15.896	21.897
C	0.947	-11.845	14.228	C	1.722	-12.524	17.352
C	6.042	-15.497	20.166	H	15.001	-11.409	20.626
C	8.375	-11.438	16.778	C	3.419	-13.798	19.371
C	6.401	-12.997	17.331	C	8.295	-14.765	23.140
H	13.334	-10.770	17.864	C	7.230	-15.471	23.823
C	2.622	-13.052	16.259	H	10.168	-8.564	17.061
C	10.077	-12.522	18.958	C	-0.036	-8.466	12.891
C	5.151	-8.029	8.910	C	5.149	-9.608	16.222
C	5.010	-9.119	12.560	C	2.342	-14.473	19.954
C	6.017	-17.554	23.631	H	6.444	-6.298	8.863
C	8.754	-15.592	22.114	C	-1.228	-8.822	13.628
C	4.317	-14.268	18.250	C	0.616	-13.152	17.935
C	-2.771	-10.676	13.780	C	3.281	-10.873	17.010
C	5.481	-10.656	15.365	H	8.535	-7.449	14.861
C	0.277	-9.520	12.034	C	6.593	-13.372	21.100
C	6.965	-16.650	23.143	C	8.376	-11.954	20.401
C	3.598	-11.911	16.134	C	3.504	-8.421	14.155
C	-1.632	-10.084	13.224	C	1.624	-9.662	14.954
C	8.827	-12.954	19.545	C	11.897	-12.157	21.778
C	6.974	-14.321	20.157	C	6.776	-10.786	18.299
C	1.933	-10.713	14.091	C	3.742	-6.653	10.888
C	3.818	-9.475	13.297	H	6.872	-6.280	12.722
C	7.148	-11.819	17.441	C	9.944	-13.096	22.604
C	9.889	-9.556	16.730	C	4.935	-12.103	19.058
H	-1.405	-12.875	15.560	C	13.047	-11.398	21.542
C	11.802	-13.458	21.310	C	6.125	-8.467	16.098
C	8.228	-8.436	14.542	C	1.849	-7.228	12.098
C	5.274	-13.112	18.159	H	11.737	-9.586	19.367
C	10.547	-14.026	21.756	C	4.866	-6.051	10.314
H	3.855	-16.864	21.491	C	5.609	-16.041	25.503

C	5.481	-13.903	21.858				
C	0.446	-10.028	15.708	C	-1.369	-9.912	17.278
C	7.725	-9.624	18.199	C	3.786	-14.125	23.546
C	4.035	-9.694	17.072	H	3.779	-8.892	17.751
C	2.118	-11.265	17.774	H	6.786	-14.223	25.532
C	4.491	-7.290	14.018	C	1.444	-10.583	18.788
C	9.259	-10.744	20.332	H	8.409	-12.819	24.118
C	8.838	-13.485	23.381	C	3.125	-11.914	20.879
C	-1.790	-11.194	16.870	H	6.934	-11.402	21.936
C	6.564	-15.140	25.004	H	0.487	-6.486	13.621
C	-3.077	-8.681	15.156	H	2.145	-7.681	15.681
C	7.257	-12.151	21.225	H	-1.607	-7.111	14.897
C	3.792	-12.544	19.826	C	2.045	-12.585	21.476
C	0.737	-7.298	12.951	H	4.452	-5.175	13.234
C	3.435	-15.381	23.013	H	10.968	-11.440	23.556
C	2.393	-8.492	15.009	H	10.542	-9.661	21.770
C	5.658	-10.908	19.140	H	5.382	-10.123	19.831
C	-1.932	-8.097	14.592	C	0.334	-11.205	19.383
H	-2.662	-11.644	17.325	H	6.195	-7.977	18.289
C	10.660	-11.742	22.532	H	4.617	-6.797	16.212
C	1.654	-13.857	21.014	H	7.686	-9.146	20.380
H	2.638	-15.954	23.467	H	9.019	-10.257	22.469
C	2.834	-6.096	11.960	H	2.991	-5.613	14.155
C	6.933	-8.326	17.537	H	5.098	-12.409	23.375
C	5.334	-7.159	15.444	H	0.090	-8.334	17.005
C	-0.079	-12.483	18.957	H	1.767	-9.602	19.112
C	8.464	-9.468	19.656	H	-1.919	-9.384	18.046
H	0.820	-14.365	21.481	H	3.257	-13.739	24.407
H	5.081	-15.811	26.419	H	3.432	-10.939	21.231
H	13.125	-10.383	21.909	H	1.511	-12.121	22.294
C	9.861	-10.538	21.802	H	-0.207	-10.699	20.172
C	3.696	-5.975	13.378	C	-1.553	-10.782	10.745
H	7.679	-7.512	17.420	C	2.031	-4.780	11.341
H	5.187	-5.066	10.629	H	1.330	-4.429	12.127
C	4.819	-13.371	22.966	H	2.781	-3.973	11.199
H	6.088	-6.356	15.308	H	-2.307	-11.585	10.881
C	-0.239	-9.317	16.695	H	-0.836	-11.144	9.977
H	-3.642	-8.142	15.905	H	-7.188	-6.501	2.634
H	-0.935	-12.954	19.422	H	-4.609	-0.217	4.203
H	9.190	-8.632	19.576				

CHAPTER 9

Triplet excitation energy transfer between quantum dots and organic molecules

9.1 Introduction

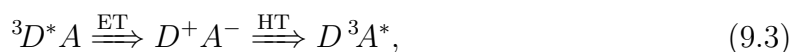
In this chapter we describe our work related to triplet exciton transfer (TET) between nanocrystals (NCs) and molecules. We investigate the TET mechanisms of direct Dexter energy transfer (DET) and sequential charge-transfer (CT) between a CdSe nanoparticle (NP) triplet sensitizer, and a modified structure of boron dipyrromethene (BODIPY) acceptor, linked to the NP. The TET kinetics in CdSe-BODIPY systems was recently reported by T. Lian and his co-workers ((a) Jin, T.; Uhlikova, N.; Xu, Z.; Zhu, Y.; Huang, Y.; Egap, E.; Lian. *T. J. Chem. Phys.* **2019**, *151*, 241101. (b) Jin, T.; Uhlikova, N.; Xu, Z.; Zhu, Y.; Huang, Y.; Egap, E.; Lian. *T. J. Chem. Phys.* **2020**, *152*, 214702.) The authors performed transient absorption spectroscopic (TAS) measurements and explored the different transport pathways to the formation of triplet excitons (TE's) in BODIPY following photoexcitation of the CdSe NP. These pathways (transport mechanisms) are described as direct, and CT in order to characterize the intermediate states that are mediating TET. In the direct mechanism the 3D TE transfers to the A without visiting an intermediate excited state (D holds for donor and A for the acceptor), i.e.,



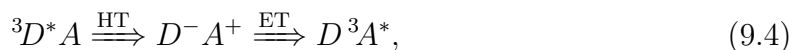
The interaction matrix element for this transition is

$$\langle {}^3D^*A | \hat{h}^{(2e)} | D^3A^* \rangle = -(\psi_{D^*} \psi_{A^*} | \psi_D \psi_A), \quad (9.2)$$

see eq. 2.61c in section 2.5.3 for details. In a CT mechanism, the D TE transfers to the A via a CT exciton state such that



i.e., electron transfer (ET) followed by hole transfer (HT), or



i.e., HT followed by ET. The ET interaction matrix element is given by

$$\langle D^* | \hat{h}^{(1e)} | A^* \rangle = V_{D^*A^*}^e, \quad (9.5)$$

whereas the HT interaction matrix element is given by

$$\langle D | \hat{h}^{(1e)} | A \rangle = -V_{DA}^h, \quad (9.6)$$

see eqs. 2.68 and 2.70 in section 2.5.4 for details. However, the physical origins of these TET mechanisms are still unclear for this particular system. In order to better understand these mechanisms, we examine the electronic-structure properties of the triplet excited states, and the opto-electronic properties of the CdSe-BODIPY assembly using theoretical methods and *ab-initio* quantum chemical computations, in order to better understand these mechanisms. This work is in collaboration with the group of Prof. D. N. Beratan at Duke University USA and it is still in progress.

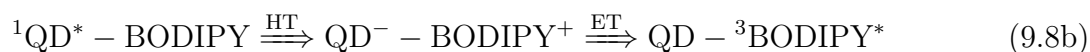
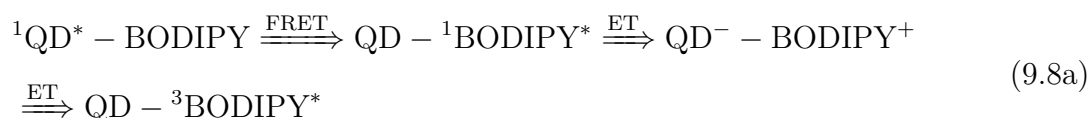
9.2 A brief description of the experimental observation

In the experiment, the authors photoexcited the CdSe quantum dot (QD), and using transient absorption (pump-probe) spectroscopy, they found that the direct DET pathway from the QD to the BODIPY does not contribute to TET (see figure 9.1(a)). They claim that the sequential CT pathways from the excited QD state to the triplet BODIPY state dominates the kinetics.²⁵⁹

The schematic diagram of figure 9.1(b) shows the three proposed pathways to the formation of triplet excited states on the acceptor molecule following photoexcitation of the donor QD. The triplet excitons in the acceptor moiety can be created through DET from the QD triplet state which is generated via intersystem crossing (ISC) from the singlet QD states i.e.,



The CT pathways as proposed in the paper are as follows (see figure 9.1(b)):



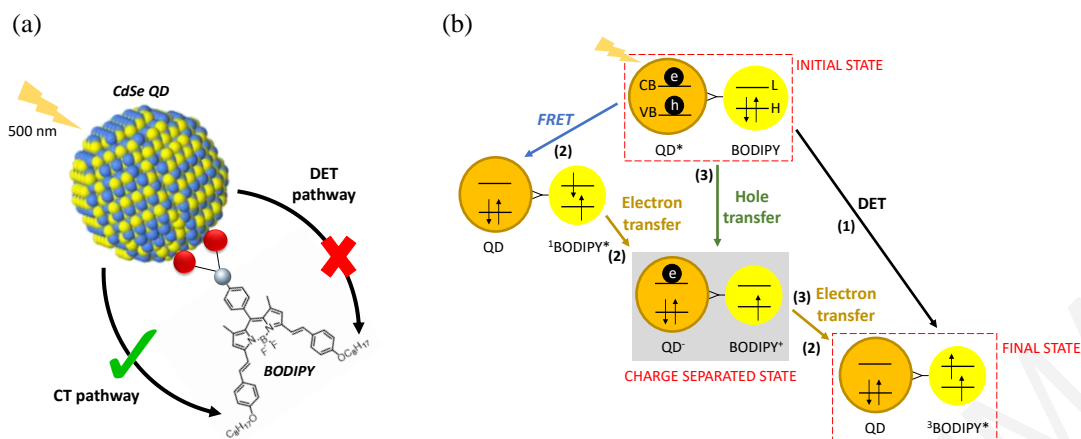
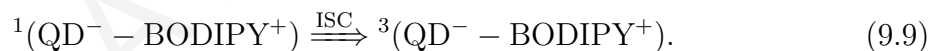


Figure 9.1: (a) Schematic representation of the TET pathways in the CdSe-BODIPY system. The BODIPY molecule is attached to the spherical surface of the CdSe NC via oxygen atoms. The QD is photo-excited at 500 nm to trigger TET to the BODIPY acceptor. According to the experimental results, TET is favored via sequential CT. (b) Schematic diagram demonstrating the possible triplet formation pathways in the QD-BODIPY complex: (i) DET pathway ($\text{QD}^*-\text{BODIPY} \rightarrow \text{QD}^--\text{}^3\text{BODIPY}^*$) [black arrow (1)], (ii) FRET $\text{QD}^*-\text{BODIPY} \rightarrow \text{QD}^--\text{}^1\text{BODIPY}^*$ followed by ET $\text{QD}^--\text{}^1\text{BODIPY}^* \rightarrow \text{QD}^--\text{BODIPY}^+$ and back ET $\text{QD}^--\text{BODIPY}^+ \rightarrow \text{QD}^--\text{}^3\text{BODIPY}^*$ [blue and yellow arrows (2)], (iii) hole transfer $\text{QD}^*-\text{BODIPY} \rightarrow \text{QD}^--\text{BODIPY}^+$ followed by ET $\text{QD}^--\text{BODIPY}^+ \rightarrow \text{QD}^--\text{}^3\text{BODIPY}^*$ [green and yellow arrows (3)].

where FRET holds for Förster resonance energy transfer (see eq. 2.60 in section 2.5.3). There is evidence that the $\text{QD}^- - \text{BODIPY}^+$ intermediate state involves an ISC transition from the singlet $^1(\text{QD}^- - \text{BODIPY}^+)$ state to the triplet $^3(\text{QD}^- - \text{BODIPY}^+)$ state, i.e.,



The mechanism of this transition is not yet resolved.²⁶⁰

The authors measured the optical spectrum of the free QD, the free BODIPY and the QD-BODIPY system. They found that the absorption peak of BODIPY is centered at 656 nm and they attributed it to the transition from the ground to the first singlet excited state of the molecule ($S_0 \rightarrow S_1$). The QD absorbs at 584 nm and this absorption is attributed to the lowest valence-to-conduction band transition ($1S_{3/2} \rightarrow 1S_e$).²⁵⁹⁻²⁶¹ At 500 nm there is negligible absorption of BODIPY. Therefore, the QD is selectively photoexcited using 500 nm laser pulse to sensitize the TET to the acceptor (see figure 1 in ref. 259).

The authors performed TAS measurements and the transient absorption spectral evolution were fitted to obtain the kinetics of each species. From the fitting they derived the rate constants for all the transitions, as shown in figure 9.1(b). Their results showed that within 1 nsec 80% of the excitons undergo fast FRET (pathway (2) in figure 9.1(b)) and HT (pathway (3) in figure 9.1(b)). Only 20% of the excitons remain in the QD. The triplet excited-state population in BODIPY begins after ~ 1 nsec. This means that the FRET and HT processes out-compete the direct DET pathway (pathway (1))

	PBE		PBE0		CAMY-B3LYP	
	Λ	$\Delta r(\text{\AA})$	Λ	$\Delta r(\text{\AA})$	Λ	$\Delta r(\text{\AA})$
S_1	0.75	1.17	0.73	1.07	0.71	1.12

Table 9.1: TD-DFT diagnostic indices Λ and Δr computed using three different methods: PBE, PBE0 and CAMY-B3LYP for the BODIPY molecule. The diagnostic tool indicates that the $S_0 \rightarrow S_1$ transition is local (for details see section 6.6).

in figure 9.1(b)). Therefore, the main pathway to the formation of TE in BODIPY, as claimed by the authors, involves the charge-separated (CS) intermediate state (see figure 9.1(b) and ref. 259 with the related supplementary material).

9.3 Theoretical computations on the molecule and the QD

Our first goal is to simulate the absorption spectrum of the BODIPY molecule and the QD, and compare with the experiment. The choice of an appropriate DFT functional to describe the optical excitations of the BODIPY molecule, requires examining the CT characteristics of the lowest-lying BODIPY excited states by computing the so-called metric of the electronic excited states (see details in section 6.6). This includes the calculation of the Λ - and Δr -indices.^{120,121} The combination of these two quantities characterizes the type of the excitation transition (local or CT) and their values are associated with the choice of an appropriate functional. To compute the metric of the excited states for the BODIPY molecule, we use the Amsterdam Density Functional (ADF) program package⁹⁴ and we compute the Λ - and Δr -indices for each of the lowest-lying excited states. This is done at three different DFT levels of theory: the generalized gradient approximation (GGA) method with the PBE functional, the global hybrid (GH) method with the PBE0 functional, and the range-separated (RS) method with the CAMY-B3LYP functional). We use the TZ2P basis set, and the ground-state geometries are initially optimized at the same level of theory as the computations of the excited-state indices. The diagnostics Λ and Δr show that the first singlet excited state (which leads to the absorption peak of interest) describes a local HOMO-LUMO transition. Conventional DFT methods such as GGA and pure GH (~ 20 - 25% Hartree-Fock (HF) exchange) are adequate for its description (see table 9.1).^{121,156}

For the computation of the absorption spectrum of the BODIPY molecule we choose the B3LYP functional combined with TZ2P basis set, and Grimme’s D3 dispersion corrections using Becke-Johnson damping are included. Solvents effects are also included via the COSMO (“Conductor-like Screening Model”) using the dielectric constant ($\epsilon = 2.38$) for toluene. The computed absorption band is centered at 644nm (1.93 eV). This is in good agreement with the experimental absorption band which is centered at 656nm (1.89 eV) with ~ 10 nm deviation from the experimental absorptive

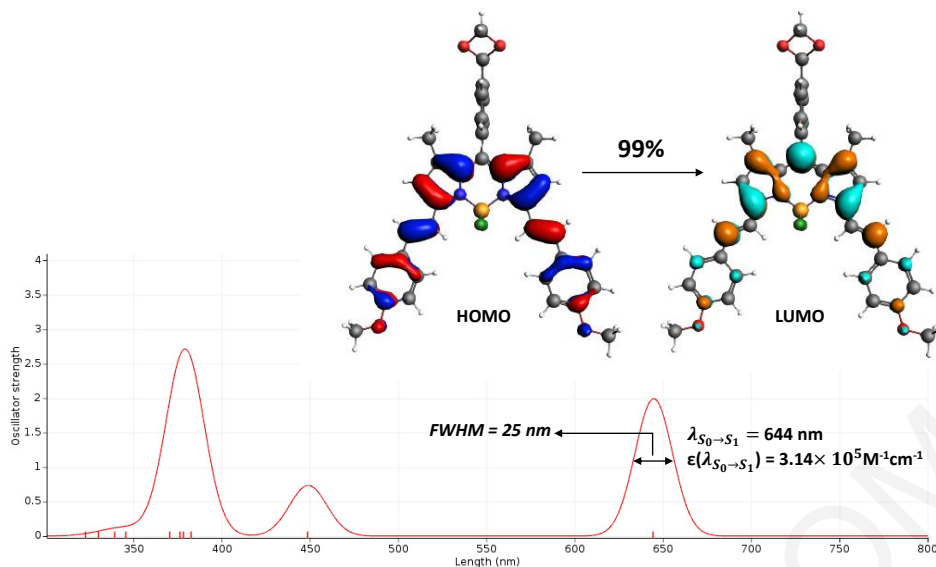


Figure 9.2: Calculated absorption spectrum of the BODIPY molecule computed at the B3LYP/TZ2P level of theory using $\text{FWHM} = 25 \text{ nm}$. The first absorption peak is centered at 644 nm and it is attributed to the transition $S_0 \rightarrow S_1$. This transition is of HOMO→LUMO character.

peak [see figure 9.2]. The computed absorption peak is broadened at $\text{FWHM} = 25 \text{ nm}$ (same as the experimental). Using the calculated oscillator strength, in combination with the FWHM and the excitation energy, we estimated the extinction coefficient via eq. 6.37. The computed extinction coefficient ($3.14 \times 10^5 \text{ M}^{-5}\text{cm}^{-1}$) is in good agreement with the experimental one ($9.18 \times 10^4 \text{ M}^{-5}\text{cm}^{-1}$).

The experimental absorption spectrum of CdSe QD shows that the first absorption band is centered at 584nm (2.12eV). From this excitonic absorption peak wavelength λ_{wav} , we can estimate the size of the QD of the experiment, using the equation²⁶²

$$d(\text{nm}) = (1.6122 \times 10^{-9})\lambda_{\text{wav}}^4 - (2.6575 \times 10^{-6})\lambda_{\text{wav}}^3 + (1.6242 \times 10^{-3})\lambda_{\text{wav}}^2 - (4.2770 \times 10^{-1})\lambda_{\text{wav}} + 41.57. \quad (9.10)$$

d is the diameter of the spherical QD and λ_{wav} is the wavelength. For $\lambda_{\text{wav}} = 584 \text{ nm}$, we deduce that the diameter of the QD used in the experiment of ref. 259 is $\sim 4 \text{ nm}$.

As a reference QD structure for our computations, we use those studied by M. V. Kovalenko and his co-workers in their recent paper.²⁶³ This CdSe NP is spherical with diameter 2.5 nm. The surface ligands are replaced by Chlorine atoms which are electronically similar to oleate capping groups (see figure 9.3(a)). We do not use a larger QD (e.g., $\sim 4 \text{ nm}$ diameter as in the experiment of ref. 259) in order to reduce computational cost. First, we perform a ground-state computation at the PBE/TZP level of theory with ADF, to estimate the HOMO and LUMO orbital densities. These results show that the LUMO orbital is delocalized over the entire spherical QD (see

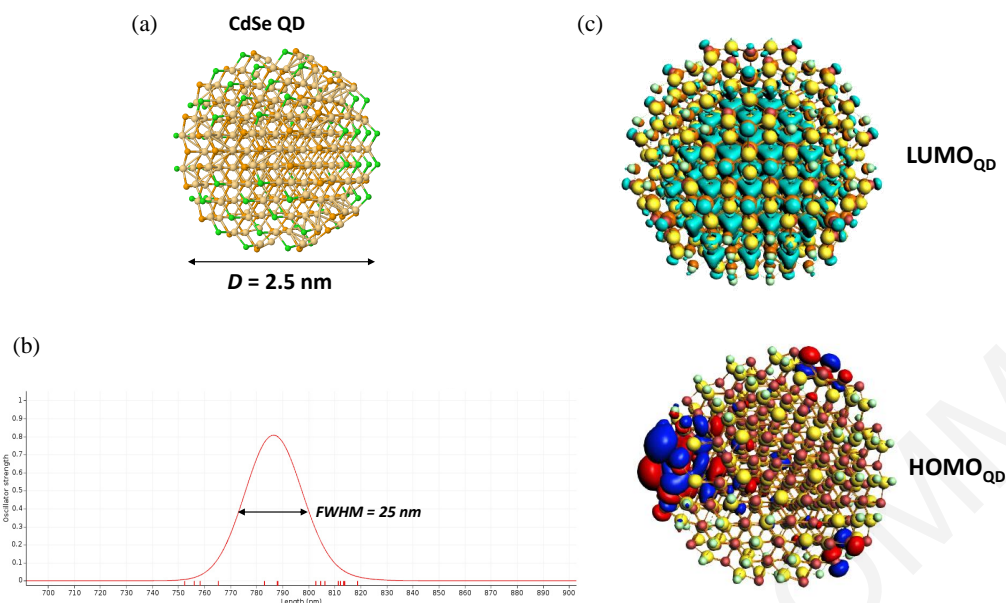


Figure 9.3: (a) Molecular structure of the CdSe NP of 2.5 nm diameter (see ref. 263). (b) Absorption spectrum of CdSe QD computed at sTDA/TZP level of theory. (c) Frontier molecular orbitals of the CdSe QD.

figure 9.3). The absorption peak of CdSe QD corresponds to the $1S_{3/2} \rightarrow S_e$ excitation. The $1S_e$ energy level implies that the electron density has a spherical symmetry, in accordance with our computations (see figure 9.3(c)).

The ionization potential (IP) of CdSe QDs passivated with oleic acid ligands (2.0 - 4.5 nm diameter size), is 6.2 - 6.6 eV.^{264–267} Our computed IP energy is ~ 6 eV which is slightly lower than the experimental observations of refs. 264–267. We also perform excited state calculations using the simplified Tamm-Dancoff approximation (sTDA) as implemented in the ADF program package. The computation uses the PBE functional in combination with the TZP basis set. The computed absorption band is centered at 783 nm (1.58 eV) which is ~ 200 nm red-shifted compared to the experimental absorption peak which is centered at 584 nm (2.12 eV) [see figure 9.3(b)]. According to eq. 9.10, for a spherical QD of 2.5 nm diameter, the expected center of the absorption peak is at 515 nm. The computed absorption peak using sTDA largely deviates from the expected value.

9.4 Conclusions and future work

Our future plans for this project are: (a) to improve our computations of the optical properties and excited states of the NP, e.g., by using TD-DFT instead of approximate methods, (b) to explore the triplet exciton structure of QD-BODIPY complex, (c) to explore using kinetic models the dynamics of ET/HT and TET processes as shown in figure 9.1 and (d) to explain whether the favored mechanism for TET in the QD-molecule interface is sequential TET via a CT intermediate state, or the direct DET.

CHAPTER 10

Conclusions

In the present thesis we explored the mechanisms of triplet energy transfer (TET) and charge transfer (CT) in molecules. We explained an experimental observation about direct optical excitation of an organic molecule from its singlet ground state to its triplet excited states. The time-resolved electron paramagnetic resonance (TR-EPR) experiments that were performed on this molecule, showed that the TR-EPR signals had intensities of similar magnitude when the molecule was optically excited in its highly absorbing region and in its non-absorbing region. To explain these observations we proposed two different pathways to the formation of triplet excited states in this molecule. The first one via direct optical excitation from the singlet ground state ($S_0 \rightarrow T_m$), and the second one via indirect optical excitation, namely through intersystem crossing (ISC) from the photoexcited singlet state ($S_0 \rightarrow S_n \xrightarrow{\text{ISC}} T_m$). We first performed relativistic *ab-initio* quantum chemical computations to calculate the absorption coefficient (absorbance) for direct optical excitation $S_0 \rightarrow T_m$. Using the computed absorption coefficient we estimated the population transfer from the ground state to the triplet excited states. To model the indirect optical excitation pathway ($S_0 \rightarrow S_n \xrightarrow{\text{ISC}} T_m$) we wrote a code in MATLAB to compute the ISC rates using as input the normal mode frequencies and the reorganization energies for the relevant singlet and triplet excited states, computed at the *ab-initio* level. The computed ISC rates were used to estimate the population transfer to the triplet excited states via indirect optical excitation. We found that upon photoexcitation within and below the optical absorption band, a measurable number of molecules (given the TR-EPR sensitivity) is created directly from the singlet ground state to the triplet excited states, even though the spin-orbit coupling interaction is weak. After optical excitation, these initial triplet populations do not substantially change, since the computed ISC rates are very slow. Thus, the initial triplet populations created for the two optical excitation regions are similar. This conclusion explains why the TR-EPR signal intensities obtained for the two excitation regions were of similar magnitude. This work was published in the Jour-

nal of Chemical Physics [Mavrommati, S. A.; Skourtis, S. S. *J. chem. Phys.* **2020**, *152*, 044304.]

In another project described in this thesis, we proposed design rules for building molecular wires that can be used as bridges linking triplet-exciton donors and acceptors, and that support fast and efficient coherent TET over long distances even at room temperature. Based on the design principles, the bridges should be homopolymeric, in π -stacked geometry, rigid without structural disorder and with low inner-sphere reorganization energy for triplet-exciton formation within each monomer. We suggested several polymer structures as TET wires, and for these structures we modeled TET. We computed the monomer-to-monomer TET coupling by *ab-initio* and molecular-dynamic simulations, and modeled the TET times using a tight-binding model and the Liouville equation for the density matrix, in order to include relaxation effects. We found that the monomer-to-monomer TET coupling for the proposed structures is large (i.e., ~ 0.1 eV) and that the triplet excitons are fully delocalized on the whole bridge, even at room temperature. The predicted time for TET from the first monomer to the last monomer can be as fast as 2 psec for bridge lengths as long as 50 chromophore units. This work was published in the Journal of Physical Chemistry letters (Mavrommati, S. A.; Skourtis, S. S. *J. Phys. Chem. Lett.*, **2022**, *13*, 9679-9687.)

In the thesis, we also described computations of CT transition rates in organic molecules using quantum mechanical approaches for describing the vibrational modes of the molecules, and comparing them to classical approximations. As an example, we computed the hole-transfer rate between two guanine molecules using *ab-initio* computations and our MATLAB code. The rate computed quantum mechanically at room temperature, was found to be approximately two orders of magnitude greater than the rate computed using the classical Marcus formula. Moreover, the rate computed quantum mechanically was largely temperature independent, but the rate computed using the classical approximation showed strong temperature dependence. Our results suggest that the classical Marcus formula might be highly inaccurate in describing CT rates in small organic molecules in dry environments (e.g., molecular junctions). This is because the majority of normal modes are high frequency and they remain quantum at room temperature. In many interpretations of molecular junction experiments, Marcus theory is assumed, and this may be incorrect.

Finally, the thesis also includes modeling of TET between nanoparticles (NPs) and an organic molecules. This work was motivated by experiments on CdSe NP linked to the BODIPY organic molecule.

BIBLIOGRAPHY

- (1) Vura-Weis, J.; Abdelwahed, S. H.; Shukla, R.; Rathore, R.; Ratner, M. A.; Wasielewski, M. R. Crossover from single-step tunneling to multistep hopping for molecular triplet energy transfer. *Science* **2010**, *328*, 1547–1550.
- (2) Hartnett, P. E.; Mauck, C. M.; Harris, M. A.; Young, R. M.; Wu, Y.-L.; Marks, T. J.; Wasielewski, M. R. Influence of anion delocalization on electron transfer in a covalent porphyrin donor–perylene diimide dimer acceptor system. *Journal of the American Chemical Society* **2017**, *139*, 749–756.
- (3) Kaufmann, C.; Bialas, D.; Stolte, M.; Würthner, F. Discrete π -stacks of perylene bisimide dyes within folda-dimers: insight into long- and short-range exciton coupling. *Journal of the American Chemical Society* **2018**, *140*, 9986–9995.
- (4) Lindquist, R. J.; Lefler, K. M.; Brown, K. E.; Dyar, S. M.; Margulies, E. A.; Young, R. M.; Wasielewski, M. R. Energy flow dynamics within cofacial and slip-stacked perylene-3, 4-dicarboximide dimer models of π -aggregates. *Journal of the American Chemical Society* **2014**, *136*, 14912–14923.
- (5) Margulies, E. A.; Miller, C. E.; Wu, Y.; Ma, L.; Schatz, G. C.; Young, R. M.; Wasielewski, M. R. Enabling singlet fission by controlling intramolecular charge transfer in π -stacked covalent perylene diimide dimers. *Nature Chemistry* **2016**, *8*, 1120–1125.
- (6) Macedo, A. G.; Christopholi, L. P.; Gavim, A. E.; de Deus, J. F.; Teridi, M. A. M.; Yusoff, A.; bin Mohd, R.; da Silva, W. J. Perylene derivatives for solar cells and energy harvesting: a review of materials, challenges and advances. *Journal of Materials Science: Materials in Electronics* **2019**, *30*, 15803–15824.
- (7) Meyer, D. L.; Lombeck, F.; Huettner, S.; Sommer, M.; Biskup, T. Direct $S_0 \rightarrow T$ excitation of a conjugated polymer repeat unit: unusual spin-forbidden transitions probed by time-resolved electron paramagnetic resonance spectroscopy. *The Journal of Physical Chemistry Letters* **2017**, *8*, 1677–1682.

- (8) Franco Jr, F. Computational study on the structural and optoelectronic properties of a carbazole-benzothiadiazole based conjugated oligomer with various alkyl side-chain lengths. *Molecular Simulation* **2017**, *43*, 222–227.
- (9) Nitzan, A. *Chemical Dynamics in Condensed Phases: Relaxation, Transfer and Reactions in Condensed Molecular Systems*; Oxford University Press, 2006.
- (10) May, V.; Kühn, O. *Charge and Energy Transfer Dynamics in Molecular Systems*; John Wiley & Sons, 2011.
- (11) Siebbeles, L. D.; Grozema, F. C. *Charge and Exciton Transport Through Molecular Wires*; John Wiley & Sons, 2011.
- (12) Klessinger, M.; Michl, J. *Excited States and Photochemistry of Organic Molecules*; VCH publishers, 1995.
- (13) Van Amerongen, H.; Van Grondelle, R., et al. *Photosynthetic Excitons*; World Scientific, 2000.
- (14) Valkunas, L.; Abramavicius, D.; Mancal, T. *Molecular Excitation Dynamics and Relaxation: Quantum Theory and Spectroscopy*; John Wiley & Sons, 2013.
- (15) Roundhill, D. M. *Photochemistry and Photophysics of Metal Complexes*; Springer Science & Business Media, 2013.
- (16) Skourtis, S. S.; Beratan, D. N.; Eds, Biological pathways for electrons, photons and photo-excitations. *Current Opinion in Chemical Biology* **2018**, *47*, A1–A3.
- (17) Vo-Dinh, T., et al. *Handbook of Spectroscopy*; John Wiley & Sons, 2006.
- (18) Forbes, M. D.; Jarocha, L. E.; Sim, S.; Tarasov, V. F. Time-resolved electron paramagnetic resonance spectroscopy: history, technique, and application to supramolecular and macromolecular chemistry. *Advances in Physical Organic Chemistry* **2013**, *47*, 1–83.
- (19) McGlynn, S. P.; Azumi, T.; Kinoshita, M., et al. *Molecular Spectroscopy of the Triplet State*; Prentice-Hall, 1969.
- (20) Turro, N. J.; Ramamurthy, V.; Scaiano, J. C., et al. *Modern Molecular Photochemistry of Organic Molecules*; University Science Books Sausalito, CA, 2010; Vol. 188.
- (21) Scholes, G. D. Long-range resonance energy transfer in molecular systems. *Annual Review of Physical Chemistry* **2003**, *54*, 57–87.
- (22) Fassioli, F.; Dinshaw, R.; Arpin, P. C.; Scholes, G. D. Photosynthetic light harvesting: excitons and coherence. *Journal of the Royal Society Interface* **2014**, *11*, 20130901.

- (23) Casanova, D. Theoretical modeling of singlet fission. *Chemical Reviews* **2018**, *118*, 7164–7207.
- (24) Li, X.; Huang, Z.; Zavala, R.; Tang, M. L. Distance-dependent triplet energy transfer between CdSe nanocrystals and surface bound anthracene. *The Journal of Physical Chemistry Letters* **2016**, *7*, 1955–1959.
- (25) Huang, Z.; Xu, Z.; Huang, T.; Gray, V.; Moth-Poulsen, K.; Lian, T.; Tang, M. L. Evolution from tunneling to hopping mediated triplet energy transfer from quantum dots to molecules. *Journal of the American Chemical Society* **2020**, *142*, 17581–17588.
- (26) Lai, R.; Liu, Y.; Luo, X.; Chen, L.; Han, Y.; Lv, M.; Liang, G.; Chen, J.; Zhang, C.; Di, D., et al. Shallow distance-dependent triplet energy migration mediated by endothermic charge-transfer. *Nature Communications* **2021**, *12*, 1–9.
- (27) Scholes, G. D. Limits of exciton delocalization in molecular aggregates. *Faraday Discussions* **2020**, *221*, 265–280.
- (28) Giannini, S.; Peng, W.-T.; Cupellini, L.; Padula, D.; Carof, A.; Blumberger, J. Exciton transport in molecular organic semiconductors boosted by transient quantum delocalization. *Nature Communications* **2022**, *13*, 1–13.
- (29) Dirac, P. A. M. The quantum theory of the emission and absorption of radiation. *Proceedings of the Royal Society of London. Series A, Containing Papers of a Mathematical and Physical Character* **1927**, *114*, 243–265.
- (30) Fermi, E. *Nuclear Physics*; University of Chicago Press, 1950.
- (31) DeVault, D. *Quantum-mechanical Tunnelling in Biological Systems*; Cambridge University Press, 1984.
- (32) Atkins, P. W.; Friedman, R. S. *Molecular Quantum Mechanics*; Oxford university press, 2011.
- (33) Petrenko, T.; Neese, F. Analysis and prediction of absorption band shapes, fluorescence band shapes, resonance Raman intensities, and excitation profiles using the time-dependent theory of electronic spectroscopy. *The Journal of Chemical Physics* **2007**, *127*, 164319.
- (34) Petrenko, T.; Krylova, O.; Neese, F.; Sokolowski, M. Optical absorption and emission properties of rubrene: insight from a combined experimental and theoretical study. *New Journal of Physics* **2009**, *11*, 015001.
- (35) Petrenko, T.; Neese, F. Efficient and automatic calculation of optical band shapes and resonance Raman spectra for larger molecules within the independent mode

- displaced harmonic oscillator model. *The Journal of Chemical Physics* **2012**, *137*, 234107.
- (36) Chan, C.-K.; Page, J. Temperature effects in the time-correlator theory of resonance Raman scattering. *The Journal of Chemical Physics* **1983**, *79*, 5234–5250.
- (37) Marcus, R. A.; Sutin, N. Electron transfer in chemistry and biology. *Biochimica et Biophysica Acta-Reviews on Bioenergetics* **1985**, *811*, 265–322.
- (38) Kuznetsov, A. M.; Ulstrup, J. *Electron Transfer in Chemistry and Biology: An Introduction to the Theory*; John Wiley & Sons, 1999.
- (39) Jortner, J.; Bixon, M.; Prigogine, I.; Rice, S. A. *Electron Transfer: From Isolated Molecules to Biomolecules*; John Wiley & Sons, 1999.
- (40) Balzani, V.; Piotrowiak, P.; Rodgers, M.; Mattay, J.; Astruc, D., et al. *Electron Transfer in Chemistry*; Wiley-VCH Weinheim, 2001; Vol. 1.
- (41) Mohseni, M.; Omar, Y.; Engel, G. S.; Plenio, M. B. *Quantum Effects in Biology*; Cambridge University Press, 2014.
- (42) Blumberger, J. Recent advances in the theory and molecular simulation of biological electron transfer reactions. *Chemical Reviews* **2015**, *115*, 11191–11238.
- (43) Mukamel, S. *Principles of Nonlinear Optical Spectroscopy*; Oxford University Press, 1995.
- (44) Fox, M. *Optical Properties of Solids*; Oxford University Press, 2010.
- (45) Schatz, G. C.; Ratner, M. A. *Quantum Mechanics in Chemistry*; Courier Corporation, 2002.
- (46) Rulliere, C., et al. *Femtosecond Laser Pulses*; Springer, 2005.
- (47) Parson, W. W. *Modern Optical Spectroscopy: with Exercises and Examples from Biophysics and Biochemistry*; Springer, 2007; Vol. 2.
- (48) Griffiths, D. J.; Schroeter, D. F. *Introduction to Quantum Mechanics*; Cambridge university press, 2018.
- (49) Szabo, A.; Ostlund, N. S. *Modern Quantum Chemistry: Introduction to Advanced Electronic Structure Theory*; Courier Corporation, 2012; Chapter 2.
- (50) Antoniou, P. F. *Controlling Electron and Exciton Transfer Paths in Molecular Systems*; University of Cyprus, 2017.
- (51) McGlynn, S. P. *Introduction to Applied Quantum Chemistry*; Holt Rinehart & Winston, 1971.

- (52) Dyllal, K. G.; Fægri Jr, K. *Introduction to Relativistic Quantum Chemistry*; Oxford University Press, 2007.
- (53) Marian, C. M. Spin-orbit coupling and intersystem crossing in molecules. *Wiley Interdisciplinary Reviews: Computational Molecular Science* **2012**, *2*, 187–203.
- (54) Miraglia Franco de Carvalho, F. *Nonadiabatic Dynamics with Spin-orbit Couplings*; EPFL, 2017.
- (55) McClure, D. S. Spin-orbit interaction in aromatic molecules. *The Journal of Chemical Physics* **1952**, *20*, 682–686.
- (56) Lawetz, V.; Orlandi, G.; Siebrand, W. Theory of intersystem crossing in aromatic hydrocarbons. *The Journal of Chemical Physics* **1972**, *56*, 4058–4072.
- (57) Penfold, T. J.; Gindensperger, E.; Daniel, C.; Marian, C. M. Spin-vibronic mechanism for intersystem crossing. *Chemical Reviews* **2018**, *118*, 6975–7025.
- (58) Sidman, J. W. Spin-orbit coupling in the ${}^3A_2 - {}^1A_1$ transition of formaldehyde. *The Journal of Chemical Physics* **1958**, *29*, 644–652.
- (59) Clementi, E.; Kasha, M. Spin-orbital interaction in N-heterocyclic molecules general results in a cylindrical potential approximation. *Journal of Molecular Spectroscopy* **1958**, *2*, 297–307.
- (60) El-Sayed, M. Spin-orbit coupling and the radiationless processes in nitrogen heterocyclics. *The Journal of Chemical Physics* **1963**, *38*, 2834–2838.
- (61) Masmanidis, C.; Jaffe, H.; Ellis, R. Spin-orbit coupling in organic molecules. *The Journal of Physical Chemistry* **1975**, *79*, 2052–2061.
- (62) Mizushima, M.; Koide, S. On the lifetime of the lower triplet states of benzene. *The Journal of Chemical Physics* **1952**, *20*, 765–769.
- (63) Cohen-Tannoudji, C.; Dupont-Roc, J.; Grynberg, G. *Atom-Photon Interactions: Basic Processes and Applications*; Wiley-VCH Weinheim, 1998.
- (64) Schlosshauer, M. A. *Decoherence and the Quantum-to-Classical Transition*; Springer Science & Business Media, 2007.
- (65) Boyd, R. W. *Nonlinear Optics*; Academic press, 2020.
- (66) Atherton, N. M. *Principles of Electron Spin Resonance*; Ellis Horwood and Prentice Hall, 1993.
- (67) Schweiger, A.; Jeschke, G. *Principles of Pulse Electron Paramagnetic Resonance*; Oxford University Press on Demand, 2001.
- (68) Weil, J. A.; Bolton, J. R. *Electron Paramagnetic Resonance: Elementary Theory and Practical Applications*; John Wiley & Sons, 2007.

- (69) Rieger, P. H. *Electron Spin Resonance: Analysis and Interpretation*; Royal Society of Chemistry, 2007.
- (70) Abragam, A.; Bleaney, B. *Electron Paramagnetic Resonance of Transition Ions*; Oxford University Press, 2012.
- (71) Goldfarb, D.; Stoll, S. *EPR Spectroscopy: Fundamentals and Methods*; John Wiley & Sons, 2018.
- (72) Cohen-Tannoudji, C.; Diu, B.; Laloe, F. *Quantum Mechanics*; 1986; Vol. 1.
- (73) Abragam, A. *The Principles of Nuclear Magnetism*; Oxford university press, 1961.
- (74) Blum, K. *Density Matrix Theory and Applications*; Springer Science & Business Media, 2012; Vol. 64.
- (75) Slichter, C. P. *Principles of Magnetic Resonance*; Springer Science & Business Media, 2013; Vol. 1.
- (76) Cantor, C. R.; Schimmel, P. R. *Biophysical Chemistry: Part II: Techniques for the Study of Biological Structure and Function*; Macmillan, 1980.
- (77) Feher, G. Sensitivity considerations in microwave paramagnetic resonance absorption techniques. *Bell System Technical Journal* **1957**, *36*, 449–484.
- (78) Wilmshurst, T. H.; Wilmshurst, T. *Electron Spin Resonance Spectrometers*; Springer, 1967.
- (79) Misra, S. K. *Multifrequency Electron Paramagnetic Resonance: Theory and Applications*; John Wiley & Sons, 2011.
- (80) Brustolon, M.; Giamello, E. *Electron Paramagnetic Resonance: A Practitioners Toolkit*; John Wiley & Sons, 2009.
- (81) Gilbert, B. C.; Davies, M.; Murphy, D. M. *Electron Paramagnetic Resonance*; Royal Society of Chemistry, 2008; Vol. 18.
- (82) Miura, T.; Carmieli, R.; Wasielewski, M. R. Time-resolved EPR studies of charge recombination and triplet-state formation within donor- bridge- acceptor molecules having wire-like oligofluorene bridges. *The Journal of Physical Chemistry A* **2010**, *114*, 5769–5778.
- (83) Weber, S.; Timmel, C.; van der Est, A. *Molecular Physics* **2019**, *117*, 2539–2539.
- (84) Biskup, T. Structure-function relationship of organic semiconductors: detailed insights from time-resolved EPR spectroscopy. *Frontiers in Chemistry* **2019**, *7*, 10.
- (85) Kerpál, C.; Richert, S.; Storey, J. G.; Pillai, S.; Liddell, P. A.; Gust, D.; Macken-

- zie, S. R.; Hore, P.; Timmel, C. R. Chemical compass behaviour at microtesla magnetic fields strengthens the radical pair hypothesis of avian magnetoreception. *Nature Communications* **2019**, *10*, 1–7.
- (86) Biskup, T.; Sommer, M.; Rein, S.; Meyer, D. L.; Kohlstädt, M.; Würfel, U.; Weber, S. Ordering of PCDTBT revealed by time-resolved electron paramagnetic resonance spectroscopy of its triplet excitons. *Angewandte Chemie International Edition* **2015**, *54*, 7707–7710.
- (87) Lin, J.; Hu, X.; Zhang, P.; Van Rynbach, A.; Beratan, D. N.; Kent, C. A.; Mehl, B. P.; Papanikolas, J. M.; Meyer, T. J.; Lin, W.; Skourtis, S. S.; Constantinou, M. Triplet excitation energy dynamics in metal–organic frameworks. *The Journal of Physical Chemistry C* **2013**, *117*, 22250–22259.
- (88) Basel, B. S.; Zirzmeier, J.; Hetzer, C.; Reddy, S. R.; Phelan, B. T.; Krzyaniak, M. D.; Volland, M. K.; Coto, P. B.; Young, R. M.; Clark, T.; Thoss, M.; Tykwinski, R. R.; Wasielewski, D. M., Michael Rand Guildi Evidence for charge-transfer mediation in the primary events of singlet fission in a weakly coupled pentacene dimer. *Chem* **2018**, *4*, 1092–1111.
- (89) Baková, R.; Chergui, M.; Daniel, C.; Vlček Jr, A.; Zális, S. Relativistic effects in spectroscopy and photophysics of heavy-metal complexes illustrated by spin–orbit calculations of $[\text{Re}(\text{imidazole})(\text{CO})_3(\text{phen})]^+$. *Coordination Chemistry Reviews* **2011**, *255*, 975–989.
- (90) Blouin, N.; Michaud, A.; Gendron, D.; Wakim, S.; Blair, E.; Neagu-Plesu, R.; Belletete, M.; Durocher, G.; Tao, Y.; Leclerc, M. Toward a rational design of poly (2, 7-carbazole) derivatives for solar cells. *Journal of the American Chemical Society* **2008**, *130*, 732–742.
- (91) Cho, S.; Seo, J. H.; Park, S. H.; Beaupré, S.; Leclerc, M.; Heeger, A. J. A thermally stable semiconducting polymer. *Advanced Materials* **2010**, *22*, 1253–1257.
- (92) Yersin, H.; Rausch, A. F.; Czerwieniec, R.; Hofbeck, T.; Fischer, T. The triplet state of organo-transition metal compounds. Triplet harvesting and singlet harvesting for efficient OLEDs. *Coordination Chemistry Reviews* **2011**, *255*, 2622–2652.
- (93) Matsuoka, H.; Retegan, M.; Schmitt, L.; Höger, S.; Neese, F.; Schiemann, O. Time-resolved electron paramagnetic resonance and theoretical investigations of metal-free room-temperature triplet emitters. *Journal of the American Chemical Society* **2017**, *139*, 12968–12975.
- (94) Te Velde, G. t.; Bickelhaupt, F. M.; Baerends, E. J.; Fonseca Guerra, C.; van

- Gisbergen, S. J.; Snijders, J. G.; Ziegler, T. Chemistry with ADF. *Journal of Computational Chemistry* **2001**, *22*, 931–967.
- (95) Versluis, L.; Ziegler, T. The determination of molecular structures by density functional theory. The evaluation of analytical energy gradients by numerical integration. *The Journal of Chemical Physics* **1988**, *88*, 322–328.
- (96) Seth, M.; Mazur, G.; Ziegler, T. Time-dependent density functional theory gradients in the Amsterdam density functional package: geometry optimizations of spin-flip excitations. *Theoretical Chemistry Accounts* **2011**, *129*, 331–342.
- (97) Van Gisbergen, S.; Snijders, J.; Baerends, E. Implementation of time-dependent density functional response equations. *Computer Physics Communications* **1999**, *118*, 119–138.
- (98) Rosa, A.; Baerends, E. J.; van Gisbergen, S. J.; van Lenthe, E.; Groeneveld, J. A.; Snijders, J. G. Electronic spectra of $M(\text{CO})_6$ ($M = \text{Cr}, \text{Mo}, \text{W}$) revisited by a relativistic TDDFT approach. *Journal of the American Chemical Society* **1999**, *121*, 10356–10365.
- (99) Wang, F.; Ziegler, T.; van Lenthe, E.; van Gisbergen, S.; Baerends, E. J. The calculation of excitation energies based on the relativistic two-component zeroth-order regular approximation and time-dependent density-functional with full use of symmetry. *The Journal of Chemical Physics* **2005**, *122*, 204103.
- (100) Samanta, P. K.; Kim, D.; Coropceanu, V.; Brédas, J.-L. Up-conversion intersystem crossing rates in organic emitters for thermally activated delayed fluorescence: impact of the nature of singlet vs triplet excited states. *Journal of the American Chemical Society* **2017**, *139*, 4042–4051.
- (101) Sando, G. M.; Spears, K. G. Ab-initio computation of the Duschinsky mixing of vibrations and nonlinear effects. *The Journal of Physical Chemistry A* **2001**, *105*, 5326–5333.
- (102) Stephens, P. J.; Devlin, F. J.; Chabalowski, C. F.; Frisch, M. J. Ab-initio calculation of vibrational absorption and circular dichroism spectra using density functional force fields. *The Journal of Physical Chemistry* **1994**, *98*, 11623–11627.
- (103) Van Lenthe, E.; Baerends, E. J. Optimized Slater-type basis sets for the elements 1–118. *Journal of Computational Chemistry* **2003**, *24*, 1142–1156.
- (104) Becke, A. D. Density-functional thermochemistry. III. The role of exact exchange. *The Journal of Chemical Physics* **1993**, *98*, 5648–5652.
- (105) Hirata, S.; Head-Gordon, M. Time-dependent density functional theory within

- the Tamm–Dancoff approximation. *Chemical Physics Letters* **1999**, *314*, 291–299.
- (106) Lenthe, E. v.; Baerends, E.-J.; Snijders, J. G. Relativistic regular two-component Hamiltonians. *The Journal of Chemical Physics* **1993**, *99*, 4597–4610.
- (107) van Lenthe, E.; Baerends, E.-J.; Snijders, J. G. Relativistic total energy using regular approximations. *The Journal of Chemical Physics* **1994**, *101*, 9783–9792.
- (108) Van Lenthe, E.; Ehlers, A.; Baerends, E.-J. Geometry optimizations in the zero order regular approximation for relativistic effects. *The Journal of Chemical Physics* **1999**, *110*, 8943–8953.
- (109) Wang, F.; Ziegler, T. A simplified relativistic time-dependent density-functional theory formalism for the calculations of excitation energies including spin-orbit coupling effect. *The Journal of Chemical Physics* **2005**, *123*, 154102.
- (110) Zhao, Y.; Truhlar, D. G. The M06 suite of density functionals for main group thermochemistry, thermochemical kinetics, noncovalent interactions, excited states, and transition elements: two new functionals and systematic testing of four M06-class functionals and 12 other functionals. *Theoretical Chemistry Accounts* **2008**, *120*, 215–241.
- (111) Zhao, Y.; Truhlar, D. G. A new local density functional for main-group thermochemistry, transition metal bonding, thermochemical kinetics, and noncovalent interactions. *The Journal of Chemical Physics* **2006**, *125*, 194101.
- (112) Seth, M.; Ziegler, T. Range-separated exchange functionals with Slater-type functions. *Journal of Chemical Theory and Computation* **2012**, *8*, 901–907.
- (113) Iikura, H.; Tsuneda, T.; Hirao, K. A long-range correction scheme for generalized-gradient-approximation exchange functionals. *The Journal of Chemical Physics* **2001**, *115*, 3540–3544.
- (114) Becke, A. D. Density-functional exchange-energy approximation with correct asymptotic behavior. *Physical Review A* **1988**, *38*, 3098.
- (115) Chai, J.-D.; Head-Gordon, M. Systematic optimization of long-range corrected hybrid density functionals. *The Journal of Chemical Physics* **2008**, *128*, 084106.
- (116) Chai, J.-D.; Head-Gordon, M. Long-range corrected hybrid density functionals with damped atom–atom dispersion corrections. *Physical Chemistry Chemical Physics* **2008**, *10*, 6615–6620.
- (117) Chai, J.-D.; Head-Gordon, M. Optimal operators for Hartree–Fock exchange from long-range corrected hybrid density functionals. *Chemical Physics Letters* **2008**, *467*, 176–178.

- (118) Chai, J.-D.; Head-Gordon, M. Long-range corrected double-hybrid density functionals. *The Journal of Chemical Physics* **2009**, *131*, 174105.
- (119) Yanai, T.; Tew, D. P.; Handy, N. C. A new hybrid exchange–correlation functional using the Coulomb-attenuating method (CAM-B3LYP). *Chemical Physics Letters* **2004**, *393*, 51–57.
- (120) Peach, M. J.; Benfield, P.; Helgaker, T.; Tozer, D. J. Excitation energies in density functional theory: an evaluation and a diagnostic test. *The Journal of Chemical Physics* **2008**, *128*, 044118.
- (121) Guido, C. A.; Cortona, P.; Mennucci, B.; Adamo, C. On the metric of charge transfer molecular excitations: a simple chemical descriptor. *Journal of Chemical Theory and Computation* **2013**, *9*, 3118–3126.
- (122) Neese, F. The ORCA program system. *Wiley Interdisciplinary Reviews: Computational Molecular Science* **2012**, *2*, 73–78.
- (123) Schäfer, A.; Huber, C.; Ahlrichs, R. Fully optimized contracted Gaussian basis sets of triple zeta valence quality for atoms Li to Kr. *The Journal of Chemical Physics* **1994**, *100*, 5829–5835.
- (124) Dreuw, A.; Head-Gordon, M. Single-reference ab-initio methods for the calculation of excited states of large molecules. *Chemical Reviews* **2005**, *105*, 4009–4037.
- (125) Bérces, A.; Dickson, R. M.; Fan, L.; Jacobsen, H.; Swerhone, D.; Ziegler, T. An implementation of the coupled perturbed Kohn-Sham equations: perturbation due to nuclear displacements. *Computer Physics Communications* **1997**, *100*, 247–262.
- (126) Wolff, S. K. Analytical second derivatives in the Amsterdam density functional package. *International Journal of Quantum Chemistry* **2005**, *104*, 645–659.
- (127) Seldenthuis, J. S.; Van Der Zant, H. S.; Ratner, M. A.; Thijssen, J. M. Vibrational excitations in weakly coupled single-molecule junctions: a computational analysis. *ACS Nano* **2008**, *2*, 1445–1451.
- (128) Ruhoff, P. T.; Ratner, M. A. Algorithms for computing Franck–Condon overlap integrals. *International Journal of Quantum Chemistry* **2000**, *77*, 383–392.
- (129) Becke, A. D. A new mixing of Hartree–Fock and local density-functional theories. *The Journal of Chemical Physics* **1993**, *98*, 1372–1377.
- (130) Sinnecker, S.; Neese, F. Spin-spin contributions to the zero-field splitting tensor in organic triplets, carbenes and biradicals - a density functional and *ab-initio* study. *The Journal of Physical Chemistry A* **2006**, *110*, 12267–12275.
- (131) Riplinger, C.; Kao, J. P.; Rosen, G. M.; Kathirvelu, V.; Eaton, G. R.;

- Eaton, S. S.; Kutateladze, A.; Neese, F. Interaction of radical pairs through-bond and through-space: scope and limitations of the point-dipole approximation in electron paramagnetic resonance spectroscopy. *Journal of the American Chemical Society* **2009**, *131*, 10092–10106.
- (132) Bhatta, R. S.; Tsige, M. Understanding structural and electronic properties of dithienyl benzothiadiazole and its complex with C70. *Polymer* **2015**, *75*, 73–77.
- (133) Matt, C.; Meyer, D. L.; Lombeck, F.; Sommer, M.; Biskup, T. TBT entirely dominates the electronic structure of the conjugated copolymer PCDTBT: insights from time-resolved electron paramagnetic resonance spectroscopy. *Macromolecules* **2018**, *51*, 4341–4349.
- (134) Pye, C. C.; Ziegler, T. An implementation of the conductor-like screening model of solvation within the Amsterdam density functional package. *Theoretical Chemistry Accounts* **1999**, *101*, 396–408.
- (135) Banerji, N.; Gagnon, E.; Morgantini, P.-Y.; Valouch, S.; Mohebbi, A. R.; Seo, J.-H.; Leclerc, M.; Heeger, A. J. Breaking down the problem: optical transitions, electronic structure, and photoconductivity in conjugated polymer PCDTBT and in its separate building blocks. *The Journal of Physical Chemistry C* **2012**, *116*, 11456–11469.
- (136) Tkachenko, N. V. *Optical Spectroscopy: Methods and Instrumentations*; Elsevier, 2006.
- (137) Grimme, S. Calculation of the electronic spectra of large molecules. *Reviews in Computational Chemistry* **2004**, *20*, 153–218.
- (138) McLauchlan, K. A.; Stevens, D. Flash photolysis electron spin resonance. *Accounts of Chemical Research* **1988**, *21*, 54–59.
- (139) Wang, C.-W.; Yang, L.; Zhu, C.; Yu, J.-G.; Lin, S.-H. Franck-Condon factors perturbed by damped harmonic oscillators: solvent enhanced $X^1A_g \leftrightarrow A^1B_{1u}$ absorption and fluorescence spectra of perylene. *The Journal of Chemical Physics* **2014**, *141*, 084106.
- (140) Mori, K.; Goumans, T.; Van Lenthe, E.; Wang, F. Predicting phosphorescent lifetimes and zero-field splitting of organometallic complexes with time-dependent density functional theory including spin-orbit coupling. *Physical Chemistry Chemical Physics* **2014**, *16*, 14523–14530.
- (141) Banerji, N.; Cowan, S.; Leclerc, M.; Vauthey, E.; Heeger, A. J. Exciton formation, relaxation, and decay in PCDTBT. *Journal of the American Chemical Society* **2010**, *132*, 17459–17470.
- (142) Etzold, F.; Howard, I. A.; Mauer, R.; Meister, M.; Kim, T.-D.; Lee, K.-S.;

- Baek, N. S.; Laquai, F. Ultrafast exciton dissociation followed by nongeminate charge recombination in PCDTBT: PCBM photovoltaic blends. *Journal of the American Chemical Society* **2011**, *133*, 9469–9479.
- (143) Zhu, Y.; Yang, L.; Zhao, S.; Huang, Y.; Xu, Z.; Yang, Q.; Wang, P.; Li, Y.; Xu, X. Improved performances of PCDTBT: PC₇₁BM BHJ solar cells through incorporating small molecule donor. *Physical Chemistry Chemical Physics* **2015**, *17*, 26777–26782.
- (144) Hintze, C.; Steiner, U. E.; Drescher, M. Photoexcited triplet state kinetics studied by electron paramagnetic resonance spectroscopy. *ChemPhysChem* **2017**, *18*, 6–16.
- (145) Eaton, G. R.; Eaton, S. S.; Barr, D. P.; Weber, R. T. *Quantitative EPR*; Springer Science & Business Media, 2010.
- (146) Möbius, K.; Savitsky, A. *High-field EPR Spectroscopy on Proteins and their Model Systems: Characterization of Transient Paramagnetic States*; Royal Society of Chemistry, 2009.
- (147) Stoll, S.; Schweiger, A. EasySpin, a comprehensive software package for spectral simulation and analysis in EPR. *Journal of Magnetic Resonance* **2006**, *178*, 42–55.
- (148) Tait, C. E.; Neuhaus, P.; Peeks, M. D.; Anderson, H. L.; Timmel, C. R. Excitation wavelength-dependent EPR study on the influence of the conformation of multiporphyrin arrays on triplet state delocalization. *Physical Chemistry Chemical Physics* **2016**, *18*, 5275–5280.
- (149) Bertrand, P.; Camensuli, P.; More, C.; Guigliarelli, B. A local spin model to describe the magnetic interactions in biological molecules containing [4Fe- 4S]⁺ clusters. Application to Ni- Fe hydrogenases. *Journal of the American Chemical Society* **1996**, *118*, 1426–1434.
- (150) Matt, C.; Lombeck, F.; Sommer, M.; Biskup, T. Impact of side chains of conjugated polymers on electronic structure: a case study. *Polymers* **2019**, *11*, 870.
- (151) van Gastel, M. The effect of spin polarization on zero field splitting parameters in paramagnetic π -electron molecules. *The Journal of Chemical Physics* **2009**, *131*, 124111.
- (152) Skourtis, S.; Nitzan, A. Effects of initial state preparation on the distance dependence of electron transfer through molecular bridges and wires. *The Journal of Chemical Physics* **2003**, *119*, 6271–6276.
- (153) Gorczak, N.; Tarkuç, S.; Renaud, N.; Houtepen, A. J.; Eelkema, R.; Siebbeles, L. D.; Grozema, F. C. Different mechanisms for hole and electron transfer

- along identical molecular bridges: the importance of the initial state delocalization. *The Journal of Physical Chemistry A* **2014**, *118*, 3891–3898.
- (154) Adamo, C.; Barone, V. Accurate excitation energies from time-dependent density functional theory: assessing the PBE0 model for organic free radicals. *Chemical Physics Letters* **1999**, *314*, 152–157.
- (155) Dreuw, A.; Head-Gordon, M. Failure of time-dependent density functional theory for long-range charge-transfer excited states: the zincbacteriochlorin- bacteriochlorin and bacteriochlorophyll- spheroidene complexes. *Journal of the American Chemical Society* **2004**, *126*, 4007–4016.
- (156) Peach, M. J.; Le Sueur, C. R.; Ruud, K.; Guillaume, M.; Tozer, D. J. TDDFT diagnostic testing and functional assessment for triazene chromophores. *Physical Chemistry Chemical Physics* **2009**, *11*, 4465–4470.
- (157) Peach, M. J.; Warner, N.; Tozer, D. J. On the triplet instability in TDDFT. *Molecular Physics* **2013**, *111*, 1271–1274.
- (158) Peach, M. J.; Williamson, M. J.; Tozer, D. J. Influence of triplet instabilities in TDDFT. *Journal of Chemical Theory and Computation* **2011**, *7*, 3578–3585.
- (159) Sears, J. S.; Koerzdoerfer, T.; Zhang, C.-R.; Brédas, J.-L. Communication: Orbital instabilities and triplet states from time-dependent density functional theory and long-range corrected functionals. *The Journal of Chemical Physics* **2011**, *135*, 151103.
- (160) Peach, M. J.; Tozer, D. J. Overcoming low orbital overlap and triplet instability problems in TDDFT. *The Journal of Physical Chemistry A* **2012**, *116*, 9783–9789.
- (161) Perdew, J. P.; Burke, K.; Ernzerhof, M. Generalized gradient approximation made simple. *Physical Review Letters* **1996**, *77*, 3865.
- (162) Ernzerhof, M.; Scuseria, G. E. Assessment of the Perdew–Burke–Ernzerhof exchange–correlation functional. *The Journal of Chemical Physics* **1999**, *110*, 5029–5036.
- (163) Adamo, C.; Barone, V. Toward reliable density functional methods without adjustable parameters: the PBE0 model. *The Journal of Chemical Physics* **1999**, *110*, 6158–6170.
- (164) Pandey, L.; Doiron, C.; Sears, J. S.; Brédas, J.-L. Lowest excited states and optical absorption spectra of donor–acceptor copolymers for organic photovoltaics: a new picture emerging from tuned long-range corrected density functionals. *Physical Chemistry Chemical Physics* **2012**, *14*, 14243–14248.

- (165) Kim, J.; Kwon, Y. S.; Shin, W. S.; Moon, S.-J.; Park, T. Carbazole-based copolymers: effects of conjugation breaks and steric hindrance. *Macromolecules* **2011**, *44*, 1909–1919.
- (166) Nan, G.; Yang, X.; Wang, L.; Shuai, Z.; Zhao, Y. Nuclear tunneling effects of charge transport in rubrene, tetracene, and pentacene. *Physical Review B* **2009**, *79*, 115203.
- (167) Wang, L.; Nan, G.; Yang, X.; Peng, Q.; Li, Q.; Shuai, Z. Computational methods for design of organic materials with high charge mobility. *Chemical Society Reviews* **2010**, *39*, 423–434.
- (168) Lee, M. H.; Dunietz, B. D.; Geva, E. Calculation from first principles of intramolecular golden-rule rate constants for photo-induced electron transfer in molecular donor–acceptor systems. *The Journal of Physical Chemistry C* **2013**, *117*, 23391–23401.
- (169) Geng, H.; Peng, Q.; Wang, L.; Li, H.; Liao, Y.; Ma, Z.; Shuai, Z. Toward quantitative prediction of charge mobility in organic semiconductors: tunneling enabled hopping model. *Advanced Materials* **2012**, *24*, 3568–3572.
- (170) Köhler, A.; Bäessler, H. Triplet states in organic semiconductors. *Materials Science and Engineering: R: Reports* **2009**, *66*, 71–109.
- (171) Yanai, N.; Kimizuka, N. New triplet sensitization routes for photon upconversion: thermally activated delayed fluorescence molecules, inorganic nanocrystals, and singlet-to-triplet absorption. *Accounts of Chemical Research* **2017**, *50*, 2487–2495.
- (172) Li, X.; Tang, M. L. Triplet transport in thin films: fundamentals and applications. *Chemical Communications* **2017**, *53*, 4429–4440.
- (173) Gray, V.; Moth-Poulsen, K.; Albinsson, B.; Abrahamsson, M. Towards efficient solid-state triplet–triplet annihilation based photon upconversion: supramolecular, macromolecular and self-assembled systems. *Coordination Chemistry Reviews* **2018**, *362*, 54–71.
- (174) Strieth-Kalthoff, F.; James, M. J.; Teders, M.; Pitzer, L.; Glorius, F. Energy transfer catalysis mediated by visible light: principles, applications, directions. *Chemical Society Reviews* **2018**, *47*, 7190–7202.
- (175) Jiang, Y.; Weiss, E. A. Colloidal quantum dots as photocatalysts for triplet excited state reactions of organic molecules. *Journal of the American Chemical Society* **2020**, *142*, 15219–15229.
- (176) Luo, X.; Han, Y.; Chen, Z.; Li, Y.; Liang, G.; Liu, X.; Ding, T.; Nie, C.; Wang, M.; Castellano, F. N., et al. Mechanisms of triplet energy transfer across

- the inorganic nanocrystal/organic molecule interface. *Nature Communications* **2020**, *11*, 1–10.
- (177) Smith, M. B.; Michl, J. Singlet fission. *Chemical Reviews* **2010**, *110*, 6891–6936.
- (178) Japahuge, A.; Zeng, T. Theoretical studies of singlet fission: searching for materials and exploring mechanisms. *ChemPlusChem* **2018**, *83*, 146–182.
- (179) Miyata, K.; Conrad-Burton, F. S.; Geyer, F. L.; Zhu, X.-Y. Triplet pair states in singlet fission. *Chemical Reviews* **2019**, *119*, 4261–4292.
- (180) Valianti, S.; Skourtis, S. S. The Role of bridge-state intermediates in singlet fission for donor–bridge–acceptor systems: a semianalytical approach to bridge-tuning of the donor–acceptor fission coupling. *The Journal of Physical Chemistry Letters* **2022**, *13*, 939–946.
- (181) Tung, C.-H.; Zhang, L.-P.; Li, Y.; Cao, H.; Tanimoto, Y. Intramolecular long-distance electron transfer and triplet energy transfer. Photophysical and photochemical studies on a norbornadiene- steroid- benzidine system. *Journal of the American Chemical Society* **1997**, *119*, 5348–5354.
- (182) Closs, G. L.; Piotrowiak, P.; MacInnis, J. M.; Fleming, G. R. Determination of long-distance intramolecular triplet energy-transfer rates. Quantitative comparison with electron transfer. *Journal of the American Chemical Society* **1988**, *110*, 2652–2653.
- (183) Eng, M. P.; Ljungdahl, T.; Mårtensson, J.; Albinsson, B. Triplet excitation energy transfer in porphyrin-based donor- bridge- acceptor systems with conjugated bridges of varying length: an experimental and DFT study. *The Journal of Physical Chemistry B* **2006**, *110*, 6483–6491.
- (184) Skourtis, S. S.; Liu, C.; Antoniou, P.; Virshup, A. M.; Beratan, D. N. Dexter energy transfer pathways. *Proceedings of the National Academy of Sciences* **2016**, *113*, 8115–8120.
- (185) Huang, Z.; Tang, M. L. Designing transmitter ligands that mediate energy transfer between semiconductor nanocrystals and molecules. *Journal of the American Chemical Society* **2017**, *139*, 9412–9418.
- (186) Blancafort, L.; Voityuk, A. A. Thermally induced hopping model for long-range triplet excitation energy transfer in DNA. *Physical Chemistry Chemical Physics* **2018**, *20*, 4997–5000.
- (187) Bai, S.; Zhang, P.; Antoniou, P.; Skourtis, S. S.; Beratan, D. N. Quantum interferences among Dexter energy transfer pathways. *Faraday Discussions* **2019**, *216*, 301–318.

- (188) Brédas, J.-L.; Beljonne, D.; Coropceanu, V.; Cornil, J. Charge-transfer and energy-transfer processes in π -conjugated oligomers and polymers: a molecular picture. *Chemical Reviews* **104**, 4971–5004.
- (189) Hestand, N. J.; Spano, F. C. Expanded theory of H- and J-molecular aggregates: the effects of vibronic coupling and intermolecular charge transfer. *Chemical Reviews* **2018**, *118*, 7069–7163.
- (190) Aragó, J.; Troisi, A. Regimes of exciton transport in molecular crystals in the presence of dynamic disorder. *Advanced Functional Materials* **2016**, *26*, 2316–2325.
- (191) Stehr, V.; Fink, R.; Tafipolski, M.; Deibel, C.; Engels, B. Comparison of different rate constant expressions for the prediction of charge and energy transport in oligoacenes. *Wiley Interdisciplinary Reviews: Computational Molecular Science* **2016**, *6*, 694–720.
- (192) Pavel, M., et al. Interplay of disorder and delocalization in photosynthetic light harvesting. *Current Opinion in Chemical Biology* **2018**, *47*, 1–6.
- (193) Jumper, C. C.; Rafiq, S.; Wang, S.; Scholes, G. D. From coherent to vibronic light harvesting in photosynthesis. *Current Opinion in Chemical Biology* **2018**, *47*, 39–46.
- (194) Gao, F.; Zhao, Y.; Liang, W. Vibronic spectra of perylene bisimide oligomers: effects of intermolecular charge-transfer excitation and conformational flexibility. *The Journal of Physical Chemistry B* **2011**, *115*, 2699–2708.
- (195) Liu, K.; Mukhopadhyay, A.; Ashcraft, A.; Liu, C.; Levy, A.; Blackwelder, P.; Olivier, J.-H. Reconfiguration of π -conjugated superstructures enabled by redox-assisted assembly. *Chemical Communications* **2019**, *55*, 5603–5606.
- (196) Ashcraft, A.; Liu, K.; Mukhopadhyay, A.; Paulino, V.; Liu, C.; Bernard, B.; Husainy, D.; Phan, T.; Olivier, J.-H. A molecular strategy to lock-in the conformation of a perylene bisimide-derived supramolecular polymer. *Angewandte Chemie* **2020**, *132*, 7557–7563.
- (197) Gorman, J.; Orsborne, S. R.; Sridhar, A.; Pandya, R.; Budden, P.; Ohmann, A.; Panjwani, N. A.; Liu, Y.; Greenfield, J. L.; Dowland, S., et al. Deoxyribonucleic acid encoded and size-defined π -stacking of perylene diimides. *Journal of the American Chemical Society* **2021**, *144*, 368–376.
- (198) Schieschke, N.; Bold, B. M.; Dohmen, P. M.; Wehl, D.; Hoffmann, M.; Dreuw, A.; Elstner, M.; Höfener, S. Geometry dependence of excitonic couplings and the consequences for configuration-space sampling. *Journal of Computational Chemistry* **2021**, *42*, 1402–1418.

- (199) Zhang, Y.; Liu, C.; Balaeff, A.; Skourtis, S. S.; Beratan, D. N. Biological charge transfer via flickering resonance. *Proceedings of the National Academy of Sciences* **2014**, *111*, 10049–10054.
- (200) Voityuk, A. A. Triplet excitation energy transfer through fluorene π stack. *The Journal of Physical Chemistry C* **2010**, *114*, 20236–20239.
- (201) Thouless, D. J. Electrons in disordered systems and the theory of localization. *Physics Reports* **1974**, *13*, 93–142.
- (202) Skourtis, S. S.; Da Silva, A. J.; Bialek, W.; Onuchic, J. N. New look at the primary charge separation in bacterial photosynthesis. *The Journal of Physical Chemistry* **1992**, *96*, 8034–8041.
- (203) Skourtis, S. S.; Beratan, D. N.; Naaman, R.; Nitzan, A.; Waldeck, D. H. Chiral control of electron transmission through molecules. *Physical Review Letters* **2008**, *101*, 238103.
- (204) Cao, J.; Silbey, R. J. Optimization of exciton trapping in energy transfer processes. *The Journal of Physical Chemistry A* **2009**, *113*, 13825–13838.
- (205) Moix, J. M.; Khasin, M.; Cao, J. Coherent quantum transport in disordered systems: I. The influence of dephasing on the transport properties and absorption spectra on one-dimensional systems. *New Journal of Physics* **2013**, *15*, 085010.
- (206) Schlawin, F.; Gessner, M.; Buchleitner, A.; Schätz, T.; Skourtis, S. S. Continuously parametrized quantum simulation of molecular electron-transfer reactions. *PRX Quantum* **2021**, *2*, 010314.
- (207) Hoyer, S.; Sarovar, M.; Whaley, K. B. Limits of quantum speedup in photosynthetic light harvesting. *New Journal of Physics* **2010**, *12*, 065041.
- (208) Kim, J.; Kang, D.-g.; Kim, S. K.; Joo, T. Role of coherent nuclear motion in the ultrafast intersystem crossing of ruthenium complexes. *Physical Chemistry Chemical Physics* **2020**, *22*, 25811–25818.
- (209) Tang, K.-C.; Liu, K. L.; Chen, I.-C. Rapid intersystem crossing in highly phosphorescent iridium complexes. *Chemical Physics Letters* **2004**, *386*, 437–441.
- (210) Juris, A.; Balzani, V.; Barigelletti, F.; Campagna, S.; Belser, P.; von Zelewsky, A. Ru (II) polypyridine complexes: photophysics, photochemistry, electrochemistry, and chemiluminescence. *Coordination Chemistry Reviews* **1988**, *84*, 85–277.
- (211) Vlček Jr, A. The life and times of excited states of organometallic and coordination compounds. *Coordination Chemistry Reviews* **2000**, *200*, 933–978.
- (212) Borgwardt, M.; Wilke, M.; Kiyani, I. Y.; Aziz, E. F. Ultrafast excited states

- dynamics of $[\text{Ru}(\text{bpy})_3]^{2+}$ dissolved in ionic liquids. *Physical Chemistry Chemical Physics* **2016**, *18*, 28893–28900.
- (213) Rangel, T.; Hamed, S. M.; Bruneval, F.; Neaton, J. B. An assessment of low-lying excitation energies and triplet instabilities of organic molecules with an ab-initio Bethe-Salpeter equation approach and the Tamm-Dancoff approximation. *The Journal of Chemical Physics* **2017**, *146*, 194108.
- (214) Hajgató, B.; Szieberth, D.; Geerlings, P.; De Proft, F.; Deleuze, M. A benchmark theoretical study of the electronic ground state and of the singlet-triplet split of benzene and linear acenes. *The Journal of Chemical Physics* **2009**, *131*, 224321.
- (215) Weigend, F.; Ahlrichs, R. Balanced basis sets of split valence, triple zeta valence and quadruple zeta valence quality for H to Rn: design and assessment of accuracy. *Physical Chemistry Chemical Physics* **2005**, *7*, 3297–3305.
- (216) Canonne, P.; Belanger, D.; Lemay, G.; Foscolos, G. B. One-step spiroannulation. Synthesis of spiro. gamma.-and. delta.-lactones. *The Journal of Organic Chemistry* **1981**, *46*, 3091–3097.
- (217) Zou, Y.; Zeng, W.; Gopalakrishna, T. Y.; Han, Y.; Jiang, Q.; Wu, J. Dicyclopenta [4, 3, 2, 1-ghi: 4', 3', 2', 1'-pqr] perylene: a bowl-shaped fragment of fullerene C70 with global antiaromaticity. *Journal of the American Chemical Society* **2019**, *141*, 7266–7270.
- (218) Neese, F. Software update: the ORCA program system, version 4.0. *Wiley Interdisciplinary Reviews-Computational Molecular Science* **2018**, *8*, e1327.
- (219) Lee, C.; Yang, W.; Parr, R. G. Development of the Colle-Salvetti correlation-energy formula into a functional of the electron density. *Physical Review B* **1988**, *37*, 785.
- (220) Izsák, R.; Neese, F. An overlap fitted chain of spheres exchange method. *The Journal of Chemical Physics* **2011**, *135*, 144105.
- (221) Neese, F.; Wennmohs, F.; Hansen, A.; Becker, U. Efficient, approximate and parallel Hartree-Fock and hybrid DFT calculations. A 'chain-of-spheres' algorithm for the Hartree-Fock exchange. *Chemical Physics* **2009**, *356*, 98–109.
- (222) Weigend, F. Accurate Coulomb-fitting basis sets for H to Rn. *Physical Chemistry Chemical Physics* **2006**, *8*, 1057–1065.
- (223) Grimme, S.; Antony, J.; Ehrlich, S.; Krieg, H. A consistent and accurate ab-initio parametrization of density functional dispersion correction (DFT-D) for the 94 elements H-Pu. *The Journal of Chemical Physics* **2010**, *132*, 154104.
- (224) Becke, A. D.; Johnson, E. R. A density-functional model of the dispersion inter-

- action. *The Journal of Chemical Physics* **2005**, *123*, 154101.
- (225) Grimme, S.; Ehrlich, S.; Goerigk, L. Effect of the damping function in dispersion corrected density functional theory. *Journal of Computational Chemistry* **2011**, *32*, 1456–1465.
- (226) Sirianni, D. A.; Alenaizan, A.; Cheney, D. L.; Sherrill, C. D. Assessment of density functional methods for geometry optimization of bimolecular van der Waals complexes. *Journal of Chemical Theory and Computation* **2018**, *14*, 3004–3013.
- (227) Sedlak, R.; Janowski, T.; Pitonak, M.; Rezac, J.; Pulay, P.; Hobza, P. Accuracy of quantum chemical methods for large noncovalent complexes. *Journal of Chemical Theory and Computation* **2013**, *9*, 3364–3374.
- (228) Silva, N. J.; Machado, F. B.; Lischka, H.; Aquino, A. J. π – π stacking between polyaromatic hydrocarbon sheets beyond dispersion interactions. *Physical Chemistry Chemical Physics* **2016**, *18*, 22300–22310.
- (229) Hanwell, M. D.; Curtis, D. E.; Lonie, D. C.; Vandermeersch, T.; Zurek, E.; Hutchison, G. R. Avogadro: an advanced semantic chemical editor, visualization, and analysis platform. *Journal of Cheminformatics* **2012**, *4*, 1–17.
- (230) Zhao, Y.; Truhlar, D. G. Density functionals with broad applicability in chemistry. *Accounts of Chemical Research* **2008**, *41*, 157–167.
- (231) Bokarev, S. I.; Bokareva, O. S.; Kühn, O. Electronic excitation spectrum of the photosensitizer $[\text{Ir}(\text{ppy})_2(\text{bpy})]^+$. *The Journal of Chemical Physics* **2012**, *136*, 214305.
- (232) Plasser, F.; Dreuw, A. High-level ab-initio computations of the absorption spectra of organic iridium complexes. *The Journal of Physical Chemistry A* **2015**, *119*, 1023–1036.
- (233) Atkins, A. J.; Talotta, F.; Freitag, L.; Boggio-Pasqua, M.; Gonzalez, L. Assessing excited state energy gaps with time-dependent density functional theory on Ru (II) complexes. *Journal of Chemical Theory and Computation* **2017**, *13*, 4123–4145.
- (234) Hartzler, D. A.; Slipchenko, L. V.; Savikhin, S. Triplet–triplet coupling in chromophore dimers: theory and experiment. *The Journal of Physical Chemistry A* **2018**, *122*, 6713–6723.
- (235) Andrae, D.; Haeussermann, U.; Dolg, M.; Stoll, H.; Preuss, H. Energy-adjusted ab-initio pseudopotentials for the second and third row transition elements. *Theoretica Chimica Acta* **1990**, *77*, 123–141.

- (236) Case, D. A.; Aktulga, H. M.; Belfon, K.; Ben-Shalom, I.; Brozell, S. R.; Cerutti, D. S.; Cheatham III, T. E.; Cruzeiro, V. W. D.; Darden, T. A.; Duke, R. E., et al. *Amber 2021*; University of California, San Francisco, 2021.
- (237) Jakalian, A.; Bush, B. L.; Jack, D. B.; Bayly, C. I. Fast, efficient generation of high-quality atomic charges. AM1-BCC model: I. Method. *Journal of Computational Chemistry* **2000**, *21*, 132–146.
- (238) Jakalian, A.; Jack, D. B.; Bayly, C. I. Fast, efficient generation of high-quality atomic charges. AM1-BCC model: II. Parameterization and validation. *Journal of Computational Chemistry* **2002**, *23*, 1623–1641.
- (239) Wang, J.; Wolf, R. M.; Caldwell, J. W.; Kollman, P. A.; Case, D. A. Development and testing of a general amber force field. *Journal of Computational Chemistry* **2004**, *25*, 1157–1174.
- (240) Pastor, R. W.; Brooks, B. R.; Szabo, A. An analysis of the accuracy of Langevin and molecular dynamics algorithms. *Molecular Physics* **1988**, *65*, 1409–1419.
- (241) Loncharich, R. J.; Brooks, B. R.; Pastor, R. W. Langevin dynamics of peptides: the frictional dependence of isomerization rates of N-acetylalanine-N'-methylamide. *Biopolymers: Original Research on Biomolecules* **1992**, *32*, 523–535.
- (242) Izaguirre, J. A.; Catarello, D. P.; Wozniak, J. M.; Skeel, R. D. Langevin stabilization of molecular dynamics. *The Journal of Chemical Physics* **2001**, *114*, 2090–2098.
- (243) Shao, Y.; Gan, Z.; Epifanovsky, E.; Gilbert, A. T.; Wormit, M.; Kussmann, J.; Lange, A. W.; Behn, A.; Deng, J.; Feng, X., et al. Advances in molecular quantum chemistry contained in the Q-Chem 4 program package. *Molecular Physics* **2015**, *113*, 184–215.
- (244) Hariharan, P.; Pople, J. Accuracy of AH_n equilibrium geometries by single determinant molecular orbital theory. *Molecular Physics* **1974**, *27*, 209–214.
- (245) Bussi, G.; Parrinello, M. Accurate sampling using Langevin dynamics. *Physical Review E* **2007**, *75*, 056707.
- (246) Martin, R. L. Natural transition orbitals. *The Journal of Chemical Physics* **2003**, *118*, 4775–4777.
- (247) Nooijen, M.; Bartlett, R. J. A new method for excited states: Similarity transformed equation-of-motion coupled-cluster theory. *The Journal of Chemical Physics* **1997**, *106*, 6441–6448.
- (248) Nooijen, M.; Bartlett, R. J. Similarity transformed equation-of-motion coupled-

- cluster theory: details, examples, and comparisons. *The Journal of Chemical Physics* **1997**, *107*, 6812–6830.
- (249) Dutta, A. K.; Nooijen, M.; Neese, F.; Izsák, R. Automatic active space selection for the similarity transformed equations of motion coupled cluster method. *The Journal of Chemical Physics* **2017**, *146*, 074103.
- (250) Dutta, A. K.; Nooijen, M.; Neese, F.; Izsák, R. Exploring the accuracy of a low scaling similarity transformed equation of motion method for vertical excitation energies. *Journal of Chemical Theory and Computation* **2018**, *14*, 72–91.
- (251) Sous, J.; Goel, P.; Nooijen, M. Similarity transformed equation of motion coupled cluster theory revisited: a benchmark study of valence excited states. *Molecular Physics* **2014**, *112*, 616–638.
- (252) Dutta, A. K.; Neese, F.; Izsák, R. Towards a pair natural orbital coupled cluster method for excited states. *The Journal of Chemical Physics* **2016**, *145*, 034102.
- (253) Head-Gordon, M.; Rico, R. J.; Oumi, M.; Lee, T. J. A doubles correction to electronic excited states from configuration interaction in the space of single substitutions. *Chemical Physics Letters* **1994**, *219*, 21–29.
- (254) Harbach, P. H.; Wormit, M.; Dreuw, A. The third-order algebraic diagrammatic construction method (ADC (3)) for the polarization propagator for closed-shell molecules: efficient implementation and benchmarking. *The Journal of Chemical Physics* **2014**, *141*, 064113.
- (255) Wormit, M.; Rehn, D. R.; Harbach, P. H.; Wenzel, J.; Krauter, C. M.; Epifanovsky, E.; Dreuw, A. Investigating excited electronic states using the algebraic diagrammatic construction (ADC) approach of the polarisation propagator. *Molecular Physics* **2014**, *112*, 774–784.
- (256) Jimenez, R.; Dikshit, S. N.; Bradforth, S. E.; Fleming, G. R. Electronic excitation transfer in the LH2 complex of Rhodobacter sphaeroides. *The Journal of Physical Chemistry* **1996**, *100*, 6825–6834.
- (257) Meier, T.; Chernyak, V.; Mukamel, S. Multiple exciton coherence sizes in photosynthetic antenna complexes viewed by pump-probe spectroscopy. *The Journal of Physical Chemistry B* **1997**, *101*, 7332–7342.
- (258) Novoderezhkin, V.; Monshouwer, R.; Van Grondelle, R. Exciton (de) localization in the LH2 antenna of Rhodobacter sphaeroides as revealed by relative difference absorption measurements of the LH2 antenna and the B820 subunit. *The Journal of Physical Chemistry B* **1999**, *103*, 10540–10548.
- (259) Jin, T.; Uhlikova, N.; Xu, Z.; Zhu, Y.; Huang, Y.; Egap, E.; Lian, T. Competition

- of Dexter, Förster, and charge transfer pathways for quantum dot sensitized triplet generation. *The Journal of Chemical Physics* **2020**, *152*, 214702.
- (260) Jin, T.; Uhlikova, N.; Xu, Z.; Zhu, Y.; Huang, Y.; Egap, E.; Lian, T. Enhanced triplet state generation through radical pair intermediates in BODIPY-quantum dot complexes. *The Journal of Chemical Physics* **2019**, *151*, 241101.
- (261) Jin, T.; Lian, T. Trap state mediated triplet energy transfer from CdSe quantum dots to molecular acceptors. *The Journal of Chemical Physics* **2020**, *153*, 074703.
- (262) Yu, W. W.; Qu, L.; Guo, W.; Peng, X. Experimental determination of the extinction coefficient of CdTe, CdSe, and CdS nanocrystals. *Chemistry of Materials* **2003**, *15*, 2854–2860.
- (263) Protesescu, L.; Nachttegaal, M.; Voznyy, O.; Borovinskaya, O.; Rossini, A. J.; Emsley, L.; Copéret, C.; Günther, D.; Sargent, E. H.; Kovalenko, M. V. Atomistic description of thiostannate-capped CdSe nanocrystals: retention of four-coordinate SnS₄ motif and preservation of Cd-rich stoichiometry. *Journal of the American Chemical Society* **2015**, *137*, 1862–1874.
- (264) Mattoussi, H.; Radzilowski, L. H.; Dabbousi, B. O.; Thomas, E. L.; Bawendi, M. G.; Rubner, M. F. Electroluminescence from heterostructures of poly (phenylene vinylene) and inorganic CdSe nanocrystals. *Journal of Applied Physics* **1998**, *83*, 7965–7974.
- (265) Coe, S.; Woo, W.-K.; Bawendi, M.; Bulović, V. Electroluminescence from single monolayers of nanocrystals in molecular organic devices. *Nature* **2002**, *420*, 800–803.
- (266) Anikeeva, P. O.; Halpert, J. E.; Bawendi, M. G.; Bulovic, V. Quantum dot light-emitting devices with electroluminescence tunable over the entire visible spectrum. *Nano Letters* **2009**, *9*, 2532–2536.
- (267) Munro, A. M.; Zacher, B.; Graham, A.; Armstrong, N. R. Photoemission spectroscopy of tethered CdSe nanocrystals: shifts in ionization potential and local vacuum level as a function of nanocrystal capping ligand. *ACS Applied Materials & Interfaces* **2010**, *2*, 863–869.

Appendices

SPYROULLA A. MAVROMMATI

APPENDIX A

Computation of the reorganization energies using ADF

Figure A.1 shows an example of a script input file of FCF-ADF, for the computation of the reorganization energies λ_α for each normal mode of frequency ω_α , for the transition $S_1 \rightarrow T_1$ in Cbz-TBT molecule. Next to the keyword “STATES” we specify the two TAPE21 filenames of the initial and final states of the transition, resulting from the two relative frequency calculations (S1_Freq.t21 and T1_Freq.t21). The keyword “QUANTA” reveals the maximum number of the vibrational quantum levels that are considered for both states for the computation of the FCFs (see figure 2.1). The FCF-ADF program is able to compute the FCFs only for a small number of vibrational levels (i.e., 2-3 depending on the size of molecule), due to large computational cost. If we include zero vibrational levels for both states (QUANTA 0 0) then the FCF-ADF program produces only the electron-phonon couplings using much smaller computational time. The FCFs can be computed using eq. 2.29 as we explained in the previous chapters. Using the keywords “TRANSLATE” and “ROTATE” we remove the six vibrational and rotational degrees of freedom. FCF-ADF produces a binary TAPE61 file (with extension .t61) that includes detailed information about the calculation. The vibrational mode frequencies with the relative electron-phonon couplings for both states are also shown in the standard FCF-ADF output file.

Figure A.2 shows the main part of the FCF-ADF output file for the ISC transition $S_1 \rightarrow T_1$ in Cbz-TBT molecule (see chapter 7). The output file of such a calculation is separated in two sections, the first one for the first state (S_1) and the second one for the second state (T_1). Each state calculation is characterized by three columns. The first column shows the mode frequencies ω_α , the second column shows the vibrational displacements, and the third column shows the electron-phonon coupling parameters $\bar{\lambda}_\alpha$ that are computed from the displacements via equation 7.1. From the output file we extract the mode frequencies ω_α and the electron-phonon couplings per mode $\bar{\lambda}_\alpha$

```
$ADFBIN/fcf << eor
STATES S1_Freq.t21 T1_Freq.t21
QUANTA 0 0
TRANSLATE
ROTATE
eor

mv TAPE61 S1_T1_FCF.t61
mv logfile S1_T1_FCF.log
```

Figure A.1: Example of the input script of the FCF-ADF program used to compute the electron-phonon coupling parameters $\bar{\lambda}_\alpha$ for each normal mode α , for the transition $S_1 \rightarrow T_1$ in the Cbz-TBT molecule.

and we use the equation 7.2 to compute the reorganization energies per mode λ_α . The reorganization energy for the electronic transition, e.g, $S_1 \rightarrow T_1$ equals to the sum over all the mode reorganization energies, i.e., $\lambda = \sum_\alpha \lambda_\alpha$. Starting from the first state (i.e., S_1) the total reorganization energy λ is computed for the $S_1 \rightarrow T_1$ transition. Starting from the second state (i.e., T_1) the total reorganization energy is computed for the $T_1 \rightarrow S_1$ transition (see figure 2.1).

```

=====
FIRST STATE
=====

```

Frequency cm ⁻¹	Displacement a0 amu ^{1/2}	Electron-Phonon coupling (dimensionless)
14.928444	-0.470345	0.117111
21.353705	-0.569143	0.169485
34.548057	0.270974	0.102639
.	.	.
.	.	.
.	.	.
3349.698379	-0.001082	0.004035
3791.325035	0.000847	0.003363

```

=====
SECOND STATE
=====

```

Frequency cm ⁻¹	Displacement a0 amu ^{1/2}	Electron-Phonon coupling (dimensionless)
13.607488	-0.852327	0.202613
18.244945	0.028333	0.007799
33.806185	0.266311	0.099784
.	.	.
.	.	.
.	.	.
3350.095652	-0.000090	0.000337
3794.659815	-0.000706	0.002801

Figure A.2: Example part of the output file of the FCF-ADF program used to compute the electron-phonon coupling parameters $\bar{\lambda}_\alpha$ for each normal mode α , for the transition $S_1 \rightarrow T_1$ in the Cbz-TBT molecule.

APPENDIX B

Short-time approximation of the quantum Franck-Condon factor to examine temperature effects

In this appendix, we investigate temperature effects on the non-adiabatic transition rate. We split the summation over the modes in equation 2.44 into its contributions from the high-frequency modes ($\hbar\omega_\alpha \gg K_B T$) and the low-frequency modes ($\hbar\omega_\alpha > K_B T$). Therefore, the finite-temperature formula for the spectral density (eq. 2.43) yields¹

$$D_{\text{inh,hom}}\left(\frac{\Delta E}{\hbar}\right) = \frac{1}{2\pi\hbar} \int_{-\infty}^{\infty} e^{i\frac{\Delta E}{\hbar}t - \Gamma t - \frac{1}{2}\Theta^2 t^2} \eta_l(t) \eta_h(t) dt. \quad (\text{B.1})$$

The time-dependent functions η_l and η_h contain the contribution from the low (l) and high (h) frequency modes respectively and are defined by

$$\begin{aligned} \eta_l(t) &= \exp \left\{ - \sum_{m=1}^{M_l} \left(\frac{\lambda_m}{\hbar\omega_m} \right) [(2\langle n_m \rangle + 1)(1 - \cos(\omega_m t)) + i \sin(\omega_m t)] \right\} \\ \eta_h(t) &= \exp \left\{ - \sum_{j=M_l+1}^M \left(\frac{\lambda_j}{\hbar\omega_j} \right) [(2\langle n_j \rangle + 1)(1 - \cos(\omega_j t)) + i \sin(\omega_j t)] \right\}. \end{aligned} \quad (\text{B.2})$$

¹see refs.: (a) Nitzan, A. *Chemical Dynamics in Condensed Phases: Relaxation, Transfer and Reactions in Condensed Molecular Systems*; Oxford University Press, 2006. (b) Petrenko, T.; Neese, F. Analysis and prediction of absorption band shapes, resonance Raman intensities, and excitation profiles using the time-dependent theory of electronic spectroscopy. *The Journal of Chemical Physics* **2007**, *127*, 164319. (c) Petrenko, T.; Krylova, O.; Neese, F.; Sokolowski, M. Optical absorption and emission properties of rubrene: insight from a combined experimental and theoretical study. *New Journal of Physics* **2009**, *11*, 015001. (d) Petrenko, T.; Neese, F. Efficient and automatic calculation of optical band shapes and resonance Raman spectra for large molecules within the independent mode displaced harmonic oscillator model. *The Journal of Chemical Physics* **2012**, *137*, 234107. (e) Chan, C.-K.; Page, J. Temperature effects in the time-correlator theory of resonance Raman scattering. *The Journal of Chemical Physics* **1983**, *79*, 5234-5250.

The summation in η_l goes over the low frequency modes (with M_l the total number of low frequency modes), while the summation in η_h goes over the high frequency modes (with $M - M_l$ the total number of high frequency modes and M the total number of vibrational modes of the system).

High-frequency modes with sufficiently strong electron-phonon couplings $\bar{\lambda}_j$, give vibrational lines in the spectrum that are well resolved. These modes determine the vibronic peak positions and intensities of the spectral profile. On the other hand, low-frequency modes are responsible for the vibronic peak shapes induced by thermal and homogeneous broadening.

The contribution of the low-frequency modes in the integral of eq. B.1 appears within the short-time approximation for which $\bar{\lambda}_m^2 \gg 1$ and $\sum_m \bar{\lambda}_m^2 \langle n_m \rangle \gg 1$. In that case, the integral is approximated by expanding the argument of the exponential in $\eta_l(t)$ to order t^2 as follows

$$\eta_l(t) = \exp \left\{ - \sum_m \bar{\lambda}_m^2 \omega_m t - \frac{1}{2} \sum_m \bar{\lambda}_m^2 \omega_m^2 (2\langle n_m \rangle + 1) t^2 \right\}. \quad (\text{B.3})$$

This approximation leads to the damping factor $e^{-\frac{1}{2}\delta^2 t^2}$ where,

$$\delta^2 = \sum_m \bar{\lambda}_m^2 \omega_m^2 (2\langle n_m \rangle + 1) \quad (\text{B.4})$$

which causes an additional broadening of the spectral density of Gaussian form that depends on the temperature T (temperature effects are included in the occupation number $\langle n_m \rangle$).

The lineshape function (eq. B.1) is now rewritten as,

$$D_{\text{inh,hom}} \left(\frac{\Delta E}{\hbar} \right) = \frac{1}{2\pi\hbar} \int_{-\infty}^{\infty} e^{i\frac{\Delta E}{\hbar}t - \Gamma t - \frac{1}{2}\Theta_{\text{eff}}^2 t^2} \eta_h dt \quad (\text{B.5})$$

where we integrate the correlation function η_h that includes only the high-frequency modes, and

$$\Theta_{\text{eff}}^2 = \sum_m \bar{\lambda}_m^2 \omega_m^2 (2\langle n_m \rangle + 1) + \Theta^2 = \delta^2 + \Theta^2 \quad (\text{B.6})$$

is the effective standard deviation. This temperature-induced broadening on the absorption lineshape arises exclusively from the low-frequency modes and leads to unresolved vibrational progressions in the spectrum. Each vibronic line is broadened into a Gaussian of full width at half maximum (FWHM) corresponding to the parameters

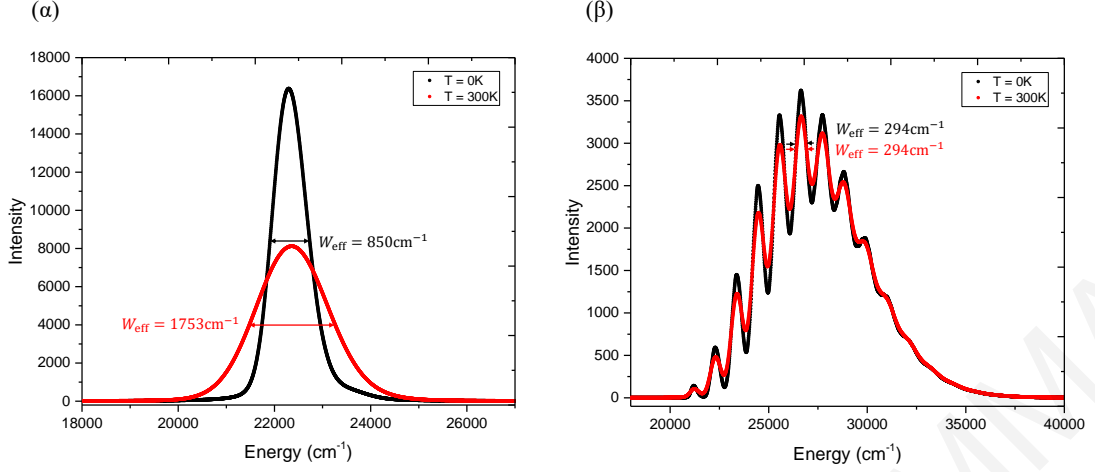


Figure B.1: Absorption spectra computed at $T = 0$ K and $T = 300$ K temperatures using $\Gamma = 50$ cm^{-1} and $\Theta = 100$ cm^{-1} . (a) the simulations were performed for a set of low-frequency modes and (b) the simulations were performed using a set of high-frequency modes.

Γ and Θ_{eff} , that is approximated by²

$$W_{\text{eff}}(\Gamma, \Theta_{\text{eff}}) = 1.0692\Gamma + \sqrt{0.8664\Gamma^2 + 8\ln(2)\Theta_{\text{eff}}^2}. \quad (\text{B.7})$$

Temperature effects are elucidated if the W_{eff} is compared to the temperature-independent broadening parameter (W) corresponding to the intrinsic parameters Γ and Θ ,

$$W(\Gamma, \Theta) = 1.0692\Gamma + \sqrt{0.8664\Gamma^2 + 8\ln(2)\Theta^2}. \quad (\text{B.8})$$

For small vibrational frequencies $\{\omega_m\}$, $m = 1 \dots M_l$ for which $\omega_m \leq 0.5W$ the short-time approximation is applicable and the modes are treated as low-frequency modes. If the spectral density contains no vibrational frequencies that follow the above condition, then all modes are treated as high-frequency modes. In that case, $\delta = 0$ and the effective standard deviation Θ_{eff} equals to the intrinsic standard deviation Θ . The temperature effects are negligible i.e., $W_{\text{eff}} = W$, and the spectrum consists of well resolved vibronic peaks that come from the high-frequency modes. On the other hand, the more normal modes of low-frequency and large contribution to the spectrum (e.g., large electron-phonon couplings ($\bar{\lambda}_m$)) we have, the greater the W_{eff} and thus the temperature-induced spectral broadening.

Figure B.1 show examples of spectra simulated using $\Gamma = 50$ cm^{-1} and $\Theta = 100$ cm^{-1} . These intrinsic broadening parameters yield a FWHM that equals to $W = 239.5$ cm^{-1} . For a set of $\{\omega_m\}$ with strong $\{\bar{\lambda}_m\}$, corresponding to low-frequency modes ($\omega_m \leq 146.8 \text{cm}^{-1}$), we computed the effective FWHM parameters at zero ($T = 0$ K)

²see ref.: Petrenko, T.; Krylova, O.; Neese, F.; Sokolowski, M. Optical absorption and emission properties of rubrene: insight from a combined experimental and theoretical study. *New Journal of Physics* **2009**, *11*, 015001.

BROADENING PARAMETETRS (cm**-1)									
State	Intrinsic			Effective					
	Gamma	Sigma	FWHM	Sigma			FWHM		
				0K	80.00K	298.15K	0K	80.00K	298.15K
1:	33.36	0.00	66.71	38.70	94.22	195.44	131.94	259.71	496.93

$$W(\Gamma, \Theta) = 1.0692\Gamma + \sqrt{0.8664\Gamma^2 + 8\ln(2)\Theta^2}$$

$$W_{\text{eff}}(\Gamma, \Theta_{\text{eff}}) = 1.0692\Gamma + \sqrt{0.8664\Gamma^2 + 8\ln(2)\Theta_{\text{eff}}^2}$$

Figure B.2: Part of the output file of the orca_asa program showing the intrinsic and effective broadening parameters and the relative FWHMs. The parameters Γ and Θ are defined in the input file (see figure C.2 in appendix C) but are shown also in the output file. This output file is related to the calculation shown in figure C.2 in appendix C for the $S_1 \rightarrow T_1$ transition in Cbz-TBT molecule.

and room ($T = 300$ K) temperatures. At $T = 0$ K the effective broadening parameter equals to $W_{\text{eff}} = 850$ cm^{-1} while at $T = 300$ K it increases to $W_{\text{eff}} = 1753$ cm^{-1} . The spectrum is completely unresolved and the temperature-induced broadening defined as $\Delta_T W = W_{\text{eff}}(T = 0\text{K}) - W_{\text{eff}}(T = 300\text{K})$ equals to 903 cm^{-1} (see figure B.1 left-hand site plot). In the opposite case, with a set of $\{\omega_j\}$ corresponding to high-frequency modes ($\omega_j \geq 146.8$ cm^{-1}), the FWHM parameters at $T = 0$ K and $T = 300$ K are the same ($W_{\text{eff}} = 294$ cm^{-1}). The temperature-induced broadening is zero and the vibrational peaks are well resolved (see figure B.1 right-hand site plot). The broadening parameters of eqs. B.7 and B.8 are derived from orca_asa program available for ORCA (see appendix C and figure B.2).

APPENDIX C

Intersystem crossing rates computed using the orca_asa program

The time-dependent approach for the transition rate between two electronic states (eqs. 2.44 and 2.30) can also be applied to simulate optical band shapes (absorption, fluorescence), resonance-Raman intensities, and excitation profiles. F. Neese and T. Petrenko developed a stand-alone computer program (orca_asa) linked to the ORCA electronic structure program package, that analyzes the absorption and fluorescence spectra of molecules, in the framework of the Independent Mode Displaced Harmonic Oscillator (IMHDO) model.¹ The model assumes: (1) harmonic ground- and excited-state PES, (2) excited state PES shifted relative to the ground-state PES (see figure C.1), (3) vibrational frequencies that do not change and normal modes that do not rotate in the excited state, and (4) an electronic transition dipole moment that has no coordinate dependence.

Within the IMHDO approach, the absorption cross section $\sigma(E_L)$ and the fluo-

¹see refs.: (a) Petrenko, T.; Neese, F. Analysis and prediction of absorption band shapes, resonance Raman intensities, and excitation profiles using the time-dependent theory of electronic spectroscopy. *The Journal of Chemical Physics* **2007**, *127*, 164319. (b) Petrenko, T.; Krylova, O.; Neese, F.; Sokolowski, M. Optical absorption and emission properties of rubrene: insight from a combined experimental and theoretical study. *New Journal of Physics* **2009**, *11*, 015001. (c) Petrenko, T.; Neese, F. Efficient and automatic calculation of optical band shapes and resonance Raman spectra for large molecules within the independent mode displaced harmonic oscillator model. *The Journal of Chemical Physics* **2012**, *137*, 234107.

rescence efficiency $A_{k0}(E_R)$ of a system have the following forms in the time domain

$$\begin{aligned} \sigma(E_L) = & \frac{4\pi}{3\hbar c} E_L \sum_k (D_{0k})^2 \text{Re} \int_0^\infty \exp \left\{ i \left(E_L - E_{0k} - \frac{s_k}{2} \right) t - \Gamma_k t - \frac{1}{2} \Theta_k^2 t^2 \right\} \\ & \times \exp \left\{ - \sum_j \frac{(\Delta_{kj})^2}{2} [(2\langle n_j \rangle + 1) (1 - \cos(\omega_j t)) + i \sin(\omega_j t)] \right\} dt \end{aligned} \quad (\text{C.1a})$$

$$\begin{aligned} A_{k0}(E_R) = & \frac{4E_R^3}{3\pi\hbar^4 c^3} (D_{0k})^2 \text{Re} \int_0^\infty \exp \left\{ i \left(E_{0k} - \frac{s_k}{2} - E_R \right) t - \Gamma_k t - \frac{1}{2} \Theta_k^2 t^2 \right\} \\ & \times \exp \left\{ - \sum_j \frac{(\Delta_{kj})^2}{2} [(2\langle n_j \rangle + 1) (1 - \cos(\omega_j t)) + i \sin(\omega_j t)] \right\} dt \end{aligned} \quad (\text{C.1b})$$

E_L and E_R denote the energies of the incident and emitted photon respectively. E_{0k} is the adiabatic minimum separation energy between states 0 and k (index 0 labels the electronic ground-state and k labels the electronic excited states). Its value corresponds to the position of the 0 – 0 vibrational peak (see figure C.1). s_k is the corresponding Stokes shift related to the energy difference between positions of the maximum of the first absorption band and the maximum of the emission spectra at the same electronic transition. ω_j is the ground-state vibrational frequency of j th normal mode and Δ_{kj} is the dimensionless origin shift of the k th excited state PES along the j th normal mode coordinate. ω_j and Δ_{kj} entirely specify the positions and the relative intensities of the different vibronic bands. Γ_k and Θ_k are the homogeneous and inhomogeneous linewidth parameters respectively. Γ_k determines the linewidth and Θ_k the shape of each vibronic band (i.e., Θ_k is the standard deviation of E_{0k}) (see figure C.1). \vec{D}_{0k} is the electric transition dipole moment evaluated at the minimum energy conformation of the ground state. It determines the overall intensity of the optical spectrum. $\langle n_j \rangle$ is the thermal average occupation number of mode j at temperature T and its is given by eq. 2.28.

The equation for the absorption cross section and the fluorescence efficiency (eq. C.1a-b) reduces to the ISC rate constant of eq. 6.15, if we choose: $E_{0k} = 0$, $s_k = 0$ and $\Theta_k = 0$. In addition, $\frac{(\Delta_{kj})^2}{2}$ corresponds to the Huang-Rhys factors $\frac{\lambda_\alpha}{\hbar\omega_\alpha}$ (see eqs. 2.25 and 2.27). The summation over the electronic excited states k is removed and the k th excited state now corresponds to the final triplet state T_{k,m_s} . The energy E_L (E_R) corresponds to the energy difference between the minima of the PES of the singlet S_n and triplet T_{k,m_s} states ($\Delta E_{S_n, T_{k,m_s}}/\hbar$). Within these replacements, the ISC rate differs from the absorption cross section $\sigma(E_L)$ (eq. C.1a) by a constant value that equals to

$$\text{constant} = \frac{\sigma(E_L)/E_L}{\text{Int}} \sim \frac{4\pi}{3\hbar c} (D_{0k})^2 \quad (\text{C.2})$$

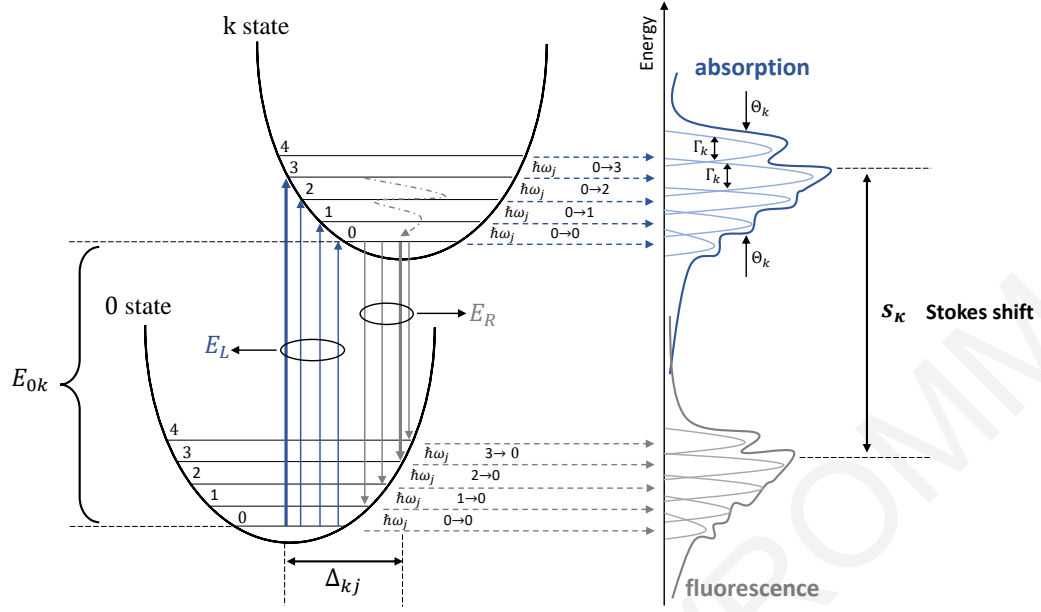


Figure C.1: Shifted potential surfaces model for absorption and emission in the single-mode representation. We show that the inhomogeneously broadened absorption band of width Θ_k , comes from the superposition of individual vibronic bands that are homogeneously broadened by Γ_k .

where Int is the time integral

$$\text{Int} = \text{Re} \int_0^\infty \exp \left\{ iE_L t - \Gamma t - \sum_j \frac{(\Delta_j)^2}{2} [(2\langle n_j \rangle + 1) (1 - \cos(\omega_j t)) + i \sin(\omega_j t)] \right\} dt. \quad (\text{C.3})$$

This is exactly the FCF integral of equation 2.29. The constant value can be evaluated empirically by computing the FCFs using our MATLAB code (i.e., to get the Int_MATLAB which is equal to Int) and the $\sigma(E_L)/E_L$ using the `orca_asa` program (see equation C.2). These computations are repeated for a variety of vibrational systems in order to derive an averaged value for the constant denoted $\langle \text{constant} \rangle$. The deduced average value $\langle \text{constant} \rangle$ can be used in combination with the $\sigma(E_L)/E_L$ to find the ISC rate as follows

$$k_{S_n \rightarrow T_{k,m_s}} (\Delta E_{S_n, T_{k,m_s}} / \hbar) = \frac{\sigma(E_L)/E_L}{\langle \text{constant} \rangle} \times \frac{|\langle S_n | \hat{H}^{\text{SOC}} | T_{k,m_s} \rangle|^2}{\hbar^2}. \quad (\text{C.4})$$

The formula of equation C.4 is an alternative way to the MATLAB code for computing the ISC rate constants using the results from the `orca_asa` program for the absorption cross section, and the computationally derived average $\langle \text{constant} \rangle$.

The ISC rate constants can also be computed using the `orca_asa` program for the fluorescence efficiency $A_{k0}(E_R)$ (see eq. C.1b). We should follow the similar above-

mentioned procedure to derive the new constant value

$$\text{constant}' = \frac{A_{k0}(E_R)}{\text{Int}} \sim \frac{4E_R^3}{3\pi\hbar^4c^3}(D_{0k})^2 \quad (\text{C.5})$$

and its average value $\langle \text{constant}' \rangle$. In that case, the ISC rate will be given by equation,

$$k_{S_n \rightarrow T_{k,m_s}}(-\Delta E_{S_n, T_{k,m_s}}/\hbar) = \frac{A_{k0}(E_R)}{\langle \text{constant}' \rangle} \times \frac{|\langle S_n | \hat{H}^{\text{SOC}} | T_{k,m_s} \rangle|^2}{\hbar^2}, \quad (\text{C.6})$$

where the minus sign in equation C.6 results from the fact that in the process of emission, the minima of the PES of the initial and final states are reversed (see also eq. 2.52).

Using orca_asa for the ISC rate simulation

The `orca_asa` (“Advances Spectral Analysis”) is an autonomous program interfaced to ORCA but can be used in combination with other quantum chemistry computational packages, to simulate and fit the absorption, fluorescence (eq. C.1a-b) and resonance Raman spectral profiles. We use this program to derive the ISC rates by computing the absorption cross section $\sigma(E_L)$ within the IMHDO model (eq. C.1a), and following the procedure that was described above (see eq. C.4).

The `orca_asa` input file for the absorption cross section includes information specified in blocks with the following order: (1) parameters that characterize the electronic transition (e.g., temperature), (2) spectral ranges and resolution of the simulation, (3) parameters that characterize each k th electronic state i.e., E_{0k} , D_{0k_x} , D_{0k_ψ} , D_{0k_z} , (4) lineshape factors Γ_k and Θ_k , (5) Stokes shift parameter s_k for each k th electronic state, (6) ground-state vibrational frequencies, and (7) dimensionless origin shifts Δ_{kj} of the k th excited state PES along the j th normal mode in terms of the ground state.

Figure C.2 shows parts of the input file used to simulate the absorption spectrum of a molecular system. In block `%sim` we specify the model for the simulation i.e., `IMHDOT` which invokes that the spectrum is simulated within the IMHDO model at a finite temperature (T), specified by the parameter “TK” (lines 6-7 in the code). Below, we specify the spectral range for the absorption simulation (“AbsRange”) in cm^{-1} (initial and final values), as well as the resolution of the spectrum by the parameter “NAbsPoints” (lines 9-10 in the code). The next block (`$el_states`) contains the total number of the electronic states involved in the transitions (line 20), and the adiabatic minima separation energy (E_{0k}), the homogeneous and inhomogeneous broadening parameters (Γ_k and Θ_k) and the x, ψ and z components of the transition dipole moment \vec{D}_{0k} (line 21 in the code). All these parameters are in units of cm^{-1} except the dipole moment which is expressed in atomic units. The block `$ss` specifies the Stokes shift s_k in units of cm^{-1} (line 31 in the code). In the previous line we specify again the total number of the excited states (line 30 in the code). The last two blocks specify the vibrational frequencies (ω_j) of the ground state (block `$vib_freq_gs`) and the origin

```

1 # CALCULATION OF THE ABSORPTION CROSS SECTION USING THE VIBRATIONAL PARAMETERS
2 # OF THE ISC TRANSITION S1-->T1 IN Cbz-TBT MOLECULE
3
4 %sim
5
6 Model IMDHOT
7 TK 80
8
9 AbsRange -50000, 50000
10 NAbsPoints 262144
11
12 end
13
14 #-----
15 # A/A Transition Gamma Sigma Transition Dipole Moment (atomic unit)
16 # Energy (cm**-1) (cm**-1) (cm**-1) Mx My Mz
17 #-----
18
19 $el_states
20 1
21 1 0.00 33.3565 0.00 1.00 0.00 0.00
22
23
24 #-----
25 # A/A Stokes shift
26 # (cm**-1)
27 #-----
28
29 $ss
30 1 # number of the excited states
31 1 0.0
32
33 #-----
34 # A/A Frequencies
35 # (cm**-1)
36 #-----
37
38 $vib_freq_gs
39 135 # number of normal modes
40 1 14.928444
41 2 21.353705
42 3 34.548057
43 .
44 .
45 .
46 134 3349.698379
47 135 3791.325035
48
49
50 #-----
51 # A/A displacement
52 # (dimensionless)
53 #-----
54
55 $sdnc
56 135 1 # number of normal modes and number of the excited states
57 1 # define the displacements of the 1st state
58 1 2.208227
59 2 1.847430
60 3 0.419573
61 .
62 .
63 .
64 134 0.049333
65 135 0.144076

```

Figure C.2: Example of the input script of the orca_asa program used to compute the absorption cross section $\sigma(E_L)$. The script contains the vibrational frequencies and normal modes of the S_1 excited state, and the relative displacements of the T_1 excited states of the Cbz-TBT molecule. The absorption cross section was used to deduce the ISC rate constants according to equation C.4.

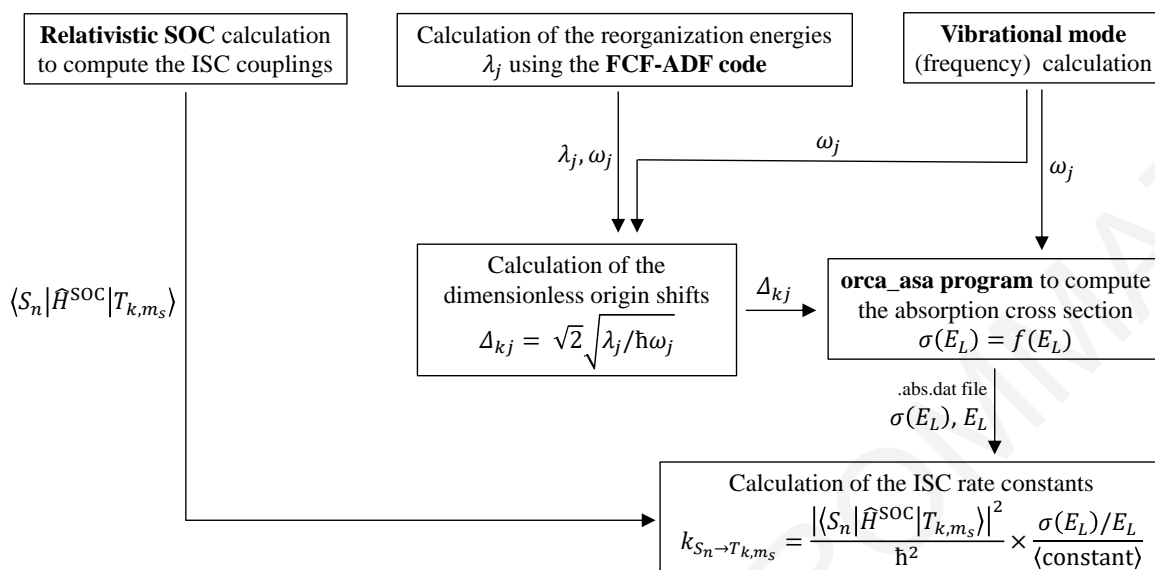


Figure C.3: Flowchart showing the computational procedure we followed to compute the ISC rate constants $S_n \rightarrow T_{k,m_s}$ using the `orca_asa` program implemented in the ORCA program package. The vibrational frequencies ω_j , the displacements Δ_{kj} and the SOC constants $\langle S_n | \hat{H}^{\text{SOC}} | T_{k,m_s} \rangle$ can be computed using any quantum chemical program. For our project we used the ADF program package.

shifts Δ_{kj} (block `$sdnc`) respectively. In the first line of the `$vib_freq_gs` block we define the total number of the normal modes (line 39 in the code). Similarly, the first line of the `$sdnc` block shows the number of normal modes and the number of the excited states (line 56 in the code). The simulated absorption spectrum ($\sigma(E_L)$) is computed in units of extinction coefficient and the results are stored in a data file of `.abs.dat` extension.

The ISC rates can be computed using the results for the absorption cross section via the eq. C.4. In that case the `orca_asa` input file is modified such that the vibrational frequencies of the ground state are replaced by those of the excited singlet state S_n , and the dimensionless displacements of the excited-state origin now refer to those of the triplet excited state T_{k,m_s} . As we described at the beginning of this section, the energy E_{0k} , the Stokes shift parameter s_k , and the Gaussian lineshape factor Θ_k are all set to zero. The transition dipole moment \vec{D}_{0k} is set to unity for convenience. In figure C.2 we show the main parts of the `orca_asa` input file that consists of the vibrational frequencies of the first singlet excited state (S_1) and the displacements of the first triplet excited state (T_1) along 135 normal coordinates. These input parameters are those that characterize the ISC transition $S_1 \rightarrow T_1$ in the Cbz-TBT molecule (see chapter 6).

The normal modes and the frequencies (ω_j) of each normal mode j of the S_1

state are taken from the vibrational frequency calculation performed using the ADF program (see description in appendix A). The origin shifts Δ_{kj} are related to the mode reorganization energies λ_j via $\Delta_{kj} = \sqrt{2}\sqrt{\lambda_j/\hbar\omega_j}$, and the λ_j parameters are computed using the FCF-ADF program according to the procedure discussed in appendix A. These are the input parameters on the `orca_asa` program and the computed absorption spectrum is printed in a two-column format where the first column corresponds to the transition energies E_L and the second column to the absorption cross section $\sigma(E_L)$. The quantity $\sigma(E_L)/E_L$ is divided by the constant value $\langle \text{constant} \rangle$ to get the FCF integrals. The ISC couplings $\langle S_1 | \hat{H}^{\text{SOC}} | T_{1,m_s} \rangle$ are computed by performing relativistic computations with the ADF program package. Then, the ISC rate is determined using the equation C.4.

Our results suggest that the ISC rates can be derived from the `orca_asa` program if one uses the vibrational frequencies and origin shifts of the singlet and triplet excited states involved in the $S_n \rightarrow T_{k,m_s}$ transition (see figure C.3). The normal mode frequencies, the Huang-Rhys factors and the electronic couplings can be deduced from any quantum chemistry computational package, regardless of whether the `orca_asa` module is implemented in ORCA. The ISC rate differs from the computed “optical spectrum” by a constant value (see equation C.4). In the following section, we propose that this constant value equals to 703.

Example calculations to estimate the constant value

In this section we describe how we computed the constant value of equation C.2 using the absorption cross section ($\sigma(E_L)$) and the FCF integral (Int_MATLAB). The constant value is an empirical parameter and can be extracted from different example calculations.

Let’s consider that we have a simple system which consists of a single (low) frequency mode ($\omega = 564.6 \text{ cm}^{-1}$) with mode reorganization energy $\lambda = 5645.9 \text{ cm}^{-1}$. We compute the $\sigma(E_L)$ using the `orca_asa` program (as described above), and the FCFs with our MATLAB program (as described in section 7.1). The simulations are performed at zero temperature ($T = 0 \text{ K}$) with homogeneous fitting parameter equal to $\Gamma = 333.6 \text{ cm}^{-1}(10 \text{ psec})$. Figure C.4 shows the simulated optical spectrum $\sigma(E_L)/E_L$ (left) and the computed FCF integrals (middle). The unresolved highest peaks are first selected (numbered as 1-3 and 1'-3' in the figure C.4), and for each peak we compute the constant value according to eq. C.2. Table C.1 summarizes the computed $\sigma(E_L)/E_L$ and Int_MATLAB together with the deduced constant value for each peak. Note that the constant value is such that the quantity $\frac{\sigma(E_L)/E_L}{\langle \text{constant} \rangle}$ has units cm. These results give an average value for the constant that equals to $703.1 \sim 703$. Therefore, if the Int_MATLAB is multiplied by this value, we get back the absorption cross section $\sigma(E_L)/E_L$ (see figure C.4).

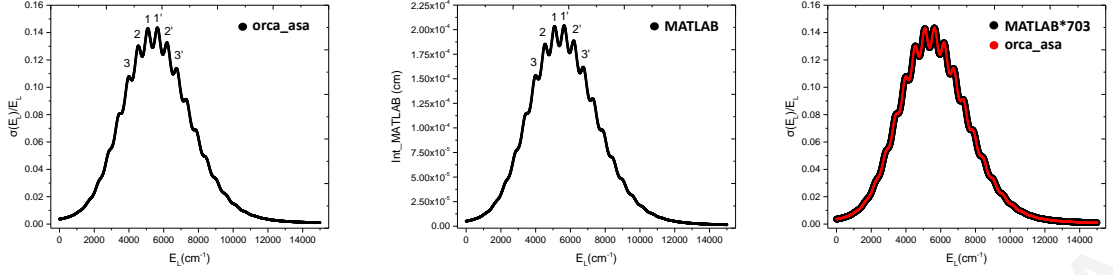


Figure C.4: Example of a single-mode system with low frequency mode. *Left.* Absorption cross section $\sigma(E_L)/E_L$ as a function of the energy E_L computed with the orca_asa program. *Middle.* FCF integral as a function of the energy E_L computed with our MATLAB code. *Right.* The FCFs computed with the MATLAB program are multiplied by the $\langle \text{constant} \rangle \sim 703$ to produce the absorption spectrum $\sigma(E_L)/E_L$.

peak No.	MATLAB		orca_asa		
	E_L (cm^{-1})	Int_MATLAB (cm)	E_L (cm^{-1})	$\sigma(E_L)/E_L$	constant (eq. C.2)
1	5090.33	2.0327E-4	5090.33	0.1429	703.1673
2	4541.02	1.8521E-4	4541.02	0.1302	703.1866
3	4003.91	1.5333E-4	4003.91	0.1078	703.1423
1'	5639.65	2.0401E-4	5639.65	0.1435	703.1621
2'	6188.96	1.8860E-4	6188.96	0.1326	703.1283
3'	6738.28	1.6179E-4	6738.28	0.1138	703.0806

Table C.1: Absorption cross section $\sigma(E_L)/E_L$ and FCF integrals (Int_MATLAB) computed at the energy E_L of each peak shown in figure C.4. The constant value was derived from equation C.2 for each peak.

We repeat the simulations for a single-mode system but now with high-frequency mode ($\omega = 967.9 \text{ cm}^{-1}$) and reorganization energy $\lambda = 22583.5 \text{ cm}^{-1}$. The simulated spectrum at zero temperature ($T = 0 \text{ K}$) with $\Gamma = 333.5 \text{ cm}^{-1}$ (10 psec) is shown in figure C.5(a). From the spectrum we deduce the $\sigma(E_L)/E_L$ ($=0.0724$) and the Int_MATLAB ($=1.0300\text{E-}4$) at the energy of the maximum peak ($E_L = 22259.52 \text{ cm}^{-1}$). These parameters yield a constant value that equals to 703.0971.

Similar calculations are also performed using more complicated systems, in order to estimate the constant value. For example, for a two-mode system consisting of a low frequency mode ($\omega_1 = 564.6 \text{ cm}^{-1}$) and a high frequency mode ($\omega_2 = 967.9 \text{ cm}^{-1}$) with mode reorganization energies $\lambda_1 = 56545.9 \text{ cm}^{-1}$ and $\lambda_2 = 22583.5 \text{ cm}^{-1}$ respectively, the constant value computed at the peak energy ($E_L = 27343.8 \text{ cm}^{-1}$) is 703.2497 (with $\sigma(E_L)/E_L = 0.0855$ and Int_MATLAB = $1.2155\text{E-}4$) [see figure C.4(b)]. The absorption spectrum of a system consisting of 42 vibrational modes is shown in figures C.5(c) (at $T = 0 \text{ K}$) and C.5(d) (at $T = 300 \text{ K}$). In the first case ($T = 0 \text{ K}$) the $\sigma(E_L)/E_L$ equals 0.1196 and the Int_MATLAB equals $1.7007\text{E-}4 \text{ cm}$ which at $E_L = 1965.3 \text{ cm}^{-1}$ yield a constant value that equals to 703.1098. In the second case ($T = 300 \text{ K}$) the $\sigma(E_L)/E_L$

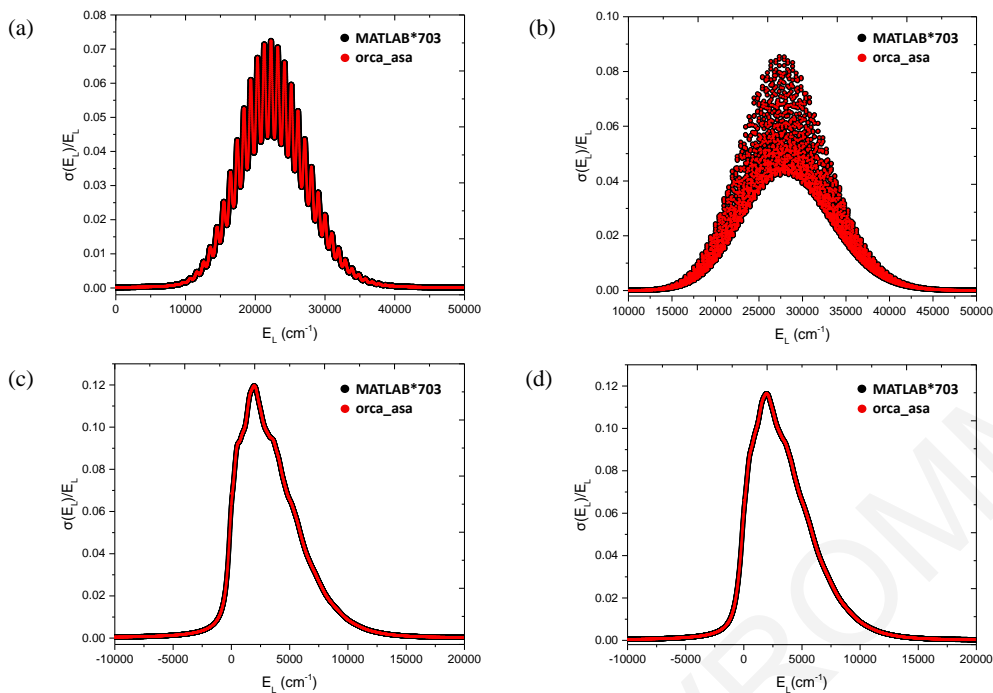


Figure C.5: Absorption spectrum $\sigma(E_L)/E_L$ as a function of the energy E_L computed with the orca_asa program (red lines) and by the MATLAB code multiplied by the $\langle \text{constant} \rangle \sim 703$ (black lines). (a) single mode system with a high frequency mode $\omega = 967.9 \text{ cm}^{-1}$, (b) two-mode system with mode frequencies $\omega_1 = 564.6 \text{ cm}^{-1}$ and $\omega_2 = 967.9 \text{ cm}^{-1}$, (c) system with 42 modes at $T = 0 \text{ K}$ and (d) the same system with 42 modes at $T = 300 \text{ K}$.

equals 0.1164 and the Int_MATLAB equals 1.6560E-4 cm. These parameters give at $E_L = 1971.4 \text{ cm}^{-1}$ a constant value that equals to 703.0797.

To summarize, we perform computations using the orca_asa program and our MATLAB code on several example systems in order to find the constant value given by eq. C.2. These systems give an average constant value that equals to 703.14 i.e., $\langle \text{constant} \rangle \sim 703$. We propose that the ISC rate parameters between singlet and triplet excited states of a quantum molecular system can be computed by computing the absorption cross section $\sigma(E_L)$ that comes from the vibrational mode frequencies and displacements of the excited states, and dividing the $\sigma(E_L)/E_L$ with the $\langle \text{constant} \rangle \sim 703$. The ISC rate is now given by eq. C.4. Note that the constant value was extracted with the assumption that the dipole moment is always set to unity ($D_x = 1, D_y = 0, D_z = 0$). The constant value is always the same and can be applied to all different systems provided that $\sigma(E_L)$ is computed by setting ($D_x = 1, D_y = 0, D_z = 0$ in the input file of the orca_asa calculation.

APPENDIX D

MATLAB code for computing the ZFS parameters

Within the distributed point dipole (DPD) model, the tensor components of the \tilde{D} matrix are given by¹

$$D_{KL} = \frac{g^2}{8} \frac{\alpha^2}{S(2S-1)} \sum_{AB} P_A^{a-b} P_B^{a-b} \left(\frac{\delta_{KL} R_{AB}^2 - 3R_{AB,K} R_{AB,L}}{R_{AB}^5} \right) \quad (\text{D.1})$$

(see section 6.4.5) where $K(L)$ refers to the Cartesian coordinates x, y, z . α is the fine structure constant ($\sim 1/137$) and S is the spin. R_{AB} is the distance between the A th and B th nuclei and $R_{AB,K(L)}$ is the $K(L)$ th coordinate distance between A and B atoms. $P_{A(B)}^{a-b}$ is the “gross” spin population on atom $A(B)$. It equals to $P_{A(B)}^{a-b} = \sum_{\mu \in A(B)} P_{\mu\mu}^a - P_{\mu\mu}^b$ where $P_{\mu\mu}^a = C_{\mu H}^a (C_{\mu H}^a)^*$ and $P_{\mu\mu}^b = C_{\mu L}^b (C_{\mu L}^b)^*$ are the diagonal matrix elements of the density matrix $P^{a(b)}$ for electron with spin $a(b)$. $C_{\mu H}^a$ and $C_{\mu L}^b$ are the expansion coefficients of the HOMO (H) and LUMO (L) molecular orbitals respectively, in the basis of the atomic orbitals.

We compute the ZFS parameters of the lowest triplet excited state (T_1) of the Cbz-TBT molecule (see chapter 6). First of all, the molecule is optimized in its triplet excited state of interest (e.g., T_1). A single-point calculation at the optimized T_1 geometry shows that the T_1 state involves the promotion of an electron from the HOMO occupied molecular orbital to the LUMO virtual molecular orbital. Therefore, the “gross” spin populations (P^{a-b}) are computed for the HOMO and LUMO orbitals. We use the ADF program package to calculate the molecular orbitals and we write a MATLAB code based on eq. D.1 to compute the ZFS parameters of the molecule.

In ADF, the molecular system is build up from fragments. Linear combinations

¹see refs.: (a) Riplinger, C.; Kao, J. P.; Rosen, G. M.; Kathirvelu, V.; Eaton, G. R.; Eaton, S. S.; Kutateladze, A.; Neese, F. Interaction of radical pairs through-bond and through-space: scope and limitations of the point-dipole approximation in electron paramagnetic resonance spectroscopy. *Journal of the American Chemical Society* **2009**, *131*, 10092-10106. (b) Bertrand, P.; Camensulli, P.; More, C.; Guigliarelli, B. A local spin model to describe the magnetic interactions in biological molecules containing $[4\text{Fe-4S}]^+$ clusters. Application to Ni-Fe hydrogenases. *Journal of the American Chemical Society* **1996**, *118*, 1426-1434.

of the fragment orbitals (FOs) that belong to the same or different fragment create symmetry-adapted basis functions that are called symmetrized fragment orbitals (SFOs) and are used as basis functions for the molecular calculation. In our case the fragments are the atoms and the FOs are the corresponding atomic orbitals. Since the computations are performed without symmetry constraints, the SFOs involve one FO from the same fragment. Therefore, each SFO corresponds to an atomic orbital.

Figure E.1 shows our MATLAB code for the computation of the ZFS parameters. The HOMO and LUMO molecular orbitals are written in the basis of the SFOs (i.e., the atomic orbitals) and the coefficients of the linear combinations are written in the matrices “coefficientsHOMO” (for the HOMO orbital) and “coefficientsLUMO” (for the LUMO orbital) [see lines 8-9 in the code]. The SFOs corresponding to each atom are written in a 2×2 matrix (“SFOs” see line 10 in the code). The SFOs are numbered from 1 up to n_SFO (see line 19 in the code) and these numbers are written in the first column of the “SFOs” matrix while the second column shows the number of the atom that each SFO corresponds to. The atomic coordinates are written (in Angstroms) in the “coordinates” matrix (see line 13 in the code).

The SFOs that belong to each atom (i.e., the atomic orbitals for each atom) are summarized in matrix “SFOsInAtoms”. The first element of each row shows the number of the atom, and the number of the SFOs that belong to each atom are written in the adjacent columns (see line 25 and lines 47-74 in the code). This matrix helps to separate which atomic orbital coefficients from matrices “coefficientsHOMO” and “coefficientsLUMO” correspond to each atom. This procedure is described in function “AtomicOrbitalCoeff” which returns two matrices (“coeffHOMO” for HOMO and “coeffLUMO” for LUMO orbitals) that contain the atomic orbital coefficients corresponding to each atom, in rows (see line 27 and lines 75-105 in the code). The “coeffHOMO” and “coeffLUMO” matrices are used to compute the “gross” spin populations per atom. The results are stored in matrix “P_atom” (see line 30 and lines 108-127 in the code). The distance R_{AB} (see eq. D.1) is computed using the atomic coordinates from matrix “coordinates”, as described in function “distance” (see “R_mn” matrix in line 32 and lines 128-141 in the code). Finally, the matrix elements $D_{KL}(K, L = x, y, z)$ (before being multiplied by the constants, see eq. D.1) are computed by use of the “P_atom” and “R_mn” matrices as input in the “D_matrix” function (see line 34 and lines 142-175 in the code). The \tilde{D} -tensor matrix is not diagonal in the (x, y, z) -axis system. Upon diagonalization of the matrix we get the three principal values of the ZFS tensor (D_{11}, D_{22}, D_{33}) (see lines 41-42 in the code). We used the “zfsframes” function of the EasySpin program available for MATLAB to find which of the three values correspond to the alignments at the X, Y and Z directions (line 46 in the code). Easyspin chooses the same notation as ORCA.²

²see ref. Stoll, S.; Schweiger, A. EasySpin, a comprehensive software package for spectral simulation and analysis in EPR, *Journal of Magnetic Resonance* **2006**, *178*, 42-55.

```

1 % PROGRAM FOR THE COMPUTATION OF THE ZFS PARAMETERS USING THE DPD MODEL FOR THE FIRST TRIPLET EXCITED STATE
2 % T1[>75% HOMO --> LUMO]
3 %
4 clear
5 clc
6 %%%%%%%%%%%%%%%%%%%%%%%%%%%%%%%%%%%%%%%%%%%%%%%%%%%%%%%%%%%%%%%%%%%%%%%%%
7 % READING THE ADF OUTPUT
8 coefficientsHOMO = readmatrix('HOMO_syn2'); % read the atomic orbital coefficients of HOMO orbital
9 coefficientsLUMO = readmatrix('LUMO_syn2'); % read the atomic orbital coefficients of LUMO orbital
10 SFOs = readmatrix('SFOs_anti2'); % symmetrized fragment orbitals
11 % 1st column: number of SFO
12 % 2nd column: number of atom
13 coordinates = readmatrix('coord_T1_syn2'); % xyz coordinates of the T1 state in Angstroms
14 % 1st column: x coordinates
15 % 2nd column: y coordinates
16 % 3rd column: z coordinates
17 %%%%%%%%%%%%%%%%%%%%%%%%%%%%%%%%%%%%%%%%%%%%%%%%%%%%%%%%%%%%%%%%%%%%%%%%%
18 % CONSTANT VALUES IN SI
19 n_SFO = 1021; % total number of SFOs in the computation
20 N_atoms = 47; % total number of atoms in the molecule
21 g = 2; % g factor of the electron (taken to be isotropic)
22 fine = 1/137; % fine structure constant in J.T^-1
23 %%%%%%%%%%%%%%%%%%%%%%%%%%%%%%%%%%%%%%%%%%%%%%%%%%%%%%%%%%%%%%%%%%%%%%%%%
24 %
25 SFOsInAtoms = SFO(N_atoms,n_SFO,SFOs); % matrix showing which SFOs corresponds to each atom
26 %
27 [coeffHOMO, coeffLUMO,num_columns] = AtomicOrbitalCoeff(N_atoms,n_SFO,SFOsInAtoms,coefficientsHOMO,coefficientsLUMO);
28 % coeffHOMO: matrix with the atomic orbital coefficients of HOMO for each atom in rows
29 % coeffLUMO: matrix with the atomic orbital coefficients of LUMO for each atom in rows
30 P_atom = GrossSpinPopulations(coeffHOMO,coeffLUMO,N_atoms,num_columns);
31 % matrix with the gross spin populations on each atom
32 R_mn = distance(N_atoms,coordinates); % squared distance between m-th and n-th nuclei
33 %
34 D_matrix = ZFS(N_atoms,coordinates,P_atom,R_mn); % ZFS matrix that is not multiplied by the constant values
35 %
36 D_matrix = D_matrix*0.529^3; % 1 a.u. of length = 0.529 Angstroms
37 D_final = D_matrix*(g^2/8)*fine^2; % ZFS matrix in Hartree
38 D_final = D_final*2.194746*10^5 % ZFS matrix in cm**^-1 (1 Hartree = 2.1947*10^5 cm^-1)
39 %
40 % Diagonalization of D matrix
41 [V_D, E_D] = eig(D_final);
42 E = diag(E_D) % the three principal values at ZFS tensor
43 %
44 % Take the 3 principal values as inputs, examine all possible eigenframe alignments, compute the scalar parameters D and E
45 for each of them and determine the conventional one
46 zfsframes(E(1),E(2),E(3))

47 %%%%%%%%%%%%%%%%%%%%%%%%%%%%%%%%%%%%%%%%%%%%%%%%%%%%%%%%%%%%%%%%%%%%%%%%%
48 % FUNCTION THAT DETERMINES WHICH SFOs CORRESPOND TO EACH ATOM
49 %%%%%%%%%%%%%%%%%%%%%%%%%%%%%%%%%%%%%%%%%%%%%%%%%%%%%%%%%%%%%%%%%%%%%%%%%
50 %
51 function [SFOsInAtoms] = SFO(N_atoms,n_SFO,SFOs)
52 %
53 SFOsInAtoms = zeros(N_atoms,n_SFO); % matrix Atoms: 1st column: the number of atoms
54 % other columns: the SFOs corresponding to each atom
55 % (each row contains the SFOs of each atom)
56
57 %
58 n = 1; % counter of the rows of matrix Atoms (counts the number of atoms)
59 s = 2; % counter for the columns of matrix Atoms (which SFOs corresponds to each atom)
60 for i = 1:n_SFO
61 SFOsInAtoms(n,1) = n;
62 if SFOs(i,2) == n
63 SFOsInAtoms(n,s) = SFOs(i,1);
64 s = s+1;
65 else
66 n = n+1;
67 s = 2;
68 if SFOs(i,2) == n
69 SFOsInAtoms(n,s) = SFOs(i,1);
70 s = s+1;
71 end
72 end
73 end
74 end

```

```

75 %%%%%%%%%%%%%%%%%%%%%%%%%%%%%%%%%%%%%%%%%%%%%%%%%%%%%%%%%%%%%%%%%%%%%%%%%
76 % FUNCTION FOR WRITING THE ATOMIC ORBITAL COEFFICIENTS CORRESPONDING TO EACH ATOM IN A MATRIX
77 %%%%%%%%%%%%%%%%%%%%%%%%%%%%%%%%%%%%%%%%%%%%%%%%%%%%%%%%%%%%%%%%%%%%%%%%%
78 %
79 function [coeffHOMO, coeffLUMO,num_columns] = AtomicOrbitalCoeff(N_atoms,n_SFO,SFOsInAtoms,coefficientsHOMO,coefficientsLUMO)
80 %
81 coeffHOMO = zeros(N_atoms,n_SFO); % matrices initially filled with zeros
82 coeffLUMO = zeros(N_atoms,n_SFO);
83 dim_coeffHOMO = zeros(n_SFO,1); % matrix that help us to find the dimensions of coeffHOMO matrix
84 %
85 k = 1; % counter for SFOs
86 p = 1; % counter for columns that we put the coefficient matrix columns
87 for i = 1:N_atoms
88     m = i+1;
89     if m <= N_atoms
90         for j = k:(SFOsInAtoms(m,2) - 1)
91             coeffHOMO(i,p) = coefficientsHOMO(j); % HOMO coefficients
92             coeffLUMO(i,p) = coefficientsLUMO(j); % LUMO coefficients
93             p = p + 1;
94         end
95         k = j + 1;
96         p=1;
97     else
98         for j = k:n_SFO
99             coeffHOMO(i,p) = coefficientsHOMO(j); % HOMO coefficients
100            coeffLUMO(i,p) = coefficientsLUMO(j); % LUMO coefficients
101            p = p + 1;
102        end
103    end
104    dim_coeffHOMO(i) = p;
105 end
106 num_columns = max(dim_coeffHOMO); % maximum number of columns in coeffHOMO matrix
107 end

108 %%%%%%%%%%%%%%%%%%%%%%%%%%%%%%%%%%%%%%%%%%%%%%%%%%%%%%%%%%%%%%%%%%%%%%%%%
109 % FUNCTION FOR COMPUTING THE GROSS SPIN POPULATIONS
110 %%%%%%%%%%%%%%%%%%%%%%%%%%%%%%%%%%%%%%%%%%%%%%%%%%%%%%%%%%%%%%%%%%%%%%%%%
111 %
112 function P_atom = GrossSpinPopulations(coeffHOMO,coeffLUMO,N_atoms,num_columns)
113 %
114 P_atom = zeros(47); % matrix initially filled with zeros
115 %
116 P = 0; % the gross spin population of each atom
117 for i = 1:N_atoms
118     for j = 1:num_columns
119         p_mm_H = coeffHOMO(i,j)*coeffHOMO(i,j); % HOMO - HOMO
120         p_mm_L = coeffLUMO(i,j)*coeffLUMO(i,j); % LUMO - LUMO
121         L_H = (p_mm_H - p_mm_L);
122         P = P + L_H;
123     end
124     P_atom(i) = P;
125     P = 0;
126 end
127 end

128 %%%%%%%%%%%%%%%%%%%%%%%%%%%%%%%%%%%%%%%%%%%%%%%%%%%%%%%%%%%%%%%%%%%%%%%%%
129 % FUNCTION FOR COMPUTING THE SQUARED DISTANCE BETWEEN m AND n ATOMS
130 %%%%%%%%%%%%%%%%%%%%%%%%%%%%%%%%%%%%%%%%%%%%%%%%%%%%%%%%%%%%%%%%%%%%%%%%%
131 %
132 function R_mn = distance(N_atoms,coordinates)
133 %
134 R_mn = zeros(47,47); % matrix initially filled with zeros
135 %
136 for m = 1:N_atoms
137     for n = 1:N_atoms
138         R_mn (m,n) = (coordinates(m,1)-coordinates(n,1))^2 + (coordinates(m,2)-coordinates(n,2))^2 + (coordinates(m,3)-coordinates(n,3))^2;
139     end
140 end
141 end

```

```

142 %%%%%%%%%%%%%%%%%%%%%%%%%%%%%%%%%%%%%%%%%%%%%%%%%%%%%%%%%%%%%%%%%%%%%%%%%
143 % FUNCTION FOR CALCULATING THE D-TENSOR MATRIX
144 %%%%%%%%%%%%%%%%%%%%%%%%%%%%%%%%%%%%%%%%%%%%%%%%%%%%%%%%%%%%%%%%%%%%%%%%%
145 %
146 %
147 function D_matrix = ZFS(N_atoms,coordinates,P_atom,R_mn)
148 %
149 D_matrix = zeros(3,3); % matrices initially filled with zeros
150 %
151 D = 0; % initial condition for D sum
152 for i = 1:3
153     for j = 1:3
154         for m = 1:N_atoms
155             for n = 1:N_atoms
156                 if m == n
157                     d = 0;
158                 else
159                     non_diagonal = (coordinates(m,i)-coordinates(n,i))*(coordinates(m,j)-coordinates(n,j));
160                     first_part = P_atom(m)*P_atom(n);
161                     if i == j
162                         second_part = (R_mn(m,n)-(3*non_diagonal))/(sqrt(R_mn(m,n)))^5;
163                     else
164                         second_part = (-3*non_diagonal)/(sqrt(R_mn(m,n)))^5;
165                     end
166                     d = first_part*second_part;
167                 end
168                 D = D + d;
169             end
170         end
171         D_matrix(i,j) = D;
172         D = 0;
173     end
174 end
175 end

```

Figure D.1: MATLAB code for the computation of the ZFS parameters according to equation D.1.

APPENDIX E

MATLAB code for computing the MFPTs

```
1 clear
2 clc
3 %
4 Format long
5 %
6 %%%%%%%%%%%%%%%%%%%%%%%%%%%%%%%%%%%%%%%%%%%%%%%%%%%%%%%%%%%%%%%%%%%%%%%%%
7 % CONSTANT VALUES
8 %
9 V = 0.15; % coupling between sites (eV)
10 N = 50; % dimensions of the Hamiltonian matrix
11 h_bar = 0.6582; % Planck constant in eV*fsec
12 g_initial = 0.0000001; % initial value of g_l 0.0000001 0.001 (* fsec)
13 g_final = 0.001; % final value of g_l 0.001 1 (* fsec)
14 g_step = 0.0000002; % step 0.0000002 0.0005
15 rate_Vs_Gamma = zeros(round(g_final/g_step),2);
16 %
17 %%%%%%%%%%%%%%%%%%%%%%%%%%%%%%%%%%%%%%%%%%%%%%%%%%%%%%%%%%%%%%%%%%%%%%%%%
18 % FIRST STEP: Building Liouvillian Matrix - PART 1
19 H = Hamiltonian(N,V); % Hamiltonian matrix
20 [Liouv_coh,stoixeia] = LiouvillianCoherent(N,H); % coherent part of Liouvillian matrix
21 %
22 s = 1; % counter of gamma
23 for g_l = g_initial:g_step:g_final
24 % FIRST STEP: Building Liouvillian Matrix - PART 2
25 gamma = MatrixGamma(N,g_l); % Matrix with gamma rates
26 Liouv_incoh = LiouvillianIncoherent(N,gamma); % incoherent part of Liouvillian matrix
27 LiouvilleMatrix = Liouv_coh + Liouv_incoh; % Liouvillian matrix with coh and incoh parts
28 %
29 %%%%%%%%%%%%%%%%%%%%%%%%%%%%%%%%%%%%%%%%%%%%%%%%%%%%%%%%%%%%%%%%%%%%%%%%%
30 % SECOND STEP: eigenstates - eigenvalues of Liouvillian Matrix
31 [right,energ,left] = eig(LiouvilleMatrix); % diagonalization of the Liouvillian matrix
32 % right: right eigenvectors (in COLUMNS)
33 % left: left eigenvectors (in COLUMNS)
34 % energ: eigenvalues
35 [right_norm, left_norm] = Eigenvectors(N,right,left); % normalized right and left eigenvectors
36 %
37 %%%%%%%%%%%%%%%%%%%%%%%%%%%%%%%%%%%%%%%%%%%%%%%%%%%%%%%%%%%%%%%%%%%%%%%%%
38 % THIRD STEP: Calculation of the transition rates 1 --> N
39 time = CalculationOfRate(N,right_norm,left_norm,energ); % in fsec
40 rate = 1/time; % in fsec^-1
41 rate_Vs_Gamma(s,2) = rate/g_l;
42 rate_Vs_Gamma(s,1) = g_l;
43 s = s + 1;
44 end
45 writematrix(rate_Vs_Gamma,'RateVsGammaVsGamma_N50.xlsx');
```

```

46 %%%%%%%%%%%%%%%%%%%%%%%%%%%%%%%%%%%%%%%%%%%%%%%%%%%%%%%%%%%%%%%%%%%%%%%%%
47 % FUNCTION TO CONSTRUCT THE HAMILTONIAN MATRIX
48 %%%%%%%%%%%%%%%%%%%%%%%%%%%%%%%%%%%%%%%%%%%%%%%%%%%%%%%%%%%%%%%%%%%%%%%%%
49 %
50 function H = Hamiltonian(N,V)
51     H = zeros(N,N);
52     for f = 1:N
53         H(f,f) = 0;
54         if f<N
55             H(f,f+1) = V;
56             H(f+1,f) = V;
57         end
58     end
59 end

60 %%%%%%%%%%%%%%%%%%%%%%%%%%%%%%%%%%%%%%%%%%%%%%%%%%%%%%%%%%%%%%%%%%%%%%%%%
61 % FUNCTION TO CONSTRUCT THE COHERENT PART OF LIOUVILLIAN MATRIX
62 %%%%%%%%%%%%%%%%%%%%%%%%%%%%%%%%%%%%%%%%%%%%%%%%%%%%%%%%%%%%%%%%%%%%%%%%%
63 %
64 function [Liouv_coh,stoixeia] = LiouvillianCoherent(N,H)
65 %
66     H_complex = ctranspose(H);           % complex conjugate of Hamiltonian matrix
67 %
68     L = 0;                               % counter for the rows of Liouville matrix
69     r = 0;                               % counter for the columns of Liouville matrix
70 %
71     Liouv_coh = zeros(N^2,N^2);
72 %
73     for j = 1:N
74         for k = 1:N
75             L = L + 1;
76             for m = 1:N
77                 for n = 1:N
78                     r = r + 1;
79                     if k == n
80                         first = H(j,m);
81                     else
82                         first = 0;
83                     end
84                     if j == m
85                         second = H_complex(k,n);
86                     else
87                         second = 0;
88                     end
89                     Liouv_coh(L,r) = first-second;
90                 end
91             end
92             r = 0;
93         end
94     end
95 end

96 %%%%%%%%%%%%%%%%%%%%%%%%%%%%%%%%%%%%%%%%%%%%%%%%%%%%%%%%%%%%%%%%%%%%%%%%%
97 % FUNCTION TO CONSTRUCT THE MATRIX WITH THE RELAXATION-DEPHASING GAMMA
98 %%%%%%%%%%%%%%%%%%%%%%%%%%%%%%%%%%%%%%%%%%%%%%%%%%%%%%%%%%%%%%%%%%%%%%%%%
99 %
100 function gamma = MatrixGamma(N,g_l)
101 %
102     gamma = zeros(N,N);                 % in units of fsec**-1 (not eV)
103 %
104     g = 0;                               % gamma
105     g_last = g_l;                       % gamma of the last site
106     g_deph = 0.2;                       % dephasing gamma
107 %
108     for j = 1:N
109         for k = 1:N
110             if j == k
111                 gamma(j,j) = g;         % diagonal elements
112             else
113                 gamma(j,k) = g_deph;   % non-diagonal elements
114             end
115         end
116     end
117     gamma(N,N) = g_last;
118 end

```

```

120 %%%%%%%%%%%%%%%%%%%%%%%%%%%%%%%%%%%%%%%%%%%%%%%%%%%%%%%%%%%%%%%%%%%%%%%%%
121 % FUNCTION TO CONSTRUCT THE INCOHERENT PART OF LIOUVILLIAN MATRIX
122 %%%%%%%%%%%%%%%%%%%%%%%%%%%%%%%%%%%%%%%%%%%%%%%%%%%%%%%%%%%%%%%%%%%%%%%%%
123 %
124 function Liouv_incoh = LiouvillianIncoherent(N,gamma)
125 %
126 h_bar = 0.6582; % Planck constant (eV*fsec)
127 Liouv_incoh = zeros(N^2,N^2);
128 %
129 L = 0; % counter for the rows of Liouville matrix
130 r = 0; % counter for the columns of Liouville matrix
131 %
132 for j = 1:N
133     for k = 1:N
134         L = L + 1;
135         for m = 1:N
136             for n = 1:N
137                 r = r + 1;
138                 if j == m && k == n
139                     Liouv_incoh(L,r) = -1i*h_bar*((gamma(j,j) + gamma(k,k))/2)-1i*h_bar*gamma(j,k);
140                 end
141                 if j == k && m == n && j == m
142                     Liouv_incoh(L,r) = -1i*h_bar*gamma(j,j);
143                 end
144             end
145         end
146         r = 0;
147     end
148 end
149 end

150 %%%%%%%%%%%%%%%%%%%%%%%%%%%%%%%%%%%%%%%%%%%%%%%%%%%%%%%%%%%%%%%%%%%%%%%%%
151 % FUNCTION TO CALCULATE THE NORMALIZED RIGHT AND LEFT EIGENVECTORS
152 %%%%%%%%%%%%%%%%%%%%%%%%%%%%%%%%%%%%%%%%%%%%%%%%%%%%%%%%%%%%%%%%%%%%%%%%%
153 %
154 function [right_norm, left_norm] = Eigenvectors(N,right,left)
155 %
156 right_norm = zeros(length(right),1);
157 left_norm = zeros(1,length(left));
158 %
159 left = ctranspose(left); % left eigenvectors IN ROWS
160 normalization = sqrt(left*right);
161 %
162 for k = 1:N^2
163     for m = 1:N^2
164         right_norm(k,m) = right(k,m)/normalization(m,m); % IN COLUMNS
165         left_norm(k,m) = left(k,m)/normalization(k,k); % IN ROWS
166     end
167 end
168 end

169 %%%%%%%%%%%%%%%%%%%%%%%%%%%%%%%%%%%%%%%%%%%%%%%%%%%%%%%%%%%%%%%%%%%%%%%%%
170 % FUNCTION TO CALCULATE THE TIME AND RATES OF TRANSITION
171 %%%%%%%%%%%%%%%%%%%%%%%%%%%%%%%%%%%%%%%%%%%%%%%%%%%%%%%%%%%%%%%%%%%%%%%%%
172 %
173 function time = CalculationOfRate(N,right_norm,left_norm,energ)
174 %
175 h_bar = 0.6582; % Planck constant in eV*fsec
176 %
177 sum = 0;
178 sum_t = 0;
179 for m = 1:N^2
180     Res = right_norm(N^2,m)*left_norm(m,1);
181     sum = sum + (h_bar*Res)/(1i*energ(m,m));
182     sum_t = sum_t - (h_bar^2*Res)/((energ(m,m)^2));
183 end
184 time = sum_t/sum; % in fsec
185 end

```

Figure E.1: MATLAB code for the computation of the mean first passage times (MFPTs) by solving the Liouville equation.